
THE UNIVERSITY *of* EDINBURGH

# New Strategies for the Synthesis of Hypercrosslinked Polymers (HCPs) Applied in Separation Processes

Liang Ding

*Thesis submitted for the degree of*
*Doctor of Philosophy*

The University of Edinburgh

2024

# Abstract

Hypercrosslinked polymers (HCPs), known for high surface area and great thermochemical stability, have gained attention in various scientific and industrial fields since they were first reported by Davankov and Tsyuruna in 1971 via Friedel-Crafts chemistry. However, their irregular pore structures, insoluble powder form, and reliance on hazardous solvents hinder their processibility and sustainability.

Hence, this thesis explores new synthesis protocols for HCPs to improve their processibility and sustainability, and systematically evaluates their performance in various separation processes. In this thesis, well-developed 3D printing technology and the eco-friendly deep eutectic solvents (DESs) are innovatively combined with Friedel-Crafts chemistry to produce HCPs monoliths and a series of HCPs from various starting monomers respectively. In particular, it emphasised the relationship between the $CO_2/N_2$ gas selectivity and the textural properties of HCPs, providing deep insight on the molecular design of porous HCPs and control over their porosity.

Necessary knowledge of the latest development of HCPs and sustainable DESs is introduced in the first two chapters. Methodology, materials and characterisation techniques are summarised in Chapter 3. The research work presented in this thesis starts with synthesising structure-retained high-impact polystyrene (HIPS) HCPs monoliths via the combination of 3D-printing technology and novel stepwise hypercrosslinking strategy. Both the mechanical strength and porosity of HIPS monoliths are maintained by adjusting the reaction time at each crosslinking step. These engineered porous HIPS monoliths (SA: 337 $m^2$ $g^{-1}$) have been employed for the adsorption of dyes, oils and even biomolecules such as taxadiene, which is an essential intermediate in the synthesis of anticancer medicine. Notably, the capacity of HIPS monoliths for taxadiene (20 mg $L^{-1}$) is comparable to that of a commercial adsorbent named HP-20.

After validating the viability of producing configuration-preserved HCPs monoliths by 3D printing, this thesis focuses on improving the sustainability of HCPs production. In Chapter 5, eco-friendly DESs replace conventional halogenated solvents, with

[ChCl][$ZnCl_2$]$_2$ and [ChCl][$FeCl_3$]$_2$ identified as feasible alternatives for synthesising HCPs while serving as the catalyst in Friedel-Crafts reactions simultaneously. This versatile protocol, utilising various monomers, yields HCPs with narrower pore size distributions, enhancing $CO_2/N_2$ gas selectivity despite the fact that the specific surface areas of HCPs synthesised in DESs were 20 – 60% lower than those produced in halogenated solvents. The highest $CO_2/N_2$ selectivity was achieved by poly-α,α'-dichloro-p-xylene that synthesised in [ChCl][$ZnCl_2$]$_2$, reaching a value of 105. Moreover, possible mechanisms for the DES-intermediate hypercrosslinking process are proposed. This work not only successfully expands the application of DES in polymerisation chemistry, but also highlight the advantage of DES in adjusting the pore size of HCPs.

Based on the findings from Chapter 5, starting materials from bio-resources are preferred to further improve the sustainability. Hence, kraft lignin processed from corn stalks is used as the starting material to crosslink with different agents in DESs. Despite the deficient BET surface area, these lignin-based HCPs proved impressive $CO_2$ capture ability because of their abundant oxygen-containing groups and uniform narrow micropores. Moreover, they exhibited outstanding $CO_2/N_2$ selectivity in the practical gas mixture, reaching 835. This work successfully verified the feasibility of DESs for post-crosslinking type synthetic route in addition to internal and external hypercrosslinking. Significantly, the advantage of DESs in promoting narrow pores was further confirmed.

To conclude, this thesis recognises the strong desire for processable HCPs and greener HCPs, developing novel synthetic protocols for HCPs and deepening the understanding of the relationship between textural properties of the HCPs and their separation performance.

# Lay summary

Porous materials have been widely used as adsorbents in the various separation process due to their considerable capacity derived from their intrinsic inner voids. Effective efforts have been devoted to the preparation of advanced porous materials such as zeolites, activated carbon, metal organic frameworks (MOFs), polymers of intrinsic microporosity (PIMs), etc. Here, the research focus on the hypercrosslinked polymers (HCPs), which are characterised by a highly crosslinked structure, resulting in a three-dimensional network with interconnected pores. This distinctive architecture imparts high surface areas, abundant micropores and remarkable thermal stability to HCPs, setting them apart from conventional porous materials.

The development of HCPs has experienced significant advancements since their initial report by Davankov and Tsyurupa in 1971. The scope of HCPs has been notably expanded following Friedel-Crafts chemistry, a basic principle that directs their rapid growth in various fields. It needs to be highlighted that extensive micropores and rigid structures in HCPs contributes to their exceptional performance in applications ranging from adsorption, catalysis, and sensing. Despite their promising prospect, challenges such as uncontrollable reaction kinetics, the shape of brittle amorphous powders and large consumption of hazardous solvents hinder the widespread use of HCPs. This thesis addresses these challenges head-on and aims at converting the synthesis of HCPs to a controllable, processable and sustainable manner. The separation performance of all obtained HCPs will be thoroughly evaluated. To be more specific, the $CO_2/N_2$ gas adsorption and separation is highlighted, providing more insight on the relationship between the textural properties of HCPs materials and their carbon capture performance.

Fundamental background knowledge of the up-to-date development of HCPs and deep eutectic solvents (DESs) is introduced in the first two chapters. Characterisation and methodology used in the research work are elaborated in Chapter 3. Chapter 4 innovatively combined well-developed 3D-printing technique and stepwise hypercrosslinking to produce high-impact polystyrene (HIPS) HCPs monoliths with

preserved mechanical strength and porosity, overcoming the problem of difficult processing of amorphous powders. These monolithic HCPs were effective in removing dyes, absorbing oils, and recovering valuable anticancer biomolecules such as taxadine. It is noteworthy that the adsorption capacity of HIPS HCPs monoliths for taxadine is comparable to commercial adsorbents named HP-20. In this project, the use of 3D printing opens up new possibilities for shaping HCPs into practical forms that can be tailored for specific applications. This work proposed a feasible method to enhance the processability of HCPs and define their configurations to satisfy different requirements.

Chapter 5 emphasises on improving the sustainability of HCPs and explores the use of eco-friendly deep eutectic solvents (DESs) as alternatives to traditional halogenated solvents which are widely used in the synthesis of HCPs. Two different DESs that containing metal halides ($ZnCl_2$ or $FeCl_3$) and choline chloride (ChCl) serve as solvents and catalysts simultaneously. These DESs not only prove their versatility for various starting monomers, but also contribute to the superior gas selectivity of HCPs. This is due to the obviously narrower pore size of HCPs that synthesised in DESs where the crosslinking kinetics were slow. In addition, the Lewis acidity of DESs and possible mechanisms for how DESs promoted the crosslinking were studied as well. This work broadened the utilisation of DESs in polymer chemistry and pointed out its advantage in fine-tuning the pore size of HCPs.

To further improving the sustainability of HCPs, I continued to deploy biobased molecules as starting materials to produce HCPs. Here in Chapter 6, kraft lignin from corn stalks was selected to crosslink with three different crosslinkers in DESs, and yielded six lignin-based HCPs. Despite having a lower surface area, these lignin-based HCPs demonstrated impressive carbon capture abilities and outstanding selectivity in practical gas mixtures. This is caused by a joint effect of ultranarrow micropores and abundant oxygen-containing groups. It is worth mentioning that the highest $CO_2/N_2$ selectivity in the practical gas mixture reached 835, demonstrating distinctive benefits of DESs. In this project, the applicability of the DESs protocol

was expanded to renewable molecules, underlining the benefits of generating narrow micropores within DESs.

In summary, this thesis addresses the need for processable and environmentally-friendly HCPs. By developing novel synthetic methods and deepening our understanding of their properties, this work is expected to inspire future research in designing and synthesising advanced HCPs for various separations, especially in gas separations and related fields. The findings in this thesis could guide future research efforts in the design and synthesis of advanced HCPs.

# Acknowledgement

I would like to express my deepest gratitude to my primary supervisor Dr. Cher Hon Lau for his invaluable patience and sturdy support during my PhD study. I would not have undertaken this meaningful journey without his thorough guidance and opportune feedback, which inspired me to research more deeply and critically. These experiences help me to grow into an independent and mature scientific researcher and would definitely have long-term effects on my future career. Additionally, I am deeply indebted to my co-supervisor Professor Xianfeng Fan and Dr. Yi Huang who generously provided their knowledge and expertise from their research perspective. Thanks are also given for their kind help in providing necessary experimental support in this PhD project.

I would like to extend my sincere thanks to some academic staff and technicians, who work in either School of Engineering or Chemistry, for their great efforts in maintaining and training of experimental equipment. Especially, many thanks to Dr. Fergus Dingwall and Dr. John Tobin for their kind help in training me on SEM instrument and BET analysis, and Dr. Lorna Murray for her professional support on solid-state NMR characterization, and Dr. Mark Lauchlan and Mr. Alex Kirkland for their participation in solving the problems of lab work timely.

I am also grateful to my group members and lab mates, in particular Nadhita Chanchaona, Shiliang Lin and Aotian Liu who worked with me and helped me in proofreading, feedback of presentations and negotiation on experimental affairs. They worked with enthusiasm and created a positive atmosphere of research for the whole team. Special thanks should also be given to other office mates, in particular Dr. Wenjing Wei and Xiuming Wei for their great help in UV-vis spectrometer and FTIR characterisation. I would like to thank all my friends in the campus, in particular Jialin Yu, Luxi Yang, Yixuan Zhang, Yu Wang who can always accompany me, explore highly-recommended restaurants and go around Edinburgh with me during the weekends.

Lastly, thanks should also go to my parents for their firm support and devoted love for me, without which I could not concentrate on my research and successfully achieved doctoral degree. Their unwavering belief and encouragement keeps motivating me to develop my career. In addition, I would be remiss in not mentioning my cohort friends, especially Dr. Siyu Li, soon-to-be Dr. Funing Liu, Dr. Yue Feng and Dr. Fan Liao who consistently support me, selflessly share their precious experience with me and give me emotional boost when I encounter problems.

# Declaration

I declare that this thesis was composed by myself, and all the work presented herein was conducted by my own. The contributions of others have been clearly indicated and acknowledged. This work has not been submitted for any other degree or professional qualification.

LIANG DING

January 2024

# Contents

# List of Figures

# List of Tables

# List of Abbreviations

| Abbreviations | Definition |
|---|---|
| ABS | Acrylonitrile butadiene styrene |
| ATR-FTIR | Attenuated total reflectance-Fourier transform infrared spectroscopy |
| BA | Benzyl alcohol |
| BCMBP | 4, 4′-bis(chloromethyl)-1,1′-biphenyl |
| BDM | 1, 4-benzenedimethanol |
| BET | Brunauer-Emmett-Teller |
| BINAP | 2, 2′-bis(diphenylphosphino)-C,1′-binaphthyl |
| BPAF | Bisphenol AF |
| CNSL | Cashew nut shell liquid |
| CMPs | Conjugated microporous polymers |
| COF | Covalent organic frameworks |
| CR | Congo Red |
| DBF | Dibenzofuran |
| DBT | Dibenzothiophene |
| DCB | 1, 4-dichlorobutane |
| DCE | Dichloroethane |
| DCH | 1, 6-dichlorohexane |
| DCM | Dichloromethane |
| DCX | α, α’-dichloro-p-xylene |
| DES | Deep eutectic solvents |
| DMB | Dimethoxybenzene |
| DMF | Dimethylformamide |
| DOX | Doxorubicin |
| FA | Formic acid |
| FDA | Formaldehyde dimethyl acetal |
| FDM | Fused deposition modelling |
| FID | Free induction decay |
| FLUO | Fluorene |
| FTIR | Fourier transform infrared spectroscopy |
| HA | Glacial acetic acid |
| HCPs | Hypercrosslinked polymers |
| HIPS | High-impact polystyrene |
| HMOCs | Hollow microporous organic capsules |
| HPLC | High-pressure liquid chromatography |
| IBU | Ibuprofen |
| IUPAC | The International Union of Pure and Applied Chemistry |
| $LC_{50}$ | Lethal concentration at 50% |
| LOM | Laminated object manufacturing |

| | |
|---|---|
| MA | Malonic acid |
| MB | Methylene blue |
| MO | Methyl orange |
| NHCs | N-heterocyclic carbenes |
| NMR | Nuclear magnetic resonance |
| NOE | Nuclear overhauser effect |
| NR | Neutral red |
| OL | Organosolv lignin |
| PA (Nylon) | Polyamide |
| PAFs | Porous aromatic frameworks |
| PC | Polycarbonate |
| PETG | Polyethylene terephthalate glycol |
| PIMs | Polymers of intrinsic microporosity |
| PLA | Polylactic acid |
| POSS | Polyhedral oligomeric silsesquioxanes |
| PP | Polypropylene |
| PSA | Pressure swing adsorption |
| PSD | Pore size distribution |
| PTPA | Polytriphenylamine |
| RhB | Rhodamine B |
| RH | Relative humidity |
| SEC | Size-exclusion chromatography |
| SEM | Scanning electron microscopy |
| sFLUO | 9, 9’-spirobifluorene |
| SLA | Stereo lithography apparatus |
| SLS | Selective laser sintering |
| SPA | Solid phase adsorption |
| SPE | Single-pulse excitation |
| SPME | Solid-phrase microextraction |
| SSNMR | Solid-state nuclear magnetic resonance |
| TEOA | Triethyl orthoacetate |
| TfOH | Trifluoromethanesulfonic acid |
| TIPO | Triisopropyl orthoformate |
| TLC | Thin layer chromatography |
| TMOA | Trimethyl orthoacetate |
| TMOF | Trimethyl orthoformate |
| TPB | 1, 3, 5-triphenylbenzen |
| TPM | Tetraphenylmethane |
| TPP | Triptycene-based polymers |
| UA | Uniblue A |
| VOCs | Volatile organic compounds |
| VSA | Vacuum swing adsorption |
| XPS | X-ray photoelectron spectroscopy |

# Chapter 1 Introduction and literature review on hypercrosslinked polymers (HCPs)

## 1.1 Hypercrosslinked polymers

During the past few decades, porous materials have gained worldwide popularity and been extensively studied for applications in environmental and energy fields. According to the composition of porous materials, their development has gone through three stages: inorganic porous material (such as zeolites, silica and activated carbon), hybrid porous materials represented by metal organic frameworks (MOFs) which combine the advantages of both components, and totally organic porous polymers or networks. Apart from some obvious advantages of last mentioned porous organic polymers (POPs) such as outstanding intrinsic porosity, designable polymer topologies, tailorable pore structures and superior chemical stability, the most conspicuous attribute of POPs is their inherent compatibility with polymeric matrix, indicating their great potential in being processed into two-dimensional membranes and three-dimensional devices.

As shown in Figure 1-1, POPs can be categorised into different subclasses such as porous aromatic frameworks (PAFs), polymers of intrinsic microporosity (PIMs), conjugated microporous polymers (CMPs), covalent organic frameworks (COFs), and hypercrosslinked polymers (HCPs) [1]. Based on the degree of long-range order, COFs and its burgeoning branch covalent triazine frameworks (CTFs) are regarded as crystalline polymers while others are generally known as amorphous [2].

Moreover, another well-known classification of POPs is on the basis of pore size. The International Union of Pure and Applied Chemistry (IUPAC) has divided porous materials into microporous (pore diameter < 2 nm), mesoporous (pore diameter between 2 nm and 50 nm) and macroporous (pore diameter > 50 nm) [3]. A consistent

classification of pore size is crucial for comprehensive study on the physisorption behaviours of porous materials [4].

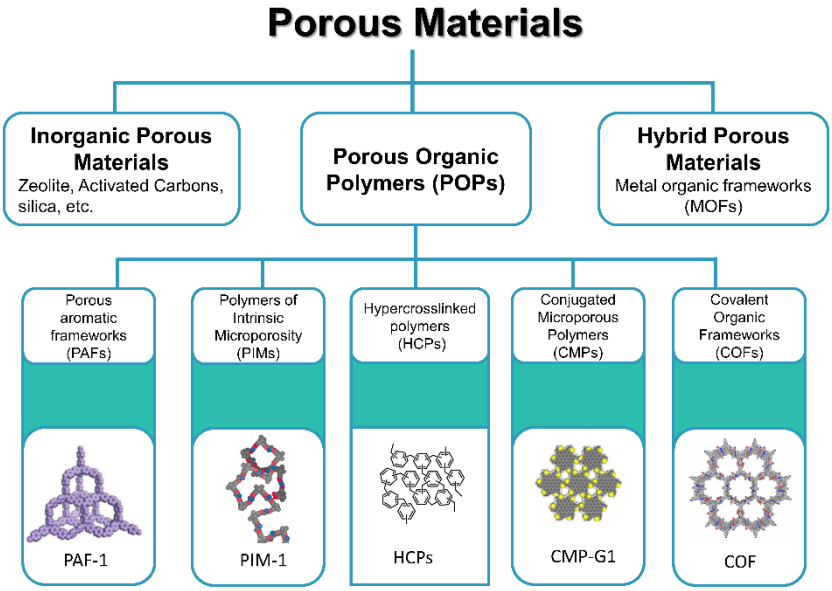


Figure 1-1: The classification of porous materials

The past few decades have witnessed the flourish in the research on hypercrosslinked polymers (HCPs) due to their advantages of mild synthetic conditions, controllable pore size, thermochemical stability, possibility of surface grafting and low cost. As the name suggests, hypercrosslinked polymers are highly crosslinked and thus possess stable and rigid polymeric networks compared with common crosslinked polymers. This could explain their super high surface area and excellent porosity without collapse of polymer networks. HCPs are nanoporous materials that synthesised mainly based on Friedel-Crafts chemistry, in which strong Lewis acids are usually required as catalysts. Here, the term ‘nanoporous’ covers both microporous and mesoporous polymers [5]. Commercialised HCPs products have been widely used as popular adsorbents for removal of volatile organic compounds [6] , hydrogen storage [7], sewage disposal [8,9], sorbents for chromatography [10], selective separation [11,12]. In addition, they show huge potential in catalysis [13], sensing, solid-phase extraction [14] etc. Hence, optimising the manufacturing process of HCPs is expected to be a

promising future research branch, which would rapidly stimulate the expansion of HCPs markets.

Basically, HCPs are not that much novel but their development have been proliferating thanks to more versatile synthetic methods proposed by researchers in recent years. The history of HCPs could be traced back to early 1970s, when Davankov and co-workers reported to synthesise highly crosslinked polystyrene-based polymers with the aid of external crosslinkers and Lewis acid catalysts [15]. Their materials possessed numerous micropores and rigid network structures benefitting from the strong linkage between aromatic rings, indicating outstanding perspectives than ordinary crosslinked polymers. After half a century of development, various HCPs materials emerged and occupied an important position in the field of chemical industry. Generally, Tan et al. [16] divided HCPs into three categories according to the synthetic methods: (1) HCPs come from post-crosslinking polymer precursors, (2) HCPs prepared by polycondensation reaction of specific monomers with functional groups, which is named as internal hypercrosslinking, (3) HCPs synthesised by knitting rigid aromatic units with external crosslinkers, which is named as external hypercrosslinking oppositely. The first method gradually became desolate as the choice of polymer precursors was mainly restricted to polystyrene-based resins. Therefore, more researchers follow the other two methods closely because of abundant starting materials.

## 1.2 Synthetic protocols of different HCPs

Hypercrosslinking could be regarded as a concept that describes more extensively crosslinked polymeric networks, which effectively increased the porosity and rigidity of materials. It was firstly introduced by Davankov's group who reported hypercrosslinked polystyrene-based materials, which are considered as third generation of polystyrene (PS) network. Thereafter, the field of HCPs has ushered in new vitality and HCPs usually refer to those polymers that follow Friedel-Crafts

chemistry. Before the emergence of HCPs, related research about crosslinked polystyrene laid the foundation for them.

First generation of polystyrene network is represented by gel-type polystyrene copolymers that copolymerised from bulk styrene and small amount of divinylbenzene (DVB) monomers (5-8%) [17]. The earliest crosslinked PS was reported by Staudinger and Heuer in 1934 and they inspected the swelling behaviours of linear PS of different molecular weights [18]. Until 1944, sulphonated styrene-DVB copolymers, which were known as cation exchange resins, had been used for cations removal from water [19]. Similarly, anion exchange resins can be prepared through amination and thus used for adsorbing anions from liquid media. These insoluble gel-type polystyrene copolymers show a difference in their swelling behaviours. Unmodified PS networks swell in non-polar solvents like dichloroethane and toluene while functionalised PS with sulfonic or ammonium groups are more vulnerable in water and strongly polar alcohols. However, these PS-based ion exchange resins beads can only work in swollen state so that the solute molecules have access to the massive internal functional sites of the beads. In dry state, the crosslinked PS beads showed extremely poor permeability and even gases cannot pass through them. This characteristic is therefore called hidden porosity. The gel-type PS copolymers became well-known for their involvement as ion exchangers in the Manhattan nuclear weapon project, in which the separation of rare earths and uranium fission products were achieved [20]. Meanwhile, the need for crosslinked polymers with permanent pores was recognised by researchers as the application of gel-type PS resins is restricted.

Second generation polystyrene networks, which are featured on permanent porosity, were first patented by McBurney in 1952 [21]. They are also named as macroporous PS because the term ‘macroporous’ was used to describe those resins that own measurable inner pores coming from pores >50Å [22]. It is worth noting that this initial name has been widely recognised as a scientific jargon even though it does not conform to the IUPAC definitions. Different from the previous generation of transparent gel-type PS, macroporous PS materials are usually opaque and swell more

quickly in solvents benefitting from their porous structures. The porosity is derived from the two-phase heterogeneous network which is copolymerised of styrene, increased DVB (6-15%) and inert porogens or diluent [20]. As the crosslinking reaction proceeds, growing polymer chains starts to precipitate and become a separate phase from the diluent. The voids are remained inside the PS beads after removing the diluent. It should be pointed out that the working life of second-generation crosslinked PS is extended because of bigger proportion of DVB. These materials generally have a total pore volume of about 1 mL $g^{-1}$ and their surface areas range from 20 to 300 $m^2$ $g^{-1}$ [17]. The average pore size of macroporous PS networks is around 20 nm, indicating their potential in capturing larger molecules [20].

This generation of PS copolymers is more friendly to all types of aqueous media and their pores do not collapse after swelling-drying cycles. Therefore, many ion exchange resins had been developed and commercialised during this period. This represents a significant milestone in the history of ion exchangers. A series of Amberlite™ products launched by Rohm and Haas manufacturer are highly recommended for their adsorbing ability and outstanding resistance against liquid media. In addition, macroporous PS networks are widely applied in catalysis [23], chromatography [24], adsorbents [25,26] and etc. They promoted the development of column chromatography including size-exclusion chromatography (SEC) and high-pressure liquid chromatography (HPLC) because they are suitable column filling materials that have high tolerance to feeding liquid, enough sorption capacity and recyclability. Except for column chromatography, they can serve as the stationary phase of thin layer chromatography. Macroporous polystyrene materials coated with a hydrophilic layer were revealed to have high affinity to proteins and applied in the purification of proteins molecules from peptides [27,28]. Some inevitable drawbacks start to appear after long-period examination. Most adsorption process can merely take place on the interface of macroporous PS materials and thus the insufficient capacity cannot meet the requirement of growing commercial applications. Unfortunately, this shortcoming is decided by the basic principle of micro-phase

separation of heterogeneous copolymers in the crosslinking reaction. Unless a new methodology is adopted, this problem will forever exist.

There is, therefore, a definite demand for porous polymers with high permeability and sorption capacity, imposing big challenges to researchers. A reasonable approach to tackle this issue was first proposed by Davankov and Tsyurupa in the early 1970s. The pioneering work of them means the start of third-generation crosslinked polystyrene networks which are based on Friedel-Crafts chemistry and have relatively high crosslinking degree (reaching 40%). Such materials are named as 'Davankov-type resins' but people are more familiar with another name 'hypercrosslinked PS'. As the choice for starting materials become variable, these obtained products are collectively called hypercrosslinked polymers (HCPs).

### 1.2.1 Post-crosslinking polymer precursors

Davankov and Tsyurupa disclosed their synthetic strategy in which linear PS or DVB-crosslinked PS fully swelled in organic solvents first to ensure polymer chains dispersed separately. The polymer chains would be anchored after adding Lewis acid catalysts (such as $AlCl_3$, $FeCl_3$, $ZnCl_2$, $SnCl_4$) and external crosslinkers. Final three-dimensional crosslinked PS networks were generated after removing the solvents and the microporosity was significantly enhanced. Scheme 1-1 displays a whole hypercrosslinking process of post-crosslinking polymer precursors [29]. The intensively crosslinked polymeric networks are rigid enough to prevent the collapse of inner voids. Unprecedentedly, many porous polymers with high specific surface area have been prepared, even reaching 2000 $m^2 g^{-1}$ [30].

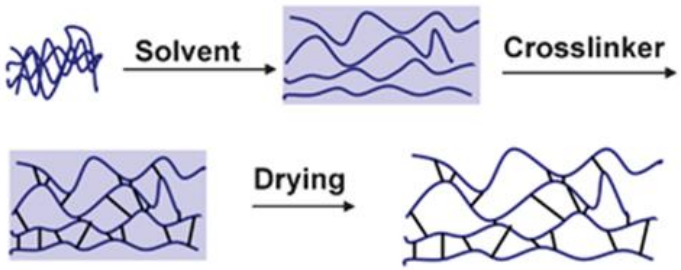


Scheme 1-1: hypercrosslinking process of polystyrene networks via post-crosslinking route [29]

Frequently used external crosslinkers generally have chloromethylene groups such as dichloro xylene (DCX) [31,32], 4,4′-bis(chloromethyl)-1,1′-biphenyl (BCMBP) [31], 1,4-bis-(p-chloromethyl-phenyl)-butane (DPB) [33,34], 1,3,5-tris-(chloromethyl)-mesitylene (CMM) [34], chloromethyl ether (CME) [35-37], and  as shown in Figure 1-2. These crosslinking agents introduce chloromethyl groups to the aromatic rings, and attack other unreacted phenyl rings to form methylene bridges between the molecules. The porosity and rigidity of HCPs can be varied depending on the combination of post-crosslinking precursors and crosslinkers. Most bifunctional crosslinkers form bridges with limited conformational mobility between PS chains and methylene bridges are the most rigid. Nevertheless, DPB is a counterexample with which conformational rearrangements are promoted because of long successive alkyl units [33,38]. And the specific surface areas of DPB-crosslinked PS networks are negligible, even less than 1 $cm^3$ $g^{-1}$. CMM, as a trifunctional crosslinker, enables the linkage between three sites simultaneously and thus creates enhanced rigidity and porosity.

However, above halogenated crosslinkers are toxic and will unavoidably yield by-products like corrosive hydrogen chloride (HCl). CME is even ranked as carcinogenic wherefore less toxic alternatives such as carbon tetrachloride ($CCl_4$) [39,40], dichloroethane (DCE) [40,41], formaldehyde dimethyl acetal (FDA) [42,43] gain popularity. DCE can function both as solvent and crosslinker during the Friedel-Crafts reaction.

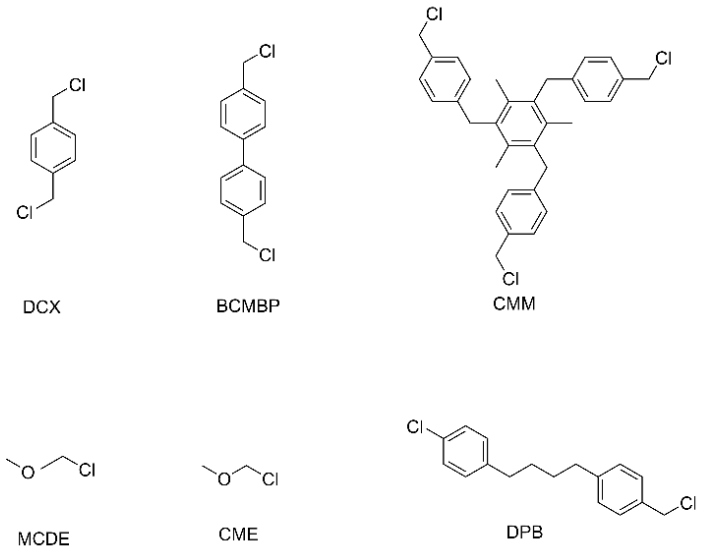


Figure 1-2: Chemical structures of frequently used crosslinkers for HCPs synthesis

Hypercrosslinking process of post-crosslinking precursors usually deploy linear PS or lightly-crosslinked PS-DVB copolymers as starting materials. The content of DVB should be controlled below 2% to generate abundant micropores [44,45]. With the increasing of DVB proportion (up to 30%), macroporous PS networks are formed. They can acquire microporosity through Friedel-Crafts reaction as well as maintaining their intrinsic macroporous structures [33,46]. But the crosslinking degree of macroporous PS precursors cannot catch up with that of linear PS because of steric effects [44]. Even though the hypercrosslinking of PS-based precursors with external electrophiles is a one-pot procedure, it involves the chloromethylation of PS-based polymers and the subsequent conversion of chloromethyl groups into crosslinking methylene bridges [47]. This inspired Nerge [48] and co-workers to use vinyl benzyl chloride-co-styrene (VBC-co-St) polymers as precursors to avoid the first chloromethylation step. They managed to synthesise hypercrosslinked polymers with high surface area and narrow distribution of small pores, up to 691 $m^2$ $g^{-1}$ when VBC monomer accounted for 90%. Similarly, Veverka and co-workers [49] deployed commercial chloromethylated gel-type styrene-divinylbenzene resins as precursors and converted these initial chloromethyl groups into methylene bridges. The surface

area of the resulting polymers was more than 900 $m^2$ $g^{-1}$. Their work broadened people's knowledge on the mechanism of hypercrosslinking process and has been extensively applied in internal hypercrosslinking, which will be illustrated in Section 1.2.2. Basically, the conversion of chloromethyl groups into methylene bridges proceeded rapidly at the first stage because they have access to neighbouring benzene rings of the polymer chains. With the construction of crosslinked networks, the residue chloromethyl groups were embedded in the highly-crosslinked domains and became inaccessible, leading to a lower conversion speed. Interestingly, the formation of porous structure lagged behind the conversion process because the polymer network needed enough methylene bridges to provide sufficient integral rigidity, which can prevent crosslinked polymers from collapse after drying.

To overcome the drawbacks of uneven commercial chloromethylated PS resins, Sherrington et al. [46] synthesised gel-type and macroporous-type divinylbenzene-vinyl benzyl chloride(DVB-VBC) precursors, whose DVB content was 2 mol% and 20 mol% respectively, for further hypercrosslinking. The surface area of HCPs obtained from gel-type DVB-VBC precursors was up to 2090 $m^2$ $g^{-1}$ by optimising experimental parameters such as Lewis acid, solvents, monomer ratio and reaction durations. The super high surface area could be explained by a more efficient crosslinking process in which doubly bridges were formed between benzyl rings as depicted in Figure 1-3. The single-pulse excitation (SPE) $^{13}C$ spectra, which allows for the quantitative determination for carbon atoms, suggested aliphatic carbon constitute a bigger portion instead of solely methylene bridges [50,51]. In addition, DVB content was an important constraint on the surface area of HCPs, which would dramatically drop to around 1400 $m^2$ $g^{-1}$ when DVB amount was increased to 8 mol%. On the other hand, HCPs synthesised from macroporous-type DVB-VBC (20 mol% DVB) precursors also exhibit high surface area, up to 1200 $m^2$ $g^{-1}$. These HCPs featured on a well-defined bimodal pore size distribution, in which the initially exist large pores was supplemented with massive micropores yielded during hypercrosslinking. Compared with conventional macroporous-type resins, this

optimisation can guarantee fast absorption kinetics and improved working capacity simultaneously. To gain a better understanding of the hypercrosslinking process, this study also investigated its kinetics. Surprisingly, taking hypercrosslinked gel-type 2% DVB-VBC as an example, more than 89% of chloromethyl groups were consumed in the first 15 minutes and its surface area approached 1200 $m^2$ $g^{-1}$. After 2 hours, the increments in both surface area and the depletion of chloromethyl groups were minor, which means reaction time longer than 2 hours was non-compulsory. Throughout the development of HCPs, varied Lewis acid can be used to facilitate the Friedel-Crafts alkylation as well as some Brønsted acid. Hence, this work compared the performance of $FeCl_3$, $AlCl_3$, and $SnCl_4$ and concluded the activity of the three metal halides catalysts follow the order: $FeCl_3$ > $AlCl_3$ > $SnCl_4$ from the perspective of surface area of all HCPs. It is possible that $AlCl_3$ has worse solubility in the reaction system and $SnCl_4$ is limited by its sheer bulk, while $FeCl_3$ become the ideal choice in terms of balancing solubility and molecular size. Sherrington's results systematically studied the effects of reaction conditions but more precise experiments are required to verify their hypotheses and conclusions.

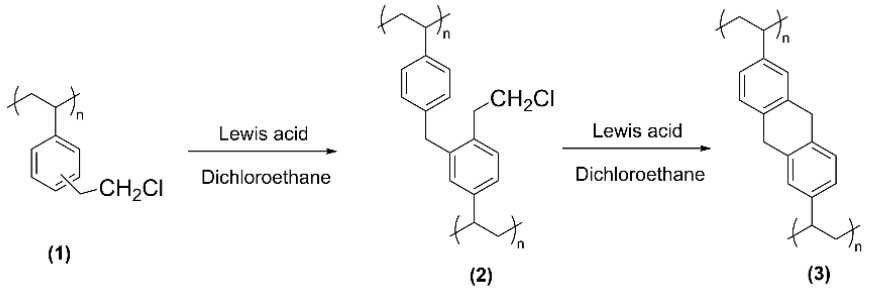


Figure 1-3: Possible chemical process of Lewis acid catalysed hypercrosslinking of DVB-VBC precursors [46]

On basis of it, Tan's group [52] accomplished in the control of pore size and distribution of a series of hypercrosslinked poly(divinylbenzene-co-vinylbenzyl chloride) (HCP-DVB-VBC) by varying the ratio of DVB from 0 to 10%. The highest surface area was achieved by HCP-DVB-VBC with 2% DVB, reaching 2064 $m^2$ $g^{-1}$. This was a turning point where the surface area of HCP-DVB-VBC increased steadily and began to decrease when the DVB content exceeded 2%. Despite the surface area

of HCP-DVB-VBC dropped after increasing DVB content, the pore structure underwent a qualitative transformation from the hierarchical porosity comprising macropores, mesopores and micropores to consistent micropores. A narrower and more uniform microporous structure was achieved if DVB content was higher than 7%. It was thus concluded that the porosity of HCP-DVB-VBC can be tailored via adjusting DVB content. The diversity of pore structures could be caused by the solubility of HCP-DVB-VBC with different DVB proportions. In the absence of DVB, the polymeric networks precursors (poly-VBC here) disperse throughout the solution in a loose and disorders manner with moveable neighbouring chains. This can explain the formation of randomly-hypercrosslinked networks combining macropores and micropores. Similar process takes place in the case of lightly-crosslinked DVB-VBC precursors (DVB<2%), in which more porous networks are generated benefitting from more organised pre-crosslinked precursors. Until DVB content reach 7%, the chains of DVB-VBC precursors are fixed, resulting in well-knit and regular pore distribution. Accordingly, more uniform hypercrosslinked polymers with mere micropores are produced.

Other than halogenated crosslinkers, polystyrene can also be hypercrosslinked with formaldehyde dimethyl acetal (FDA), which is a less toxic alternative. Thanchanok et al. prepared a series of FDA-crosslinked PS catalysed by iron chloride, and their surface areas ranged from 10 to 980 $m^2 g^{-1}$ depending on the degree of polymerisation (DP) [43]. This study revealed that the BET surface area of PS HCPs increased until DP of PS precursors reached 32. However, no substantial increase in the BET surface area was observed beyond this DP. In addition to linear PS, expanded polystyrene (EPS) waste can be upcycled into porous absorbents for water purification [53]. The capacity of EPS-FDA for 4-dichlorophenol (2, 4-DCP) and tetracycline hydrochloride (TC) contaminants reached 621.12 mg $g^{-1}$, which is much higher than some commercial activated carbon materials. The research presented in this work offers an affordable approach for transforming plastic waste into valuable absorbent materials suitable for treating wastewater, demonstrating practical implications. Yang and

coworkers [54] successfully synthesised solution-processable HCPs that can expand HCPs application to more scenarios. Distinguished from the typical insoluble HCPs that isolate from solvents, solution-processable HCPs retain the solubility even after storing in the dry state. Here, their synthetic strategy was to slowly add FDA and $FeCl_3$ catalyst into the diluted solution and thus control the kinetics of crosslinking to avoid precipitation of crosslinked segments. These soluble HCPs can be made into thin films via solution casting. Polymeric molecular sieve membranes were also reported on basis of same synthetic chemistry [55]. PS membrane quickly reacted with FDA to form a microporous cross-linked polymer shell, hindering the conversion of interior PS to porous polymer. Diffusion of FDA and $FeCl_3$ through the microporous layer resulted in the formation of a macroporous core according to Kirkendall effect. Therefore, sandwich-like hierarchical pore structure was obtained due to Kirkendall effect polymerisation as shown in Figure 1-4. The hypercrosslinked PS membranes exhibited excellent molecular sieve properties, characterised by high gas permeability and selectivity for smaller gas molecules such as $CO_2$ and $O_2$. The best membrane with a thickness of 97 μm showed high $CO_2$ uptake (up to 1.7 mmol $g^{-1}$), high $CO_2$ permeability (43 GPU) and outstanding $CO_2/N_2$ selectivity (around 40) at 273 K under 1 bar. This result is still competitive in today's research. Very recently, Zhao and co-workers reported An amine-riched molecular nodule-assembled membrane with arranged 5 Å channels, displaying a high $CO_2$ permeance of 752 GPU as well as a high $CO_2$ /$N_2$ selectivity of 67 at 1 bar [56].

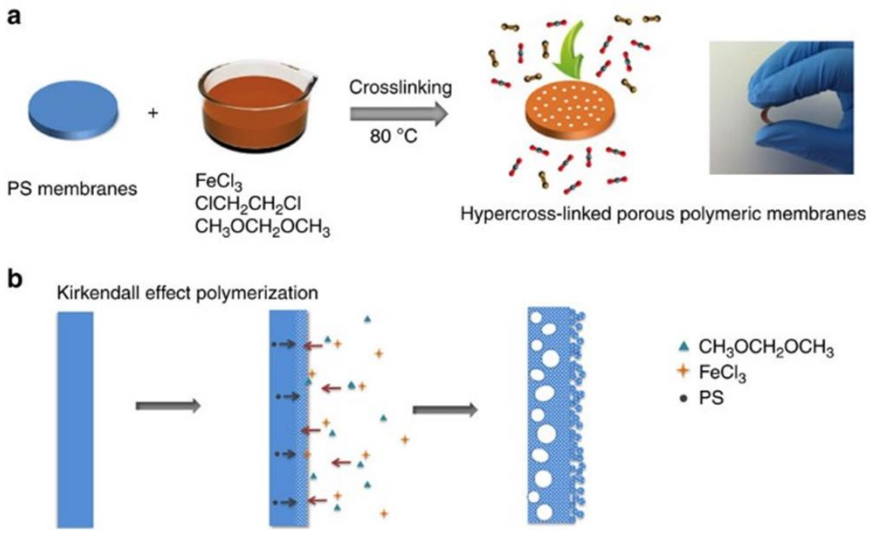


Figure 1-4: (a) The process for preparing the porous polymeric membranes, (b) hierarchical membrane interface induced by Kirkendall effect polymerisation [55]

To enhance the ability of PS-based HCPs in specific separations apart from size sieving mechanism, functional groups are introduced to increase molecular interaction. Ogawa and co-workers [57] reported spherical maleic anhydride-styrene-divinylbenzene(MA-St-DVB) polymer beads synthesised via suspension polymerisation. The anhydride groups of the beads served as acylating reagents and exhibited high reactivity towards some compounds like amines. These beads can be employed as starting materials for chelating resins containing cyclic hydrazide groups, revealing high selectivity for mercury (II) ions. Porous DVB-MA copolymers with moderate BET surface area of 460 $m^2$ $g^{-1}$ can be obtained by suspension polymerisation, in which water was dispersing medium and mixture of 1,4-dioxane and n-dodecane was porogen [58]. Huang et al. synthesised a series of amine-functionalised HCPs via two-step modification from highly-crosslinked divinylbenzene-maleic anhydride (DVB-MA) copolymers [59]. The BET surface areas of these as-prepared HCPs ranged from 183 to 500 $m^2$ $g^{-1}$, and both micropores and mesopores were present in the HCPs. Even though the preparation of these hypercrosslinked MA-DVB copolymers did not comply with Friedel-Crafts chemistry, they are still regarded as HCPs. Honestly, their surface areas are only moderate but their capacity for $CO_2$ can reach 1.53 mmol $g^{-1}$ under 273 K at 1 bar, indicating that

amine groups have stronger affinity to $CO_2$ gas molecules. This discovery was further confirmed by later researchers and utilised to synthesise other amine-containing HCPs. In Liu's research, they soaked hypercrosslinked polystyrene in the polyethyleneimine (PEI) solution for the incorporation of amine groups [60]. These PEI-functionalised HCPs showed great potential in the capture of $CO_2$ and the maximum $CO_2$ uptake reached 3.24 mmol $g^{-1}$ at 298 K.

In general, HCPs based on Friedel-Crafts reactions generate enhanced microporosity by varying experimental parameters despite macropores can still be maintained if they exist intrinsically in the polymers. The intentional control over mesopores was realised by Seo and Hillmyer [61], who polymerised a mixture of styrene and divinylbenzene (DVB) with a macro polylactide chain transfer agent (PLA-CTA) via the reversible addition fragmentation chain-transfer (RAFT) polymerisation. Polymerisation-induced phase separation divided obtained block copolymers into crosslinked PS domain and chemically-etchable PLA domain. Sub-10-nm pores could be generated after removing PLA domain and formed continuous mesopores. Soon after, the same group succeeded in the precise control over mesopore size from 6 to 15 nm by adjusting the portion of PLA in the hypercrosslinked block polymer PLA-b-P(VBC-co-DVB) [62]. This optimised protocol generated micropores in the P(VBC-co-DVB) domain and etched PLA domain simultaneously during hypercrosslinking reaction catalysed by $FeCl_3$. Thus, the hierarchical porous structures provided polymers with fast kinetics in gas adsorption process.

Besides polystyrene-based HCPs, other chain polymers such as polysulfone [37], polyacrylates [37], polyaniline [29], polypyrrole [63] and polyphenol [64], can also be used as precursors and hypercrosslinked into porous networks.

Hypercrosslinked polysulfone was achieved by bromomethylation [65] of each aromatic rings and subsequent crosslinking between internal electrophiles [37]. The as-prepared polymers had a noticeable but not high apparent surface area, not even exceeding 80 $m^2$ $g^{-1}$. The insufficient porosity could be attributed to the denser chain packing facilitated by higher conformational flexibility, and the deactivation of

benzene rings by each sulfone group. Hypercrosslinked polyacrylates [37] also had inferior surface areas and this reaction needed to be performed at dilute solutions comparing with concentration of polystyrene (0.125 g $mL^{-1}$), otherwise porosity cannot be produced. It is noteworthy that polyacrylates precursors with large pendant substituents can yield HCPs with higher porosity due to their rigidity.

Hypercrosslinked polyaniline and polypyrrole can be achieved with highly reactive α,ω-diiodoalkanes crosslinker to promote N-alkylation [29], of which the surface areas were 632 and 732 $m^2$ $g^{-1}$ respectively. A microwave-assisted technique can be applied for accelerating the rate of N-alkylation. The length of diiodoalkanes is crucial for the porosity of resulting HCPs. In other words, longer diiodoalkanes crosslinked polyaniline had lower surface area because longer crosslinkers cannot provide enough rigidity to retain the pores. Hypercrosslinked polyaniline and polypyrrole demonstrated great potential in hydrogen storage not only because of their narrower porosity, but also owing to the aromatic rings bearing electron donating groups which have better affinity to hydrogen. Especially, boron-crosslinked polypyrrole had ultra-small that were only accessible for hydrogen molecules, indicating smaller crosslinkers would directly lead to small pores [63]. Bimodal micro-mesoporous phenolic resins (PR) were synthesised via Friedel-Crafts alkylation of pristine PR and removal of incorporated triblock copolymer F127 ($EO_{106}PO_{70}EO_{106}$) template. Meso-PR-36 that reacted for 36 hours exhibited the highest specific surface area (up to 782 $m^2$ $g^{-1}$) and mesopore surface area was 481 $m^2$ $g^{-1}$, which was even higher than calcined Meso-PR at 350 ℃. This work proposed a soft chemistry synthetic strategy for mesoporous polymers in which microporosity from Friedel-Crafts reaction can preserve the rigid polymer architecture and promote the solvent etching of templates. The as-prepared hierarchical porous structure can overcome the mass diffusion restrictions in small pores and ensure the accessibility of guest molecules, which is advantageous for $CO_2$ capture.

So far, several companies have commercialised HCPs as sorbents for chemical separations, water purification and food industry. Generally, these products are

hypercrosslinked polystyrene resins such as Amberlite XAD resins [66], Purolite series resins [67], Macronet MN200 [68], and Dowex Optipore resins[69]. To improve the market competitiveness of HCPs products, energy-saving synthetic methods and low-cost raw materials are desired. Through one-pot Friedel-Crafts reactions with $FeCl_3$, DCX and BCMBP, respectively, were used to crosslink corncob lignin [70]. Compared with pristine corncob lignin that only has a surface area of 6 $m^2$ $g^{-1}$, the hypercrosslinked products generate predominant porosity and BCMBP-crosslinked lignin exhibited a high surface area of 1144 $m^2$ $g^{-1}$, which is more than twice that of DCX-crosslinked lignin (463 $m^2$ $g^{-1}$), indicating that bigger crosslinker can create more space in the porous networks. These lignin-based HCPs possess good chemical stability and exhibit adequate capacity of 375 mg $g^{-1}$ for bisphenol AF (BPAF). Overall, these results indicate that the developed lignin-based HCPs have favorable properties for potential applications in various environments.

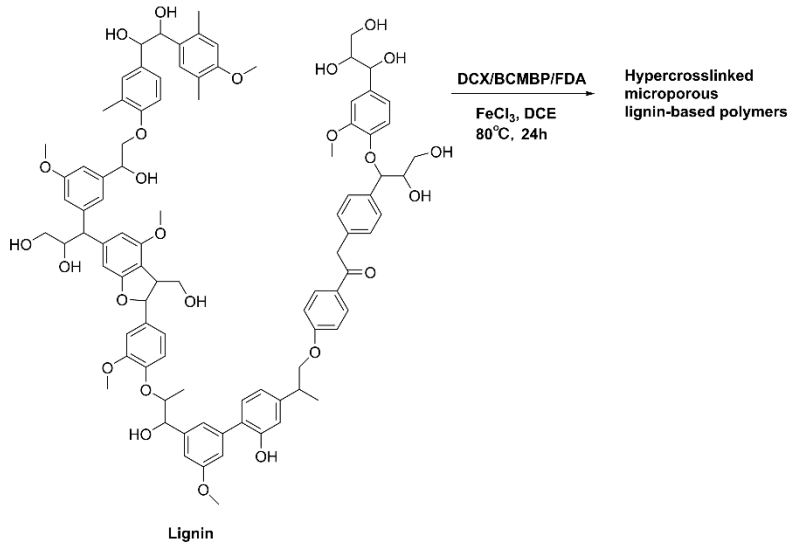


Figure 1-5: Synthetic process of hypercrosslinked lignin polymers

## 1.2.2 Internal hypercrosslinking

The hypercrosslinking of polystyrene using halogen-containing crosslinkers experiences chloromethylation and successive conversion of methylene bridges [47]. This prompts researchers to deploy small multifunctional molecules as internal electrophiles to build rigid HCPs via self-condensation or poly-condensation. This

type of synthetic strategy is known as internal hypercrosslinking. Actually, many organic coupling reactions can be applied to crosslink different building units and formed porous polymers such as conjugated microporous polymers (CMPs) supported by Sonogashira-Hagihara coupling, porous aromatic frameworks (PAFs) underpinned by Yamamoto coupling and porous organic polymers (POPs) constructed by phosphorus–carbon (P–C) coupling. The examples listed in this section are mainly based on Friedel-Crafts alkylation for clarity.

First HCP synthesised via internal hypercrosslinked was poly-dichloroxylene catalysed by stannic tetrachloride ($SnCl_4$) in DCE [37]. Its surface area was as high as 1000 $m^2$ $g^{-1}$ and the crosslinked networks expanded by nearly two times its original volume when swelling in acetone or methanol. Later, Cooper's group developed a series of HCPs with super-high surface areas by poly-condensation of dichloroxylene (DCX), 4,4-bis(chloromethyl)-1,10-biphenyl (BCMBP), and 9,10-bis(chloromethyl)anthracene (BCMA) catalysed by $FeCl_3$ instead [71,72]. The surface areas of resulting HCPs ranged from 600 to 1900 $m^2$ $g^{-1}$ by varying the monomer concentration, $FeCl_3$ ratios and reaction time. From the $^1H$-$^{13}C$ solid-state NMR spectra, the ratio of substituted aromatic carbons to nonsubstituted ones (S/NS) can be calculated for evaluating the degree of crosslinking, and a higher crosslinking degree usually corresponded to a high specific surface area. Figure 1-6 displayed the hypothetical idealised crosslinked *p*-DCX structure of which S/NS was 1. Meanwhile, double methylene bridges crosslinked *p*-DCX unit (Figure 1-6b) could also exist in the real networks as S/NS ratio of this segment was 1 as well. From the perspective of homo-condensation, hypercrosslinked BCMBP polymers gained the highest surface area of 1874 $m^2$ $g^{-1}$, while those of *p*-DCX and BMCA based polymers were merely 1391 and 921 $m^2$ $g^{-1}$ respectively. This can be ascribed to their molecular structure and steric effect. Comparing with DCX, the rigid para geometry between neighbouring aryl rings that crosslinked by larger BCMBP molecules contributed to the increased porosity. In the case of BMCA, its structure might resemble ortho substitution on both sides of a *p*-DCX monomer, and thus steric effect hindered the crosslinking between

adjacent aryl rings. The highest HCP was obtained from the copolymerisation of *p*-DCX and BCMBP with a molar ratio of 1:3, and its surface area reached 1904 $m^2$ $g^{-1}$. This work demonstrated that the porosity of HCPs can be precisely adjusted by controlling the crosslinking degree and molecular design of starting monomer geometry.

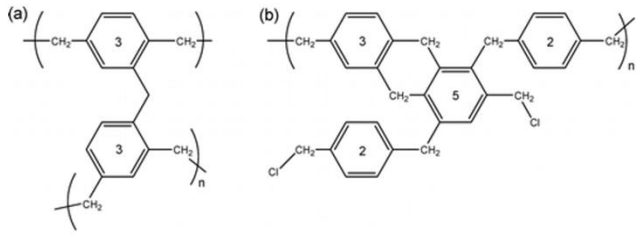

Figure 1-6: (a) The supposed idealised p-DCX-based polymeric network of which substituted to non-substituted aromatic carbons (S/NS) was 1 integrating from 1H−13C CP/MAS NMR spectra. (b) Possible fragment of a real p-DCX network, which is also consistent with S/NS = 1 and an average aromatic functionality of 3 [71].

Therefore, BCMBP was selected as a crosslinker to co-polymerise with four non-functionalised fluorene-based monomers to study the effects of molecular geometry and comonomers [73]. As shown in Figure 1-7, fluorene (FLUO), 9, 9'-spirobi(fluorene) (sFLUO), dibenzofuran (DBF) and dibenzothiophene (DBT) were chosen for their high reactivity in Friedel-Crafts alkylation and these non-functionalised monomers accounted for 10-25 mol% proportion. DBF-10 exhibited the highest surface area of 1800 $m^2$ $g^{-1}$. Universally, the linear relationship was observed between the BET surface area and methane uptake for HCPs. But their actual capacity for methane or hydrogen gas was also affected by chemical structure and polarity of the HCPs surface.

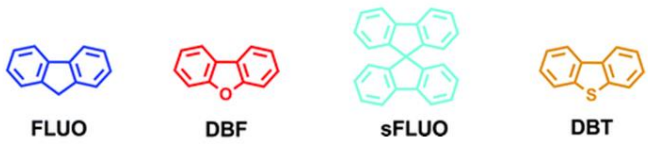


Figure 1-7: Chemical structures of fluorene-based monomers including Fluorene (FLUO), 9,9'-spirobi(fluorene)(sFLUO), dibenzofuran (DBF) and dibenzothiophene (DBT)

Yang et al. reported a series of microporous copolymers prepared from triphenylamine and *p*-dichloro-xylene (*p*-DCX) and their surface areas increased with an increasing content of *p*-DCX, ranging from 318 to 1530 $m^2$ $g^{-1}$ [74,75]. These HCPs possessed high $CO_2$ capture ability and remained stable after 5 consecutive runs of $CO_2$ adsorption-desorption because nitrogen heteroatoms in the HCPs can enhance the affinity between HCPs and $CO_2$ molecules. Also, they can be applied for oil/water separation due to their outstanding hydrophobicity and oleophilicity. Following these successful cases, Chen and co-workers employed DCX and BCMBP to link carbazole, ferrocene and triptycene respectively and the resulting HCPs thus possessed polar functional groups, open metal sites and enhanced microporosity predictably [76]. DCX revealed to support HCPs networks with increased microporosity featuring narrower pore size distribution, while longer BCMBP brought more mesoporosity considering its potential in obstruct the micropores created by hypercrosslinking process. Interestingly, ferrocene-based HCPs behaved relatively high $CO_2/N_2$ selectivity despite their lowest $CO_2$ uptake caused by larger proportion of mesopores. This can be attributed to the strong interaction between electron-rich ferrocene building blocks and $CO_2$ molecules.

Similarly, α,α′-dibromo-p-xylene (DBX) was also reported to crosslink carbazole based on $FeCl_3$ catalysed Friedel-Crafts alkylation, and the resulting hypercrosslinked polymers had noticeable surface area of 913 $m^2$ $g^{-1}$ [77]. Meanwhile, Han's group synthesised microporous polycarbazole via oxidative coupling polymerisation catalysed by $FeCl_3$ under room temperature [78]. The BET surface area of generated polymer, CPOP-1, was much higher than DBX-crosslinked polycarbazole, reaching 2220 $m^2$ $g^{-1}$. The narrow nanopores guaranteed it to store small gas molecules such as $H_2$ (2.8 wt% at 1 bar and 77 K) and $CO_2$ (21.2 wt% at 1 bar and 273 K). Furthermore, the electron-rich polycarbazole had abundant nitrogen sites that enhanced the interaction with polarizable $CO_2$ and thus presented good selectivity towards $CO_2$ over $N_2$ or $CH_4$. Following this cost-effective oxidative coupling, the same group synthesised a series of hypercrosslinked polycarbazole from the vinyl or

hydroxymethyl functionalised carbazole monomers by combining oxidative coupling and Friedel-Crafts reaction in $FeCl_3$ catalysed one-pot process [79]. These materials proved to have high porosity (>700 $m^2$ $g^{-1}$) and great performance in gas storage and adsorption of harmful volatile vapours like toluene and formaldehyde.

Tris(bromomethyl)benzene crosslinkers were used to construct benzene/biphenyl/1,3,5-triphenylbenzene-based networks respectively by Liu and co-workers [80]. Among them, hypercrosslinked poly-triphenylbenzene catalysed by anhydrous aluminium chloride ($AlCl_3$) manifested the highest surface area of 1783 $m^2$ $g^{-1}$. The HCPs mentioned in this work have superior $H_2$ and $CO_2$ uptake, indicating they are promising alternatives for energy applications. However, one notable shortcoming of this research is the absence of explanations for the relationships between final porosity and monomer structures, highlighting the necessity for further research in this area. They only managed to a vague conclusion that the characteristic of HCPs closely depends on the monomers and catalyst.

Previous research has pointed out that introducing N heteroatoms in the HCPs could increase their affinity to $CO_2$, therefore Jia and co-workers used several multi-chloromethylated N-containing diazine and triazine to link triphenylbenzene [81]. The resulting HCPs have high surface areas up to 1951 $m^2$ $g^{-1}$ and triazine-crosslinked HCPs behaved superb $CO_2/N_2$ selectivity of 75.4 at 295 K, proving their promising perspective in carbon capture field. Ionic imidazolinium based polymers were first announced by Li et al. who employed one-step Friedel-Crafts alkylation of 2-phenylimidazoline and benzyl halide including DCX and DBX [82]. Their method, which composed of copolymerisation and quaternization, managed to tackle the difficulty that electron-withdraw groups in the ionic monomers could hinder the Friedel-Crafts chemistry. These ionic HCPs demonstrated not only improved $CO_2$ capture (3.8 mmol $g^{-1}$ at 273 K and 1 bar), but also exceptional performance in the cycloaddition of $CO_2$ with epoxides at mild experimental conditions.

In addition to the small organic monomers, cage molecules terminated with chloromethyl groups has also been reported to be converted into hypercrosslinked

polymers by self-condensation. Yuan et al. synthesised porous carborane-based polymers by the self-condensation of benzyl chloride terminated carborane molecules or the co-polymerisation of BCMBP and carborane [83]. These electron-deficient carborane blocks can effectively strengthen the affinity between polymers and hydrogen. Hyprecrosslinked siloxane-organic hybrid with an ultrahigh BET surface area (2500 $m^2$ $g^{-1}$) was prepared via self-condensation of benzyl chloride-terminated double-four-ring cubic siloxane cages, setting a new record for siloxane-based materials [84]. During the Lewis acid-driven crosslinking process, double-four-ring cages revealed to be destructed but this destruction was regarded as beneficial to more effective crosslinking and finally caused enhanced surface area. This could be attributed to the combined impact of cage structural distortion and production of acid side products (HCl) resulting from the Friedel-Crafts reaction.

Apart from multi-functionalised (halomethyl) monomers, molecules containing hydroxymethyl can also satisfy the requirement of self-condensation. It should be emphasised that frequently-used solvents for Friedel-Crafts reaction, such as dichloroethane and dichloromethane, also contribute to the crosslinking to some degree, serving not only as a solvent. Motivated by the successful practice of aliphatic alcohols in Friedel-Crafts alkylation, Luo and co-workers first managed to synthesise HCPs from the self-condensation of 1, 4-benzenedimethanol (BDM) and benzyl alcohol (BA), and BET surface areas for corresponding porous networks were 847 and 742 $m^2$ $g^{-1}$ respectively [85]. It should be emphasised that BA was a monohydroxymethyl compound, which broke the previous cognition that internal hypercrosslinking required multifunctional monomers. Despite HCP-BA had moderate surface area, it was capable of storing a considerable amount of $CO_2$ (8.46 wt%) and $H_2$ (0.97 wt%) at 1.0 bar, and at 273 K and 77 K, respectively. Another advantage of this reaction was that it produced non-toxic by-products, such as water, thereby avoiding environmental pollution.

With the target to expand monomers for internal hypercrosslinking, Tan’s group suggested a simplified strategy to synthesise HCPs based on Scholl coupling reaction

using Lewis acid and protonic acid as catalysts [86]. The Scholl reaction, which forms aryl-aryl bond between neighbouring aromatic rings via the elimination of two aryl-bound hydrogen atoms, can be perceived as an advancement since Friedel and Crafts reported the formation of biphenyl from benzene catalysed by anhydrous $AlCl_3$ [87]. This approach does not require specific starting materials with functional groups and realise the direct crosslinking of various monomers those are stable to Lewis acid. For example, monomers containing aryl rings, fused-rings, heterocyclic rings, acidic and alkaline groups and even polyhedral oligomeric silsesquioxanes (POSS) cages [88] have been confirmed to be applicable to Scholl coupling and the resulting HCPs have adequate surface area. The HCPs hold promising prospects for optics and electronics applications because of their unique conjugated structure coming from direct linking of aryl rings. Moreover, these HCPs based on Scholl reaction can serve as qualified scaffolds for catalysts by coordinating metal ions such as Pd(II) and Cu(II) with the embedded ligands. The resulting heterogeneous catalyst demonstrated distinguish catalytic effects in Suzuki-Miyaura reaction and alcohol oxidation reactions [89].

To summarise, internal hypercrosslinking was achieved via either self-condensation of specific functionalised monomers which requires complex multistep synthesis of precursors and release hazardous substances, or Scholl coupling reactions that are strict on experimental conditions. Therefore, more environmentally-friendly and facile synthetic methods are still appreciated.

### 1.2.3 External hypercrosslinking

In 2011, Tan's group proposed a novel 'knitting' strategy to crosslink various rigid aromatic molecules using formaldehyde dimethyl acetal (FDA) as an external crosslinker, further extending the choice of starting materials of HCPs [90]. Benzene, biphenyl, triphenylbenzene, chlorobenzene, methylbenzene and phenol were employed as monomers in this work and corresponding insoluble HCPs had high surface areas up to 1391 $m^2 g^{-1}$. The porosity of HCPs can be tuned by changing the molar ratio of FDA versus monomers, and improved FDA ratio can effectively

increase BET surface area, pore volume and gas adsorption capacity. The functional groups of the monomers were also crucial for determining the pore structures of resulting HCPs networks [91]. Methyl groups are responsible for the ultra-micropores in the methylbenzene-based HCPs while phenolic hydroxyl groups are beneficial for $H_2/CO_2$ gas adsorption despite their lower BET surface area. The possible mechanism of FDA involved crosslinking could be divided into two steps: the introduction of methoxymethyl groups and further conversion into methylene linkages, accompanied by the release of methanol by-products.

Following this facile and cost-effective synthetic strategy, diverse HCPs with different functional groups and spatial structures have emerged. Polycyclic aromatic hydrocarbon such as naphthalene, anthracene and phenanthrene were reported to crosslinked by 1,3,5-trioxane, and ultraviolet-visible diffuse reflectance (DRS UV-Vis) and the Fourier transform infrared (FTIR) spectra of these resulting HCPs confirmed the formation of quinonoid chromophore as shown in Figure 1-8 [92]. It is widely understood that such conjugated quinonoid structures could have characteristic optical and electronic properties because of their delocalised π electrons systems. Drawing from previous study, researchers were mainly concerned with the pore properties and adsorption performance of HCPs materials while the optical and electron-conductive behaviours were ignored. Rajangam and co-workers proposed that the generation of quinonoid structures came from the dehydrogenation of methylene bridges between the aromatic rings, hence the resulting HCPs had a broad light adsorption across the wavelength range of 200 to 1000 nm [92]. This can explain the brown colour of insoluble HCPs. This work significantly deepens people's insights into the inner structures of HCPs and highlighted their potential for diverse applications such as solar cell devices, infrared detectors and semiconductors. Similar HCPs were synthesised by Wang et al. who employed benzene, naphthalene, phenanthrene, pyrene and thiophene to crosslink with FDA under the catalysis of $FeCl_3$ [93]. They observed a noticeable trend in the prepared HCPs, wherein the specific surface area, pore volume and micropores proportion exhibited a consistent drop as the monomer

size increase. It indicates that the larger monomers have stronger steric hindrance for the continuous crosslinking process, resulting in reduced crosslinking degree and less porosity. As was mentioned in the internal hypercrosslinking, BA was capable for self-condensation. Here, a series of hydroxyl-based HCPs were prepared from benzyl alcohol (BA) by FDA knitting strategy catalysed by $FeCl_3$. The surface area of resulting BA-HCP can reach 1101 $m^2$ $g^{-1}$ by optimising experimental conditions, which is higher than that of BA self-polymers made by internal hypercrosslinking. Besides improved porosity, BA-HCP has larger $CO_2$ uptake (up to 3.03 mmol $g^{-1}$ at 273 K and 1 bar) because of enough remained hydroxyl groups in the HCPs.

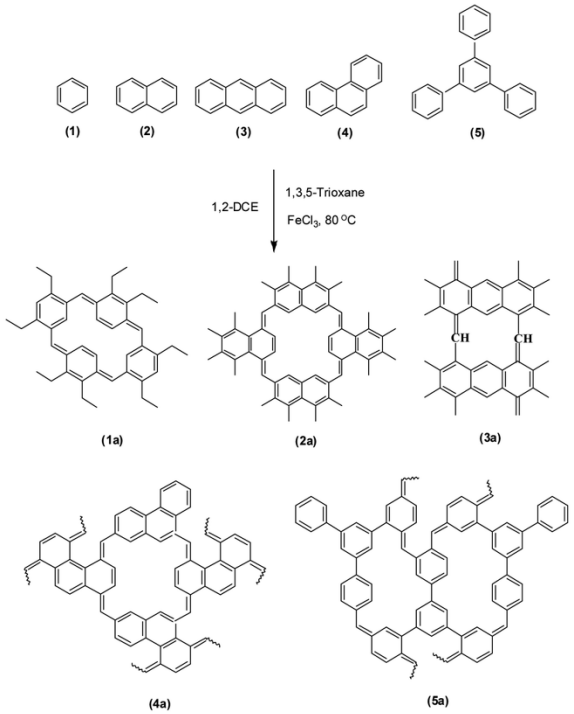


Figure 1-8: Chemical structures of starting monomers and resulting hypercrosslinked polymers containing quinonoid chromophore *[92]*

Rigid three-dimensional(3D) monomers including triptycene [94,95], tetraphenyl-X (X=C, Si, Ge centre atoms) [96-99], 9, 9'-spirobifluorene (sFLUO ) [100], and polyhedral oligomeric silsesquioxanes (POSS) [88,101,102] were also revealed to be compatible for this 'knitting' method. Most 3D monomers have unstacked π planes, allowing for the preservation of the intrinsic properties of the building blocks. Triptycene [103] and its derivatives such as tricarbazolytriptycene [104], hexaphenylbenzene-based triptycene

[105], and nitrogen-rich triptycene [106], have demonstrated their impressive adaptability to Friedel-Crafts hypercrosslinking, of which the highest BET surface area reached 1426 $m^2$ $g^{-1}$ [94]. Their abundant micropores are expected to favour gas capture and some heteroatom-containing units could benefit specific separation application.

The effects of functional groups to the triptycene-based polymers (TPP) were comprehensively compared by He and co-workers, who synthesised a series of TPP functionalised with amino (-$NH_2$), formyl (-CHO), acetyl (-$COCH_3$) and nitro (-$NO_2$) groups [107]. TPP-$NH_2$ had the highest BET surface area (863 $m^2$ $g^{-1}$) while TPP-$NO_2$ only had 140 $m^2$ $g^{-1}$. However, the $CO_2$ uptake of four TPP did not completely follow this order. Despite TPP-$NO_2$ had the lowest porosity, its $CO_2$ uptake was even higher than TPP-CHO which can be attributed to higher polarity of nitro groups. Therefore, the evaluation of porous HCPs is determined by the combination of specific surface area, pore size and the interaction between HCPs and adsorbates. Robert and co-workers successfully synthesised tetraphenylmethane (TPM)-based HCP using FDA as an external crosslinker and its BET surface area was up to 1470 $m^2$ $g^{-1}$ accompanied by moderate $CO_2$ uptake of 2.95 mmol $g^{-1}$ at 273 K and 1 bar [98]. Errahali et al. continued to explore the adsorption performance of TPM-based HCPs for more gases such as methane [99]. A series of TPM-based HCPs were prepared by varying the molar ratio of FDA-to-TPM from 3 to 30. The results of their BET surface area revealed a pattern of initial rise culminating in a peak where the molar ratio of FDA-to-TPM was 16, followed by a subsequent decrease when the ratio reached 30. This can be explained by the inadequate crosslinking caused by excessive crosslinker. The best HCP in this work, poly-TPM-16, exhibited the highest adsorption for both $CH_4$ (21.7 $cm^3$ $g^{-1}$ at 273 K and 1 bar) and $CO_2$ (2.82 mmol $g^{-1}$ at 273 K and 1 bar) gases, which aligned well with its highest surface area and micropore volume. On basis of these research, Pillaiyar et al. replaced centred atom carbon (C) of TPM with larger silicon (Si) and germanium (Ge) atoms to synthesise desirable ordered silicon- and germanium-containing porous polymers based on Friedel-Crafts reaction, providing a facile and efficient synthetic strategy [97]. The as-prepared HCPs from

tetraphenylsilane or tetraphenylgermanium had surface areas of 1137 and 1059 $m^2$ $g^{-1}$ respectively, which are slightly lower compared to the carbon analogue. They demonstrated a remarkable capacity for $CO_2$ adsorption (104.3-114.4 mg $g^{-1}$) with an isosteric heat of adsorption ranging from 26.5 to 27.3 kJ $mol^{-1}$ at 273 K and 1 bar. Cui et al. continued to investigate the sorption ability of tetraphenylsilane-based HCP to water and methanol vapours, and it demonstrated good capacity value of 72 mg $g^{-1}$ and 308 mg $g^{-1}$ respectively [96]. 9, 9'-spirobifluorene (sFLUO), a rigid compound which can incorporate vertical knots in the polymers, has been transferred into porous polymers under the catalysis of $FeCl_3$ [100].

It should be highlighted that $FeCl_3$ serves not only as a potent Lewis acid in Friedel–Crafts reactions but also functions as a common oxidant for oxidative coupling of polyaromatic hydrocarbons. Therefore, Modak and co-workers synthesised three different sFLUO-based porous networks via FDA-involved Friedel-Crafts reaction, oxidative coupling and a combination of both reactions [100], and the corresponding polymers possessed a BET surface area of 1490, 940 and 1980 $m^2$ $g^{-1}$ respectively. This illustrated the superiority of external knitting strategy which can create more porosity in the polymers. The structure of fluorine monomer can exert a significant impact on the porosity of the final HCPs as another 9, 9'-dimethylfluorene-based HCP only had a surface area of 70 $m^2$ $g^{-1}$. The FDA-dominated knitting method was validated for POSS monomers and the resulting HCP exhibited a surface area of 795 $m^2$ $g^{-1}$, which surpassed that of POSS-based porous polymers synthesised vid Scholl reaction (472 $m^2$ $g^{-1}$) [88]. Subsequently, Tian et al. compared the properties of DCX-crosslinked POSS polymers with those of FDA-crosslinked POSS polymers and the former one had a higher surface area(up to 1041 $m^2$ $g^{-1}$) because xylylene linkage is larger than methylene linkage [102]. In other words, longer crosslinking bridges between the POSS units were associated with higher surface area, demonstrating a positive correlation. Furthermore, the microporosity of POSS-based polymers can be enhanced after removing the inorganic components via carbonization.

The versatility of ‘knitting strategy’ was further confirmed by aromatic heterocyclic monomers. Thiophene, pyrrole and furan were successfully converted into microporous polymers by simple one-pot Friedel-Crafts reaction in which FDA and $FeCl_3$ served as external crosslinker and catalyst respectively [108]. The BET surface areas of the corresponding polymers were modest: 726 $m^2 g^{-1}$ for poly-thiophene, 514 $m^2 g^{-1}$ for poly-furan and 437 $m^2 g^{-1}$ for poly-pyrrole. These microporous heterocyclic polymers exhibited a significant adsorption capacity for $H_2$ (1.11 wt%, 77 K and 1.13 bar) and $CO_2$ (12.7 wt%, 273 K and 1 bar) respectively due to their narrow pore size and heteroatom-rich pore surface. The long pair electrons of heteroatoms along the polymer skeleton provide interaction sites with $CO_2$ molecules through dipole-dipole interactions.

To further improve the properties of heterocyclic HCPs, Cooper’s group carbonized them by potassium hydroxide (KOH) activation method to get enhanced surface area while restricting the swelling behaviour of HCPs simultaneously [109]. The porosity of carbonized HCPs increased dramatically, and the surface area of poly-pyrrole treated at 800 ℃ even reached 4334 $m^2 g^{-1}$, indicating their huge potential in energy storage, gas separation and catalysis. In addition, fused heterocyclic rings including indole, benzothiophene, benzofuran, carbazole, dibenzofuran and dibenzothiophene were knitted with FDA and the resulting HCPs exhibited surface areas ranging from 243 to 1022 $m^2 g^{-1}$ [110]. Theoretical calculations confirmed that the binding energies of N-containing monomers and $CO_2$ molecules are higher than those of S-containing and O-containing monomers due to the delocalised long pair electrons of good electron-donors N atoms. These heterocyclic HCPs also demonstrated good $CO_2/CH_4$ selectivity which means they are well-suited for natural and landfill gas purification.

The applicable scope of ‘knitting’ strategy can be extended to macromolecules such as the most common styrene-based precursors and related block copolymers. Further elaboration on the details of these PS-related publications will not be provided here, as they overlap with the previously discussed post-crosslinking practices. Apart from

these artificial polymer precursors, researchers have turned their attention to explore the possibility of using bio-based and natural raw materials.

Lignin, thereby, garnered the interest of scientists because it is one of the most abundant natural polymers on Earth. Organosolv lignin (OL), the most available phenolic polymers from nature, revealed to be crosslinked by FDA following Friedel-Crafts reactions [111]. Despite having a surface area of less than 5 $m^2$ $g^{-1}$, hypercrosslinked lignin exhibited good selectivity for $CO_2$ over $N_2$, which can be attributed to the presence of dominant ultramicropores that are inaccessible to $N_2$ molecules. Grand canonical monte carlo (GCMC) simulations of $CO_2$ adsorption confirmed a narrower pore size distribution in the hypercrosslinked lignin. After a 6-hour treatment at 550 ℃ under $N_2$ atmosphere, hypercrosslinked lignin's surface area rose to approximately 100 $m^2$ $g^{-1}$ while maintaining its $CO_2$ selectivity and experiencing an increase in $CO_2$ uptake. Very recently, Tang and co-workers reported to add biphenyl in the copolymerisation of alkali lignin and FDA, effectively improving the BET surface area to 402 $m^2$ $g^{-1}$ [112]. Benefitting from their abundant oxygen-containing groups, these hypercrosslinked lignin (HCP-L) verified their outstanding adsorption capacity for different dyes from water, reaching 1332 mg $g^{-1}$ for rhodamine B (RhB) and 228 mg $g^{-1}$ for methylene blue (MB). However, anionic dye such as Congo Red (CR) only exhibited relatively low uptake (89 mg $g^{-1}$) because of electrostatic repulsion. Pitch, a residual product left during the distillation of crude oil, was also synthesised into porous HCPs with the aid of FDA crosslinker [113]. The finest pitch-based HCP was achieved when the weight ratio of FDA and pitch was 1, and its BET surface area attained 758 $m^2$ $g^{-1}$. These HCPs exhibit impressive $CO_2$ capture capacities, reaching 11.8% at 1.0 bar and 273 K, as well as a notable $H_2$ uptake of 0.95% at 1.13 bar and 77.3 K due to their heterocyclic characteristic. This research further highlights the versatility of the 'knitting' crosslinking strategy, and motivates researchers to explore more cost-effective and sustainable building blocks for the large-scale production of practical HCPs. Liu et al. managed to synthesise HCPs from cashew nut shell liquid (CNSL) and applied them in the removal of

volatile organic compounds (VOCs) from the exhaust [114]. CNSL contains large amounts of aromatic molecules such as cardanol and cardol with hydroxyl groups. Hence the resulting HCPs only had low BET surface area of 93 $m^2$ $g^{-1}$, but the oxygen-rich nature ensured their good adsorption ability to VOCs. CNSL-based HCPs exhibited outstanding capacity for o-xylene up to 217 mg $g^{-1}$, which was even better than silica gel [115] considering the significant lower initial concentration of VOCs. Catechol-based HCPs were designed for the removal of iron from wastewater considering its strong affinity to iron (Fe) ions [116]. Despite having a negligible surface area of 3 $m^2$ $g^{-1}$catechol-HCP exhibited an impressive removal efficiency of 94% for Fe ions, surpassing that of toluene-HCP, phenol-HCP, and hydroquinone-HCP. This indicated that the strong interaction between catechol structure and guest iron molecules dominated the adsorption.

In summary, the knitting strategy proposed by Tan's group has been revealed as a versatile and easy method for synthesising HCPs from various starting materials. Besides the FDA, some other crosslinkers have been documented to promote the growth and advancement of external hypercrosslinking such as dimethoxybenzene (DMB) [117], paraformaldehyde, glyoxylic acid [118], orthoformate [119] and halogenated molecules [120-122]. DMB was used to incorporate benzyl linkage between aromatic monomers and construct long-range conjugated HCPs [117]. Benzene, biphenyl, methylbenzene, chlorobenzene, phenol and triptycene were chosen to be crosslinked by DMB and the resulting HCPs displayed surface areas ranging from 424 to 800 $m^2$ $g^{-1}$. Due to their conjugated characteristic, which was confirmed by solid fluorescence excitation and emission spectra, these DMB-crosslinked HCPs are expected to be applied in electric and photoelectric field. Wang and co-workers used paraformaldehyde and glyoxylic acid to crosslink triptycene hydroquinone [118]. Due to their hydroxyl and carboxyl functional groups, these resulting triptycene-based HCPs exhibited high aliphatic amines vapours, reaching up to 5 times their own weight, Additionally, they exhibit impressive selectivity of over 30 times for aliphatic amines compared to n-hexane. Zhang et al. expanded the repertoire of cost-effective

crosslinkers that can be incorporated into HCPs to enhance their porosity [119]. They synthesised polytriphenylamine networks (PTPAs) through a one-step oxidative coupling reaction and Friedel–Crafts alkylation, utilising $FeCl_3$ as a catalyst. Notably, this study introduced trimethyl orthoformate (TMOF), trimethyl orthoacetate (TMOA), triethyl orthoacetate (TEOA), and triisopropyl orthoformate (TIPO) as crosslinkers to construct different porous PTPAs. TEOA crosslinked PTPAs demonstrated the highest BET surface area of 1543 $m^2\ g^{-1}$ as well as exceptional $CO_2$ uptake capacity of 2.65 mmol $g^{-1}$ at 1.0 bar and 273 K.

Halogenated crosslinkers usually serve as electrophiles in the Friedel-Crafts alkylation and promote the formation of substituted aromatic compounds. For example, 2,4,6-trichloro-1,3,5-triazine was employed to crosslink benzene, biphenyl and terphenyl in dichloromethane (DCM) with aluminium chloride ($AlCl_3$) serving as a catalyst [120]. This could be attributed to the electron-deficient nature of the carbons on the triazine ring, which enables electrophilic substitution reactions with aromatic compounds. With the increase of the length of aromatic monomers, the surface areas increased from 558 to 1266 $m^2\ g^{-1}$. These triazine-based HCPs showed high $CO_2$ uptake (up to 51 $cm^3\ g^{-1}$) at 298 K and 1 bar due to their N-rich nature. Moreover, 2,4,6-trichloro-1,3,5-triazine was also reported to link 1,3,5-triphenylbenzene and trans-stilbene monomers, and the resulting HCPs demonstrated either high $CO_2$ uptake (204.3 mg $g^{-1}$, 273 K and 1 bar) or exceptional $CO_2/N_2$ selectivity [121].

To conclude, the utilisation of external hypercrosslinking in HCPs provides a powerful strategy to incorporate a variety of functionalised units, leading to the creation of materials with enhanced properties and expanded possibilities for tailoring their characteristics to suit specific application needs.

## 1.3 Catalysts and solvents for HCPs synthesis

The synthesis of HCPs is underpinned mostly by Friedel-Crafts chemistry. Therefore, the careful selection of catalysts and solvents for the Friedel-Crafts reactions is crucial

to optimise the reaction conditions, enhance product yields, and achieve the desired properties of the synthesised HCPs. Through thoughtful considerations and experimental adjustments, researchers can effectively control the synthesis process, leading to the development of innovative and tailored HCP materials for various applications.

### 1.3.1 The choice of catalysts for HCPs synthesis

The synthesis of HCPs is mainly dominated by Friedel-Crafts chemistry, in which Lewis acids are essential to catalyse the formation of strong linkage between monomer units. Principally, all Lewis acids can promote the Friedel-Crafts reactions while metal halides such as $ZnCl_2$ [123-126], $SnCl_4$ [124,127-129], $AlCl_3$ [124,130-133] and $FeCl_3$ [79,124,134-137] are the most frequently employed catalysts. To be more specific, the latter two are widely used for their better catalytic performance. Sherrington and co-workers reported that $FeCl_3$ was the most superior catalyst in the hypercrosslinking of poly(DVB-VBC) precursors when compared to $AlCl_3$ and $SnCl_4$ [46]. Generally, the activity of the three catalysts follows the order of $FeCl_3$>$AlCl_3$>$SnCl_4$. The exact reasons behind the substantial variations observed among these species remain somewhat uncertain. However, one possibility is that $AlCl_3$ exhibits relatively lower solubility compared to the other two Lewis acids under the specific reaction conditions employed. Additionally, the sheer size of $SnCl_4$ may impose steric limitations to the second bridging alkylation step where new six-membered rings are formed preferably. Therefore, it is plausible that $FeCl_3$ that has balanced characteristics of solubility and molecular size, offers the most favourable compromise in this regard. Following this research, worldwide scientists have agreed upon the choice of anhydrous $FeCl_3$ as an effective catalyst in the synthesis of porous HCPs.

However, this conclusion has been challenged by Liu's study demonstrating that the performance of the catalysts are decided by the combination of reactants and reaction conditions [80]. They also evaluated the catalytic effects of $FeCl_3$ and $AlCl_3$ in the synthesis of tribromomethylated benzene-crosslinked HCPs where benzene, biphenyl

and triphenylbenzene were used as monomers. With the elimination of hydrogen bromide molecules, methylene bridges were successfully formed. In this case, the HCPs catalysed by $AlCl_3$ exhibited superior properties compared to those catalysed by $FeCl_3$ from the aspects of porosity including specific surface area, micropore volume, $CO_2/N_2$ capacity. It could be ascribed to the higher polymerisation degree of $AlCl_3$-catalysed HCPs which means more bromomethyl groups were converted in to methylene linkages. Hence, the resulting HCPs were more rigid and gained better preservation of porosity. This point of view was supported by Watcharop's work, in which $AlCl_3$ exhibited nearly almost full conversion of chlorine end groups into alkyl linkage during the synthesis of siloxane-organic hybrid HCPs [84]. Moreover, similar conclusion was proposed by Xu et al. who argued that the catalytic effect of three metal halides was in the order of $AlCl_3$>$FeCl_3$>$ZnCl_2$ based on empirical evidence [138]. Until now, the understanding of the difference between the catalysts has remained incomplete. But it is widely accepted that both $AlCl_3$ and $FeCl_3$ are strong catalysts for HCPs synthesised via Friedel-Crafts reactions.

The amount of Lewis acid catalyst is also determinative for the properties of HCPs. Based on the extensive experimental evidence, Colin and co-workers pointed out that the optimal $FeCl_3$ ratio fell within the range of 0.5-2 mol $mol^{-1}$ on the basis of the monomers [71]. Below this range, lower yields and surface areas were obtained, while excessively high concentrations of the catalyst had a counterproductive impact on the surface area of the resulting polymers.

Besides Lewis acid catalyst, Brønsted acids were also proved to accelerate the reactions such as methanesulfonic acid [139], trifluoromethanesulfonic acid (TfOH) and sulfuric acid ($H_2SO_4$) [140]. It is indisputable that the production of HCPs is a Lewis acid-mediated process and stoichiometric amounts of metal halides are required, which exceeds the amount it should provide as catalysts. Therefore, the large consumption of metal halides would pose a substantial burden on the environment. This encourages researchers to replace these common Lewis acid catalysts with Brønsted acids, stepping towards the direction of green chemistry.

Xiong et al. synthesised 1,3,5-trazine-based HCPs *via* methabesulfonic acid-catalysed Friedel-Crafts reaction [139]. The best sample stood out with its impressive BET specific surface area of up to 894 $m^2$ $g^{-1}$ and a total volume exceeding 0.41 $m^3$ $g^{-1}$. This exceptional porosity contributed to its notable $H_2$ adsorption capacity (1.14 wt% at 77 K and 1.0 bar) as well as remarkable $CO_2$ uptake (11.03 wt% at 273 K and 1.0 bar). In this work, methabesulfonic acid was proven compatible for Friedel-Crafts chemistry, and it outperformed conventional metal halides catalysts for its complete miscibility with the reaction system and relatively non-toxic quality. Schute and Rose revealed the feasibility of $H_2SO_4$ and trifluoromethanesulfonic acid in both internal and external hypercrosslinking, demonstrating the Brønsted acids are ideal alternatives for producing HCPs materials on a large scale [140]. However, the HCPs catalysed by the two Brønsted acids were inferior compared to those catalysed by $FeCl_3$ while $H_2SO_4$ displayed the worst catalytic effect. This could be attributed to the sulfonation side reaction accompanied with the crosslinking, leading to reduced specific surface area of HCPs. The advantage of $H_2SO_4$ route is the good tolerance to small amount of water and atmospheric conditions, allowing the reactions to proceed under milder conditions. Despite the loss of porosity, Brønsted acid-catalysed pathway offered significantly improved control over the reaction temperature because large amount of heat energy would be released when adding solid $FeCl_3$ into the reaction solutions. Therefore, Brønsted acid routes are more favourable in the scale-up production of HCPs. Subsequently, Lau et al. employed trifluoromethanesulfonic acid as a liquid catalyst to promote the synthesis of triptycene-based HCPs in the continuous flowing reactors [141]. They held a different view and declared that HCPs with high surface area could be obtained under the catalysis of TfOH if the reaction time was prolonged to 24 hours. In other words, TfOH-catalysed HCPs need longer reaction durations for complete crosslinking and enhanced porosity. By replacing batch reactors with flow synthesis setup, the kinetics of crosslinking can be accelerated due to the effective heat and mass transfer in the smaller confined tubular reactors. Another reason for choosing TfOH is that liquid catalyst can be miscible

with the solvent and avoid being clogged in the tube. Compared with batch-synthesised HCPs, the flow-produced HCPs exhibited a 24% increase in $CO_2$ uptake while the reaction time was only one-twelfth the time that batch reactions needed. The research reviewed here suggest that Brønsted acids are good substitutes for the synthesis of HCPs, prioritising environmental friendliness.

### 1.3.2 The choice of solvents for HCPs synthesis

The selection of solvents is crucial for determining the porosity and pore size distribution of HCPs. During the early stages of HCPs development, significant research efforts were dedicated to the comparison of solvents used for HCPs. The focus on solvent choice emerged as researchers sought to optimise experimental parameters of post-crosslinking route and raised the overall performance of HCPs to new records. Generally, hypercrosslinking involves swelling or dissolving a precursor or monomer in a solvent, followed by crosslinking to form a network before the partially cross-linked polymer undergoes precipitation. This process is dependent on the kinetics of two competing reactions: crosslinking and desolvation of the polymer during the whole crosslinking process [142]. Theoretically, a suitable solvent for HCPs synthesis should be compatible with Friedel-Crafts reactions and thermodynamical good for the polymer.

Base on this principal, Sherrington's group investigated the effects of four different solvents including chlorobenzene, hexane, dichloroethane(DCE) and a mixture of DCE and hexane on the synthesis of PVBC type HCPs [46]. As expected, DCE yielded HCPs with the highest surface area. Hexane, typically considered as a poor solvent for polystyrene, unexpectedly yielded a resin with a remarkable surface area exceeding 600 $m^2 g^{-1}$, even higher than that of HCPs synthesised in chlorobenzene. This research provided valuable insights for tailoring and optimizing the synthesis conditions, but the reasons behind solvent-dependent differences are still unclear. Similar conclusions were proposed by Liu an co-workers, who employed five solvents including benzene, cyclohexane, n-hexane, 1,1,2-trichloroethane (TCE) and DCE as the medium for the self-crosslinking of DCX [143]. Among them, the poly-DCX synthesised in DCE

undoubtedly had the highest surface area (up to 1398 $m^2$ $g^{-1}$) while those synthesised in benzene, cyclohexane, and n-hexane did not even exceed 60 $m^2$ $g^{-1}$. Despite the conclusion, this work was lack of explanation for how solvents influence the synthesis of HCPs. They only provided a general explanation for this difference, attributing it to variations in solvent solubility and polarity, which finally led to different crosslinking degrees in the resulting HCPs. Urban et al. conducted a study on the effects of dichloro-based solvents, including DCE, 1,4-dichlorobutane (DCB) and 1,6-dichlorohexane (DCH), on the synthesis of hypercrosslinked poly(styrene-co-vinylbenzyl chloride-co-divinylbenzene) monoliths in columns [144]. They observed that as the alkyl chain length of the swelling solvent increased, the column permeability decreased.

Previous studies on solvents and their effects on the formation of HCPs are limited and lack comprehensive understanding. The underlying reasons for how solvents influence the formation of HCPs are not well-explored. Recently, Duan systematically studied the interactions between solvents and reactants based on their Hansen three-dimensional parameters, in which twelve solvents were involved [145]. They divided all solvents into four types according to their solvation to polymers and compatibility with Friedel-Crafts reaction. When the solvent is suitable for both factors, such as DCE, it results in high yields. In contrast, when the solvent is incompatible with the Friedel-Crafts reaction, such as DMSO or isopropyl alcohol, no products are obtained. However, when the solvent exhibits good compatibility with the Friedel-Crafts reaction but poor solvation of the polymer, such as acetic acid or acetone, greater yields are observed because catalysts could be trapped inside.

We have to admit that there is a need for further research to elucidate the specific mechanisms and factors that contribute to solvent-induced changes in the properties and characteristics of HCPs. By addressing these gaps, we can enhance our understanding and optimise the selection of solvents for HCP synthesis, ultimately improving the quality and performance of these materials.

Conventional synthesis of HCPs usually requires toxic organic solvents, which is not in line with the development trend of green chemistry. To bring more attention to this issue, researchers have set out to replace them with more sustainable solvents or even non-solvent reaction systems. Fredrik Björnerbäck innovatively introduced sulfolane, an organosulfur renewable solvent, into the polymerisation of biobased monomers [146]. Sulfolane, which can be derived from butadiene, $SO_2$, and $H_2$, is biodegradable under aerobic conditions. Although its toxicity is still under investigation, sulfolane has been confirmed compatible with Friedel-Crafts reactions. The HCPs synthesised in sulfolane had high $CO_2$ uptake (up to 3.94 mmol $g^{-1}$ at 0 °C and 1 bar), total pore volumes (up to 1.86 $cm^3$ $g^{-1}$), and specific surface areas (up to 1440 $m^2$ $g^{-1}$).

Very recently, mechanosynthesis of HCPs has been attractive because it can greatly shorten the reaction time and do not require homogeneous reaction system [147,148]. Mechanosynthesis is an old technology while it has only recently emerged within the focus of researchers as it can be a solvent-free process. Typically, mechanosynthesis utilises a ball mill as a reactor in which a cylindrical bowl with a rounded edge is filled with spherical balls of known diameters. After adding all reactants in it, the bowl is sealed and stirred for a predetermined duration, either continuously or with intermittent pauses. Lee et al. innovatively reported a superfast non-solvent mechanosynthesis method to produce HCPs from various aromatic monomers, and this method was proved to be suitable for both Friedel-Crafts knitting reaction and Scholl coupling process [147]. To be more precise, this method avoids using conventional toxic solvents like DCE and excess FDA liquid can partly serve as solvents. Surprisingly, HCPs can be generated in only 10 seconds, while the optimum HCP was obtained in mere 5 minutes, the surface area of which reached 782 $m^2$ $g^{-1}$. This protocol allowed a sustainable, time-saving and scalable route for the production of porous HCPs materials.

## 1.4 Applications of HCPs materials

Hypercrosslinked polymers was originally developed as ion exchange resins and they have undergone significant advancements, incorporating enhanced properties that

expand their applicability to a wider range of applications. So far, HCPs have been mainly used in gas storage, water treatment, chromatography, catalysis, drug delivery, sensing, etc.

### 1.4.1 Gas storage

The wide range of HCPs available for gas storage stems from the synthetic versatility of the knitting strategy, allowing for the incorporation of various building blocks. These multifunctional groups endow the HCPs with the ability to adsorb different gases. Among them, hydrogen ($H_2$), carbon dioxide ($CO_2$) and methane ($CH_4$) have gained the most concern because of the urgent environmental burden of eliminating green-house gases and developing clean energies.

Hydrogen, as a clean and efficient energy carrier, is regarded as a desirable alternative for traditional fossil fuels. However, the safe storage and controlled release of $H_2$ still restrict the widespread use of hydrogen resource. Porous HCPs featuring large pore volume, irreversible sorption and good stability have emerged as an ideal option for gas storage [149]. Germain et al. studied hydrogen adsorption behaviour of a series of HCPs synthesised from gel-type and macroporous-type precursors respectively via $FeCl_3$ catalysed Friedel-Crafts reactions [150]. The best obtained HCPs with a surface area of 1930 $m^2$ $g^{-1}$ can adsorb 1.5 wt% of $H_2$ under 77 K and 0.12 MPa reversibly. Cooper's group conducted similar research on Davankov-type HCPs represented by poly-VBC [41]. The generated microporous VBC-HCPs can adsorb 3.14 wt% of $H_2$ at 77 K and 15 bar. However, it is important to note that HCPs still have a significant journey ahead to meet the sorption target of 6.5 wt% set by the US Department of Energy. Later, Colin and co-workers continued to study the hydrogen storage of HCPs synthesised *via* internal hypercrosslinking [71]. The $H_2$ uptake recorded was raised to 3.68 wt% at 77 K and 15 bar due to the enhancement of surface area. This work also pointed out that narrower pore size was favourable in the adsorption of small molecules. To further improve the hydrogen uptake ability of HCPs, Tan et al. incorporated Pt nanoparticles into porous HCPs, drawing inspiration from the 'hydrogen spillover' phenomenon occurred on the metal catalysts [151]. Incorporating 2

wt% of Pt nanoparticles boosted the hydrogen storage capacity of HCPs to 0.21 wt% at 298 K and 19 bar. This represented a 1.75-fold increase in $H_2$ adsorption compared to similar materials lacking Pt nanoparticles. The increase in hydrogen adsorption can be attributed to the dissociation of $H_2$ molecules on the Pt surface, followed by the surface diffusion and adsorption of atomic hydrogen on the microporous polymer surface. Additionally, metal-containing HCPs such as ferrocene-based HCPs displayed notably higher than $H_2$ uptake than those of porous polymers with a higher surface area under the same conditions [152]. With the aid of DFT calculations, the interaction between $Fe^{2+}$ and $H_2$ is confirmed to be physical adsorption.

Methane is also regarded as a potential clean energy for replacing the finite fossil fuels. Therefore, the methane adsorption behaviours in HCPs materials have captivated the interest of researchers. Colin et al. reported the methane gravimetric capacity of HCPs derived from DCX and BCMBP monomers reached 5.2 mmol $g^{-1}$ (116 $cm^3$ $g^{-1}$) at 298 K and 20 bar while possess the highest surface area of 1904 $m^2$ $g^{-1}$ [72]. Despite the moderate surface area, these materials demonstrated one of the highest reported peak isosteric heat of sorption for methane (20.8 kJ $mol^{-1}$) at that time, placing them in the same league as many reported microporous systems. Gatti and co-workers synthesised HCPs (named as UPO16) by knitting tetraphenylmethane (TPM) and FDA in DCE [153]. The measured $CH_4$ capacity of UPO16 and KOH-activated KUPO16-2-750 was 9 and 18 wt% respectively at 100 bar while both materials did not reached saturation. Tong et al. found that the continuous monolithic structure of HCPs are more beneficial because they can fully occupy the available volume of the container [154]. The volumetric storage capacity of monolithic HCPs was therefore twice as high as that of hypercrosslinked beads.

The significance of HCPs' capacities for carbon dioxide gas has been underscored in response to the escalating concerns about climate change and the emission of greenhouse gases. Different from $H_2$ and $CH_4$, the adsorption process of $CO_2$ is closely related to grafted functional groups as well. Previous research showed that the introduction of amine and carboxyl groups can effectively enhance $CO_2$ capacity and

$CO_2/N_2$ selectivity simultaneously by strengthening the interaction between $CO_2$ and HCPs [155]. Robert synthesised a series of HCPs with different functional building blocks and compared their $CO_2$ uptake [98]. Among all HCPs, the triazole-based networks exhibited the highest $CO_2$ capacity of 3.36 mmol $g^{-1}$ at 298 K and 1 bar. This work concluded that there is no inherent correlation between high BET surface area and $CO_2$ uptake. On the contrary, factors such as isosteric heat and pore size could be dominant in the $CO_2$ adsorption under low pressure. This research group continued to synthesise amine-containing HCPs and increased their selectivity for $CO_2$ [156]. The porosity of these $NH_2$-HCPs can be tuned by varying the molar ratio between aniline and benzene as mere aniline would only yield a nonporous network. With the increasing proportion of aniline in the final HCPs, the BET surface area dropped while $CO_2/N_2$ selectivity rose. Hence, the best $NH_2$-HCP was composed of 40% aniline and 60% benzene of which the $CO_2$ uptake was 1.18 mmol $g^{-1}$ and $CO_2/N_2$ selectivity was 25, taking the trade effect into consideration. Moreover, hydroxyl groups have also been verified useful for improving $CO_2$ uptake. Dawson et al. prepared six alcohol-containing HCPs by external hypercrosslinking using FDA as a crosslinker [157]. The HCP that synthesised from 1,1'-bi-2-naphthol monomers exhibited the highest $CO_2$ uptake (up to 3.96 mmol at 273 K and 1 bar), corresponding to its highest surface area of 1015 $m^2$ $g^{-1}$. However, the researchers found that the $CO_2$ adsorption capacity decreased by 50% under realistic wet conditions, comparing with the ideal dry conditions in lab. This indicated that alcohol-containing HCPs may adsorb $CO_2$ and water simultaneously, thereby diminishing the efficacy of such hydrophilic HCPs in the practical use. Jing and co-workers confirmed that hydroxyl and amine groups can effectively enhance the $CO_2$ capacity of HCPs because of improved isosteric heat in the adsorption process [158]. Except above mentioned gases, HCPs have been applied for the adsorption of volatile organic compounds such as benzene [159], cyclohexane [159], toluene [160], etc.

Generally, HCPs materials with higher surface area always indicates larger adsorption uptake of gas molecules. Another key fact is pore size distribution (PSD) which not

only decides the pore structure but also significantly influences the adsorption enthalpy. In addition, the functional groups of the HCPs can contribute to better gas adsorption if they have stronger affinity with some gas molecules.

### 1.4.2 Water treatment

HCPs materials have been used as solid adsorbents and ion exchange resins for water treatment purposes since their inception. With the development of various HCPs, these materials have been set apart from the conventional inorganic adsorbents because the hydrophobic skeletons of HCPs exhibit a higher affinity for organic molecules. In addition, the porous characteristic of HCPs can provide channels for adsorbates to enter the inner space, benefiting the adsorption capacity.

HCPs have been widely used for removing heavy metals from water. Li and co-workers employed sulfonic acid-modified HCPs (SAM-HCPs) synthesised *via* sulfonation of Davankov-type HCPs to remove toxic metal ions from water [161]. SAM-HCPs showed remarkable efficiency in removing toxic metal ions including $Pb^{2+}$, $Cu^{2+}$, $Cr^{3+}$ and $Ni^{2+}$, achieving complete removal (99%) even at low concentrations (20 mg $L^{-1}$). Notably, the adsorption behaviour appears to be unaffected by the valence state of metal ions. Take $Cu^{2+}$ as an example, the kinetics of its adsorption fitted well with the pseudo-second order model. This indicated that there were massive active sulfonic sites on the surface of HCPs and the rate-limiting step for the adsorption of $Cu^{2+}$ onto these active sites is under kinetic control. Anito et al. synthesised iminodiacetic acid-functionalised HCP (IDA-HCP) and compared its adsorption ability to $Pb^{2+}$ from a solution mixture of $Pb^{2+}$, $Hg^{2+}$, $Cd^{2+}$, $Co^{2+}$, $Fe^{3+}$, $Zn^{2+}$, $Mg^{2+}$, and $Na^{+}$ metal ions [162].Compared with sole adsorption to a specific metal ion, this model is closer to the actual water treatment requirements. The IDA-HCP demonstrated exceptional uptake capacity, with a value of 1138 mg $g^{-1}$ for $Pb^{2+}$. Furthermore, this polymer exhibited an outstanding initial adsorption rate of 320 mg $g^{-1}$ $min^{-1}$. Moreover, IDA-HCP displayed a strong affinity for $Pb^{2+}$ over a wide pH range of 1 to 12, and it also exhibited good selectivity for multiple toxic transition metals, including $Pb^{2+}$, $Hg^{2+}$ and $Cd^{2+}$. Very recently, Masoumi reviewed the

development of HCPs in the removal of hazardous metal ions [163]. Drawing from extensive research findings, it has been observed that HCPs containing carboxyl and sulfuric groups exhibit the highest level of activity compared to other functional groups. They recommended sodium alginate and hydroxyphtalic acid as the most favourable precursors for synthesising polymers because of high adsorption capacity and distinguishing recyclability.

In addition to the removal of metal ions, Waheed mentioned that HCPs materials can play a role in the disposal of organic contaminants in wastewater [9]. Typically, HCPs used in the dyes adsorption from water consist of aromatic rings to facilitate π-π interactions, amine and hydroxyl groups for hydrogen bonding, carboxylate groups for hydrogen bonding and Coulombic interactions, and a surface charge for ionic interactions. Castaldo synthesised novel amino-functionalised vinylbenzyl chloride/divinylbenzene-based HCPs to enhance the polarity and affinity of hypercrosslinked resins towards polar dyes [164]. Despite the reduction in the total pore volume caused by amino functionalization, narrower micropores were formed. The amino-modified HCPs exhibited an indigo carmine adsorption capacity that was four times higher than unmodified ones. Apart from dyes, Liu et al. managed to use a nanoscale Davankov-type HCP particles to adsorb benzene-ring-containing organic pollutants including benzene, toluene, ethylbenzene, *o*-xylene and long-chain *n*-alkanes *via* solid-phrase microextraction (SPME) [165]. The mixture of HCPs and adsorbed rhodamine B exhibited a highly noticeable fluorescent quenching phenomenon, providing strong evidence for the existence of a π-π stacking effect between the HCPs and aromatic compounds. HCP-nanoparticles-coated SPME fibres exhibited excellent extraction ability towards the benzene-ring-containing pollutants. When they were applied for realistic water samples such as lake water, river water and treated waste water, the recoveries of the analytes ranged from 79.2% to 108.9% depending on the original concentration. Song and co-workers reported a highly water-dispersible HCP modified with carboxyl groups, and they exhibited prominent capacity for water-soluble contaminants such as tetracycline (up to 418.41 mg $g^{-1}$ at

298 K) [166]. Besides, this HCP-COOH also displayed improved adsorption uptake to cationic methylene blue (422.08 mg $g^{-1}$). Dai's group innovatively synthesised a hypercrosslinked β-cyclodextrin porous polymer (BnCD-HCPP) *via* Friedel-Crafts reactions [167]. BnCD-HCPP revealed outstanding capture of water-soluble aromatic molecules due to the characteristic janus structure composed of a hydrophobic centre and hydrophilic shell. The molar ratio of the adsorbates, such as 4-nitrophenol, 4-chlorophenol and phenol, to β-cyclodextrin surpassed 300%, indicating that the adsorption took place not only within the cyclodextrin cavities through 1:1 complexation but also within the nanopores of the BnCD-HCPP resulting from hypercrosslinking.

### 1.4.3 Catalysis

HCPs possess desirable attributes for catalytic purposes due to their high specific surface, large pore volume and tailored functionality. Therefore, they are expected to be appropriate platforms for anchoring catalysts, and provide wide interface and active sites for heterogeneous reactions.

Metal catalysts account for a large proportion of conventional catalysis. Hence, researchers instinctively consider incorporating metal components into HCPs to fabricate catalysts. Generally, two distinct approaches can be employed to prepare metal-containing HCPs [168]. The first one is to introduce metal ligands into the prepared HCPs *via* postfunctionalisation. On the other hand, the second method directly utilises metal coordination complexes as building blocks for HCPs. Obviously, the second option can preserve the coordination environment of the metal within the final HCPs, indicating better stability and recyclability. According to the statistics, palladium (Pd) [169-176] and ruthenium (Ru) [177-180] are the commonly employed metals in HCP-based catalyst formulations, while rare research have reported aluminium (Al) [181-183], first row transition metal [86,182,184-187] and noble metal [179,188-190].

Pd-containing HCPs have been widely used as catalysts for classic organic reactions such as Suzuki−Miyaura [170] and Heck C−C couplings, C−H halogenation, Ullman coupling etc. Tan's group first reported the synthesis of a high-reactive and

recoverable palladium-phosphine catalyst *via* postfunctionalisation [169]. They prepared HCPs by knitting triphenylphosphine ($PPh_3$) with aromatic monomers, and then coordinated Pd with $PPh_3$. Under gentle conditions (80 °C), this catalyst facilitated rapid Suzuki-Miyaura coupling reactions in an aqueous ethanol solution, demonstrating its superiority compared with homogenous catalyst such as $PdCl_2$. In this work, HCPs not only served as support materials but also as protective shields for the metal catalyst, consequently enhancing the catalytic activity. Following this work, Tan's group overcame the challenges and confirmed this catalyst can be used for Suzuki−Miyaura coupling reactions of aryl chlorides and benzyl chlorides bearing electron-withdrawing groups [170]. Apart from $PPh_3$, N-heterocyclic carbenes (NHCs) were also been knitted into HCPs and coordinated with $Pd(OAc)_2$ to prepare poly-NHCs-$Pd^{2+}$ complexs [171]. The surface area of poly-NHCs dropped dramatically after incorporating $Pd^{2+}$. These poly-NHCs-$Pd^{2+}$ catalysts effectively improved the rate of Suzuki–Miyaura coupling reaction in an aqueous ethanol solution under mild conditions. Additionally, N-pyridine-NHC ligands, which are bidentate ligands with both strong and weak donor groups, are better options for coordinating with $Pd^{2+}$ because of the chelating effect [191]. Immobilisation of palladium onto the hypercrosslinked polymer was achieved through the formation of a six-membered ring involving $Pd^{2+}$ ions and the bidentate ligands of NHC and pyridine. These pyridine-functionalised NHC-palladium HCPs exhibited remarkable versatility in accommodating different aryl halides and aryl boronic acids, making them good candidates for Suzuki-Miyaura coupling reactions conducted in aqueous environments. Parallelly, bidentate building blocks such as 1,10-Phenanthroline [192], 4,7-diphenyl-1,10-phenanthroline [193], and 2,2'-bipyridine [194] are also capable of forming complexes with $Pd^{2+}$.

Wang and co-workers first synthesised Ru-coordinated HCPs that exhibited excellent performance in terms of both activities (up to 99.5%) and enantioselectivity(up to 97%) during the asymmetric hydrogenation of β-keto esters [180]. 2,2'-bis(diphenylphosphino)-1,1'-binaphthyl (BINAP), a chiral ligand, was employed to

copolymerise with benzene, biphenyl and TPB *via* FDA-involved external hypercrosslinking method. The as-prepared HCPs were then coordinated with $RuCl_2$ to form catalysts. Moreover, Wang et al. managed to synthesise heterogeneous ruthenium compound catalyst with single-atomic sites (PPRu) by one step knitting process of the Ph-$PN^3$P-pincer ruthenium monomer and FDA based on Friedel-Crafts chemistry [178]. The PPRu synthesised *via* direct crosslinking of Ru-containing monomers exhibited outstanding stability and reusability, and they showed distinctive selectivity and catalytic activity in the conversion of formic acid (FA) into $H_2$, in which the turnover frequency and turnover number reached 266 $h^{-1}$ and 145300 respectively.

Generally, metal-coordinated HCPs prepared through direct metal-containing monomer knitting exhibit lower specific surface areas compared to those prepared via postfunctionalisation of preformed HCPs. Surprisingly, no discernible relationship between surface area and catalytic activity is observed. However, a significant correlation is discovered between catalytic activity and nanoparticle size, highlighting the importance of particle size in determining the catalytic performance.

Apart from metal-containing HCPs catalysts, pure organic, metal-free and visible light photocatalysts provide another sustainable route for heterogeneous reactions. Zhang et al. reported a highly porous HCP, containing photoactive conjugated organic semiconductor units, served as effective photocatalyst for selective bromination of electron-rich aromatic compounds [195]. They directly knitted 4,7-diphenylbenzo[c][1,2,5]thiadiazole (BT-$Ph_2$), which was photoactive unit, with FDA crosslinker. The conversion rate can be increased by 16% after adding the resulting HCPs. Two active oxygen species, superoxide and singlet oxygen were confirmed to be involved in the reaction, indicating the occurrence of photocatalysis. HCPs can also be combined with ionic liquid and subsequently applied as catalysts in the production of biodiesel, simplifying practical application of ionic liquids in the industry [196]. Gao et al. innovatively designed dipolar HCPs with flexible dimethylformamide (polylactic acid (PLA) and) moiety as porous polymer solvents,

which can catalysing the reactions by creating dipolar solvation microenvironment [197]. These HCPs successfully converted $NaN_3$ to benzylic azides and 1,2,3-triazoles in ethanol, benefiting the products purification process and disposal of waste.

### 1.4.4 Chromatography

HCPs also play a role in the chromatography because of their abundant pores and possibility for tailoring different end groups. Maya and Svec synthesised hypercrosslinked PS-co-DVB monoliths *via* $FeCl_3$ catalysed Friedel-Crafts reaction in which DCX, BCMBP and FDA served as external crosslinkers [198]. These HCPs monoliths were used as the stationary phase in the capillary columns for liquid chromatography. BCMBP-crosslinked monoliths exhibited the highest surface area up to 900 $m^2$ $g^{-1}$ and the reaction time was greatly shortened to 2.5 hours. The performance of HCPs monoliths in the capillary columns was evaluated through an isocratic reversed phase liquid chromatography separation for a mixture containing acetone and six alkylbenzenes. The column efficiency for the retained analytes surpassed 70,000 plates $m^{-1}$. In addition to reversed phase mode, Maya and Svec continued to synthesise phenolic hydroxyl-functionalised PS-co-DVB-co-VBC HCPs in the capillary column and the resulting hypercrosslinked monoliths can work under normal phrase mode for separating small molecules [199]. For instance, the column efficiency for nitrobenzene can reach 31800 plates $m^{-1}$. Later, Shiryaeva tried to use a PS-based HCP as the stationary phase for capillary gas chromatography [200]. However, they failed to obtain porous HCPs by direct synthesis in a column and this led to poor separation ability towards light hydrocarbons. This can be attributed to continuous spikes of shed particles, which means poor adhesion between HCPs microspheres and capillary walls. Very recently, Kanateva and co-workers achieved progress in synthesising highly efficient porous layer open tubular columns using HCPs as stationary phase [201]. They used simpler suspension technique to synthesise HCPs in the capillary column and these HCPs were bound to pre-treated anchor amino groups on the surface of capillary walls. Moreover, Liu et al. coated HCPs, which were knitted by benzene and FDA, on the surface of the column for gas chromatography

[202]. The column coated with HCPs exhibited exceptional gas chromatography separation capabilities for a range of volatile organic compounds (VOCs), including the difficult-to-resolve ethylbenzene and xylene isomers. In contrast, these isomers could not be adequately separated on the commercially available 5% phenyl polysiloxane stationary phase.

### 1.4.5 Drug delivery

Hollow microporous organic capsules (HMOCs) were synthesised and employed in drug delivery application by Li and co-workers [45]. HMOCs had enough empty chambers caused by the removal of inner templates and the microporosity of organic shell was provided by the hypercrosslinking process. Such unique structure enabled them to be ideal candidates for molecules storage while the micropores distributed in the polymeric shell can grant access to movement of molecules. The researchers investigated the drug loading and release behaviour of HMOCs using ibuprofen (IBU) as a model molecule. HMOCs exhibited significantly higher IBU uptake capacity, ranging from 1.68 to 2.04 g of IBU per gram, surpassing the achieved uptake of solid HCP nanoparticles (0.80 g of ibuprofen per gram) prepared without a silica core template using a similar synthesis process. It implied that the IBU drug molecules were trapped in the hollow cavity of HMOCs. The release of IBU was implemented by soaking the drug-loaded HMOCs in simulated body fluid (PBS, pH 5 7.4, buffer solution). The release kinetics curves of different HMOCs were closely related to the porosity of polymeric shells. To be more specific, HMOCs possessing both meso- and micropores, of which the DVB proportion was from 0.5% to 5%, fitted a consistent first-order kinetic model. This meant that the release mechanism of ibuprofen was predominantly governed by simple diffusion. The drug was released from HMOCs at a rate proportional to the remaining amount of drug within the interior. Conversely, HMOCs consisting purely of micropores, of which the DVB proportion was 10% or 15%, aligned well with the zero-order model featuring with a constant releasing rate. This can be attributed to the constrained diffusion of drug molecules within narrow micropore channels. The superiority of pure microporous HMOCs is obvious because

the constant release rate helps maintain a stable drug concentration in the bloodstream, which is particularly desired in clinical therapy. Song et al. also utilised similar carboxyl groups grafted-hollow polymeric capsules to delivery doxorubicin (DOX) to cancer cells [203]. Interestingly, the hollow HCPs were obtained through the one-pot Lewis acid catalysed polymerisation and self-assembly, without the use of any templates. Due to their inherent hollow porosities and the presence of specific targeting agents, these materials exhibited a remarkable drug encapsulation efficiency of up to 86%. Additionally, they demonstrated a controlled drug release of up to 50% within a 30-hour timeframe in an acidic environment.

### 1.4.6 Sensing

Zhang's group reported a series of lithium-modified HCPs sensors that have good stability and rapid response to humidity [204,205]. They first synthesised hydrophilic HCPs (named as P3HBA) from 3-hydroxybenzoic acid via FDA-involved external hypercrosslinking reaction, and loading lithium chloride (LiCl) inside to prepare an electrochemical humidity sensor. Compared with pristine P3HBA, LiCl-loaded P3HBA sensors had lower impedances because LiCl can interact with water and ionise simultaneously. By adjusting the loading amount of LiCl, the one utilizing 4 wt% LiCl-loaded P3HBA exhibited the highest level of linearity and sensitivity. This sensor demonstrated exceptional sensitivity across the entire humidity range, with the impedance experiencing a significant change of nearly four orders of magnitude from 11% to 95% relative humidity (RH). The response time and the recovery time of the sensor was 2 seconds and 7 seconds respectively, suggesting its superiority to similar sensors composed of hydrophilic polymers. Following these results, they replace LiCl with lithium hydroxide (LiOH) to be the lithium source. LiOH can also greatly improve the sensitivity of P3HBA sensors. Razzaque and co-workers managed to use hypercrosslinked hollow microporous capsules grafted with dithiocarbamate functional groups as an electrode material, to detect Cu(II) ions [206]. This was realised by the strong interaction between dithiocarbamate functional groups and Cu(II) ions, and the lower limit of detection reached $1.02\times10^{-11}$ M. In addition, hypercrosslinked

furan modified-carbon paste electrode were verified to be sensitive for Pb(II) ions, indicating its potential in the detection of heavy metals in the wastewater [108].

## 1.5 Promising research directions in HCPs materials

Many efforts have been devoted to developing economical and versatile synthetic strategies to expand the types of HCPs. By employing a wide range of monomers and introducing diverse functional groups, HCPs materials are well-designed for specific applications such as water treatment, carbon capture and other high-value separation process. HCPs feature on abundant micropores which could be tuned and modified for precise molecule sieving. Despite the achievements of current research on HCPs, we have to admit that there is still space to be filled in this field. It is challenging to precisely control the pore structure from a molecular level because of the fast kinetics accompanied by Lewis acid catalysed Friedel-Crafts reactions, wherefore HCPs are generally polymerise in an irregular manner and have asymmetric pore distributions. Further study on the accurate control over the pore structures of HCPs is highly needed.

Moreover, the current production of HCPs is criticised for their large consumption of toxic organic solvents, catalysts and subsequent post-treatments. The solvents included in Friedel-Crafts reactions are usually halogenated solvents like dichloromethane (DCM), dichloroethane (DCE), chloroform and chlorobenzene which are classified as toxic solvents. Additionally, some corrosive by-products, like hydrogen chloride (HCl) caused by hydrolysis of metal halides, could be released during the reactions. Global energy and environmental issues have been drawing people’s attention as everyone is responsible for our living habitats. The International Energy Agency (IEA) published a special report on how to reach net-zero emissions by 2050, leading the development of high-efficiency technologies [207]. The energy consumption of industrial sector accounted for 38 % of total global final energy in 2021, while chemical and petrochemical industry usually occupied 30 % of the whole

industry, emitting 1.37 gigatons (Gt) of $CO_2$ [208-210]. Therefore, strong desire for more sustainable synthetic protocols has been a consensus for academic researchers [211]. The development of HCPs will also step towards a greener and more efficient way. For instance, replacing undesirable solvents with more renewable solvents such as sulfolane and ionic liquids (ILs). Natural products and bio-derived molecules should be considered as starting resource and further processed into high-value HCPs products. On the other hand, novel technologies, except conventional chemical synthetic methods, are given high expectations to promote large-scale fabrication of HCPs. The utilisation of biobased solvents, metal-free catalysts, catalyst-free synthesis, and catalyst recycling holds significant promise for enhancing the sustainability of synthesising similar HCPs. These approaches offer the potential to replace environmentally-harmful and unsustainable processes that are commonly employed in HCP synthesis.

Another promising direction for HCPs is to improve their processablity. HCPs usually exist in the form of insoluble powders macroscopically, which brings inconvenience to practical applications. The key obstacle to be resolved is to prevent pore structures from collapse if solubility of HCPs is increased. Yang et al. first successfully reported soluble hypercrosslinked polystyrene by controlling the concentration of each reactants [54]. They decelerated the reaction kinetics via slowly adding crosslinker into the diluted solution, limiting the crosslinking between intermolecular polymer chains. This strategy enabled the linkage mostly distributed in intramolecular folding of single polymer chains and thus retained the solubility of as-prepared HCPs. A film could be obtained via solution-casting and it proved to have uniform surface morphology without obvious defects. Dai and co-workers [55] managed to synthesise polymeric molecular sieve membranes for gas separation via facile in-situ hypercrosslinking technology. The resulting membranes owned a hierarchical sandwich structure composed of a microporous core, a layer of dense micropores and a mesoporous surface, demonstrating both good gas permeability and selectivity. Very recently, Tan’s group reported processable HCPs monoliths via 2-step controlled

knitting method [212]. They used DVB as a self-crosslinking monomer which experienced pre-crosslinking and subsequent deep-crosslinking under the catalysis of small amount of $FeCl_3$ at room temperature. The porosity and mechanical strength of as-synthesised DVB-HCP monoliths can be tuned by adjusting the concentration of DVB, and their BET surface area and mechanical strength reach 1056 $m^2$ $g^{-1}$ and 65 MPa respectively. These studies achieved the purpose of controlling the hypercrosslinking degree from the point of reaction kinetics and equilibrium. This is an immediate countermeasure to alleviate the insolubility and unprocessablity caused by fast Friedel-Crafts reactions. Furthermore, HCPs materials have been reported to be prepared into specific shapes for multiple applications. Svec and his colleagues successfully synthesised styrenics-based monolithic layers for the purpose of peptide and protein separation in thin layer chromatography (TLC) [213]. These monolithic layers were created through thermal-induced polymerisation followed by a Friedel-Crafts alkylation reaction. Notably, the inclusion of chloromethylstyrene units in the structure resulted in a significant increase in surface area, enabling the separation of smaller molecules such as dyes. Su et al. successfully synthesised hypercrosslinked aerogels that serve as substrates for various molecular separation processes [214]. They utilised tetrahedral monomers as starting materials and achieved hierarchical porous hypercrosslinked (HCP) gels via thermally-induced polymerisation. These HCP gels were found to be excellent platforms for incorporating functional two-dimensional polymers, enabling their successful application in column-based and membrane-based molecular separation systems. This work introduces a novel methodology for fabricating processable HCP devices that hold great potential for diverse separation applications. Therefore, investigating the processablity of HCPs is a continuing concern within both the academic and industrial areas.

## 1.6 Thesis motivation

The development of HCPs materials holds immense promise for a wide range of applications. However, several challenges still need to be addressed to fully harness their potential. This thesis is motivated by the pressing need to overcome these challenges and advance the field of HCPs materials towards more precise control over pore structures, greener synthetic protocols, and improved processability.

The practical applications of HCPs are hindered by their macroscopic form as insoluble powders, limiting their processability. This thesis recognises the need to overcome this challenge and improve the practical utility of HCPs. By exploring novel strategies such as 3D printing, this research aims to enhance the processability of HCPs. The objective is to transform HCPs into more versatile forms which can be defined by 3D printing program, enabling their integration into various applications while preserving their unique porous properties.

Moreover, the sustainability is a paramount concern in materials science. This thesis recognises the strong desire for greener and more efficient synthesis methods for HCPs and set up to develop more sustainable synthetic protocols for HCPs. By investigating the feasibility of environmentally friendly deep eutectic solvents (DES) and optimizing the experimental parameters, this research aims to offer a sustainable synthetic protocol that minimise environmental impact and resource consumption. The ultimate goal is to contribute to the consensus among academic researchers for more sustainable practices in HCPs synthesis. Simultaneously, the control over the porosity of HCPs can also be achieved in the new reaction system dominated by DES. By understanding the underlying mechanisms and developing innovative synthesis approaches, this research strives to pave the way for tailored and well-defined pore architectures in HCPs.

## 1.7 The framework and design of the thesis

This thesis is comprised of seven chapters. Chapter 1 gives an overall introduction to the latest development of hypercrosslinked polymers (HCPs) as well as research

motivation of this thesis. A literature review including the categorization, application and promising prospects of HCPs materials is also provided. Chapter 2 is a literature review on deep eutectic solvents (DES), which are regarded as green alternatives for conventional organic solvents. This brief review introduces background knowledge of DES and emphasised on the progress of DES applied in multiple chemical reactions. Methodology, materials and characterisation techniques used in this thesis are summarised in Chapter 3. The following three chapters will elaborate the research work and findings achieved on the optimisation of synthetic methods of HCPs, including structural characterization, discussion on materials performance and summaries on each work.

In Chapter 4, well-developed 3D-printing technology and novel stepwise hypercrosslinking strategy are combined to synthesise structure-retained porous high-impact polystyrene (HIPS) monoliths for adsorption process. By adjusting the reaction time of each step of crosslinking, we managed to maintain the mechanical strength and porosity of HIPS monoliths simultaneously. The prepared porous HIPS monoliths are used for dyes removal, oil absorption and recovery of taxadiene, which is an intermediate in the synthesis of anticancer medicine. This work revealed a feasible strategy to produce processable HCPs materials that can adapt to different circumstances instead of traditional powdered HCPs.

To further overcome the drawback of consuming large amount of hazardous halogenated solvents in the traditional synthesis of HCPs, Chapter 5 mainly reports applying DES including $[ChCl][ZnCl_2]_2$ and $[ChCl][FeCl_3]_2$ in the preparation of HCPs, which is demonstrated to be a versatile strategy for varied starting monomers. The results showed that reaction durations, temperatures, monomer reactivity and the molar ration between monomers and metal halide could effectively affect the pore structures of HCPs. Additionally, the physical and chemical properties of two DES systems are studied and the possible mechanisms of how DES systems work for hypercrosslinking reactions are proposed as well.

In Chapter 6, we further expand the starting materials to bio-based materials and manage to synthesise HCPs using totally green method. Several kinds of bio-based monomers such as phenol, benzyl alcohol, alkali lignin will be employed. Despite the deficient BET surface area, these HCPs proved impressive $CO_2$ capture ability because of their abundant hydroxyl groups.

Finally, Chapter 7 summarises the main conclusions made from this work, followed by the outlook for future research directions based on this PhD thesis.

## 1.8 References


[1] Zhang, T., et al., *Porous organic polymers: a promising platform for efficient photocatalysis.* Materials Chemistry Frontiers, 2020. **4**(2): p. 332-353.

[2] Giri, A., et al., *The order–disorder conundrum: a trade-off between crystalline and amorphous porous organic polymers for task-specific applications.* Journal of Materials Chemistry A, 2022. **10**(33): p. 17077-17121.

[3] Thommes, M., et al., *Physisorption of gases, with special reference to the evaluation of surface area and pore size distribution (IUPAC Technical Report).* Pure and applied chemistry, 2015. **87**(9-10): p. 1051-1069.

[4] Zdravkov, B., et al., *Pore classification in the characterization of porous materials: A perspective.* Open Chemistry, 2007. **5**(2): p. 385-395.

[5] Dawson, R., A.I. Cooper, and D.J. Adams, *Nanoporous organic polymer networks.* Progress in Polymer Science, 2012. **37**(4): p. 530-563.

[6] Zhang, L., et al., *Preparation and characterization of micro-mesoporous hypercrosslinked polymeric adsorbent and its application for the removal of VOCs.* Chemical engineering journal, 2012. **192**: p. 8-12.

[7] Tang, Z., et al., *Hypercrosslinked porous poly (styrene-co-divinylbenzene) resin: a promising nanostructure-incubator for hydrogen storage.* Journal of Materials Chemistry, 2012. **22**(25): p. 12752-12758.

[8] Yang, W., et al., *Effective removal of effluent organic matter (EfOM) from bio-treated coking wastewater by a recyclable aminated hyper-cross-linked polymer.* Water research, 2013. **47**(13): p. 4730-4738.

[9] Waheed, A., et al., *Removal of hazardous dyes, toxic metal ions and organic pollutants from wastewater by using porous hyper-cross-linked polymeric materials: A review of recent advances.* Journal of Environmental Management, 2021. **287**: p. 112360.

[10] Tsyurupa, M., et al., *Hypercrosslinked polystyrene: The first nanoporous polymeric material.* Nanotechnologies in Russia, 2009. **4**: p. 665-675.

[11] Sun, Y., et al., *Evaluating adsorptive separation of aniline from aqueous solution by an aminated hypercrosslinked polymer.* Separation Science and Technology, 2011. **46**(4): p. 687-693.

[12] Beker, U., et al., *Adsorption of phenol by activated carbon: Influence of activation methods and solution pH.* Energy Conversion and Management, 2010. **51**(2): p. 235-240.

[13] Schukraft, G.E., et al., *Hypercrosslinked polymers as a photocatalytic platform for visible-light-driven CO2 photoreduction using H2O.* ChemSusChem, 2021. **14**(7): p. 1720-1727.

[14] Fontanals, N., et al., *Evaluation of a new hypercrosslinked polymer as a sorbent for solid-phase extraction of polar compounds.* Journal of Chromatography A, 2005. **1075**(1-2): p. 51-56.

[15] Davankov, V., V. Rogozhin, and M. Tsjurupa, *Macronet polystyrene structures for ionites and method of producing same*. 1973, Google Patents.

[16] Tan, L. and B. Tan, *Hypercrosslinked porous polymer materials: design, synthesis, and applications.* Chemical Society Reviews, 2017. **46**(11): p. 3322-3356.

[17] Davankov, V., et al., *Hypercross-linked polystyrene and its potentials for liquid chromatography: a mini-review.* Journal of Chromatography A, 2002. **965**(1-2): p. 65-73.

[18] Staudinger, H. and W. Heuer, *Über hochpolymere Verbindungen, 93. Mitteil.: Über das Zerreißen der Faden-Moleküle des Poly-styrols.* Berichte der deutschen chemischen Gesellschaft (A and B Series), 1934. **67**(7): p. 1159-1164.

[19] *Production of synthetic polymeric compositions comprising sulphonated polymerizates of poly-vinyl aryl compounds and treatment of liquid media therewith*. 1944, Google Patents.

[20] Davankov, V.A. and M.P. Tsyurupa, *Hypercrosslinked polymeric networks and adsorbing materials: synthesis, properties, structure, and applications*. 2010: Elsevier.

[21] Mcburney, C.H., *Resinous insoluble reaction products of tertiary amines with haloalkylated vinyl aromatic hydrocarbon copolymers*. 1952, Google Patents.

[22] Abrams, I.M. and J.R. Millar, *A history of the origin and development of macroporous ion-exchange resins.* Reactive and Functional Polymers, 1997. **35**(1-2): p. 7-22.

[23] Howdle, S., et al., *Reversibly collapsible macroporous poly (styrene-divinylbenzene) resins.* Polymer, 2000. **41**(19): p. 7273-7277.

[24] Galia, M., F. Svec, and J.M. Frechet, *Monodisperse polymer beads as packing material for high-performance liquid chromotography: Effect of divinylbenzene content on the porous and chromatographic properties of poly (styrene-co-divinylbenzene) beads prepared in presence of linear polystyrene as a porogen.* Journal of polymer science part A: polymer chemistry, 1994. **32**(11): p. 2169-2175.

[25] Liu, Y. and D.J. Pietrzyk, *Capillary-electrochromatographic separations with copolymeric reversed-stationary phase and ion-exchanger-packed columns.* Journal of Chromatography A, 2001. **920**(1-2): p. 367-375.

[26] dos Santos, F.K.F., C.M. de Rezende, and V.F. da Veiga Júnior, *Macroporous polymeric resins as a tool to obtain bioactive compounds in food and food-waste: a review.* Journal of Food Composition and Analysis, 2022: p. 104703.

[27] Janson, J.-C., *Protein purification: principles, high resolution methods, and applications*. 2012: John Wiley & Sons.

[28] Leonard, M., C. Fournier, and E. Dellacherie, *Polyvinyl alcohol-coated macroporous polystyrene particles as stationary phases for the chromatography of proteins.* Journal of Chromatography B: Biomedical Sciences and Applications, 1995. **664**(1): p. 39-46.

[29] Germain, J., J.M. Fréchet, and F. Svec, *Hypercrosslinked polyanilines with nanoporous structure and high surface area: potential adsorbents for hydrogen storage.* Journal of Materials Chemistry, 2007. **17**(47): p. 4989-4997.

[30] Germain, J., J.M. Fréchet, and F. Svec, *Nanoporous polymers for hydrogen storage.* small, 2009. **5**(10): p. 1098-1111.

[31] Davankov, V., S. Rogoshin, and M. Tsyurupa. *Macronet isoporous gels through crosslinking of dissolved polystyrene*. in *Journal of Polymer Science: Polymer Symposia*. 1974. Wiley Online Library.

[32] Grassie, N. and J. Gilks, *Thermal analysis of polystyrenes crosslinked by p-di (chloromethyl) benzene.* Journal of Polymer Science: Polymer Chemistry Edition, 1973. **11**(8): p. 1985-1994.

[33] Davankov, V. and M. Tsyurupa, *Structure and properties of hypercrosslinked polystyrene—the first representative of a new class of polymer networks.* Reactive Polymers, 1990. **13**(1-2): p. 27-42.

[34] Tsyrupa, M., V. Lalaev, and V. Davankov, *On reasons determining unusual properties of hypercrosslinked styrene polymers, Dokl.* AN SSSR, 1984. **279**: p. 156-160.

[35] Davankov, V., et al., *From a dissolved polystyrene coil to an intramolecularly-hyper-cross-linked "Nanosponge".* Macromolecules, 1996. **29**(26): p. 8398-8403.

[36] Tsyurupa, M., et al., *On the nature of "functional groups" in non-functionalized hypercrosslinked polystyrenes.* Reactive and Functional Polymers, 2012. **72**(12): p. 973-982.

[37] Tsyurupa, M. and V. Davankov, *Hypercrosslinked polymers: basic principle of preparing the new class of polymeric materials.* Reactive and Functional Polymers, 2002. **53**(2-3): p. 193-203.

[38] Davankov, V. and M. Tsyurupa, *Anomalous properties of hypercrosslinked.* Polymer Networks' 91, 1992. **91**: p. 167-182.

[39] Wu, D., et al., *Nanoporous polystyrene and carbon materials with core–shell nanosphere-interconnected network structure.* Macromolecules, 2011. **44**(15): p. 5846-5849.

[40] Gadwdzik, B. and J. Osypiuk, *Modification of porous poly (styrene-divinylbenzene) beads by Friedel-Crafts reaction.* Chromatographia, 2001. **54**: p. 323-328.

[41] Lee, J.-Y., et al., *Hydrogen adsorption in microporous hypercrosslinked polymers.* Chemical Communications, 2006(25): p. 2670-2672.

[42] Hou, S., S. Razzaque, and B. Tan, *Effects of synthesis methodology on microporous organic hyper-cross-linked polymers with respect to structural porosity, gas uptake performance and fluorescence properties.* Polymer Chemistry, 2019. **10**(11): p. 1299-1311.

[43] Ratvijitvech, T., et al., *The effect of molecular weight on the porosity of hypercrosslinked polystyrene.* Polymer Chemistry, 2015. **6**(41): p. 7280-7285.

[44] Fontanals, N., et al., *Hypercrosslinked materials: preparation, characterisation and applications.* Polymer Chemistry, 2015. **6**(41): p. 7231-7244.

[45] Li, B., et al., *Hollow microporous organic capsules.* Scientific reports, 2013. **3**(1): p. 1-6.

[46] Ahn, J.-H., et al., *Rapid generation and control of microporosity, bimodal pore size distribution, and surface area in Davankov-type hyper-cross-linked resins.* Macromolecules, 2006. **39**(2): p. 627-632.

[47] Hauptmann, R., *Chloromethylation of styrene-divinylbenzene copolymers.* Plaste und Kautschuk, 1971. **18**(5): p. 330-331.

[48] Negre, M., M. Bartholin, and A. Guyot, *Autocrosslinked isoporous polystyrene resins.* Die Angewandte Makromolekulare Chemie: Applied Macromolecular Chemistry and Physics, 1979. **80**(1): p. 19-30.

[49] Veverka, P. and K. Jeřábek, *Mechanism of hypercrosslinking of chloromethylated styrene–divinylbenzene copolymers.* Reactive and Functional Polymers, 1999. **41**(1-3): p. 21-25.

[50] Law, R.V., et al., *Solid-state 13C MAS NMR studies of hyper-cross-linked polystyrene resins.* Macromolecules, 1996. **29**(19): p. 6284-6293.

[51] Mohanraj, S. and W.T. Ford, *Analysis of cross-linking of poly [(chloromethyl) styrene] by high-resolution carbon-13 NMR spectroscopy.* Macromolecules, 1985. **18**(3): p. 351-356.

[52] Li, B., et al., *Tailoring the pore size of hypercrosslinked polymers.* Soft Matter, 2011. **7**(22): p. 10910-10916.

[53] Hu, A., et al., *A green and low-cost strategy to synthesis of tunable pore sizes porous organic polymers derived from waste-expanded polystyrene for highly efficient removal of organic contaminants.* Chemical Engineering Journal, 2019. **370**: p. 251-261.

[54] Yang, Y., B. Tan, and C.D. Wood, *Solution-processable hypercrosslinked polymers by low cost strategies: a promising platform for gas storage and separation.* Journal of Materials Chemistry A, 2016. **4**(39): p. 15072-15080.

[55] Qiao, Z.-A., et al., *Polymeric molecular sieve membranes via in situ cross-linking of non-porous polymer membrane templates.* Nature communications, 2014. **5**(1): p. 3705.

[56] Zhao, S., et al., *Amine-Rich Molecular Nodule-Assembled Membrane Having 5 Angstrom Channels for CO2/N2 Separation.* Advanced Functional Materials, 2024: p. 2314469.

[57] Ogawa, N., et al., *Preparation of spherical polymer beads of maleic anhydride–styrene–divinylbenzene and metal sorption of its derivatives.* Journal of applied polymer science, 1984. **29**(9): p. 2851-2856.

[58] Maciejewska, M., Ł. Szajnecki, and B. Gawdzik, *Investigation of the surface area and polarity of porous copolymers of maleic anhydride and divinylbezene.* Journal of applied polymer science, 2012. **125**(1): p. 300-307.

[59] Huang, J., et al., *Nanoporous highly crosslinked polymer networks with covalently bonded amines for CO2 capture.* Polymer, 2018. **154**: p. 55-61.

[60] Liu, F., W. Fu, and S. Chen, *Adsorption behavior and kinetics of CO2 on amine-functionalized hyper-crosslinked polymer.* Journal of Applied Polymer Science, 2020. **137**(12): p. 48479.

[61] Seo, M. and M.A. Hillmyer, *Reticulated nanoporous polymers by controlled polymerization-induced microphase separation.* Science, 2012. **336**(6087): p. 1422-1425.

[62] Seo, M., et al., *Hierarchically porous polymers from hyper-cross-linked block polymer precursors.* Journal of the American Chemical Society, 2015. **137**(2): p. 600-603.

[63] Germain, J., J.M. Fréchet, and F. Svec, *Nanoporous, hypercrosslinked polypyrroles: effect of crosslinking moiety on pore size and selective gas adsorption.* Chemical communications, 2009(12): p. 1526-1528.

[64] Zhang, J., et al., *Hypercrosslinked phenolic polymers with well-developed mesoporous frameworks.* Angewandte Chemie International Edition, 2015. **54**(15): p. 4582-4586.

[65] Warshawsky, A., A. Deshe, and R. Gutman, *Safe halomethylation of aromatic polymers via BCME-free long chain haloalkylethers.* British polymer journal, 1984. **16**(4): p. 234-238.

[66] Ahmad, A., et al., *New generation Amberlite XAD resin for the removal of metal ions: A review.* Journal of Environmental Sciences, 2015. **31**: p. 104-123.

[67] Nur, T., et al., *Effectiveness of purolite A500PS and A520E ion exchange resins on the removal of nitrate and phosphate from synthetic water.* Desalination and Water Treatment, 2012. **47**(1-3): p. 50-58.

[68] İpek, İ.Y., et al., *Application of adsorption–ultrafiltration hybrid method for removal of phenol from water by hypercrosslinked polymer adsorbents.* Desalination, 2012. **306**: p. 24-28.

[69] Wegmann, C., E.S. García, and P. Kerkhof, *Kinetics of acrylonitrile adsorption from an aqueous solution using Dowex Optipore L-493.* Separation and purification technology, 2011. **81**(3): p. 429-434.

[70] Sun, L., et al., *One-pot fabrication of lignin-based aromatic porous polymers for efficient removal of bisphenol AF from water.* International Journal of Biological Macromolecules, 2021. **175**: p. 396-405.

[71] Wood, C.D., et al., *Hydrogen storage in microporous hypercrosslinked organic polymer networks.* Chemistry of materials, 2007. **19**(8): p. 2034-2048.

[72] Wood, C.D., et al., *Microporous organic polymers for methane storage.* Advanced Materials, 2008. **20**(10): p. 1916-1921.

[73] Schwab, M.G., et al., *Nanoporous copolymer networks through multiple Friedel–Crafts-alkylation—studies on hydrogen and methane storage.* Journal of Materials Chemistry, 2011. **21**(7): p. 2131-2135.

[74] Yang, Y., et al., *Triphenylamine-containing microporous organic copolymers for hydrocarbons/water separation.* RSC advances, 2014. **4**(11): p. 5568-5574.

[75] Yang, Y., et al., *Synthesis and characterization of triphenylamine-containing microporous organic copolymers for carbon dioxide uptake.* Polymer, 2013. **54**(21): p. 5698-5702.

[76] Chen, D., et al., *Tunable porosity of nanoporous organic polymers with hierarchical pores for enhanced CO 2 capture.* Polymer Chemistry, 2016. **7**(20): p. 3416-3422.

[77] Bhunia, S., B. Banerjee, and A. Bhaumik, *A new hypercrosslinked supermicroporous polymer, with scope for sulfonation, and its catalytic potential for the efficient synthesis of biodiesel at room temperature.* Chemical Communications, 2015. **51**(24): p. 5020-5023.

[78] Chen, Q., et al., *Microporous polycarbazole with high specific surface area for gas storage and separation.* Journal of the American Chemical Society, 2012. **134**(14): p. 6084-6087.

[79] Pan, L., et al., *Hypercrosslinked porous polycarbazoles via one-step oxidative coupling reaction and Friedel–Crafts alkylation.* Polymer Chemistry, 2015. **6**(13): p. 2478-2487.

[80] Liu, G., et al., *A facile synthesis of microporous organic polymers for efficient gas storage and separation.* Journal of Materials Chemistry A, 2015. **3**(6): p. 3051-3058.

[81] Jia, Z., J. Pan, and D. Yuan, *High Gas Uptake and Selectivity in Hyper-Crosslinked Porous Polymers Knitted by Various Nitrogen-Containing Linkers.* ChemistryOpen, 2017. **6**(4): p. 554-561.

[82] Li, J., et al., *Imidazolinium based porous hypercrosslinked ionic polymers for efficient CO 2 capture and fixation with epoxides.* Green Chemistry, 2017. **19**(11): p. 2675-2686.

[83] Yuan, S., et al., *Porous organic polymers containing carborane for hydrogen storage.* International journal of energy research, 2013. **37**(7): p. 732-740.

[84] Chaikittisilp, W., et al., *Porous siloxane–organic hybrid with ultrahigh surface area through simultaneous polymerization–destruction of functionalized cubic siloxane cages.* Journal of the American Chemical Society, 2011. **133**(35): p. 13832-13835.

[85] Luo, Y., et al., *Microporous organic polymers synthesized by self-condensation of aromatic hydroxymethyl monomers.* Polymer Chemistry, 2013. **4**(4): p. 1126-1131.

[86] Li, B., et al., *Multifunctional microporous organic polymers.* Journal of Materials Chemistry A, 2014. **2**(30): p. 11930-11939.

[87] Vingiello, F.A., J. Yanez, and J.A. Campbell, *New Approach to the Synthesis of Dibenzo [a, l] Pyrenes.* The Journal of Organic Chemistry, 1971. **36**(15): p. 2053-2056.

[88] Wang, S., et al., *Novel POSS-based organic–inorganic hybrid porous materials by low cost strategies.* Journal of Materials Chemistry A, 2015. **3**(12): p. 6542-6548.

[89] Song, K., et al., *Highly active palladium nanoparticles immobilized on knitting microporous organic polymers as efficient catalysts for Suzuki–Miyaura cross-coupling reaction.* Journal of Porous Materials, 2016. **23**: p. 725-731.

[90] Li, B., et al., *A new strategy to microporous polymers: knitting rigid aromatic building blocks by external cross-linker.* Macromolecules, 2011. **44**(8): p. 2410-2414.

[91] Wilson, C., et al., *Swellable functional hypercrosslinked polymer networks for the uptake of chemical warfare agents.* Polymer Chemistry, 2017. **8**(12): p. 1914-1922.

[92] Vinodh, R., et al., *Novel microporous hypercross-linked conjugated quinonoid chromophores with broad light absorption and CO 2 sorption characteristics.* RSC Advances, 2014. **4**(8): p. 3668-3674.

[93] Wang, C., et al., *The influence of the size of aromatic monomers on the structure and catalytic activity of polymer solid acids.* New Journal of Chemistry, 2022. **46**(2): p. 767-778.

[94] Zhang, C., et al., *Triptycene-based hyper-cross-linked polymer sponge for gas storage and water treatment.* Macromolecules, 2015. **48**(23): p. 8509-8514.

[95] Jin, T., et al., *Efficient adsorptive desulfurization by task-specific porous organic polymers.* AIChE Journal, 2016. **62**(5): p. 1740-1746.

[96] Cui, P., et al., *Synthesis of porous aromatic framework with Friedel–Crafts alkylation reaction for CO2 separation.* Chinese Chemical Letters, 2016. **27**(9): p. 1479-1484.

[97] Puthiaraj, P. and W.-S. Ahn, *CO2 capture by porous hyper-cross-linked aromatic polymers synthesized using tetrahedral precursors.* Industrial & Engineering Chemistry Research, 2016. **55**(29): p. 7917-7923.

[98] Dawson, R., et al., *Microporous organic polymers for carbon dioxide capture.* Energy & Environmental Science, 2011. **4**(10): p. 4239-4245.

[99] Errahali, M., et al., *Microporous hyper-cross-linked aromatic polymers designed for methane and carbon dioxide adsorption.* The Journal of Physical Chemistry C, 2014. **118**(49): p. 28699-28710.

[100] Modak, A., et al., *Synthesis of 9, 9′-spirobifluorene-based conjugated microporous polymers by FeCl 3-mediated polymerization.* Polymer Chemistry, 2016. **7**(6): p. 1290-1296.

[101] Zhang, A., et al., *Hybrid microporous polymers from double-decker-shaped silsesquioxane building blocks via Friedel-Crafts reaction.* Polymer, 2016. **101**: p. 388-394.

[102] Tian, Z., et al., *Organic-inorganic hybrid microporous polymers based on Octaphenylcyclotetrasiloxane: Synthesis, carbonization and adsorption for CO2.* Microporous and Mesoporous Materials, 2016. **234**: p. 130-136.

[103] Zhang, Q.M., et al., *Hyperporous carbon from triptycene-based hypercrosslinked polymer for iodine capture.* Advanced Materials Interfaces, 2019. **6**(9): p. 1900249.

[104] Zhai, T.L., et al., *Microporous Polymers from a Carbazole-Based Triptycene Monomer: Synthesis and Their Applications for Gas Uptake.* Chemistry–An Asian Journal, 2016. **11**(2): p. 294-298.

[105] Zhang, C., et al., *Synthesis and properties of organic microporous polymers from the monomer of hexaphenylbenzene based triptycene.* Polymer, 2016. **82**: p. 100-104.

[106] Ma, H., et al., *Nitrogen-rich triptycene-based porous polymer for gas storage and iodine enrichment.* ACS Macro Letters, 2016. **5**(9): p. 1039-1043.

[107] He, Y., et al., *Efficient CO2 capture by triptycene-based microporous organic polymer with functionalized modification.* Microporous and Mesoporous Materials, 2015. **214**: p. 181-187.

[108] Luo, Y., et al., *Hypercrosslinked aromatic heterocyclic microporous polymers: a new class of highly selective CO2 capturing materials.* Advanced Materials, 2012. **24**(42): p. 5703-5707.

[109] Lee, J.S.M., et al., *Hyperporous carbons from hypercrosslinked polymers.* Advanced Materials, 2016. **28**(44): p. 9804-9810.

[110] Saleh, M., et al., *Highly stable CO2/N2 and CO2/CH4 selectivity in hyper-cross-linked heterocyclic porous polymers.* ACS applied materials & interfaces, 2014. **6**(10): p. 7325-7333.

[111] Meng, Q.B. and J. Weber, *Lignin-based microporous materials as selective adsorbents for carbon dioxide separation.* ChemSusChem, 2014. **7**(12): p. 3312-3318.

[112] Tang, C., et al., *Weaving Hyper-crosslinked Polymer from Alkaline Lignin for Adsorption of Organic Dyes from Wastewater.* ChemistrySelect, 2022. **7**(31): p. e202200638.

[113] Li, W., et al., *Massive preparation of pitch-based organic microporous polymers for gas storage.* Chemical Communications, 2016. **52**(13): p. 2780-2783.

[114] Liu, Z., et al., *Preparation of hypercrosslinked polymers with cashew nut shell liquid for removal of volatile organic compounds.* Polymer Engineering & Science, 2022. **62**(6): p. 1823-1832.

[115] Sui, H., et al., *Removal and recovery of o-xylene by silica gel using vacuum swing adsorption.* Chemical Engineering Journal, 2017. **316**: p. 232-242.

[116] Ratvijitvech, T., *Bio-inspired catechol-based hypercrosslinked polymer for iron (Fe) removal from water.* Journal of Polymers and the Environment, 2020. **28**(8): p. 2211-2218.

[117] Tan, L., et al., *Knitting hypercrosslinked conjugated microporous polymers with external crosslinker.* Polymer, 2015. **70**: p. 336-342.

[118] Wang, H., et al., *One-pot synthesis of triptycene-based porous organic frameworks with tailored micropore environments for highly efficient and selective amine adsorption.* Polymer Journal, 2016. **48**(7): p. 787-792.

[119] Zhang, D., et al., *A facile synthesis of cost-effective triphenylamine-containing porous organic polymers using different crosslinkers.* Polymer, 2016. **82**: p. 114-120.

[120] Lim, H., M.C. Cha, and J.Y. Chang, *Preparation of microporous polymers based on 1, 3, 5-triazine units showing high CO2 adsorption capacity.* Macromolecular Chemistry and Physics, 2012. **213**(13): p. 1385-1390.

[121] Puthiaraj, P., et al., *Microporous covalent triazine polymers: efficient Friedel–Crafts synthesis and adsorption/storage of CO 2 and CH 4.* Journal of Materials Chemistry A, 2015. **3**(13): p. 6792-6797.

[122] Xiang, L., et al., *A luminescent hypercrosslinked conjugated microporous polymer for efficient removal and detection of mercury ions.* Macromolecular Rapid Communications, 2015. **36**(17): p. 1566-1571.

[123] Davankov, V., et al., *Formation of regular clusters through self-association of intramolecularly hypercrosslinked polystyrene-type nanosponges.* Journal of Polymer Science Part A: Polymer Chemistry, 1997. **35**(17): p. 3847-3852.

[124] Barar, D.G., K.P. Staller, and N.A. Peppas, *Friedel-Crafts cross-linking methods for polystyrene modification. 3. Preparation and swelling characteristics of cross-linked particles.* Industrial & Engineering Chemistry Product Research and Development, 1983. **22**(2): p. 161-166.

[125] Huang, J., et al., *Hyper-cross-linked polystyrene-co-divinylbenzene resin modified with acetanilide: synthesis, structure, and adsorptive removal of salicylic acid from aqueous solution.* Industrial & engineering chemistry research, 2011. **50**(5): p. 2891-2897.

[126] Huang, J., *Treatment of phenol and p-cresol in aqueous solution by adsorption using a carbonylated hypercrosslinked polymeric adsorbent.* Journal of hazardous materials, 2009. **168**(2-3): p. 1028-1034.

[127] Blinnikova, Z., et al., *Hypercrosslinked polycondensation networks: copolymers of p-xylylene dichloride.* Polymer Science, Series B, 2018. **60**: p. 91-98.

[128] Popov, A.Y., et al., *Synthesis and physicochemical properties of hypercrosslinked polysterene restricted-access materials.* Polymer Science, Series B, 2018. **60**: p. 680-687.

[129] Joseph, R., et al., *Solid-state 13C-NMR analysis of hypercrosslinked polystyrene.* Journal of Polymer Science Part A: Polymer Chemistry, 1997. **35**(4): p. 695-701.

[130] Tian, K., et al., *Massive preparation of coumarone-indene resin-based hyper-crosslinked polymers for gas adsorption.* Chinese Journal of Polymer Science, 2018. **36**: p. 1168-1174.

[131] Cheng, Y., et al., *Construction and gas uptake performance of cyano-functional hypercrosslinked polymers via knitting strategy.* Chemical Engineering Journal, 2021. **426**: p. 130731.

[132] Jia, J., et al., *Conversion of waste polystyrene foam into sulfonated hyper-crosslinked polymeric adsorbents for cadmium removal in a fixed-bed column.* Chemical Engineering Research and Design, 2019. **142**: p. 346-354.

[133] Yang, S., X. Wang, and B. Tan, *Porosity Engineering of Hyper-Cross-Linked Polymers Based on Fine-Tuned Rigidity in Building Blocks and High-Pressure Methane Storage Applications.* Macromolecules, 2023. **56**(3): p. 1213-1222.

[134] Liu, Y., et al., *Synthesis and evaluation of N, O-doped hypercrosslinked polymers and their performance in CO2 capture.* Applied Organometallic Chemistry, 2019. **33**(8): p. e5025.

[135] Yang, X., et al., *Hypercrosslinked microporous polymers based on carbazole for gas storage and separation.* Rsc Advances, 2014. **4**(105): p. 61051-61055.

[136] Kundu, S.K. and A. Bhaumik, *Novel nitrogen and sulfur rich hyper-cross-linked microporous poly-triazine-thiophene copolymer for superior CO2 capture.* ACS Sustainable Chemistry & Engineering, 2016. **4**(7): p. 3697-3703.

[137] Yao, S., et al., *High surface area hypercrosslinked microporous organic polymer networks based on tetraphenylethylene for CO 2 capture.* Journal of Materials Chemistry A, 2014. **2**(21): p. 8054-8059.

[138] Xu, C., et al., *Enhancement mechanism behind the different adsorptive behaviors of nitro/amine modified hypercrosslinked resins towards phenols.* Journal of the Taiwan Institute of Chemical Engineers, 2019. **102**: p. 340-348.

[139] Xiong, S., et al., *Liquid acid-catalysed fabrication of nanoporous 1, 3, 5-triazine frameworks with efficient and selective CO 2 uptake.* Polymer Chemistry, 2014. **5**(10): p. 3424-3431.

[140] Schute, K. and M. Rose, *Metal-free and Scalable Synthesis of Porous Hyper-cross-linked Polymers: Towards Applications in Liquid-Phase Adsorption.* ChemSusChem, 2015. **8**(20): p. 3419-3423.

[141] Lau, C.H., et al., *Continuous flow knitting of a triptycene hypercrosslinked polymer.* Chemical Communications, 2019. **55**(59): p. 8571-8574.

[142] Germain, J., F. Svec, and J.M. Fréchet, *Preparation of size-selective nanoporous polymer networks of aromatic rings: potential adsorbents for hydrogen storage.* Chemistry of Materials, 2008. **20**(22): p. 7069-7076.

[143] Liu, Y., et al., *Hypercrosslinked polymers: controlled preparation and effective adsorption of aniline.* Journal of Materials Science, 2016. **51**: p. 8579-8592.

[144] Urban, J. and V. Škeříková, *Effect of hypercrosslinking conditions on pore size distribution and efficiency of monolithic stationary phases.* Journal of separation science, 2014. **37**(21): p. 3082-3089.

[145] Duan, Z.-Y., et al., *Hypercrosslinking Polymers Fabricated from Divinyl Benzene via Friedel-Crafts Addition Polymerization.* Chinese Journal of Polymer Science, 2022. **40**(3): p. 310-320.

[146] Björnerbäck, F. and N. Hedin, *Highly porous hypercrosslinked polymers derived from biobased molecules.* ChemSusChem, 2019. **12**(4): p. 839-847.

[147] Lee, J.-S.M., T. Kurihara, and S. Horike, *Five-minute mechanosynthesis of hypercrosslinked microporous polymers.* Chemistry of Materials, 2020. **32**(18): p. 7694-7702.

[148] Borrero-López, A.M., A. Celzard, and V. Fierro, *Eco-Friendly Production of Hyper-Cross-Linked Polymers Using Mechanosynthesis and Bioresources: A Critical Review.* ACS Sustainable Chemistry & Engineering, 2022. **10**(49): p. 16090-16112.

[149] Ramirez-Vidal, P., et al., *Irreversible deformation of hyper-crosslinked polymers after hydrogen adsorption.* Journal of colloid and interface science, 2022. **605**: p. 513-527.

[150] Germain, J., et al., *High surface area nanoporous polymers for reversible hydrogen storage.* Chemistry of Materials, 2006. **18**(18): p. 4430-4435.

[151] Li, B., et al., *Catalyzed hydrogen spillover for hydrogen storage on microporous organic polymers.* International Journal of Hydrogen Energy, 2012. **37**(17): p. 12813-12820.

[152] Peng, Q., et al., *Investigation of hydrogen adsorption sites in ferrocene-based hypercrosslinked polymers by DFT calculations.* Journal of Materials Research and Technology, 2023. **24**: p. 7189-7197.

[153] Gatti, G., et al., *On the Gas storage properties of 3D porous carbons derived from hyper-crosslinked polymers.* Polymers, 2019. **11**(4): p. 588.

[154] Tong, W., Y. Lv, and F. Svec, *Advantage of nanoporous styrene-based monolithic structure over beads when applied for methane storage.* Applied Energy, 2016. **183**: p. 1520-1527.

[155] Chen, S., et al., *Multiroute synthesis of porous anionic frameworks and size-tunable extraframework organic cation-controlled gas sorption properties.* Journal of the American Chemical Society, 2009. **131**(44): p. 16027-16029.

[156] Dawson, R., et al., *Microporous copolymers for increased gas selectivity.* Polymer Chemistry, 2012. **3**(8): p. 2034-2038.

[157] Dawson, R., et al., *Impact of water coadsorption for carbon dioxide capture in microporous polymer sorbents.* Journal of the American Chemical Society, 2012. **134**(26): p. 10741-10744.

[158] Jing, X., et al., *Facile synthesis of cost-effective porous aromatic materials with enhanced carbon dioxide uptake.* Journal of Materials Chemistry A, 2013. **1**(44): p. 13926-13931.

[159] Grätz, S., et al., *Mechanochemical synthesis of hyper-crosslinked polymers: influences on their pore structure and adsorption behaviour for organic vapors.* Beilstein Journal of Organic Chemistry, 2019. **15**(1): p. 1154-1161.

[160] Li, X., et al., *Adsorption materials for volatile organic compounds (VOCs) and the key factors for VOCs adsorption process: A review.* Separation and Purification Technology, 2020. **235**: p. 116213.

[161] Li, B., et al., *Hypercrosslinked microporous polymer networks for effective removal of toxic metal ions from water.* Microporous and Mesoporous Materials, 2011. **138**(1-3): p. 207-214.

[162] Anito, D.A., et al., *Iminodiacetic acid-functionalized porous polymer for removal of toxic metal ions from water.* Journal of Hazardous Materials, 2020. **400**: p. 123188.

[163] Masoumi, H., A. Ghaemi, and H.G. Gilani, *Evaluation of hyper-cross-linked polymers performances in the removal of hazardous heavy metal ions: A review.* Separation and Purification Technology, 2021. **260**: p. 118221.

[164] Castaldo, R., et al., *Amino-functionalized hyper-crosslinked resins for enhanced adsorption of carbon dioxide and polar dyes.* Chemical Engineering Journal, 2021. **418**: p. 129463.

[165] Liu, S., et al., *The sensitive and selective adsorption of aromatic compounds with highly crosslinked polymer nanoparticles.* Nanoscale, 2015. **7**(40): p. 16943-16951.

[166] Song, S., et al., *Synthesis of carboxyl-modified hyper-cross-linked polymers with conspicuous removal capability for various water-soluble contaminants.* Journal of Environmental Chemical Engineering, 2021. **9**(5): p. 106047.

[167] Li, H., et al., *Hyper-crosslinked β-cyclodextrin porous polymer: an adsorption-facilitated molecular catalyst support for transformation of water-soluble aromatic molecules.* Chemical science, 2016. **7**(2): p. 905-909.

[168] Valverde-Gonzalez, A., M. Iglesias, and E.M. Maya, *Metal catalysis with knitting aryl polymers: design, catalytic applications, and future trends.* Chemistry of Materials, 2021. **33**(17): p. 6616-6639.

[169] Li, B., et al., *Highly dispersed Pd catalyst locked in knitting aryl network polymers for Suzuki–Miyaura coupling reactions of aryl chlorides in aqueous media.* Advanced Materials, 2012. **24**(25): p. 3390-3395.

[170] Guan, Z., et al., *A highly efficient catalyst for Suzuki–Miyaura coupling reaction of benzyl chloride under mild conditions.* RSC Advances, 2014. **4**(69): p. 36437-36443.

[171] Xu, S., et al., *Palladium catalyst coordinated in knitting N-heterocyclic carbene porous polymers for efficient Suzuki–Miyaura coupling reactions.* Journal of Materials Chemistry A, 2015. **3**(3): p. 1272-1278.

[172] Fu, Y.-F., et al., *External cross-linked sulfonate-functionalized N-heterocyclic carbenes: an efficient and recyclable catalyst for Suzuki–Miyaura reactions in water.* Transition Metal Chemistry, 2018. **43**: p. 665-672.

[173] Bi, J., et al., *The study and application of three highly porous hyper-crosslinked catalysts possessing similar catalytic centers.* Polymer, 2019. **164**: p. 183-190.

[174] Meng, D., et al., *Salen-based hypercrosslinked polymer-supported Pd as an efficient and recyclable catalyst for C–H halogenation.* Chemical Communications, 2020. **56**(19): p. 2889-2892.

[175] Sadak, A.E., et al., *Triazatruxene-based ordered porous polymer: high capacity CO2, CH4, and H2 capture, heterogeneous Suzuki–Miyaura catalytic coupling, and thermoelectric properties.* ACS Applied Energy Materials, 2020. **3**(5): p. 4983-4994.

[176] Wang, X., et al., *Spatially isolated palladium in porous organic polymers by direct knitting for versatile organic transformations.* Journal of Catalysis, 2017. **355**: p. 101-109.

[177] Jia, Z., et al., *Ruthenium complexes immobilized on functionalized knitted hypercrosslinked polymers as efficient and recyclable catalysts for organic transformations.* Advanced Synthesis & Catalysis, 2017. **359**(1): p. 78-88.

[178] Wang, X., et al., *Single-Site Ruthenium Pincer Complex Knitted into Porous Organic Polymers for Dehydrogenation of Formic Acid.* ChemSusChem, 2018. **11**(20): p. 3591-3598.

[179] Valverde-González, A., et al., *A step forward in solvent knitting strategies: ruthenium and gold phosphine complex polymerization results in effective heterogenized catalysts.* Catalysis Science & Technology, 2019. **9**(17): p. 4552-4560.

[180] Wang, T., et al., *Ru coordinated with BINAP in knitting aryl network polymers for heterogeneous asymmetric hydrogenation of methyl acetoacetate.* RSC advances, 2016. **6**(34): p. 28447-28450.

[181] Chen, Y., et al., *State-of-the-art aluminum porphyrin-based heterogeneous catalysts for the chemical fixation of CO2 into cyclic carbonates at ambient conditions.* ChemCatChem, 2017. **9**(5): p. 767-773.

[182] Ganesan, V. and S. Yoon, *Hyper-cross-linked porous porphyrin aluminum (III) tetracarbonylcobaltate as a highly active heterogeneous bimetallic catalyst for the ring-expansion carbonylation of epoxides.* ACS applied materials & interfaces, 2019. **11**(20): p. 18609-18616.

[183] Jiang, J. and S. Yoon, *An aluminum (iii) picket fence phthalocyanine-based heterogeneous catalyst for ring-expansion carbonylation of epoxides.* Journal of Materials Chemistry A, 2019. **7**(11): p. 6120-6125.

[184] Wang, S., et al., *A novel metalporphyrin-based microporous organic polymer with high CO 2 uptake and efficient chemical conversion of CO 2 under ambient conditions.* Journal of Materials Chemistry A, 2017. **5**(4): p. 1509-1515.

[185] Dou, Z., et al., *Metalloporphyrin-Based Hypercrosslinked Polymers Catalyze Hetero-Diels–Alder Reactions of Unactivated Aldehydes with Simple Dienes: A Fascinating Strategy for the Construction of Heterogeneous Catalysts.* Chemistry–A European Journal, 2016. **22**(29): p. 9919-9922.

[186] Tang, C., et al., *Highly Dispersed DPPF Locked in Knitting Hyper-Crosslinked Polymers as Efficient and Recyclable Catalyst.* ChemistrySelect, 2018. **3**(21): p. 5987-5992.

[187] Jia, Z., et al., *Functionalized hypercrosslinked polymers with knitted N-heterocyclic carbene–copper complexes as efficient and recyclable catalysts for organic transformations.* Catalysis Science & Technology, 2016. **6**(12): p. 4345-4355.

[188] Gunasekar, G.H. and S. Yoon, *A phenanthroline-based porous organic polymer for the iridium-catalyzed hydrogenation of carbon dioxide to formate.* Journal of Materials Chemistry A, 2019. **7**(23): p. 14019-14026.

[189] Shen, Y., et al., *Highly Efficient and Selective N-Formylation of Amines with CO2 and H2 Catalyzed by Porous Organometallic Polymers.* Angewandte Chemie International Edition, 2021. **60**(8): p. 4125-4132.

[190] Liang, H.-P., et al., *Rhenium-metalated polypyridine-based porous polycarbazoles for visible-light CO2 photoreduction.* ACS Catalysis, 2019. **9**(5): p. 3959-3968.

[191] Liu, X., et al., *Palladium immobilized on functionalized hypercrosslinked polymers: A highly active and recyclable catalyst for Suzuki–Miyaura coupling reactions in water.* New Journal of Chemistry, 2019. **43**(31): p. 12206-12210.

[192] Xu, W., et al., *Palladium catalyst immobilized on functionalized microporous organic polymers for C–C coupling reactions.* RSC advances, 2019. **9**(59): p. 34595-34600.

[193] Wang, C.-A., et al., *Phenanthroline-based microporous organic polymer as a platform for an immobilized palladium catalyst for organic transformations.* RSC advances, 2019. **9**(15): p. 8239-8245.

[194] Liu, C., et al., *Palladium Immobilized on 2, 2'-Dipyridyl-Based Hypercrosslinked Polymers as a Heterogeneous Catalyst for Suzuki–Miyaura Reaction and Heck Reaction.* Catalysis Letters, 2020. **150**: p. 2558-2565.

[195] Li, R., et al., *Photocatalytic selective bromination of electron-rich aromatic compounds using microporous organic polymers with visible light.* Acs Catalysis, 2016. **6**(2): p. 1113-1121.

[196] Pei, B., et al., *Preparation of chloromethylated pitch–based hyper–crosslinked polymers and an immobilized acidic ionic liquid as a catalyst for the synthesis of biodiesel.* Catalysts, 2019. **9**(11): p. 963.

[197] Gao, F., et al., *Dipolar HCP materials as alternatives to DMF solvent for azide-based synthesis.* Green Chemistry, 2021. **23**(19): p. 7499-7505.

[198] Maya, F. and F. Svec, *A new approach to the preparation of large surface area poly (styrene-co-divinylbenzene) monoliths via knitting of loose chains using external crosslinkers and application of these monolithic columns for separation of small molecules.* Polymer, 2014. **55**(1): p. 340-346.

[199] Maya, F. and F. Svec, *Porous polymer monoliths with large surface area and functional groups prepared via copolymerization of protected functional monomers and hypercrosslinking.* Journal of Chromatography A, 2013. **1317**: p. 32-38.

[200] Shiryaeva, V., et al., *Stationary Phase Based on Hypercrosslinked Polystyrene for Capillary Gas Chromatography.* Russian Journal of Physical Chemistry A, 2020. **94**: p. 1930-1935.

[201] Kanateva, A.Y., A.A. Korolev, and A.A. Kurganov, *Preparation and properties of GC capillary column with hypercrosslinked stationary phase.* Journal of Separation Science, 2021. **44**(24): p. 4395-4401.

[202] Lu, C., et al., *Exploitation of a microporous organic polymer as a stationary phase for capillary gas chromatography.* Analytica Chimica Acta, 2016. **902**: p. 205-211.

[203] Song, W., et al., *Efficient synthesis of folate-conjugated hollow polymeric capsules for accurate drug delivery to cancer cells.* Biomacromolecules, 2020. **22**(2): p. 732-742.

[204] Jiang, K., et al., *Preparation of lithium-modified porous polymer for enhanced humidity sensitive properties.* Sensors and Actuators B: Chemical, 2014. **203**: p. 752-758.

[205] Jiang, K., T. Fei, and T. Zhang, *Humidity sensing properties of LiCl-loaded porous polymers with good stability and rapid response and recovery.* Sensors and Actuators B: Chemical, 2014. **199**: p. 1-6.

[206] Razzaque, S., et al., *Facile synthesis of hypercrosslinked hollow microporous organic capsules for electrochemical sensing of CuII ions.* Chemistry–A European Journal, 2019. **25**(2): p. 548-555.

[207] Pales, A.F., et al., *Net zero by 2050 hinges on a global push to increase energy efficiency*. 2021, IEA.

[208] Hodgson, D., et al., *Industry Sectoral overview*. 2022, IEA.

[209] Agency, I.E., *Technology Roadmap - Energy and GHG Reductions in the Chemical Industry via Catalytic Processes*. 2013, IEA, ICCA, DECHEMA.

[210] Agency, I.E., *World Energy Balances (2022 Edition)*. 2023, IEA

[211] Song, W., et al., *Green synthesis of hypercrosslinked polymers for CO 2 capture and conversion: Recent advances, opportunities, and challenges.* Green Chemistry, 2024.

[212] Wang, S., et al., *Unprecedented processable hypercrosslinked polymers with controlled knitting.* Macromolecular Rapid Communications, 2022. **43**(2): p. 2100449.

[213] Lv, Y., et al., *Preparation of porous styrenics-based monolithic layers for thin layer chromatography coupled with matrix-assisted laser-desorption/ionization time-of-flight mass spectrometric detection.* Journal of Chromatography A, 2013. **1316**: p. 154-159.

[214] Su, Y., et al., *Hypercrosslinked Polymer Gels as a Synthetic Hybridization Platform for Designing Versatile Molecular Separators.* Journal of the American Chemical Society, 2022. **144**(15): p. 6861-6870.

# Chapter 2 Introduction and literature review on deep eutectic solvents (DESs)

## 2.1 Introduction of DESs

### 2.1.1 The definition of DESs

The concept of deep eutectic solvents (DESs) was first introduced in 2003 by Abbott and co-workers as a subclass of ionic liquids (ILs), but with a different composition and lower melting points. Basically, DESs are formed by the combination of two or more components, typically a hydrogen bond donor (HBD) and a hydrogen bond acceptor (HBA). HBA is represented by quaternary ammonium salts while HBD is often a small organic compound like a carboxylic acid, alcohol, or amine. With the increasing awareness and understanding of DESs, it is important to highlight the difference between DESs and ILs despite they have similar physical properties such as ionic nature, low volatility, high thermal stability and non-flammability [1,2]. Meanwhile, a clear definition for DESs is highly needed although significant progress has been achieved in the application of DESs. This fundamental concept and knowledge are crucial for constructing systematic research of DESs. This, in turn, guides the design and selection of DESs for various application scenarios.

Coutinho and Pinho proposed that some widespread misconceptions on DESs should be corrected [3]. DESs should not merely be regarded as low-cost substitutes for ILs as they have unique characteristics. Moreover, it needs to be clear that DESs are mixtures composed of two or three ingredients instead of any newly isolated pure compounds. The term ‘deep eutectic’ refers to the fact that the mixture forms a eutectic point that is significantly lower than the melting points of each individual component [4]. The hydrogen bonding interactions between the components substantially decrease the lattice energy of DESs mixtures and lead to reduced eutectic point [5]. Until now, a more precise definition of DESs was put forward by Martin, who pointed out that DESs is a mixture of pure compounds in which the real eutectic point temperature($T_E$) is below that of an ideal liquid mixture($T_{E,ideal}$), and the

temperature depression between $T_{E,ideal}$ and $T_E$ is marked as $\Delta T_2$ which is a positive value [6]. In addition, the temperature reduction should ensure that the mixture remains in a liquid state within a specified range of compositions when an operating temperature is applied. Moreover, the thermodynamic research on DESs identified that the reason for $\Delta T_2$ can be merely the melting properties of pure compounds instead of hydrogen bonding [6]. In another words, hydrogen bonding cannot assure the formation of DESs, and it is not mandatory in the DESs.

### 2.1.2 Types and compositions of DESs

Based on above proposed definition, hydrogen bonding is not a compulsory factor in the DESs despite it exist in most known DESs. However, the composition of DESs can still be recognised as HBD and HBA for better understanding the role of each pure component in the DESs. According to the components, DESs can be divided into five types as shown in the Table 2-1. The general standardised formula of DESs can be written as $Cat^+X^-zY$. Here, $Cat^+$ denotes cations such as ammonium, phosphonium and sulfonium cations while $X^-$ refers to a Lewis base, frequently taking the form of a halide anion. The term 'Y' represents either a Lewis or Brønsted acid that can form anionic complex with $X^-$, and z is the number of interacted Y molecules [2,7].

Table 2-1: Four types of deep eutectic solvents (DESs)

| Type | Formula | Terms |
|---|---|---|
| I | $Cat^+X^- \cdot MCl_x$ | M=Zn, Sn, Fe, Al, Ga, In |
| II | $Cat^+X^- \cdot MCl_x \cdot yH_2O$ | M=Cr, Co, Cu, Ni, Fe |
| III | $Cat^+X^- \cdot RZ$ | Z=$CONH_2$, COOH, OH |
| IV | $MCl_x \cdot RZ$ | M=Al, Zn; Z=$CONH_2$, OH |
| V | non ionic | COOH, OH |

Type I DESs is formed by quaternary salt and metal halide. Examples of this type DESs are represented by quaternary ammonium halides/$ZnCl_2$ mixtures where $ZnCl_2$ can be replaced by $FeCl_3$, $SnCl_2$, etc. [8]. The scope of DESs has broadened with the introduction of hydrated metal halides, a development known as type II. This

expansion offers a wider array of options for selecting hydrogen bond donors (HBD) with lower melting points, bringing hope to industrial-scale manufacturing. Type III DESs comprises of quaternary ammonium salt and organic molecules such as amide, alcohols and carboxylic acid that serve as the HBD. This type of DESs has gained wide research interest for their merits of low cost, biodegradability, water insensitivity and easy preparation. The varied alternatives for HBD indicate that this class of DESs can be tuned for different application purposes. Type IV DESs were formed by incorporating a range of transition metals into ambient temperature eutectics, breaking the prejudice that inorganic cations usually form relatively high melting eutectics for their high charge density [9]. Recently, non-ionic DESs, which encompass all deep eutectics made exclusively from non-ionic, molecular HBAs and HBDs, have been added as the fifth category of DESs [10]. Figure 2-1 shows the chemical structures of some frequently used HBDs and HBAs used in the preparation of DESs.

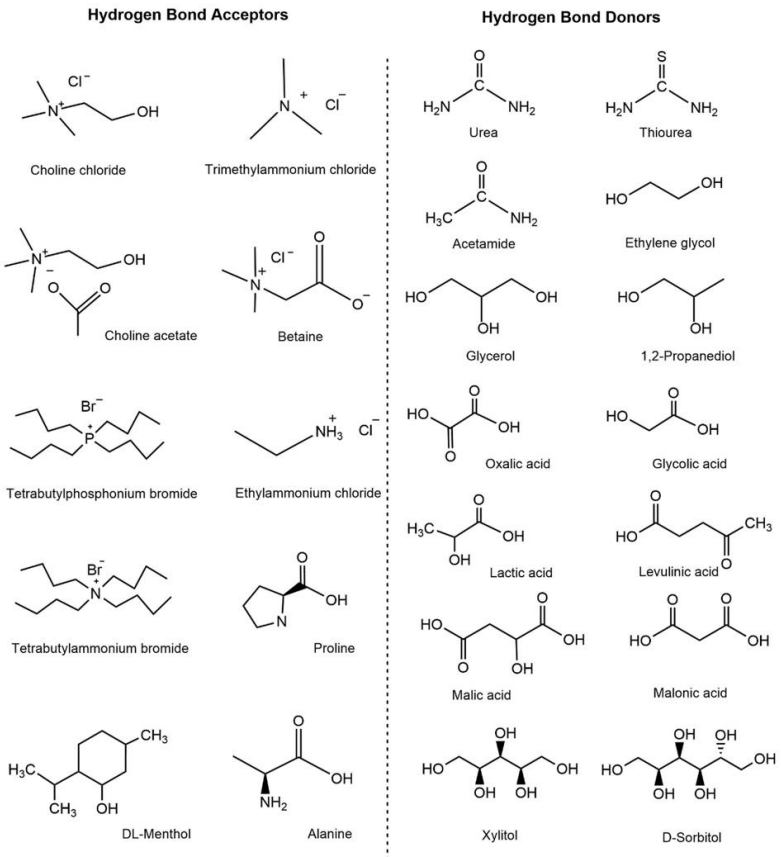


Figure 2-1: Chemical structures of frequently used HBD and HBA used in the preparation of DESs [11]

Apart from the components, the composition of DESs needs to be valued. Most reported DESs were prepared at fixed stoichiometric proportions of HBA and HBD, including molar ratios like 3:1, 2:1, 1:1, 1:2, and 1:3. In rare cases, some researchers also explore uncommon compositions. This is due to the lack of adequate understanding of DESs and thus researchers tend to conservatively use the confirmed ratios to prepare DES. As mentioned above, hydrogen bonding interactions in the DESs, which are possible reasons for the reduced eutectic points, are not eligible to reveal the essence of DESs. It is the temperature depression ($\Delta T_2 > 0$) indeed tell the basic nature. Therefore, the formation of DESs should be within a range of compositions instead of specific fixed ratios. Abbott's group, who is a pioneer in the field of DESs, realised this issue and started to draw the solid-liquid phase diagrams of reported DESs systems [12-14]. Figure 2-2 describes the phase diagram of a two-component mixture. The eutectic point represents the lowest melting temperature for a mixture at a certain composition of components, and it can be obtained from the intersection of melting curves of pure components. At an operating temperature, any mixture of which the composition is between $x_1$ and $x_2$ satisfies the definition of DESs. This can correct people's view that DESs have fixed stoichiometric proportions, and endue DESs with more flexibility and tunability [15]. It allows for the refinement of phase behavior and physical characteristics. As a result, DES assumes the role of a designer solvent, offering tailored properties that meet specific requirements in a range of applications.

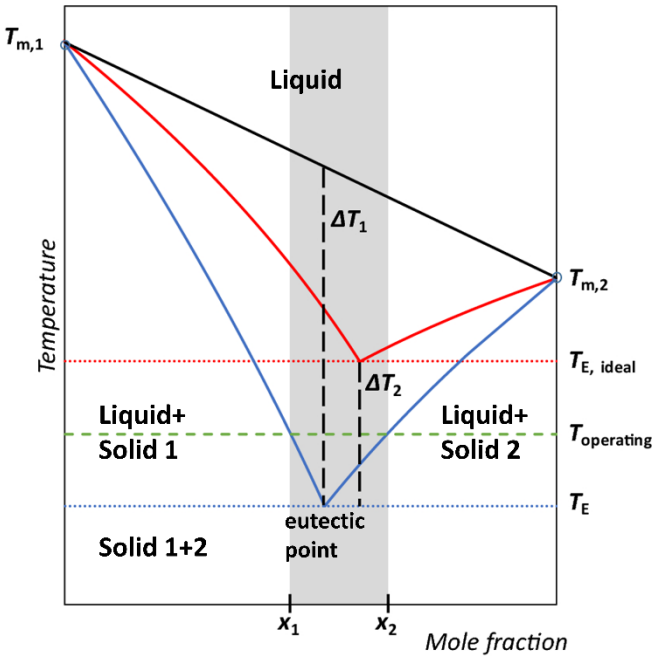


Figure 2-2: The phase diagram of a two-component mixture representing the real eutectic point ($T_E$), $T_{E,ideal}$ is theoretical eutectic point of an ideal mixture [6]

Deep eutectic solvents hold great promise for a wide array of applications across multiple industries due to their unique properties and environmentally friendly nature. Some potential applications of DESs include green chemistry processes [16], catalysis [17], biomass conversion [18,19], extraction [20,21], and as electrolytes in batteries [22,23]. However, despite their promising characteristics, the practical use of DESs is still explored, and further research is needed to fully understand their properties and optimise their application in different fields.

## 2.2 DESs used in Friedel-Crafts reaction

Deep eutectic solvents have demonstrated their efficacy in organic reactions. In this section, our attention is directed toward their utilisation in Friedel-Crafts reactions, which serve as the foundational chemistry underpinning the core thesis. Friedel-Crafts reaction is an organic coupling process that entails electrophilic aromatic substitution, developed by Charles Friedel and James Crafts in the 1870s [24]. Friedel-Crafts reactions can be divided into two primary types: alkylation and acylation, according to the substitution groups. From the point of macromolecular chemistry, Friedel-

Crafts reactions are good mediates for linking organic molecules and increasing the molecular weight of polymers. Until now, the study of DESs used in Friedel-Crafts reactions is still limited in the small organic compounds. DESs find utility in Friedel-Crafts reactions, primarily due to the presence of Lewis acid components within them. It means that DES serves as both a solvent and a catalyst, promoting Friedel-Crafts reactions. Nonetheless, these studies provide insights into the role of DESs in the Friedel-Crafts reactions and inspire other researchers to further expand the application of DESs.

Wang's group systematically studied the feasibility of six kinds of DESs for the catalysis of Friedel–Crafts alkylation reaction of electron-rich arenes with aldehydes to synthesise either triarylmethanes (TRAMs) or diarylalkanes (DIAAs) as shown in Figure 2-3a [25]. Among all, $[ChCl][ZnCl_2]_2$ exhibited the highest catalytic effects followed by $[Me_4NCl][ZnCl_2]_2$. The electron cloud density on the benzene ring is determinative for the alkylation. To be more specific, arenes that bearing more electron-donating groups are more vulnerable and yield more targeted products in shorter time. Although the precise role of $[ChCl][ZnCl_2]_2$ in the reaction remains unverified, a possible mechanism is proposed in Figure 2-3b. The sequence began with the aromatic nucleophilic addition to benzaldehyde, initiating a series of intermediate reactions leading to the formation of a diarylmethanol. The generated diarylmenthanol continued to react with a second molecule of the electron-rich arene to form the triarylmethanes. Moreover, recycling of $[ChCl][ZnCl_2]_2$ DES was accomplished and its catalytic effects retained at least 89% after five consecutive cycles.

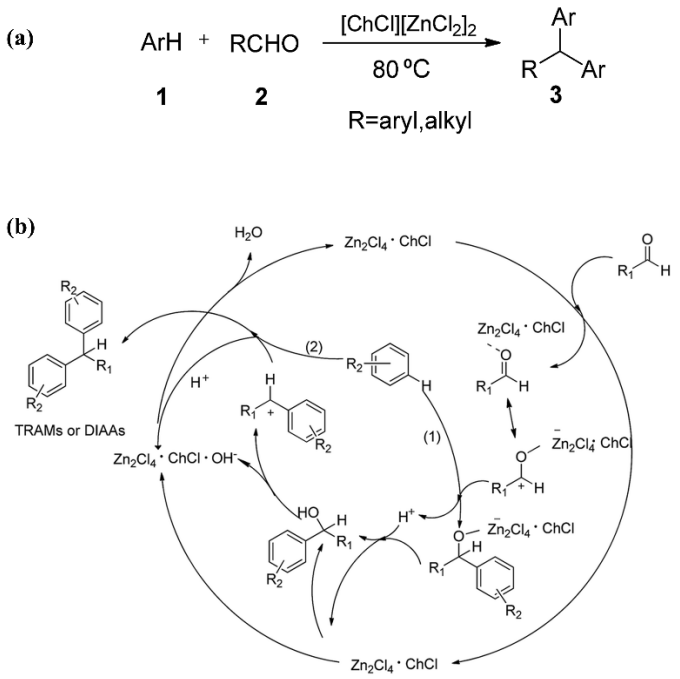


Figure 2-3: (a) Synthesis of TRAMs and DIAAs catalysed by $[ChCl][ZnCl_2]_2$, (b) possible mechanism of Friedel–Crafts alkylation reaction catalysed by $[ChCl][ZnCl_2]_2$ [25]

Sanap and Shankarling managed to synthesise C-3 substituted indoles using 1,3-dicarbonyl compounds, which are crucial building blocks in the synthesis of medicinal compounds [26]. In this work, take the reaction of 2-methylindole and acetylacetone alkenylation/alkylation as a model reaction, DES that consists of choline chloride and oxalic acid demonstrated the highest yield of 89% while each individual component showed little catalytic effects. Other ChCl-based DES comprising acidic HBDs such as malonic acid, succinic acid, tartaric acid, and citric acid also exhibited moderate catalytic effects with yield ranging from 50% to 75%. It is noteworthy that only [ChCl][urea] DES failed to catalyse this reaction among all the DESs studied in this work. The mechanism of acidic DES catalyst has yet been confirmed, it supposed that acid HBDs form hydrogen bonds with oxygen atoms from the 1,3-dicarbonyl as well as ChCl. It is easier for indole molecules to attack this complex due to its increased electrophilicity. As shown in Figure 2-4b, C-3 alkenylated products are gained finally accompanied with undesired

bis(indolyl)carbonyl molecules if another adjacent indole molecule continues to react with alkenylated molecules.

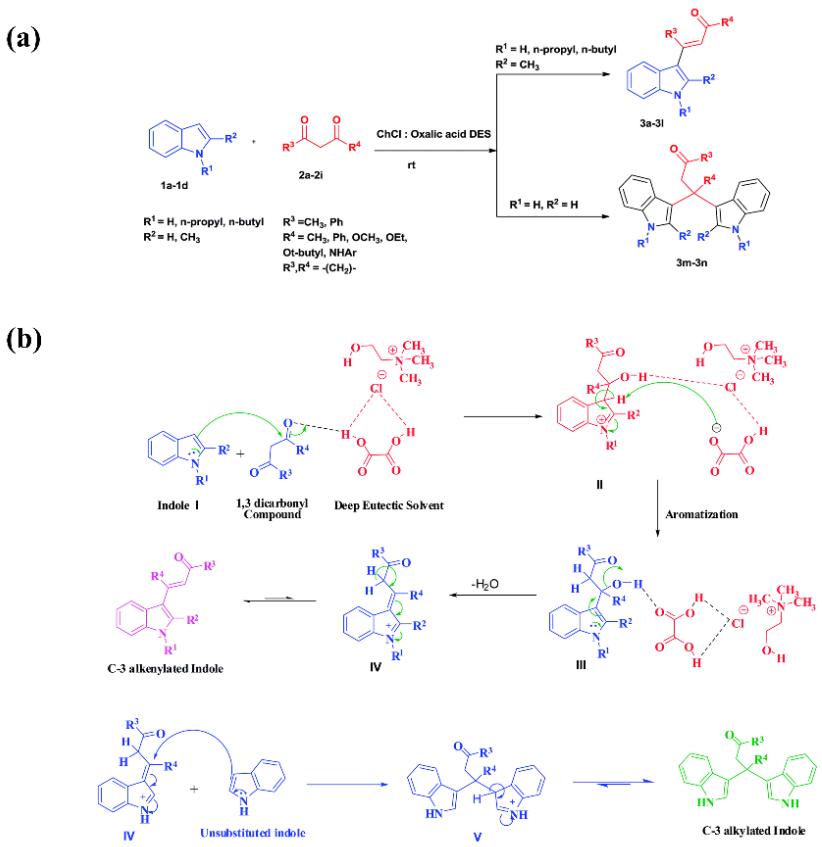


Figure 2-4: (a) C-3 alkenylation/alkylation of indoles and 1,3-dicarbonyl within ChCl: oxalic acid DES, (b) plausible mechanism for C-3 alkenylation/alkylation

Kumar and co-workers continued to study the Friedel-Crafts alkylation of indoles in DESs [27]. To avoid the formation of a potent complex between ketone and metal halide, they opted against employing Lewis acids such as $ZnCl_2$, $AlCl_3$ and $InCl_3$ in DESs. In the model reaction of 1-methylisatin and indole (Figure 2-5), [urea][ChCl] DES exhibited outstanding catalytic performance, with a superhigh product yield (94%) at room temperature. At an elevated reaction temperature, the yield of desired 3b product dropped greatly (less than 58%), suggesting the loss of product selectivity. In addition, the stoichiometric ratio should be maintained as 1:1, otherwise the yield of undesired product $3b^{I}$ would surge to 92%. While the study provides valuable insights, it does not explore the possible mechanism of how [urea][ChCl] DES work

for this reaction and why [urea][ChCl] DES is effective for this alkylation but not catalytic for C-3 alkenylation/alkylation[26] mentioned before.

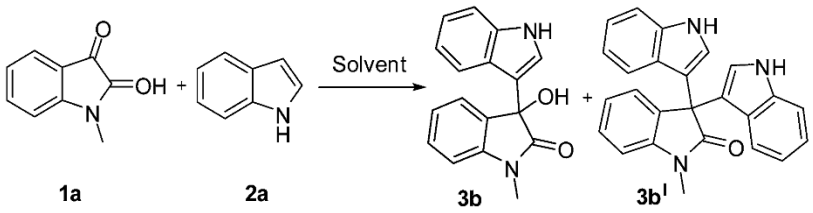


Figure 2-5: Model reaction of 1-methylisatin and indole

Apart from ChCl-based DESs, type IV DESs such as mixtures of $AlCl_3$ and acetamide or urea were also reported as excellent catalysts for the olefin alkylation thiophenic sulfur (OATS) in 3-methylthiophene (3-MT) model oil and real gasoline within 40 min at 50 °C [28]. The catalytic performance could be further boosted after adding 1 wt.% toluene or benzene. This can be attributed to their inhibition of DESs acidity via π–π interaction between them and thiophenic compounds. As shown in Figure 2-6, toluene form complex with $AlCl_3$ and HCl, the resulting active catalytic sites could be represented as $[Htoluene]^+AlCl_4^-$ and $[Htoluene]^+Al_2Cl_7^-$. The alkylation occurs at the interface of DES and oil phase, in which both mono-alkyl and di-alkyl 3-MT products are obtained, with the former being the predominant product.

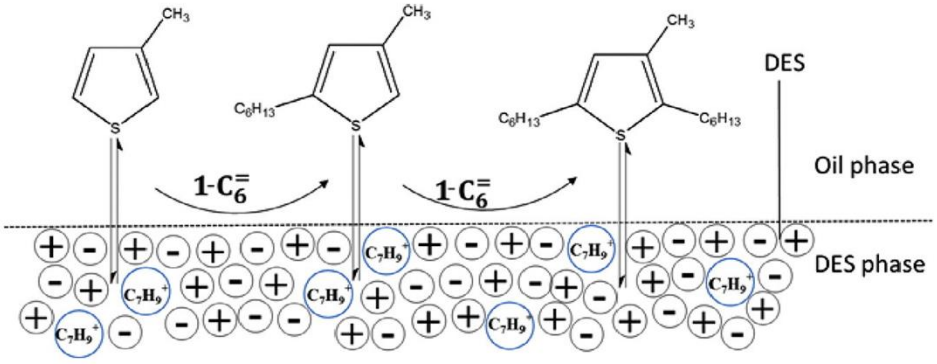


Figure 2-6: The process of olefin alkylation thiophenic sulfur (OATS) catalysed by $AlCl_3$-based DES

DESs have also been demonstrated superiority in Friedel-Crafts acylation to synthesise aromatic ketones (Figure 2-7) [29]. The researchers were astonished to discover that indole derivatives can be acylated with regioselectivity at the 3-position, achieving high yields under mild conditions, all without the need for NH protection. This can be attributed to the moisture-insensitivity of $[ChCl][ZnCl_2]_n$ DESs. Moreover, the effects of $[ChCl][ZnCl_2]_n$ DESs' composition on the catalytic performance was also investigated while n was set as 1, 2 and 3. It was proved that $[ChCl][ZnCl_2]_3$ exhibited enhanced reaction conversion up to 99% in the acylation of anisole and indole with propionic anhydride, while $[ChCl][ZnCl_2]$ and $[ChCl][ZnCl_2]_2$ exhibited equivalent effects as pure $ZnCl_2$. This is due to its stronger Lewis acidity as more zinc chloride was incorporated. The recovery and reuse of $[ChCl][ZnCl_2]_3$ can be obtained via diethyl ether extraction and its catalytic activity remained more than 80% even after 5 cycles.

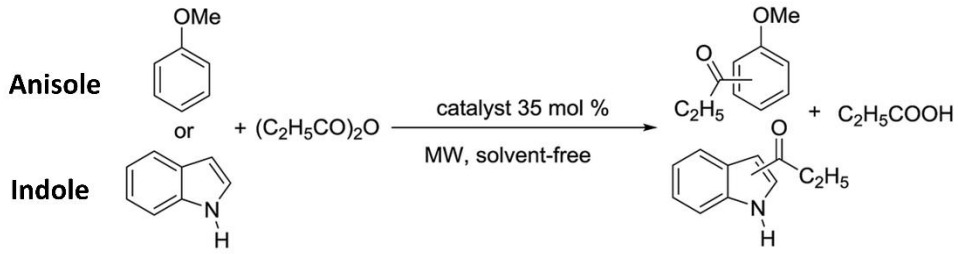


Figure 2-7: Synthetic routes for Friedel-Crafts acylation from anisole and indole small molecules [29]

On the basis of reported exploratory research, DESs have shown promising performance in Friedel-Crafts reactions. In most cases, acidic DESs or DESs containing Lewis acid component are expected to be effective for Friedel-Crafts reactions because they can promote the formation of electrophilic species needed for subsequent reactions. The standards to select DESs for specific reactions have yet to be confirmed, it is encouraging to apply DESs in the organic synthesis via choosing appropriate components and adjusting ratios to fine-tune their properties. Even more exciting is the fact that DESs can be recycled, which not only reduce the environmental footprint but also cut down expenses linked to solvent disposal.

## 2.3 Toxicity evaluation of DESs

DESs have been recognised as next-generation green solvents and grabbed researchers' eyeball because of their biodegradability, low volatility, and sustainability. As such, the number of the published papers about DESs has increased exponentially during the past decades. Although many achievements have been obtained in this field, scientists emphasise on developing new DESs and their potential applications while the fundamental properties of DESs are ignored. This is, however, an inevitable result considering the massive quantity of possible DESs and lack of predictive models to generalise the properties of DESs [30]. The inadequacy in the evaluation of DESs' toxicity needs to be highlighted. Many published manuscripts adopted the idea that all DESs are green solvents and asserted that their DESs were environmentally-friendly and safe for biosomes as well. Obviously, this is a misunderstanding unless the (eco)toxicity of each DES was verified [31]. Another common cognitive mistake is to evaluate the toxicity of each component other than assessing them as a whole. This method naturally excludes the synergistic effect between different components, which may bring about uncertain effects on the DESs mixtures [32].

Laura and co-workers realised the lack of systematic study on the examination of human and environmental toxicity of DESs [30]. Thus, they carried out adequate analyses on main-stream DESs using in vitro and in vivo assays assessments. Several bio-models including bacteria, crustacean, algae, and fish were investigated to study the ecotoxicity. They successfully recognised some crucial factors that may contribute to the cytotoxicity of the DESs such as the match of different HBAs and HBDs, the inclusion of organic acids as HBDs that can affect pH level, components that can change viscosity level and the molar ratio of two components. Consistently, this group also pointed out the significance of synergistic effects widely found in the DESs. It means the toxicity of the individual starting materials cannot serve as a reliable predictor for the final DESs. However, the starting components of the DESs can still provide insights into the biodegradability characteristics of the eventual DESs without being disturbed by synergistic effects.

Juneidi et al. published a toxicological guideline for 10 choline chloride (ChCl)-based DESs, in which four fungi strains and *Cyprinus carpio* fish were selected as bio-models [33]. According to them, $[ChCl][ZnCl_2]_2$ exhibited the highest toxicity towards fungi growth, followed by acidic ChCl-based DESs such as p-toluenesulfonic acid and malonic acid (MA). The rest DESs that incorporate HBD like glycerol, ethylene glycol, diethylene glycol, triethylene glycol, fructose and glucose are rated as harmless. Generally, the toxicity of these ChCl-based DESs weakens compared with the original components. Specially, [ChCl][MA] DES was in fact untoxic as its value of lethal concentration at 50% ($LC_{50}$) greatly increased. However, the toxicity profiles of DESs may vary depending on the experimental targets. Hayyan et al. reported that DESs composed of ChCl and HBD containing alcohol groups proved their cytotoxicity towards brine shrimps [34]. Therefore, despite the great potential of DESs in many fields, thorough safety assessments of DESs are compulsory before embracing them on a larger scale.

The toxicity research on phosphonium-based DESs was also investigated in which glycerine, ethylene glycol and triethylene glycol were employed as HBDs [35]. It is confirmed that the hydrogen bonding between HBDs and HBAs influence both physical properties and chemical structures of DESs. The toxicity of these phosphonium-based DESs was higher than corresponding individual components, which can be attributed to the charge delocalisation existing through hydrogen bonding [36]. Moreover, the high viscosity of DESs may limit the oxygen contents in water, thus leading to the cytotoxicity on the brine shrimps.

Juneidi and co-workers selected N,N’-diethyl ethanol ammonium chloride (EAC) as a fixed HBA and prepared four types of DESs respectively [37]. By comparing the comprehensive toxicity profile of these DESs, they found that type III DESs which consist of HBA and organic molecules exhibited the lowest toxicity. Conversely, type I DESs, comprising HBA and metal salts, were found to be the most toxic among all studied DESs. The toxicity difference between different living organisms emphasised the importance on the exhaustive toxicity investigation towards natural species.

From the perspective of promoting DESs' development, establishing a comprehensive database for the properties of DESs is a crucial initial step in understanding their roles. This database should encompass all reported DESs systems and necessary information like potential harm to human, ecotoxicity and biodegradability. Such a database would not only facilitate research and regulatory efforts but also provide valuable insights into the safety and sustainability of DESs. For some DESs that are difficult to prepare and characterise, computational predictive methods are expected to be very beneficial tools that can account for the variability in components within DES mixtures and different environmental conditions. Computational modeling can help researchers and industries predict how specific DES formulations will behave under different circumstances, such as temperature variations or exposure to different types of organisms.

## 2.4 References


[1] Płotka-Wasylka, J., et al., *Deep eutectic solvents vs ionic liquids: Similarities and differences.* Microchemical journal, 2020. **159**: p. 105539.

[2] Smith, E.L., A.P. Abbott, and K.S. Ryder, *Deep eutectic solvents (DESs) and their applications.* Chemical reviews, 2014. **114**(21): p. 11060-11082.

[3] Coutinho, J.A. and S.P. Pinho, *Special issue on deep eutectic solvents: a foreword.* Fluid Phase Equilib, 2017. **448**(1).

[4] Florindo, C., et al., *Deep eutectic solvents: Overcoming 21st century challenges.* Current Opinion in Green and Sustainable Chemistry, 2019. **18**: p. 31-36.

[5] Perna, F.M., P. Vitale, and V. Capriati, *Deep eutectic solvents and their applications as green solvents.* Current Opinion in Green and Sustainable Chemistry, 2020. **21**: p. 27-33.

[6] Martins, M.A., S.P. Pinho, and J.A. Coutinho, *Insights into the nature of eutectic and deep eutectic mixtures.* Journal of Solution Chemistry, 2019. **48**: p. 962-982.

[7] Mannu, A., et al., *Promising technological and industrial applications of deep eutectic systems.* Materials, 2021. **14**(10): p. 2494.

[8] Abbott, A.P., et al., *Ionic liquids based upon metal halide/substituted quaternary ammonium salt mixtures.* Inorganic chemistry, 2004. **43**(11): p. 3447-3452.

[9] Abbott, A.P., et al., *Eutectic-based ionic liquids with metal-containing anions and cations.* Chemistry–A European Journal, 2007. **13**(22): p. 6495-6501.

[10] Abranches, D.O., et al., *Phenolic hydrogen bond donors in the formation of non-ionic deep eutectic solvents: the quest for type V DES.* Chemical communications, 2019. **55**(69): p. 10253-10256.

[11] El Achkar, T., H. Greige-Gerges, and S. Fourmentin, *Basics and properties of deep eutectic solvents: a review.* Environmental chemistry letters, 2021. **19**: p. 3397-3408.

[12] Abbott, A.P., et al., *Deep eutectic solvents formed between choline chloride and carboxylic acids: versatile alternatives to ionic liquids.* Journal of the American Chemical Society, 2004. **126**(29): p. 9142-9147.

[13] Abbott, A.P., et al., *Novel solvent properties of choline chloride/urea mixtures.* Chemical communications, 2003(1): p. 70-71.

[14] Abbott, A.P., et al., *Extraction of glycerol from biodiesel into a eutectic based ionic liquid.* Green Chemistry, 2007. **9**(8): p. 868-872.

[15] Tang, B. and K.H. Row, *Recent developments in deep eutectic solvents in chemical sciences.* Monatshefte für Chemie-Chemical Monthly, 2013. **144**: p. 1427-1454.

[16] Nkuku, C.A. and R.J. LeSuer, *Electrochemistry in deep eutectic solvents.* The Journal of Physical Chemistry B, 2007. **111**(46): p. 13271-13277.

[17] Khandelwal, S., Y.K. Tailor, and M. Kumar, *Deep eutectic solvents (DESs) as eco-friendly and sustainable solvent/catalyst systems in organic transformations.* Journal of Molecular Liquids, 2016. **215**: p. 345-386.

[18] Kalhor, P. and K. Ghandi, *Deep eutectic solvents for pretreatment, extraction, and catalysis of biomass and food waste.* Molecules, 2019. **24**(22): p. 4012.

[19] Azizi, N., et al., *Efficient deep eutectic solvents catalyzed synthesis of pyran and benzopyran derivatives.* Journal of Molecular Liquids, 2013. **186**: p. 76-80.

[20] Socas-Rodríguez, B., et al., *Deep eutectic solvents for the extraction of bioactive compounds from natural sources and agricultural by-products.* Applied Sciences, 2021. **11**(11): p. 4897.

[21] Lefebvre, T., E. Destandau, and E. Lesellier, *Selective extraction of bioactive compounds from plants using recent extraction techniques: A review.* Journal of Chromatography A, 2021. **1635**: p. 461770.

[22] Millia, L., et al., *Bio-inspired choline chloride-based deep eutectic solvents as electrolytes for lithium-ion batteries.* Solid State Ionics, 2018. **323**: p. 44-48.

[23] Li, Q., et al., *Rapid self-healing gel electrolyte based on deep eutectic solvents for solid-state lithium batteries.* ACS Applied Materials & Interfaces, 2022. **14**(44): p. 49700-49708.

[24] Friedel, C., *Crafts. JM, Sur une Méthode Générale Nouvelle de Synthèse d'Hydrocarbures, d'Acétones, etc.* Compt. Rendus, 1877. **84**: p. 1450-1454.

[25] Wang, A., et al., *Deep eutectic solvent catalyzed Friedel–Crafts alkylation of electron-rich arenes with aldehydes.* RSC Advances, 2015. **5**(73): p. 59022-59026.

[26] Sanap, A.K. and G.S. Shankarling, *Choline chloride based eutectic solvents: direct C-3 alkenylation/alkylation of indoles with 1, 3-dicarbonyl compounds.* RSC advances, 2014. **4**(66): p. 34938-34943.

[27] Kumar, A., et al., *Friedel–Crafts alkylation of indoles in deep eutectic solvent.* RSC Advances, 2015. **5**(64): p. 52062-52065.

[28] Tang, X.-d., Y.-f. Zhang, and J.-j. Li, *Alkylation of thiophenic compounds catalyzed by deep eutectic solvents.* Catalysis Communications, 2015. **70**: p. 40-43.

[29] Tran, P.H., et al., *An efficient and green method for regio-and chemo-selective Friedel–Crafts acylations using a deep eutectic solvent ([CholineCl][ZnCl 2] 3).* RSC advances, 2016. **6**(43): p. 37031-37038.

[30] Lomba, L., et al., *Deep eutectic solvents: Are they safe?* Applied Sciences, 2021. **11**(21): p. 10061.

[31] Torregrosa-Crespo, J., et al., *New guidelines for testing "Deep eutectic solvents" toxicity and their effects on the environment and living beings.* Science of the Total Environment, 2020. **704**: p. 135382.

[32] Hayyan, M., et al., *In vitro and in vivo toxicity profiling of ammonium-based deep eutectic solvents.* PloS one, 2015. **10**(2): p. e0117934.

[33] Juneidi, I., M. Hayyan, and O. Mohd Ali, *Toxicity profile of choline chloride-based deep eutectic solvents for fungi and Cyprinus carpio fish.* Environmental Science and Pollution Research, 2016. **23**: p. 7648-7659.

[34] Hayyan, M., et al., *Are deep eutectic solvents benign or toxic?* Chemosphere, 2013. **90**(7): p. 2193-2195.

[35] Hayyan, M., et al., *Assessment of cytotoxicity and toxicity for phosphonium-based deep eutectic solvents.* Chemosphere, 2013. **93**(2): p. 455-459.

[36] Modica-Napolitano, J.S. and J.R. Aprille, *Delocalized lipophilic cations selectively target the mitochondria of carcinoma cells.* Advanced drug delivery reviews, 2001. **49**(1-2): p. 63-70.

[37] Juneidi, I., M. Hayyan, and M.A. Hashim, *Evaluation of toxicity and biodegradability for cholinium-based deep eutectic solvents.* RSC advances, 2015. **5**(102): p. 83636-83647.

# Chapter 3 Methodology

In this chapter, all materials and purchased chemicals as well as instruments used in Chapter 4 to Chapter 6 are summarised in 3.1. Characterisation techniques used in this thesis for examining chemical structures, morphology, porosity, gas selectivity of HCPs materials are described clearly in 3.2.

## 3.1 Chemical reagents and instruments

All reagents and solvents used for HCPs synthesis are listed in the Table 3-1. All chemicals are used as received without further purification. Deionised water used for washing samples and preparing solutions is obtained from the centralised purification and distribution system (CENTRA-R200).

Table 3-1: Chemicals used in this thesis

| Chemical | Purity | Supplier |
|---|---|---|
| Acetic acid (glacial) | ACS reagent, ⩾99.7% | Sigma-Aldrich |
| Acetone | ACS reagent, ⩾99.5% | Fisher scientific |
| Benzyl alcohol (BA) | anhydrous, 99.8% | Sigma-Aldrich |
| 4,4′-bis(chloromethyl)-1,1′-biphenyl (BCMBP) | 95% | Sigma-Aldrich |
| Choline chloride | ⩾98% | Alfa Aesar |
| α, α'-dichloro-p-xylene (DCX) | 98% | Sigma-Aldrich |
| Dichloroethane (DCE) | anhydrous, 99.8% | Sigma-Aldrich |
| Ethanol | anhydrous, 99.8% | Fisher scientific |
| Formaldehyde dimethyl acetal (FDA) | *ReagentPlus*®, 99% | Alfa Aesar |
| HIPS filament | Pure | Prusa |
| Hydrochloride acid (HCl) | ACS reagent, 37% | Alfa Aesar |
| Iron chloride | reagent grade, 97% | Sigma-Aldrich |
| Lignin | | Local factory |

| | | |
|---|---|---|
| Methanol | anhydrous, 99.8% | Fisher scientific |
| Pyridine | anhydrous, 99.8% | Sigma-Aldrich |
| 1,3,5-triphenylbenzene (TPB) | 97% | Sigma-Aldrich |
| Triptycene | 98% | Sigma-Aldrich |
| Zinc chloride | reagent grade, ⩾98% | Sigma-Aldrich |

3D printer (i3 MK3S) and HIPS filaments were purchased from Prusa research a.s. and then established and calibrated in our lab. All synthetic experiments were carried out using a ceramic coated steel hotplate (MS-H280-Pro) with the magnetic stirring that can reach 1500 rpm. Filtration setup was composed of a vacuum pump (Welch 2511 dry compressor) and a Buchner funnel which is connected to a side-arm glass flask via neoprene adapter. All prepared HCPs samples were dried in the vacuum oven (Gallenkamp digital touch screen vacuum oven SKURO96) which can be heated up to 200 ℃ before further characterization.

All samples were examined by attenuated total reflectance-Fourier transform infrared spectroscopy (ATR-FTIR) to investigate chemical bonds of HCPs and Lewis acidity of different DES systems. FTIR spectra were obtained in attenuated total reflectance mode on a Nicolet™ iS™ 20 FTIR Spectrometer (Thermo Scientific™) equipped with a Smart iTX™ diamond accessory. The working range covers 500-4000 $cm^{-1}$. Solid-state Nuclear Magnetic resonance (NMR) was also used to detect the chemical structures of HCPs with a Perkin ava 300M machine. XPS measurements were performed at the EPSRC XPS facility at Harwell equipped with an Al Kα X-ray source (1486.7 eV), a spherical sector analyser, three multichannel resistive plate detectors and 128 channel delay line detectors. All spectra were recorded at a pressure below $10^{-8}$ Torr and at a temperature of 150 K and calibrated with the C1s peak at 284.8 eV. Surface morphology of HCPs was determined by scanning electron microscopy (SEM) using a JEOS JSM-IT100 instrument. For powder samples, they were firstly dispersed uniformly in ethanol and dropped on carbon tapes that stuck on the stubs. Ultraviolet-visible (UV-vis) curves of all dyes were achieved from a UV-vis

spectrophotometer from Thermo Fisher Scientific. The adsorption and desorption isotherms of $N_2$ and $CO_2$ were obtained from a Micrometrics ASAP 2420 volumetric adsorption analyser at 77 K, 273 K and 298 K respectively.

## 3.2 Characterisation techniques and application

### 3.2.1 Three-dimensional (3D) printing

3D-printing technology has been well developed as a distinguished additive manufacturing method for constructing intricate geometries as defined from various starting materials. This innovative technique has given an enormous boost to the development and productivity of designed 3D objects applied in wide fields such as energy storage devices [1], tissues and scaffolds [2], electrochemical sensors [3] and advanced functional materials [4]. Basically, 3D-printing technology fabricates three-dimensional objects layer by layer with the precise control of computer-aided programs. Currently, common 3D-printing technology could be categorised into main five types based on its working model: fused deposition modelling (FDM), stereo lithography apparatus (SLA), selective laser sintering (SLS), laminated object manufacturing (LOM) and 3D inkjet printing (3DP). These sufficient 3D printing methods provide enough choices for targeted prototypes to meet up with the requirement of different sizes, strength, precision and even productivity in multiple circumstance. Among the above technologies, FDM is widespread for its advantages such as cost-effective budget, variety of material choices, reusable filaments, high printing quality and user-friendly operation [5]. A typical FDM printing process, where melted thermalplastic polymeric filaments are extruded through the heated nozzle and subsequently deposited on the hot bed layer by layer, is applicable for most filaments products on the market. With the fast expansion of commercial filaments market, most popular filaments like polylactic acid (PLA) and acrylonitrile butadiene styrene (ABS) account for great proportion due to their great processability, low prices and good recyclability. PLA filaments have superior mechanical strength, strong stiffness, low

melting temperature and low shrinking ratio, while ABS filaments have higher heat resistance and durability. According to their different intrinsic properties, PLA is widely used to print decorative components or toy models etc., and ABS is more common in engineering field such as prototypes, tools and gears. To deal with the growing demand of more printing materials that could adapt to different working circumstance, more polymer filaments like polyethylene terephthalate glycol (PETG), high-impact polystyrene (HIPS) polypropylene (PP), polycarbonate (PC), polyamide(PA, Nylon) have emerged [6].

Considering hypercrosslinking reaction is supposed to occur between phenyl rings of linear polystyrene-based polymers, HIPS filaments are selected for building the monoliths firstly. Apart from relatively high content of styrene units, HIPS filaments also have excellent dimensional stability, high rigidity and outstanding impact strength, which could guarantee the mechanical strength and completion of monoliths after hypercrosslinking modification.

All 3D models used in Chapter 4 were first sliced and converted into readable gcode files for further printing via PrusaSlicer software. The temperature of the extruder and heating bed is set as 220 ℃ and 80 ℃ respectively. The whole printing process needs to be performed under good ventilation as HIPS may release some toxic volatile organic compounds and ultrafine powders at high temperature [7]. It is noteworthy that special adhesive solution would be helpful for making printed objects tightly stick on the heating plate, which could largely improve the printing quality. Before spraying adhesive solution evenly on the printable surface, the plate should be cleaned and dried under room temperature. The structure of Prusa 3D printer and the names of each component are shown in Figure 3-1.

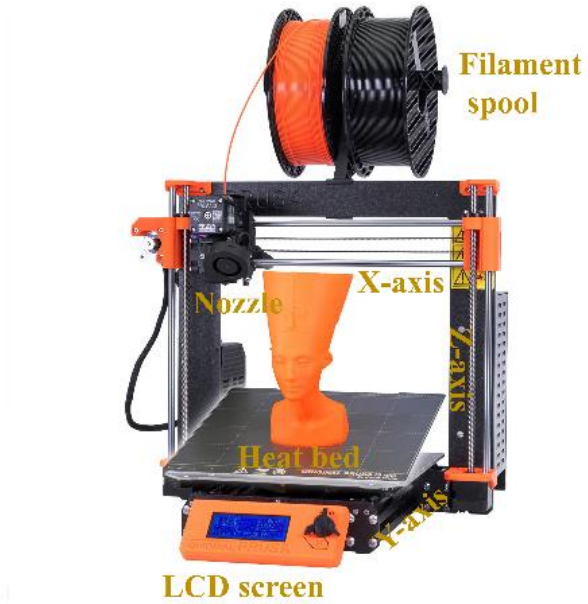


Figure 3-1: Structure of Prusa 3D printer used in this thesis

### 3.2.2 Attenuated Total Reflectance-Fourier Transform Infrared Spectroscopy (ATR-FTIR)

ATR-FTIR is a well-established technique for characterising molecule structures and chemical bonds, which enables the analysis on both solid and liquid samples. When infrared light passes through the ATR crystal, it is reflected internally and partially absorbed by the sample placed on the crystal. The reflected light signals carry the characteristic absorption information of the sample and are finally collected by the detector, which are known as ATR spectra. In this thesis, ATR-FTIR is used to study the chemical structure changes before and after the reactions and explore whether new chemical bonds form. Moreover, it is also used for investigating the Lewis acidity of different DES systems in Chapter 5 and explains their different catalytic effects.

### 3.2.3 Nuclear Magnetic Resonance (NMR) Spectroscopy

NMR is a comprehensive technique for determining chemical compositions and studying relations between structure and property, which is widely applied in many disciplines. The working principle of NMR spectroscopy is to apply a magnetic field to atomic nuclei and measure the energy transfer caused by magnetic resonance. NMR

spectrum, which is interpreted from free induction decay (FID) signals, is known as a plot of intensities versus chemical shift. NMR could be loosely divided into solution-state and solid-state depending on the solubility of materials [8,9]. Considering the HCPs materials synthesised in this thesis are mostly insoluble, solid-state nuclear magnetic resonance (SSNMR) is employed to characterise their chemical structures. The most common nuclei used for NMR are $^{1}H$ and $^{13}C$ as hydrogen and carbon elements are principal components of organic molecules. $^{13}C$ NMR spectra usually have a better resolution as the chemical shift of $^{13}C$ ranges from 10 to 220 ppm while that of $^{1}H$ occurs from 0 to 14 ppm, guaranteeing that collected signals could be more spread out. However, $^{13}C$ NMR spectra obtained from traditional magic angle spinning (MAS) SSNMR usually are not used for quantitative analysis because of the nuclear overhauser effect (NOE) coming from proton decoupling. This means that the number of carbon atoms is independent of integrated peak area, which is different from the linear relationship between hydrogen atoms numbers and their integrated peak area in $^{1}H$ NMR spectra. In this thesis, different types of HCPs and lignin-based HCPs were successfully synthesised for study the universality of DES reaction system in Chapter 5 and 6 respectively. Most HCPs were crosslinked by methylene bridges, which may have similar chemical environment to alkyl hydrogens. To distinguish the structures of HCPs better, $^{13}C$ SSNMR is more effective as it can give sufficient information on the carbon skeleton and various carbon-containing functional groups. Therefore, the analysis on HCPs chemical would mainly focus on their $^{13}C$ NMR spectra.

### 3.2.4 Scanning Electron microscopy (SEM)

Scanning electron microscopy (SEM) is a versatile technology for materials characterization, expanding the researchers' understanding of materials at microscale and nanoscale level [10]. Basically, the SEM instrument comprises of an electron column, a specimen chamber and the computer/electronic controls. The electron beam, which is emitted by the electron gun, penetrates a few microns into the surface of the

sample and interacts with its atoms. The obtained signals, including secondary electrons, backscattered electrons and characteristic X-rays, are collected and processed to generate detailed surface images of the sample. Most materials in this thesis are HCPs with abundant micropores whose pore size is usually below 2 nm. These micropores could hardly be detected and captured due to limited magnification of SEM. However, larger pores such as mesopores and macropores could be clearly imaged by SEM technique. Here, SEM mainly focus on the surface morphology and particle aggregations of HCPs materials instead of analysing the pore distributions. Typically, the electron gun in the SEM accelerates electrons under the voltage from 1 to 30 kV, while routine imaging is usually conducted under 10-20 kV. Before putting HCPs specimen into the vacuum chamber, they are suggested to be clean and covered with an ultrathin gold or platinum coating for removing possible accumulated surface electrostatic charge. Moreover, high-quality images could be achieved by adjusting the working distance of specimen stage, increasing voltage, reducing current and decreasing scanning speed.

### 3.2.5 Ultraviolet-visible (UV-Vis) spectroscopy

UV-vis spectroscopy is a quantitative analytical technique by measuring the absorbance or transmittance of light going through the cuvettes compared with blank sample. The working wavelength of the UV-vis spectrophotometer used in this thesis ranges from 300 to 800 nm, which is in the ultraviolet-visible light region. To determine the adsorption ability of porous HIPS monoliths to different dyes in Chapter 4, UV-vis spectroscopy is used to calculate the concentration and amount of dyes accurately. It is well known that organic dyes molecules could absorb specific light energy and cause corresponding electronic transition within the molecules when they are exposed to a light source. The absorption behaviour is recorded as a function of wavelength by the spectrophotometer. Maximum absorbance ($\lambda_{max}$) refers to the wavelength corresponding to the maximum absorption peak in the UV-vis spectrum, which is a characteristic value for different molecules. After deciding $\lambda_{max}$, the

construction of standard calibration curves of each dye is compulsory for later quantitative measurement. A typical practice could be described as: standard dye solutions whose concentration is 2, 4, 6, 8, 10 mg $L^{-1}$ respectively were prepared first. The absorbance of each solution at $\lambda_{max}$ was plotted versus the concentration and fitted into a linear model. According to Beer-Lambert law, there is a linear relationship between the light absorbance of the solution and its concentration. Therefore, the fitted linear equation could be used to calculate the concentration of solutions to be tested. To improve the accuracy of the results, quartz cuvettes were used for the whole experiment. Baseline was automatically deducted from the spectrum of each sample to minimise the possible absorbance brought by solvents.

### 3.2.6 Brunauer–Emmett–Teller (BET) analysis

BET analysis is a well-established tool for determining the surface area, pore volume and pore size distribution of porous materials from nitrogen ($N_2$) adsorption isotherms. Gas adsorption isotherm is defined as the relation between the amount of adsorbed gas and the corresponding equilibrium pressure at a constant temperature. According to the latest physisorption technical report supported by The International Union of Pure and Applied Chemistry (IUPAC) in 2015, phsisorption isotherms could be categorised into eight types as shown in Figure 3-2 [11,12] . Among them, type I isotherm is used to describe microporous materials, which exhibits a rapid rise until reaching the plateau of the maximum capacity. This platform represents the completion of monolayer adsorption. As HCPs materials have plenty of mircropores, their $N_2$ adsorption isotherms usually present such characteristic behaviours. BET analysis is an extension of Langmuir theory and states that multilayer adsorption happens on the interface. The linear form of BET equation is shown as:

$$\frac{x}{V(1-x)} = \frac{1}{V_m C} + \frac{C-1}{V_m C}x \qquad (1)$$

where **x** represents relative pressure $\mathbf{P/P_0}$, **V** is the amount of gas adsorbed, $\mathbf{V_m}$ is the specific monolayer capacity and **C** is BET constant value. In the practical application of BET analysis, $\mathbf{V_m}$ and **C** could be first estimated by plotting the relative pressure **x**

against **x/(V·(1-x))** from raw isotherm data. Normally, isotherm data points ranging from 0.05 to 0.3 relative pressure are used for linear regression. Hence the slope and intercept obtained from the fitted curve are abbreviated as **S** and **i.** The equations for calculating $\mathbf{V_m}$ and **C** are shown as follows:

$$V_m = \frac{1}{S + i} \tag{2}$$

$$\mathrm{C} = \frac{S}{i} + 1 \tag{3}$$

It should be noted that the value of constant **C** should be positive. Otherwise, it indicates the selection of relative pressure range is inappropriate for linear fitting and narrower relative pressure range should be adjusted. Subsequently, the specific surface area ($S_{BET}$) could be calculated by equation (4):

$$S_{BET} = \frac{V_m \cdot L \cdot \sigma_m}{V_0 \cdot m} \tag{4}$$

where **L** is the Avogadro constant ($6.022\times10^{23}$ $mol^{-1}$), $\boldsymbol{\sigma_m}$ is the cross-section area of an adsorbate molecule (0.162 $nm^2$ for $N_2$), $\mathbf{V_0}$ is the molar volume of an adsorbate molecule (gas molecule usually occupied 22.4 L of volume) at standard condition, and **m** is the mass of adsorbents.

Particularly, the assessment of microporosity is valued in the study of porous materials as micropores can significantly increase the specific surface area. Also, pore size distribution can be gained and it is a vital parameter in further determination of pore structures. Insights into the porosity of materials could provide decisive guidance for their practical applications. It has been generally recognised that nitrogen adsorption isotherm at 77 K is a standard method for micropores analysis. However, nitrogen molecules may have interactions with specific surface functional groups, directly affecting the orientation of $N_2$ molecules on the surface and associated pore filling pressure. Another ensuing problem is affected pore filling pressure would not be correlated with its real pore structure due to the slow diffusion of $N_2$ molecules under ultralow pressure. To solve this problem, carbon dioxide adsorption isotherm at 273 K has been a good substitution for the measurements of narrow micropores and the detection limit of $CO_2$ can even reach 0.4 nm.

Prior to the start of an adsorption test, the samples are required to remove all adsorbed volatile species via degassing process under vacuum at elevated temperature for desired durations. This is decided by the thermal stability of the samples and degassing temperature needs to be lower than the decomposition temperature. In this thesis, all samples were degassed at 110 ℃ for 12 hours and then analysed by a gas adsorption analyser. During the tests, glass rods are also inserted in the sample cells to minimise the void volume and help to reach the adsorption equilibrium faster.

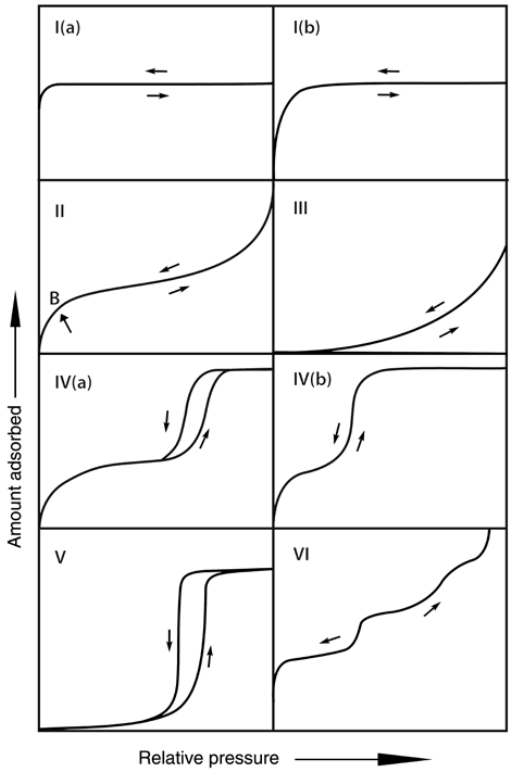


Figure 3-2: The classification of physisorption isotherms

### 3.2.7 $CO_2/N_2$ selectivity calculations using IAST method

The Ideal Adsorbed Solution Theory (IAST) was first developed by Myera and Prausnitz in 1965. It is regarded as a powerful tool to predict the equilibrium adsorption isotherms for multi-components on basis of single-component isotherms. $CO_2/N_2$ selectivity was calculated using $CO_2$ and $N_2$ adsorption isotherms under 273 K. The premise of IAST is that all components are supposed to show ideal behaviours. Here, in the binary gas mixture system, the selectivity could be defined as follows:

$$S_{1,2} = \frac{\frac{x_1}{y_1}}{\frac{x_2}{y_2}} \quad (5)$$

where $x_1$ and $x_2$ refer to the molar fraction of corresponding component in the adsorbed phase under given pressure and temperature, while $y_1$ and $y_2$ refer to the molar fraction of gas component 1 and 2 in the gas mixture. According to the IAST assumptions, the link between total pressure ($P$) of gas mixture and pure adsorbate vapour pressure ($P_i^O$) of component *i* could be written as follows:

$$P \cdot y_1 = P_1^o \cdot x_1 \quad (6)$$

$$P \cdot y_2 = P_2^o \cdot x_2 \quad (7)$$

$$\int_0^{P_1^o} \frac{Q_1(P)}{P} dP = \int_0^{P_2^o} \frac{Q_1(P)}{P} dP = \frac{\pi A}{RT} \quad (8)$$

As shown in the equation (8), the spreading pressure($\pi$) for gas mixture could be linked with $P_i^O$ via integral equation, where $R$ is ideal gas constant ($8.31\times10^{-3}$ kJ mol$^{-1}$), T is ambient temperature, A is surface area of the adsorbent, $Q_i$ is adsorbed quantity of component ***i*** and it is a variable related to $P$.

The relationship between adsorbed quantity ($Q$) and pressure ($P$) could be described by single site Langmuir-Freundlich (SSLF) model which is shown in equation (9). The parameters such as **q**, **b** and **n** represented the maximum adsorbed quantity of pure single gas at adsorption sites, affinity for different adsorption sites and solid heterogeneity parameter respectively.

$$Q = \frac{qbP^n}{1 + bP^n} \quad (9)$$

Figure 3-3 shows the MATLAB code used for solving $CO_2/N_2$ selectivity:

para.m

```
function sol=para(a,b,n,c,d,m,Pt,y1,y2)
    function f=fun1(P)
        f=a.*b.*(P.^(n-1))/(1+b.*(P.^n));
    end
    function f=fun2(Q)
        f=c.*d.*(Q.^(m-1))/(1+d.*(Q.^m));
    end
    function h=fun3(X)
        h=integral(@fun1,0,X,'ArrayValued',true)-integral(@fun2,0,X*Pt*y2/(X-Pt*y1),'ArrayValued',true);
    end
sol=fzero(@fun3,[Pt*y1 Pt*y1+10]);
end
```

Figure 3-3: MATLAB code used for solving $CO_2/N_2$ selectivity

### 3.2.8 $CO_2/N_2$ selectivity calculations using initial slope method

Meanwhile, initial slope from Henry's law constants for specific single-component adsorption isotherms is also used to evaluate the selectivity between $CO_2$ and $N_2$. In this method, the selectivity is decided by Henry's constant for each gas following equation (10)

$$S_{\frac{CO_2}{N_2}} = \frac{K_H(CO_2)}{K_H(N_2)} \quad (10)$$

### 3.2.9 Experimental setup for $CO_2$ adsorption from mixed gases

The adsorption of $CO_2$ from mixed gases was performed using a self-made lab-scale setup at room temperature (298 K) and standard atmospheric pressure, as shown in Figure 3-4. Before mixing, $N_2$ and $CO_2$ gases were passed through dryer tubes comprising zeolite/silica. The flow rates of $N_2$ and $CO_2$, ranging from 0 to 400 mL $min^{-1}$, were controlled by Brook Instruments GF-series valves. To simulate the composition of post-combustion flue gas, the volume ratio of $CO_2$ and $N_2$ was set as 15:85 here. The mass flow of $CO_2$ and $N_2$ was 3 mL $min^{-1}$ and 17 mL $min^{-1}$, respectively. All gas lines were purged with $N_2$ each time we started a new adsorption cycle. A self-programmed data collection software was employed to constantly monitor and record all experimental parameters, such as temperature, gas flow rates, and the actual $CO_2$ concentration in the mixed gas. 0.5 g of lignin-based HCPs were placed in a quartz container with a 12 mm inner diameter and a 1 mm wall thickness. Dry gas mixtures of $N_2$ and $CO_2$ passed through the quartz container in which adsorption took place. Continuously, the mixed gas would go through the condenser which was necessary for preventing the adsorbents powders being blown away. The ultimate concentration of $CO_2$ in the treated gas mixtures were determined by a non-dispersive infrared $CO_2$ sensor (COZIR-W-100). The whole testing adsorption process lasted for 10 minutes. The adsorption capacity for $CO_2$ ($Q_{ads}$, mg $g^{-1}$) and adsorption rate ($k_{ads}$, mg $g^{-1}$ $s^{-1}$) were calculated using these equations:

$$Q_{ads} = \int_0^t k_{ads} dt \tag{11}$$

$$k_{ads} = \frac{1}{m} \times \frac{C_{blank,CO_2} \cdot f_{mix} - C_{out,CO_2} \cdot f_{mix}}{60} \tag{12}$$

where $C_{out,CO_2}$(mg mL$^{-1}$) is the concentration of $CO_2$ in the out flue gas mixtures after adsorption, while $C_{blank,CO_2}$ (mg mL$^{-1}$) is the concentration of $CO_2$ without using adsorbents. In addition, *m* represents the mass of adsorbents, $f_{mix}$(mL min$^{-1}$) is the actual flow rate of the gas mixtures and *t* is the duration of adsorption.

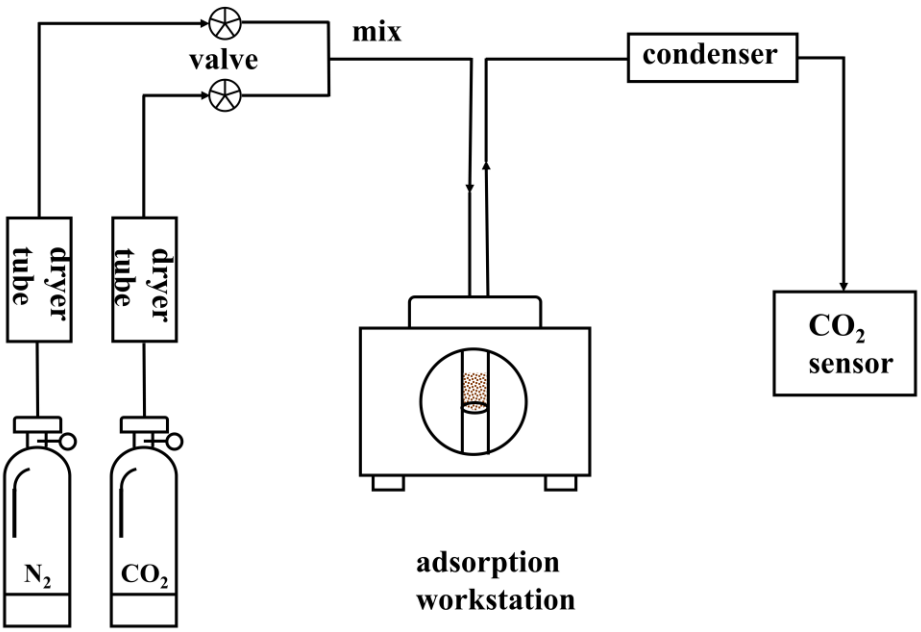


Figure 3-4: The experimental setup for $CO_2$ adsorption from mixed gases

In the binary gas mixtures comprising $CO_2$ and $N_2$, the $CO_2/N_2$ selectivity was calculated as follows:

$$S_{\frac{CO_2}{N_2}} = \frac{n(CO_2)}{n(N_2)} \frac{y(N_2)}{y(CO_2)} \tag{13}$$

where n($CO_2$) and n($N_2$) are the amounts of $CO_2$ and $N_2$ adsorbed in solid adsorbents, and y($CO_2$) and y($N_2$) represent the gas phase concentration.

### 3.2.10 Oil absorption

Oil absorption tests are conducted to evaluate the capacity of porous HIPS monoliths (in Chapter 4) to different hydrophobic solvents. All hypercrosslinked HIPS monoliths were dried in the oven at 60 ℃ before oil adsorption process. A monolith was totally soaked in the different types of oils for 2 minutes until it reached its maximum capacity. After taking it out and wiping the excess oil on the surface with tissues, the weight of the monolith was measure for at least 3 times to get an average value. Oil capacity of HCPs was calculated according to the equation below: $Q = \frac{m_1 - m_0}{m_0}$. Here, Q is oil adsorption capacity of the monolith. $m_0$ and $m_1$ represent the initial and final weight of the monolith before and after the adsorption respectively. The regeneration of the monolith could be achieved by directly flushing used monoliths with methanol.

### 3.2.11 Dyes adsorption

Dyes adsorption tests are also performed to evaluate the capacity of porous HIPS monoliths (in Chapter 4) to different dyes molecules. Four kinds of different dyes including rhodamine B(RhB), methyl orange (MO), neutral red (NR) methylene blue (MB) are selected for the adsorption tests. The standard curves of above dyes were firstly determined by a UV-vis spectrophotometer using calibration dye solutions with different concentrations. In a typical adsorption test, an HCP monolith (weighs around 0.06g) was totally immersed into 10 mL of aqueous dye solution whose initial concentration is 5 mg $L^{-1}$ for 24 hours. The concentration of residual dye could be determined by UV-vis spectra.

### 3.2.12 Taxadiene adsorption

Taxadiene is an intermediate in the synthesis of paclitaxel (Taxol®), which is a chemotherapy medication for treatment of a wide range of cancers and diseases. Taxadiene is hydrophobic as most other terpenoids. Facing with the growing global demand on paclitaxel, researchers have been working on cost-effective production of it to supplement current expensive semi-synthesis process. In recent years, taxol and related precursors have been reported to be successfully produced via biosynthesis

such as *Escherichia coli* and *Saccharomyces cerevisiae* [13,14]. Even though the full pathway of taxol is not completely elucidated, taxadiene, which is the yielding product in the first committed step in the taxol biosynthetic pathway, is verified in both *E. coli* and *S. cerevisiae* based on scientists' efforts. The recovery and purification of taxadiene is important for supplying more source of the drug and studying the downstream pathway of taxol biosynthesis.

In this thesis, in-situ solid phase adsorption (SPA) program proposed by Jorge was adopted to recover taxadiene from *Saccharomyces cerevisiae* cell factories. The whole recovery of taxadiene generally comprises of three steps: cultivation, extraction and quantitative detection analysis, as shown in Figure 3-5 [15]. Yeast, solid adsorbents and the media for the yeast cultivation are firstly added in the shake flask to yield terpenoids and other natural products. The media used here is yeast extract peptone (YP, yeast extract 1 % (w/v), peptone 2 % (w/v)) supplemented with 2% (w/v) galactose (YPG) or 2 % (w/v) glucose (YPD). After thorough fermentation, produced taxadiene disperse in both liquid phase and solid phase including adsorbents and biomass. Adsorption of taxadiene was made *in-situ* by the adsorbent materials and desorption was made by acetone. Taxadiene titres were subsequently determined by gas chromatography-mass spectrometry (GC-MS), the amount of biomass was measured using a spectrophotometer at 600 nm. The control group used yeast only without any adsorbents. In Chapter 4, the recovery of taxadiene could be realised using hypercrosslinked HIPS monoliths as adsorbents.

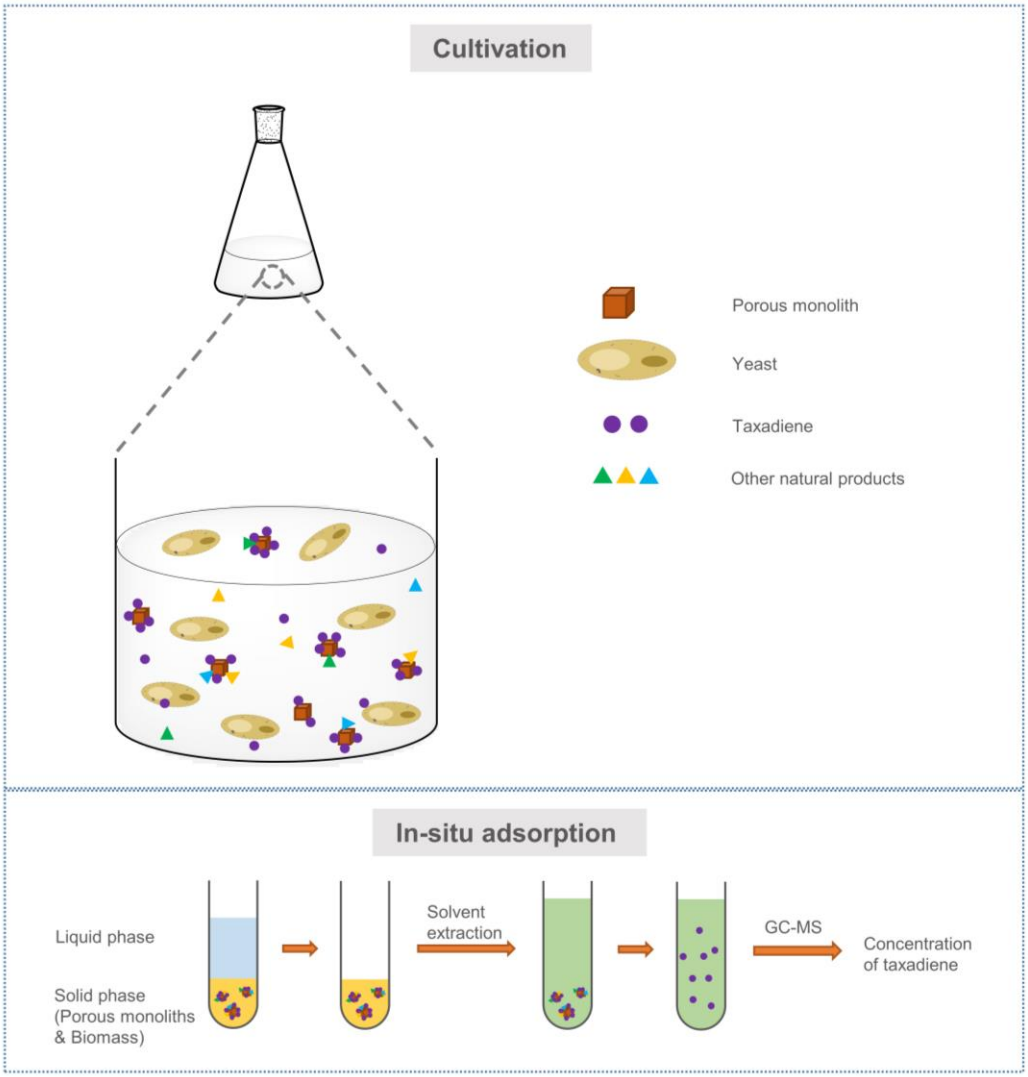


Figure 3-5: The methodology of in situ extracting taxadiene produced by the engineered yeast

## 3.3 Experiments of HCPs synthesis

### 3.3.1 Synthetic Procedure of hypercrosslinked HIPS monoliths

Synthesis of hyper-crosslinked 3d-printed HIPS monoliths and powders: In a typical experiment, 1 g of 3d-printed HIPS monoliths were added in the mixture of glacial acetic acid (50 mL), FDA (5 g) and $FeCl_3$(5 g) and heated at 80 ℃ under stirring for 12 or 24 hours. The resulting pre-HIPS cubes were washed with acetone, methanol and water for three times each. The products were dried at 80 ℃ for overnight before next step. Afterwards, 1 g of above pre-HIPS cubes were added in the mixture of DCE (50 mL), FDA (5 g) and $FeCl_3$ (5 g) and heated at 80 ℃ under stirring for 2

hours. The final hyper-crosslinked HIPS cubes were washed with acetone, methanol and water and dried at 80 ℃ for overnight. The resulting polymers were abbreviated as HIPS HCP-12h-2h (yield: 1.16 g) and HIPS HCP-24h-2h (yield: 1.24 g) according to the reaction time of each crosslinking step. By prolonging the reaction duration of second step to 18 hours, powdered HIPS HCPs could be obtained and they were denoted as HIPS HCP-12h-18h (yield: 1.36 g) and HIPS HCP-24h-18h (yield: 1.52 g).

### 3.3.2 Synthetic Procedure of all HCPs using DESs

**Synthesis of deep eutectic solvents (DES)**

Two DES were prepared as follows: Choline chloride and zinc chloride (or iron chloride) were mixed directly and stirred at 120 ℃ for 5 hours until homogenous solutions formed. The molar ratio of choline chloride and metal chloride is 1:2. This ratio was a compromise considering reducing the amount of catalyst while maintaining its catalytic effect. The obtained DES could be used in the next steps.

**Internal hypercrosslinking—Synthesis of *p*-DCX**

α, α'-dichloro-p-xylene (DCX, 1 g, 5.71 mmol) were added in the $[ChCl][ZnCl_2]_2$ (32.97 g, 79.97 mmol). The whole reaction was kept at 100 ℃ for 24 hours. The resulting mixture was washed by water, acetone and ethanol for three times each. The product was dried in vacuum oven at 100 ℃ for 12 hours and named as *p*-DCX. The similar practice was applied when $[ChCl][FeCl_3]_2$ served as solvent.

**Internal hypercrosslinking—Synthesis of *p*-BCMBP**

4,4′-bis(chloromethyl)-1,1′-biphenyl (BCMBP, 1 g, 4 mmol) were added in the $[ChCl][ZnCl_2]_2$ (23.08 g, 56 mmol). The whole reaction was kept at 130 ℃ for 24 hours. The resulting mixture was washed by water, acetone and ethanol for three times each. The product was dried in vacuum oven at 100 ℃ for 12 hours and named as *p*-BCMBP. The similar practice was applied when $[ChCl][FeCl_3]_2$ served as solvent.

**External hypercrosslinking—Synthesis of *p*-TPB**

1,3,5-triphenylbenzene (TPB, 1.53 g, 5 mmol) and formaldehyde dimethyl acetal (FDA, 3.04 g, 40 mmol) were added in the $[ChCl][FeCl_3]_2$ (9.28 g, 20 mmol). The

whole reaction was kept at 120 ℃ for 24 hours. The resulting mixture was washed by water, DCE and methanol for three times each. The product was dried in vacuum oven at 100 ℃ for 12 hours and named as *p*-TPB.

**External hypercrosslinking—Synthesis of *p*-triptycene**

Triptycene (1.27 g, 5 mmol) and formaldehyde dimethyl acetal (FDA, 3.04 g, 40 mmol) were added in the $[ChCl][FeCl_3]_2$ (9.28 g, 20 mmol). The whole reaction was kept at 100 ℃ for 24 hours. The resulting mixture was washed by water, DCE and methanol for three times each. The product was dried in vacuum oven at 100 ℃ for 12 hours and named as *p*-triptycene.

**External hypercrosslinking—Synthesis of *p*-BA**

Benzyl alcohol (0.541, 5 mmol) and formaldehyde dimethyl acetal (FDA, 3.04 g, 40 mmol) were added in the $[ChCl][FeCl_3]_2$ (9.28 g, 20 mmol). The whole reaction was kept at 100 ℃ for 24 hours. The resulting mixture was washed by water, DCE and methanol for three times each. The product was dried in vacuum oven at 100 ℃ for 12 hours and named as *p*-BA. The similar practice was applied when $[ChCl][ZnCl_2]_2$ served as solvent.

### 3.3.3 Synthetic Procedure of lignin-based HCPs

**Synthesis of DCX-crosslinked lignin polymers**

Lignin (1.57 g) was added into $[ChCl][ZnCl_2]_2$ (28.26 g, 0.069 mol) and stirred for 12 hours at 100 ℃ until a uniform dispersion was formed. DCX (3 g, 0.017 mol) was added into this uniform mixture as a crosslinker and the reaction temperature was increased to 150 ℃ and maintained for 24 hours. The resulting mixture was washed with deionised water, acetone, and ethanol for three times each. The product was dried in a vacuum oven at 100 ℃ for 12 hours and named as lignin-DCX-ZnDES. We also deployed this protocol to synthesise lignin-DCX-FeDES when $[ChCl][FeCl_3]_2$ (31.81 g, 0.069 mol) was used as the catalytic solvent. In addition, we also synthesised a control sample, lignin-DCX-DCE, according to a published protocol [16].

**Synthesis of BCMBP-crosslinked lignin polymers**

Lignin (1.57 g) was added in $[ChCl][ZnCl_2]_2$ (28.26 g, 0.069 mol) and stirred for 12 hours at 100 ℃ until they dispersed uniformly in the DES. The whole reaction was kept at 150 ℃ for 24 hours after adding BCMBP (4.3 g, 0.017 mol) as a crosslinker. The resulting mixture was washed with water, acetone and ethanol for three times each. The product was dried in a vacuum oven at 100 ℃ for 12 hours and named as lignin-BCMBP-ZnDES. The similar practice was applied when $[ChCl][FeCl_3]_2$ (31.81 g, 0.069 mol) served as solvent and the obtained product was named as lignin-BCMBP-FeDES. In addition, lignin-BCMBP-DCE was synthesised according to a previous study [16].

**Synthesis of FDA-crosslinked lignin polymers**

Lignin (1.57 g) was added in the $[ChCl][ZnCl_2]_2$ (28.26 g, 0.069 mol) and stirred for 12 hours at 100 ℃ until they dispersed uniformly in the DES. The whole reaction was kept at 150 ℃ for 24 hours after adding FDA (5.2 g, 0.068 mol) as a crosslinker. The amount of FDA used here was comparatively higher when compared to BCMBP and DCX content. This was to ensure more crosslinking as the boiling point of FDA was significantly lower (42 ℃). The resulting mixture was washed with water, acetone and ethanol for three times each. The product was dried in vacuum oven at 100 ℃ for 12 hours and named as lignin-FDA-ZnDES. We used this protocol to synthesise lignin-FDA-FeDES, using $[ChCl][FeCl_3]_2$ (31.81 g, 0.069 mol) as a catalytic solvent. In addition, lignin-FDA-DCE was synthesised as control samples according to a previous study [17].

## 3.4 Pressure swing adsorption (PSA) analysis

A five-step operating vacuum swing adsorption (VSA) cycle, including feed adsorption, heavy rinse, counter-current depressurisation, light-product purge and light-product depressurisation, is described in Figure 3-6. Firstly, a feed gas mixture comprising of 15 v/v% $CO_2$ and 85 v/v% $N_2$ is continuously introduced to the column from the feed end (z=0), pressurizing the bed to 1 bar under 298 K. The faster-diffusing $CO_2$ is adsorbed by the adsorbents inside the column, while the slower-

diffusing $N_2$ is obtained from the product end (z=L). A fraction of the obtained pure $N_2$ is collected as the light product, while the rest is utilised for purging and pressurizing the column. In the next heavy rinse step, a portion of $CO_2$ generated from the third blowdown section is used as the heavy purge gas to flush the column at 1 bar, displacing the remaining $N_2$ within the column. The adsorption column should be saturated with $CO_2$ at the end of this step, while the effluent gas can be recycled due to its identical composition to the feed gas. Subsequently, the column pressure reduces to a vacuum level, where the $CO_2$ is recovered and adsorbent is regenerated. Pure $CO_2$ is collected at the end and part of it can be recompressed to 1 bar for heavy rinse. Meanwhile, pure $N_2$ generated from the first step serve as the light purge gas to push the remaining $CO_2$ out. The adsorption column is therefore saturated with pure $N_2$ and ready for the next VSA cycle. Finally, the adsorption column is pressurised by $N_2$.

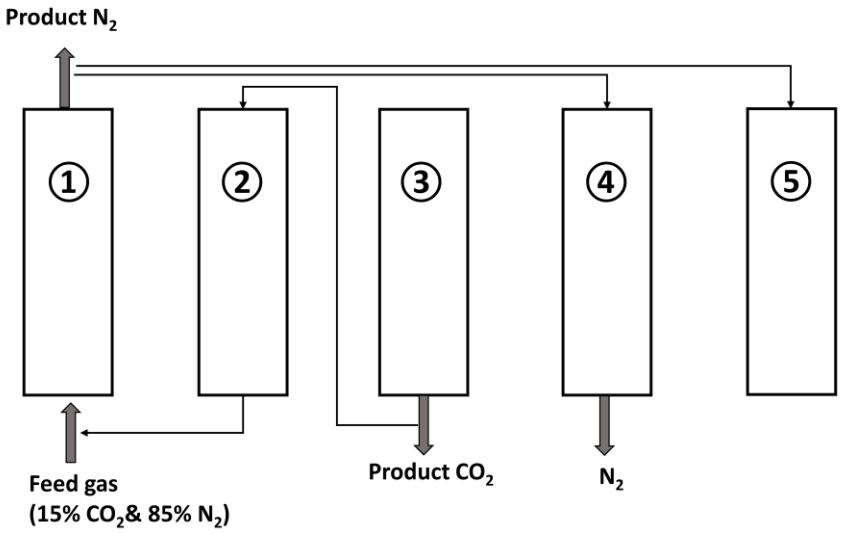


Figure 3-6: The procedure of the five-step vacuum pressure adsorption (VSA) cycle. ① feed adsorption,② heavy rinse, ③ counter-current depressurisation(blowdown), ④ light product purge, ⑤ light product purge pressurisation

The mathematics model applied here is based on the equilibrium theory model demonstrated by Kayser and Knaebel [18]. The following assumptions are made to derive the mathematics expressions:

(1) The column is operated isothermally.

(2) The gas behaviour follows the ideal gas law.

(3) The axial dispersion, radial variation and the diffuional resistance are neglected.

(4) The pressure drop along the column is neglected. The pressure is only a function of time during pressure-vary steps.

(5) The $N_2$ isotherms on all the materials are assumed to be linear.

Based on these assumptions, the component mass balances for $CO_2$ and $N_2$ are given as:

$$\frac{\partial\left(Py_{CO_2}\right)}{\partial t}+\frac{\partial\left(uPy_{CO_2}\right)}{\partial z}+\frac{1-\varepsilon}{\varepsilon}\rho_p RT\frac{\partial q_{CO_2}}{\partial t}=0 \tag{14}$$

$$\frac{\partial\left(Py_{N_2}\right)}{\partial t}+\frac{\partial\left(uPy_{N_2}\right)}{\partial z}+\frac{1-\varepsilon}{\varepsilon}\rho_p RT\frac{\partial q_{N_2}}{\partial t}=0 \tag{15}$$

When the temperature is fixed, the partial derivatives with time can be expressed as:

$$\frac{\partial q_{CO_2}}{\partial t}=\frac{1}{RT}f'_{CO_2}\frac{\partial Py_{CO_2}}{\partial t} \tag{16}$$

$$\frac{\partial q_{N_2}}{\partial t}=k_{N_2}\frac{\partial Py_{N_2}}{\partial t} \tag{17}$$

Substituting equation (16) and (17) into equation (14) and (15), respectively, yields:

$$\frac{\partial Py_{CO_2}}{\partial t}+\beta_{CO_2}\frac{\partial uPy_{CO_2}}{\partial z}=0 \tag{18}$$

$$\frac{\partial Py_{N_2}}{\partial t}+\beta_{N_2}\frac{\partial uPy_{N_2}}{\partial z}=0 \tag{19}$$

Where $\beta_{CO_2}=\frac{1}{1+\frac{1-\varepsilon}{\varepsilon}f'_{CO_2}\rho_p}$ and $\beta_{N_2}=\frac{1}{1+\frac{1-\varepsilon}{\varepsilon}\rho_p q_{N_2}RT}$. It is noted that $\beta_{CO_2}$ depends on the $CO_2$ partial pressure, while $\beta_{N_2}$ is constant and independent of the pressure. Then the overall mass balance is obtained by adding equations (18) and (19):

$$\frac{1}{\beta_{N_2}}\frac{\partial P}{\partial t}+\frac{\partial uP}{\partial z}+\left(\frac{1}{\beta_{CO_2}}-\frac{1}{\beta_{N_2}}\right)\frac{\partial Py_{CO_2}}{\partial t}=0 \tag{20}$$

Eliminating $\frac{\partial u}{\partial z}$ between equations (18) and (20), yields:

$$\frac{\partial y_{CO_2}}{\partial t}+\frac{u\beta_{CO_2}}{1+(\beta-1)y_{CO_2}}\frac{\partial y}{\partial z}=\frac{(\beta-1)(1-y)y_{CO_2}}{1+(\beta-1)y_{CO_2}}\frac{1}{P}\frac{\partial P}{\partial t} \tag{21}$$

Solving equation (20) by applying the method of characteristics obtains the following ordinary differential equation, with $\beta=\frac{\beta_{CO_2}}{\beta_{N_2}}$. Equation (22) implies the characteristic trajectories in the z-t plane. Whereas equation (23) indicates that the composition stays constant when the pressure is fixed.

$$\frac{dz}{dt} = \frac{u\beta_{CO_2}}{1 + (\beta - 1)y_{CO_2}} \tag{22}$$

$$\frac{dy_{CO_2}}{dP} = \frac{(\beta - 1)(1 - y_{CO2})y_{CO_2}}{[1 + (\beta - 1)y]P} \tag{23}$$

Additionally, eliminating $\frac{\partial Py}{\partial t}$ can also by combining equation (18) and (20):

$$\frac{1}{\beta_{N_2}}\frac{\partial P}{\partial t} + (\beta - 1)\frac{\partial\left(uPy_{CO_2}\right)}{\partial z} + \frac{\partial(uP)}{\partial z} = 0 \tag{24}$$

When the pressure is constant, the relation between the gas composition and the velocity can be evaluated:

$$ln\frac{u_2}{u_1} = \int_{y_{CO_2,1}}^{y_{CO_2,2}} \frac{1 - \beta}{1 + (\beta - 1)y_{CO_2}} dy_{CO_2} \tag{25}$$

Since the mole fraction determines the displacement of the characteristics, the characteristics may develop the shock or simple waves. The shock appears when the heavy component presented in the feed is more than it at the entrance inside the column. During the adsorption and rinse step, a composition shock wave is formed and propagated. The shock velocity ($u_{SH}$) is determined by the interstitial velocities in front of and behind the wave:

$$u_{SH} = \left.\frac{dz}{dt}\right|_s = \theta_{CO_2}\frac{u_2 y_{CO_2,2} - u_1 y_{CO_2,1}}{y_{CO_2,2} - y_{CO_2,1}} \tag{26}$$

Where

$$\theta_{CO2}\left(P, y_{CO_2,1}, y_{CO_2,2}\right) = \frac{1}{1 + \frac{1 - \varepsilon}{\varepsilon}\frac{f_{CO_2,2} - f_{CO_2,1}}{y_{CO_2,2} - y_{CO_2,1}}\frac{\rho_p RT}{P}} \tag{27}$$

A balance around the shock front in terms of the $CO_2$ is given by:

$$\frac{u_1}{u_2} = \frac{1 + (\theta - 1)y_{CO_2,2}}{1 + (\theta - 1)y_{CO_2,1}} \tag{28}$$

Where $\theta = \frac{\theta_{CO_2}}{\theta_{N_2}}$ and $\theta_{N_2} = \frac{1}{1 + \frac{1-\varepsilon}{\varepsilon}k_{N_2}\rho_P RT}$. Noted that subscripts 1 and 2 are referred to the positions in front of and behind the shock wave respectively, and $f_{CO_2,i} = f_{CO_2,i}\left(\frac{Py_{CO_2,i}}{RT}\right)$ (*i=1,2*).

Overall, above equations are utilised to obtain the numbers of moles of influent or effluent during each step. Moreover, complete utilisation of the adsorption column is presumed, and the cycle starts at a cyclic steady state.

(A) Pressurisation

The adsorption time is determined by integrating Equation (26) with $y_{CO_2,1} = 0$ and $y_{CO_2,2} = y_f$, corresponding to the column length, the interstitial velocity, and the adsorption isotherm, giving:

$$u_{F,in} t_{AD} = \frac{L}{\theta_{CO_2}(P_H, 0, y_f)} \tag{29}$$

Where $P_H$ is adsorption pressure. Thus, the total number of moles fed to the column is given by:

$$N_{FI} = \varepsilon A \frac{P_H}{RT} u_{F,in} t_{AD} = \frac{\varepsilon A P_H L}{\theta_{CO_2}(P_H, 0, y_f) RT} \tag{30}$$

Where $N_{FI}$ represents the number of moles that enter the column during the adsorption step.

(B) Heavy rinse

Similar to the adsorption step, the propagation of the shock wave is dominated inside the column during heavy rinse step. Noted that the column performance is not affected by the gas flow direction, as the ideal shock front is presented when using the local equilibrium mathematical model. Here, the gas is assumed to flow counter-currently. The governing equations during this step are similar to those during the adsorption step. Based on equations 22, 25, 26, and 28, the inlet ($u_{R,in}$) and outlet ($u_{R,out}$) interstitial velocities correspond to the bed length, isotherm and step time, expressed as:

$$u_{R,out} t|_R = \frac{L}{\theta_{N_2}} \tag{31}$$

$$u_{R,in} = \frac{1 + (\theta - 1) y_{CO2,1}}{1 + (\theta - 1) y_{CO2,2}} u_{R,out} \tag{32}$$

Thus, the corresponding expressions of the total number of moles leaving ($N_{RO}$) or entering ($N_{RI}$) the column are:

$$N_{RO} = \varepsilon A \frac{P_H}{RT} u_{R,out} t_R = \frac{\varepsilon A P_H L}{\theta_{N_2} RT} \tag{33}$$

$$N_{RI} = \varepsilon A \frac{P_H}{RT} u_{R,in} t_R = N_{RO} \frac{1 + \left[\theta\left(P_H, 1, y_f\right) - 1\right] y_f}{\theta\left(P_H, 1, y_f\right)} \tag{34}$$

(C) Counter-current depressurisation

Following the heavy rinse step, the column is presumed to be saturated with pure $CO_2$. The amount of $CO_2$ produced is determined by the difference in $CO_2$ amounts between the initial and final states.

$$N_{BO} = \frac{\varepsilon A L P_H}{\theta_{CO_2}(P_H, 1,0) RT} - \frac{\varepsilon A L P_L}{\theta_{CO_2}(P_L, 1,0) RT} \tag{35}$$

Here, $N_{BO}$ means the number of moles that leave the column during the blowdown step. It is noted that the $CO_2$ isotherms of adsorbents is fitted with Langmuir-Freundlich model, the value of $\beta_{CO_2}(P_L, 0)$ is meaningless due to a negative exponential. Hence, the amount of purge gas and $N_2$ recovery is unable to predict. This section only focuses on the column performance in terms of the $CO_2$ recovery. The $CO_2$ recovery is calculated as:

$$Re_{CO_2} = \frac{N_{BO} - N_{RI}}{y_f (N_{FI} - N_{RO})} = \frac{\frac{P_H}{P_L}\left[\frac{\theta_{CO_2}(P_H, 1, y_f)}{\theta_{CO_2}(P_H, 1,0)} + y_f\left(1 - \frac{\theta_{CO_2}(P_H, 1, y_f)}{\beta_{N_2}}\right) - 1\right] - \frac{\theta_{CO_2}(P_H, 1, y_f)}{\theta_{CO_2}(P_L, 1,0)}}{\frac{P_H}{P_L} y_f \left(\frac{\theta_{CO_2}(P_H, 1, y_f)}{\theta_{CO_2}(P_H, y_f, 0)} - \frac{\theta_{CO_2}(P_H, 1, y_f)}{\beta_{N_2}}\right)} \tag{36}$$

## 3.5 References


[1] Zhang, F., et al., *3D printing technologies for electrochemical energy storage.* Nano Energy, 2017. **40**: p. 418-431.

[2] An, J., et al., *Design and 3D printing of scaffolds and tissues.* Engineering, 2015. **1**(2): p. 261-268.

[3] Cardoso, R.M., et al., *Additive-manufactured (3D-printed) electrochemical sensors: A critical review.* Analytica chimica acta, 2020. **1118**: p. 73-91.

[4] Jiang, Z., et al., *Extrusion 3D printing of polymeric materials with advanced properties.* Advanced Science, 2020. **7**(17): p. 2001379.

[5] Kristiawan, R.B., et al., *A review on the fused deposition modeling (FDM) 3D printing: Filament processing, materials, and printing parameters.* Open Engineering, 2021. **11**(1): p. 639-649.

[6] Zhou, L.Y., J. Fu, and Y. He, *A review of 3D printing technologies for soft polymer materials.* Advanced Functional Materials, 2020. **30**(28): p. 2000187.

[7] Azimi, P., et al., *Emissions of ultrafine particles and volatile organic compounds from commercially available desktop three-dimensional printers with multiple filaments.* Environmental science & technology, 2016. **50**(3): p. 1260-1268.

[8] Borisov, A.S., P. Hazendonk, and P.G. Hayes, *Solid-state nuclear magnetic resonance spectroscopy: A review of modern techniques and applications for inorganic polymers.* Journal of Inorganic and Organometallic Polymers and Materials, 2010. **20**: p. 183-212.

[9] Ibbett, R.N., *NMR spectroscopy of polymers*. 2012: Springer Science & Business Media.

[10] Inkson, B.J., *Scanning electron microscopy (SEM) and transmission electron microscopy (TEM) for materials characterization*, in *Materials characterization using nondestructive evaluation (NDE) methods*. 2016, Elsevier. p. 17-43.

[11] Thommes, M., et al., *Physisorption of gases, with special reference to the evaluation of surface area and pore size distribution (IUPAC Technical Report).* Pure and applied chemistry, 2015. **87**(9-10): p. 1051-1069.

[12] Naderi, M., *Surface area: brunauer–emmett–teller (BET)*, in *Progress in filtration and separation*. 2015, Elsevier. p. 585-608.

[13] Wang, T., et al., *Recent research progress in taxol biosynthetic pathway and acylation reactions mediated by Taxus acyltransferases.* Molecules, 2021. **26**(10): p. 2855.

[14] Tong, Y., Y.F. Luo, and W. Gao, *Biosynthesis of paclitaxel using synthetic biology.* Phytochemistry Reviews, 2021: p. 1-15.

[15] Santoyo-Garcia, J.H., et al., *In situ solid-liquid extraction enhances recovery of taxadiene from engineered Saccharomyces cerevisiae cell factories.* Separation and Purification Technology, 2022. **290**: p. 120880.

[16] Sun, L., et al., *One-pot fabrication of lignin-based aromatic porous polymers for efficient removal of bisphenol AF from water.* International Journal of Biological Macromolecules, 2021. **175**: p. 396-405.

[17] Meng, Q.B. and J. Weber, *Lignin-based microporous materials as selective adsorbents for carbon dioxide separation.* ChemSusChem, 2014. **7**(12): p. 3312-3318.

[18] Kayser, J.C. and K.S. Knaebel, *Pressure swing adsorption: development of an equilibrium theory for binary gas mixtures with nonlinear isotherms.* Chemical engineering science, 1989. **44**(1): p. 1-8.

# Chapter 4 3d-printed microporous HIPS monoliths

This work is in submission, named as ‘3D printed microporous high-impact polystyrene (HIPS) monoliths for water purification’.

## 4.1 The intention and target of this project

Hypercrosslinked polymers (HCPs) feature on abundant hierarchical pores and tuneable porosity, showing great potential in energy and environmental fields like gas storage [1-3], removal of water pollutants [4-6] and catalysis, etc [7,8]. Traditional synthetic method for HCPs could be traced to Davankov resins which were first reported by Tsyurupa and Davankov in 1971 [9]. They dispersed polystyrene-based precursors in the halogenated solvent and continued to add extra crosslinkers to post-crosslink them into porous HCPs under the catalysis of Lewis acid. Their protocol followed Friedel-Crafts chemistry, boosting the emergence of great amounts of porous HCPs sorbents. Afterwards, Tan and his group found the relatively active formaldehyde dimethyl acetal (FDA) reagent as a universal external crosslinker for knitting aromatic monomers into HCPs, representing a milestone towards much wider selections for starting materials [8,10].

Due to the intrinsic fast kinetics of Friedel-Crafts reaction, the extensively crosslinked HCPs have highly rigid polymeric networks. Generally, the crosslinking takes place irregularly, encompassing both intermolecular and intramolecular bonding. The obtained HCPs are hence isolated as insoluble networks and they usually exist in the form of powders macroscopically after drying, which brings inconvenience to practical applications [11,12].

Many efforts have been made to produce processable HCPs such as two-dimensional membranes and three-dimensional monoliths via hypercrosslinking strategy. Dai and co-workers [13] reported polymeric molecular polystyrene (PS) sieve membranes via facile in-situ hypercrosslinking technology, demonstrating both good gas permeability

and selectivity. The resulting PS membranes featured a hierarchical sandwich structure composed of a macroporous core, a layer of dense micropores and a mesoporous surface. As the crosslinking time increased from 1.5 h to 12 h, the BET surface areas of the porous PS membrane increased from 218 to 618 $m^2$ $g^{-1}$. Despite complete crosslinking, the BET surface area is still inferior to hypercrosslinked PS powders (1225 $m^2$ $g^{-1}$)[14]due to the greater macropores proportion in the hypercrosslinked PS membranes. Tan et al. [15] obtained hierarchical porous polystyrene monoliths via high internal phase emulsion polymerisation(HCP-PolyHIPE) and further external hypercrosslinking method. By controlling the ratio of styrene and divinylbenzene in the PolyHIPE precursors, the researchers managed to adjust the surface area of final monoliths varied from 196 to 595 $m^2$ $g^{-1}$. Basically, PolyHIPE is macroporous while mesopores and micropores are created in the subsequent hypercrosslinking process. Such macroporous substrates almost suggest that the BET surface area of HCP-PolyHIPE monoliths should be insufficient. Both of the research maintained the shape of HCPs via limiting the microporosity and rigidity, avoiding the collapse of monoliths. Their work indicated the existence of trade-off effect between porosity and completion of the HCP monoliths.

On the other hand, researchers attempt to improve the processability via increasing the solubility of HCPs. This means the crosslinking should be restricted in the diluted condition and avoid intermolecular crosslinking as much as possible. Su et al. [16] managed to synthesise hypercrosslinked aero gels via thermally induced polymerisation from tetrahedral monomers, offering suitable platforms for hybridisation with functional two-dimensional polymer. This work proposed a novel methodology for processable HCP devices but special starting materials are required. Recently, Tan's group [17] has reported processable HCPs materials from aromatic vinyl starting materials via a two-step method at room temperature. They firstly prepared uniform lightly-crosslinked precursors in diluted solution at low temperature, and then continued to form crosslinking networks with residual unreacted vinyl groups at elevated temperature. The crosslinking bridges mostly distribute

intramolecularly under the diluted solution, retaining the solubility of yielded HCPs. However, the BET surface areas of solution processable HCPs are expected to be lower than powdered HCPs because of the limited crosslinking degree. Moreover, some researchers produced HCPs monoliths via templates polymerisation. For example, porous polystyrene-based monoliths have been successfully prepared to serve as the stationary phase for liquid chromatography and thin layer chromatography (TLC) [18,19]. The drawback of this method is its heavy reliance on the shape of the template.

Even though researchers have made great contributions to the synthesis of processable HCPs materials, we have to admit that related research is still limited. Summarising the above researches, the selection of monomers for processable HCPs were limited to some molecules with self-crosslinking functional groups and the shapes of final HCPs products were usually decided by templates. Therefore, it is highly advocated to develop more versatile strategies for batch production of porous HCPs materials.

Here, we successfully prepared structure-retained microporous HIPS monoliths by controlling the reaction time of stepwise hypercrosslinking process [20] after printing initial monoliths. 3D printing technology can fabricate complex designs, print multiple patterns simultaneously in a single-step process, and utilize materials more efficiently [21]. The strategy could be described in Figure 4-1. Uniform HIPS monoliths were printed via 3d-printing technology which can freely define the shape of monoliths according to user's settings. After that, they were first pre-crosslinked using FDA as an external crosslinker in acetic acid which is a poor solvent for this reaction. This step aimed at forming lightly-crosslinked polymeric networks and keeping the topological structure of HIPS monoliths as much as possible. And thus, dissolution of monoliths could be avoided in the next step. It is worth mentioning that longer reaction time of pre-crosslinking process has negative effects on the surface area of final HCPs [20]. Then the pre-crosslinked HIPS monoliths were further crosslinked in DCE which is good solvent for Friedel-Crafts reactions. The inner lightly cross-linked HIPS provided necessary mechanical strength while the outer

hypercrosslinked HIPS provided major porosity. We had to admit that the reservation of mechanical properties was achieved by sacrificing tiny porosity. Different from the HCPs monoliths reported previously, our strategy innovatively introduced 3D printing technology to provide various shape options for HCPs monoliths so that they can adapt to different circumstances.

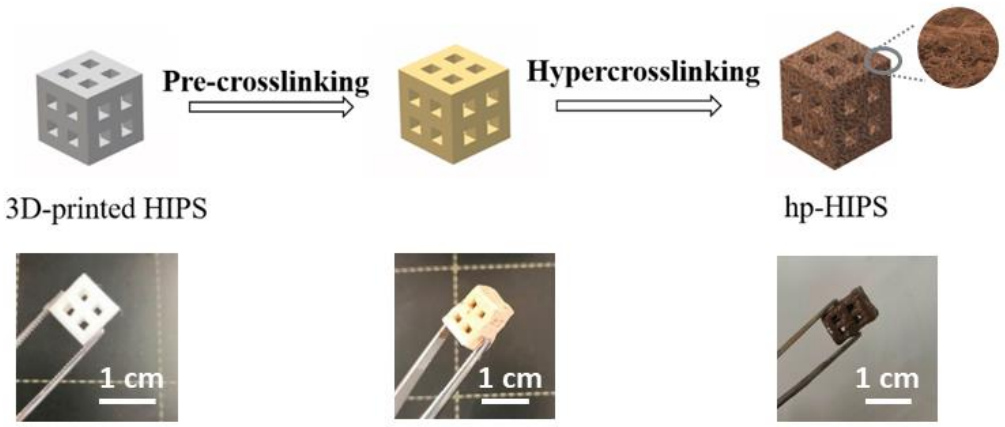


Figure 4-1: The illustration of hypercrosslinking process of 3D-printed HIPS monoliths and corresponding images of HIPS monoliths after each step

## 4.2 Results and Discussion

3D-printed HIPS monoliths were pre-crosslinked in acetic acid to gain enough mechanical strength and subsequently crosslinked in DCE to create enough porosity. In the both crosslinking process, FDA served as an external crosslinker and provide HIPS networks with methylene bridges. Obvious dimension changes can be observed after each crosslinking step (Figure 4-1). The average weights and dimension changes of the two structure-retained HIPS HCP-12h-2h and HIPS HCP-24h-2h monoliths are shown in Table 4-1. Despite differing pre-crosslinking durations, the weight enhancements of HIPS HCP-12h-2h and HIPS HCP-24h-2h monoliths in the initial step were comparable, indicating slow crosslinking reactions in the poor solvent. However, subsequent exposure to DCE for 2 hours, aimed at introducing micropores within the HIPS monoliths, resulted in a 6.6% greater weight for HIPS HCP-24h-2h

compared to HIPS HCP-12h-2h. This discrepancy can be attributed to different pre-crosslinking degrees, implying that HIPS monoliths pre-crosslinked for 12 hours exhibited less crosslinking degree and thus higher dissolution in DCE. Apart from the weight changes, noticeable dimensional changes of these HIPS monoliths were observed. Take a cubic HIPS monolith with dimensions of 1 cm×1 cm×1 cm (length×width×height) as an example, the length and width dimensions experienced slight expansion, ranging from 1% to 5% after the two-step crosslinking process. However, the height change was remarkable, with an increase ranging between 40% and 49%. This resulted from the bottom-to-top printing model decided by fused deposition modelling (FDM), which is one of the most common techniques in 3D printing. This method involves melting a thermoplastic filament and depositing it layer by layer to create the desired object. Hence, the bonding quality between layers along the z-axis is affected by the temperature of the interface layer [22]. Generally, the layers can still be distinguished under a microscope despite the printed object is integral macroscopically, implying the weak interaction and adhesion between layers. HIPS HCP-24h-2h monoliths behaved less deformation than HIPS HCP-12h-2h monoliths although the former gained more weight after crosslinking. It demonstrated that HIPS HCP-24h-2h monoliths were more likely to resist deformation as they were pre-crosslinked adequately. Based on the above comparison, it is convincing that longer pre-crosslinking duration is favourable in maintaining the integrity of monoliths.

Table 4-1: The weights and dimension changes of structure-retained HIPS monoliths during each step

| | Initial weight /g | Weight in 1st step /g | Weight in 2nd step /g | Initial dimension /cm×cm×cm | Dimension in 1st step /cm×cm×cm | Dimension in 2nd step /cm×cm×cm |
|---|---|---|---|---|---|---|
| HIPS HCP-12h-2h | 0.05 | 0.053 | 0.058 | 1×1×1 | 1.03×1.01×1.4 | 1.05×1.02×1.49 |
| HIPS HCP-24h-2h | 0.05 | 0.053 | 0.062 | 1×1×1 | 1.02×1.0×1.41 | 1.04×1.01×1.45 |

SEM was utilised to examine the surface morphology and pore structures of pristine HIPS monoliths and corresponding hypercrosslinked monoliths. As shown in Figure 4-2a and 4-2b, the pristine HIPS monoliths have dense and compact morphology despite rough surface caused by fused deposition modelling printing process. Combined with the results from BET analysis, the specific surface area of the pristine HIPS is even below 5 $m^2$ $g^{-1}$. Therefore, it can be concluded that both the surface and the cross-section of the pristine HIPS monoliths are non-porous. After the two steps of reactions, they were successfully crosslinked and maintained their original shapes with little deformation. Here, we take HIPS HCP-12h-2h as an example. As shown in the Figure 4-2c, macropores and mesopores co-existed in the HIPS HCP monoliths, demonstrating the hierarchical porosity within HIPS HCP monoliths. Figure 4-2d further confirmed that hierarchical structure can be observed spreading on the outer surface of HIPS HCP monoliths while the central section of the HIPS monoliths was still relatively denser. This is because the crosslinking started from the surface and formed micropores at first. The surface HIPS quickly crosslinked with FDA and formed a layer comprising micropores. This microporous HIPS layer slowed down the dissolution of interior HIPS, and the reaction relied on the diffusion of FDA, $FeCl_3$ and DCE through the monoliths. On the solid-liquid interface, the diffusion rate of HIPS molecules from interior to surface was faster than those of FDA and $FeCl_3$, resulting in the formation of vacancies near the interface. According to the nanoscale Kirkendall effect, meso and macropores emerged steadily via the coalescence of the vacancies [13].As the crosslinking reaction proceeded continuously, the surface micropores underwent the gradual conversion into mesopores and even macropores, leading to the formation of an open polymeric networks. The solvent and catalyst can thus diffuse into the inner space and promote the crosslinking more easily. Such hierarchical porous structure indicated that the BET surface areas of the HIPS HCP monoliths would decrease significantly compared with those of the HIPS HCP powders which were fully hypercrosslinked. On the contrary, fully-crosslinked HIPS HCP powders exhibited an aggregated particle morphology, ranging in size from

micrometers to nanometers (Figure 4-2e, 4-2f). Therefore, the asymmetric structure of the HIPS HCP monoliths was composed of two parts: porous outer layer that provided necessary porosity and dense inner core which preserved structural strength and integrity.

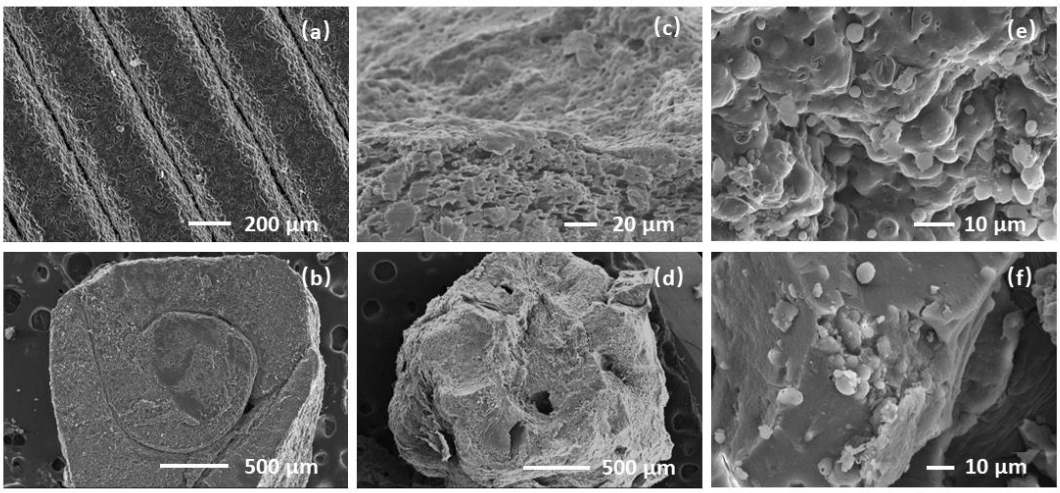


Figure 4-2: SEM images of morphologies of (a) the surface of pristine HIPS monoliths, (b) the cross-section of pristine HIPS monoliths, (c) the surface of HIPS HCP-12h-2h monoliths, (d) the cross-section of HIPS HCP-12h-2h monoliths, (e, f) HIPS HCP-12h-18h powders.

To inspect the chemical structure of HIPS HCPs, Fourier transform infrared (FTIR) was used. The spectra of original HIPC filament and as-synthesised HIPS HCPs were shown in Figure 4-3. It was observed that the peaks centred at 3058 and 3024 $cm^{-1}$ represented the stretching of aromatic C-H stretching while peaks at 2923 and 2865 $cm^{-1}$ corresponded to the presence of methylene (-$CH_2$-) stretching vibrations. The new peak occurred at 1710 $cm^{-1}$ could be attributed to the conversion from mono-substituted aromatic rings to multi-substituted rings, indicating the formation of connecting bridges between aromatic rings. In addition, the strong peak at 755 and 694 $cm^{-1}$, which corresponds to the C-H bending vibrations in aromatic rings, diminished after polymerisation [23]. This can further support the formation of the crosslinking structures. The band around 1450 $cm^{-1}$ could be assigned to C-H bending vibrations of methylene groups. Furthermore, peaks at 1603, 1570, and 1505 $cm^{-1}$ are attributed to the stretching vibrations of aromatic C=C bonds.

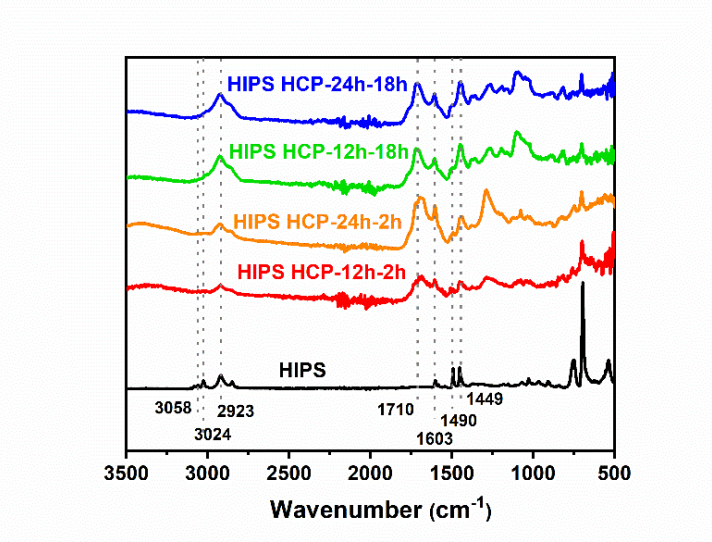


Figure 4-3: FTIR spectra of pristine HIPS filament and as-prepares HIPS HCPs

The pore structures of the HIPS HCP monoliths were investigated by nitrogen sorption isotherms measured at 77 K. The BET surface areas and pore volume of HIPS HCP monoliths and powdered HIPS HCPs were summerised in Table 4-2. Powdered HIPS HCPs samples were obtained by prolonging the reaction time of second step to 18 hours to ensure fully crosslinking. Generally, HIPS HCP-12h-2h and HIPS HCP-24h-2h monoliths were less porous than corresponding HIPS HCP powdered samples. The BET surface area of HIPS HCP-12h-2h was 337 $m^2 g^{-1}$, dropping by 68% as the reaction duration of second hypercrosslinking step dramatically shortened from 18h to 2h. This was due to the scant reaction time that limited the formation of abundant pores. The remarkable reduction of HIPS HCP-12h-2h was as expected considering the inadequate crosslinking. Meanwhile, longer reaction time of the first pre-crosslinking step would significantly degrade the porosity of final HCPs. The BET surface area of HIPS HCP-24h-18h sharply decreased to 595 $m^2 g^{-1}$, only 56% of that of HIPS HCP-12h-18h. Similarly, the BET surface area of HIPS HCP-24h-2h monoliths reduced by 32% comparing to that of HIPS HCP-12h-2h monoliths. Therefore, the reaction time of the first step should be minimised to guarantee the feasibility of the following pore-formation. The aim of

pre-crosslinking step is to obtain a lightly crosslinked structure which can tolerate harsher experimental conditions of next step and maintain their architecture.

Table 4-2: Surface areas and pore volume of HIPS HCPs

| Sample | BET surface area / $m^2 g^{-1}$ | Pore volume / $cm^3 g^{-1}$ |
|---|---|---|
| HIPS HCP-12h-18h (powders) | 1057 | 1.21 |
| HIPS HCP-12h-2h (monoliths) | 337 | 0.305 |
| HIPS HCP-24h-18h (powders) | 595 | 0.448 |
| HIPS HCP-24h-2h (monoliths) | 229 | 0.17 |

We measured the nitrogen adsorption isotherms and pore size distribution of HIPS HCP monoliths and powdered HIPS HCPs for comparison (Figure 4-4). As shown in Figure 4-4a, the $N_2$ isotherms of HIPS HCP-12h-18h corresponded to a Type IV curve that is associated with mesopores based on IUPAC classification [24]. In addition, a desorption hysteresis loop was observed, indicating mesoporous structures co-existed with abundant micropores. Its pore size distribution (Figure 4-4b) displayed two prominent peaks around 2.8 and 4.8 nm, providing further evidence for large amount of sizable mesopores. The remaining three HIPS HCP samples exhibited the characteristic of Type I curve which features on rapid $N_2$ uptake under very low $P/P_0$ and final saturation plateau [24]. Therefore, microporous structures dominated HIPS HCP-24h-18h, HIPS HCP-12h-2h and HIPS HCP-24h-2h despite few mesopores. This was confirmed by their pore size distribution curves where main remarkable peaks were below 2 nm. Moreover, the pore volume of these four materials followed the order of HIPS HCP-12h-18h > HIPS HCP-24h-18h > HIPS HCP-12h-2h > HIPS HCP-24h-2h, which was consistent with their BET surface areas.

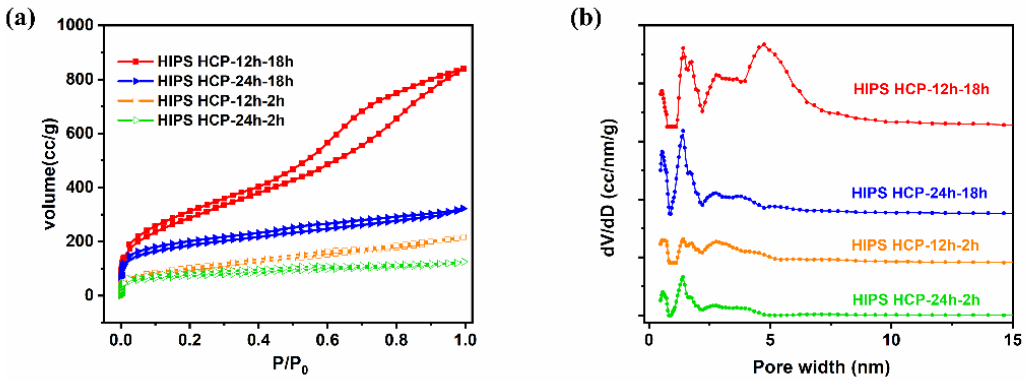


Figure 4-4: (a) $N_2$ adsorption and desorption isotherms (b) Pore size distributions of HIPS HCP-12h-18h, HIPS HCP-24h-18h, HIPS HCP-12h-2h and HIPS HCP-24h-2h under 77 K

To determine the heterogenous crosslinking of HIPS HCP-12h-2h and HIPS HCP-24h-2h, we soaked both monoliths in DCE to remove the incompletely crosslinked parts, as the fully-crosslinked HCPs were insoluble. Figure 4-5 compared the weights of these HIPS HCP monoliths before and after the immersing in DCE completely. As expected, HIPS-HCP-12h-2h monoliths exhibited a higher weight loss than HIPS-HCP-24h-2h monoliths, reaching 28% while the later only dropped by 18.5%. This confirmed that longer pre-crosslinking time can improve the resistance of HIPS HCP monoliths to dissolution. These partially crosslinked soluble components were responsible for providing mechanical support for HIPS HCP monoliths. Moreover, the porosity of the remaining insoluble parts was also tested to investigate the porous structures of HIPS HCP monoliths. The BET surface areas of insoluble HIPS HCP-12h-2h and HIPS HCP-24h-2h monoliths residues were 132.2 and 133.4 $m^2\ g^{-1}$, respectively. Theses similar values suggested that HIPS HCP monoliths comprised a porous outer shell and a microporous dense core, wherein the outer shell was insoluble while the inner core was soluble. Since the BET surface areas of the whole monolith and insoluble partes were known already, the BET surface area of the soluble microporous parts in HIPS HCP-12h-2h and HIPS HCP-24h-2h monoliths can be calculated as 864 and 652 $m^2\ g^{-1}$. This explained the significant surface area drop of HIPS HCP monoliths compared with corresponding powdered samples. Another possible reason for the decreased porosity of HIPS HCP monoliths could be the

flexible polybutadiene chains in the commercial HIPS filaments [13]. Basically, HIPS is made from styrene monomer along with an elastomeric phase comprising polybutadiene rubber and styrene butadiene copolymer. These additives are aimed at improving the impact resistance of polystyrene materials. However, these components may block some parts of the micropores and lead to the decreased porosity. Clearly, the drop in porosity is an unavoidable result in order to maintain the constructure of monoliths. By adjusting the crosslinking time and choosing suitable polystyrene-based filaments, the porosity and shape of the final monoliths can be tuned accordingly.

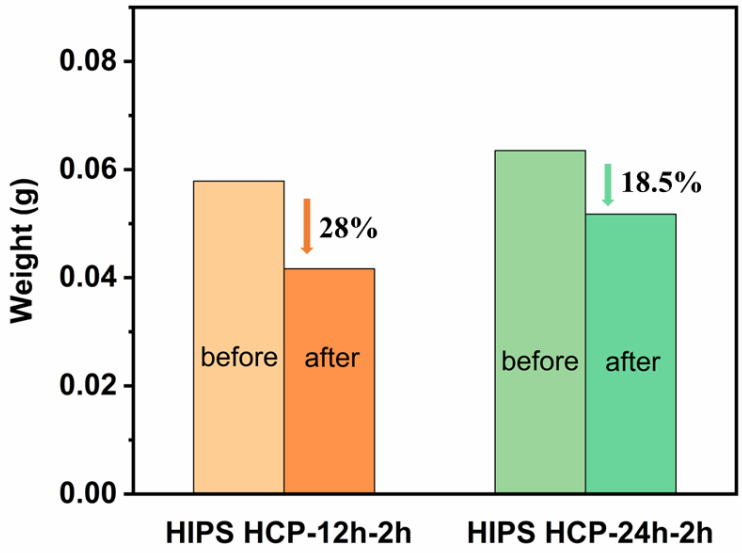


Figure 4-5: The weights changes of HIPS HCP-12h-2h and HIPS HCP-24h-2h monoliths after soaking in DCE to fully remove the uncrosslinked parts.

## 4.3 Applications

The porous and hydrophobic traits of HIPS HCP monoliths suggest that they are promising adsorbents for separation process. Here, we investigated their performance in oil adsorption, dyes removal and recovery of taxadiene.

### 4.3.1 Oil adsorption

As summarised in Table 4-3, a variety of solvents and oils were employed for measuring the capacity of HIPS HCP-12h-2h and HIPS HCP-24h-2h monoliths respectively. Varying the polarities, densities and viscosities of selected sorbates,

HIPS HCP-12h-2h demonstrated adsorption capacities within the range of 0.8 to 2.6 g $g^{-1}$, whereas HIPS HCP-24h-2h exhibited slightly lower capacities, ranging from 0.5 to 2.1 g $g^{-1}$. These minor advantages could be attributed to the higher BET surface area of HIPS HCP-12h-2h monoliths. Compared with some reported porous solid sorbents [15], the adsorption capacities of these HIPS monoliths for different oils are poor. This could mainly be attributed to their insufficient specific surface area.

Table 4-3: Oil adsorption of HIPS HCP monoliths

| Oil | HIPS HCP-12h-2h / g $g^{-1}$ | HIPS HCP-24h-2h / g $g^{-1}$ |
|---|---|---|
| Acetone | 1.2 | 2.1 |
| Methanol | 0.9 | 0.6 |
| Ethanol | 1 | 0.8 |
| Paraffin oil | 1 | 0.5 |
| Chloroform | 2.6 | 1.8 |
| Hexane | 0.8 | 0.6 |

Apart from the adsorption of pure solvents, HIPS HCP monoliths can also selectively adsorb oils from oil/water mixtures due to their hydrophobicity. The adsorption process was shown in Figure 4-6, immiscible chloroform was dyed with red oil O for clear distinction from mass colourless water. The chloroform droplets sunk in water because of its larger density. After soaking a HIPS HCP monolith into the mixture, red chloroform was quickly adsorbed.

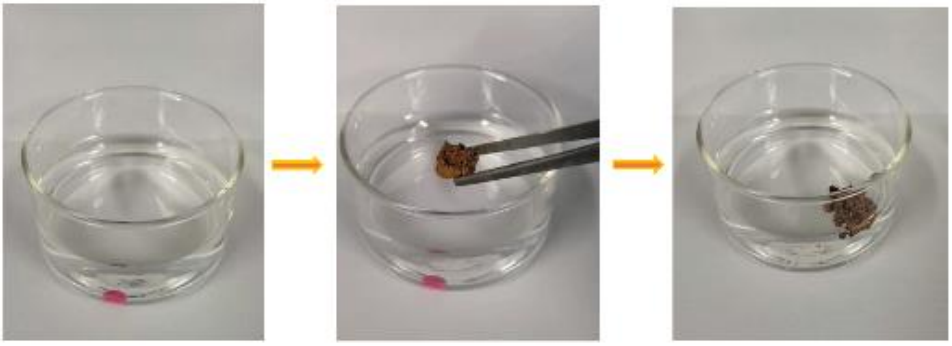

Figure 4-6: A HIPS HCP monolith can adsorb oil from oil/water mixture due to its hydrophobicity

### 4.3.2 Dyes adsorption

HIPS HCP monoliths can also be applied for the dyes adsorption from aqueous solutions. The standard curves of four dyes including RhB, MO, MB and NR were determined with UV-vis spectrometer (Figure 4-7) using calibration aqueous solutions with different concentrations. Their concentrations showed good linear correlation with their characteristic UV peak.

These HIPS HCP monoliths had visible adsorption capacity for dyes such as RhB as the colour fading indicated. HIPS HCP-12h-2h, which had a higher BET surface area than HIPS HCP-24h-2h, exhibited comparatively better adsorption capacity towards all dyes including MB, MO, NR, RhB (Figure 4-8). The capacity of HIPS HCP-12h-2h monoliths for the dyes ranged from 0.59 to 0.78 mg $g^{-1}$, while that of HIPS HCP-12h-2h monoliths fluctuated between 0.49 and 0.71 mg g-1. Although the capacity of HIPS HCP-12h-2h was overall higher than that of HIPS HCP-24h-2h, it was still inferior compared with solid adsorbents on the market. Activated carbon (AC) with a surface area of 285 $m^2$ $g^{-1}$ was reported to have a maximum adsorption capacity towards MB, reaching 101 mg $g^{-1}$ [25]. The outstanding performance of AC could be attributed to the plenty of surface functional groups such as hydroxyl groups and carbon-oxygen bonds. These groups facilitate the formation of hydrogen bonds and electrostatic interactions between AC and MB molecules, thereby enhancing the capacity. The comparison between HIPS HCP-12h-2h (SA: 337 $m^2$ $g^{-1}$) and AC (285

$m^2$ $g^{-1}$) indicated that surface functional groups could significantly improve the affinity between adsorbents and adsorbates. These interactions are believed to be more effective than intrinsic porosity in the adsorption process. Moreover, the HIPS HCP monoliths did not exhibit specific adsorption of any dye regardless of their surface charge. It suggested that the only driving force in the HIPS HCP monoliths was their porosity, which can trap the dyes inside the adsorbents.

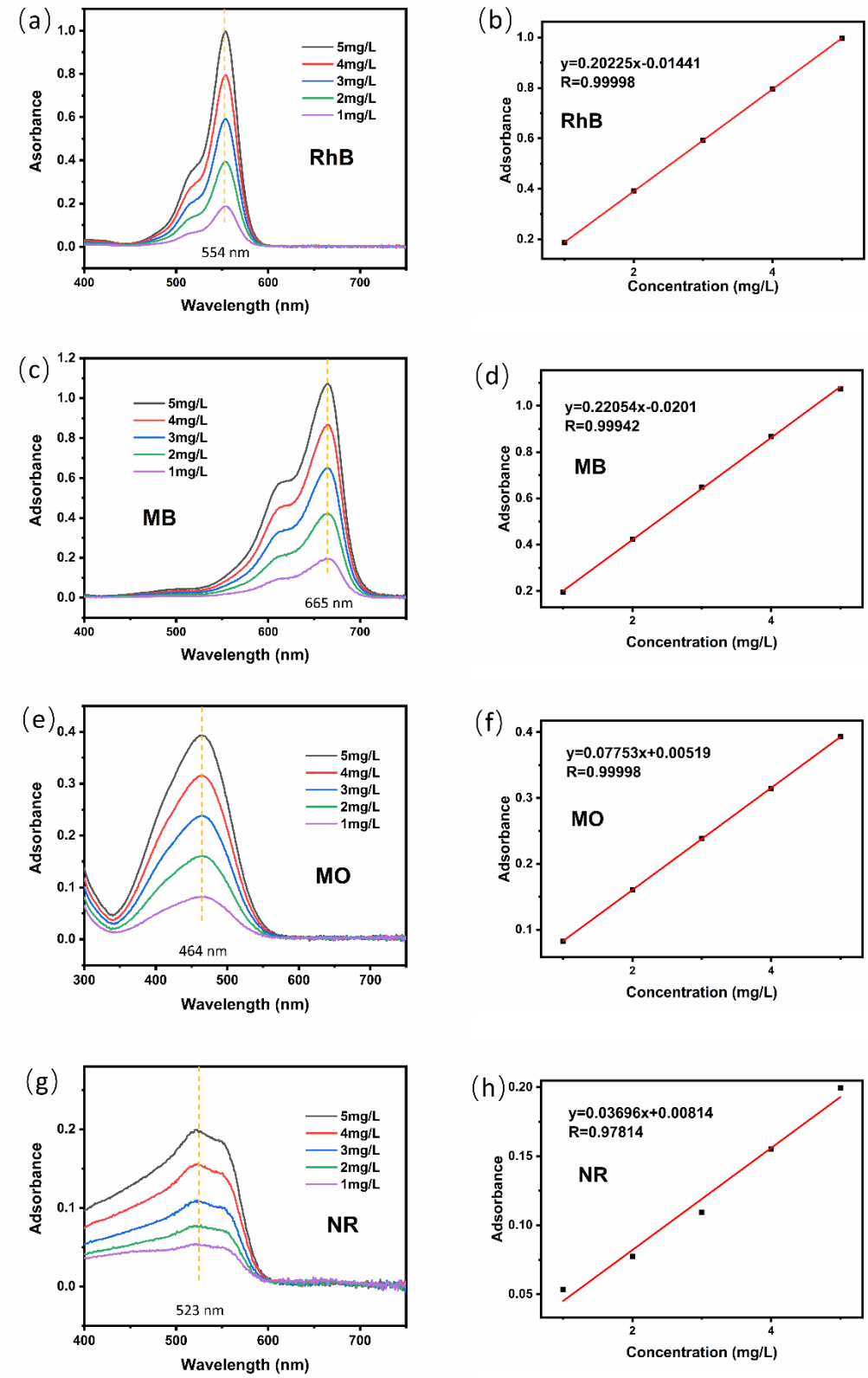


Figure 4-7: The standard curves of four dyes such as RhB, MO, MB and NR and the fitted equations

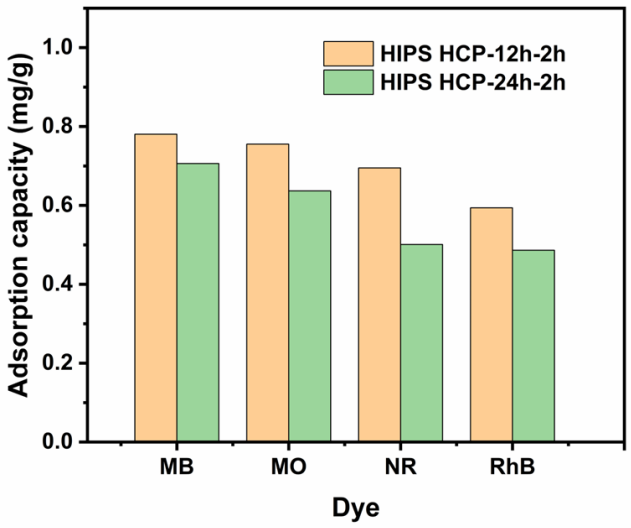


Figure 4-8: The capacity of HIPS HCP-12h-2h and HIPS HCP-24h-2h monoliths towards five dyes

### 4.3.3 Taxadiene adsorption

Typically, a clear positive correlation exists between the performance of the adsorbents and their specific surface areas, signifying materials with high specific surface areas usually have better adsorption capacity. We have proved that HIPS HCP monoliths are eligible for selective removal of oils and dyes respectively despite the capacities are not competitive. This is due to its relatively low BET surface areas. To further explore the application of HIPS HCP monoliths, we employed them in the adsorption of larger bio-molecules such as taxadiene.

Taxadiene is a natural organic compound that belongs to the class of diterpenoids. It is a precursor in the biosynthesis of paclitaxel (Taxol®), which is an important anticancer drug [26,27]. The majority of terpenoids exhibit hydrophobic characteristics and can often reach toxic levels for heterologous hosts at concentrations that are feasible for industrial purposes. To mitigate the harmful impact of terpenoids on the host, one possible approach is the implementation of an in-situ product recovery method, which allows for the retrieval of terpenoids. By employing in-situ extraction, the process of removing terpenoids from the cultivation medium can be carried out simultaneously with their production. This approach effectively reduces the build-up

of terpenoids, minimises product loss, and helps prevent cell death. Jorge et al. reported the in-situ solid-liquid extraction of taxadiene using commercial HP-20 beads [28]. Here, the recovery of taxadiene could be realised with HIPS HCP-12h-2h monoliths as adsorbents using the same protocol. The control group represented the taxadiene yielded without any solid adsorbents in the cultivation process. With the in-situ adsorption proceeding, the taxadiene produced in the fermentation was adsorbed promptly so that the concentration of taxadiene in the liquid phase remained low. Therefore, it tended to produce more taxadiene according to the chemical equilibrium theory.

As shown in the Figure 4-9a, taxadiene yield increased from 26.2 mg $L^{-1}$ to 39.6 mg $L^{-1}$ after adding HIPS HCP-12h-2h monoliths as adsorbents in the flask, marking an increase of nearly 51% compared to that of the control group. This proved that timely removal of generated taxadiene in the liquid phase could effectively promote the output of target product. Moreover, the existence of HIPS HCP-12h-2h monoliths led to the slight decrease of solid biomass, reduced by 4.9%, which is negligible compared with the increment of taxadiene yield. Taxadiene adsorption of the commercial HP-20 resin (SA: 850-1000 $m^2$ $g^{-1}$) beads is around 60 mg $L^{-1}$ [28] , while that of our structure-retained HCP-HIPS-12h-2h monoliths (SA: 337 $m^2$ $g^{-1}$) is around 20 mg $L^{-1}$. Therefore, the adsorption performance of HCP-HIPS monoliths towards taxadiene are comparable to commercial materials.

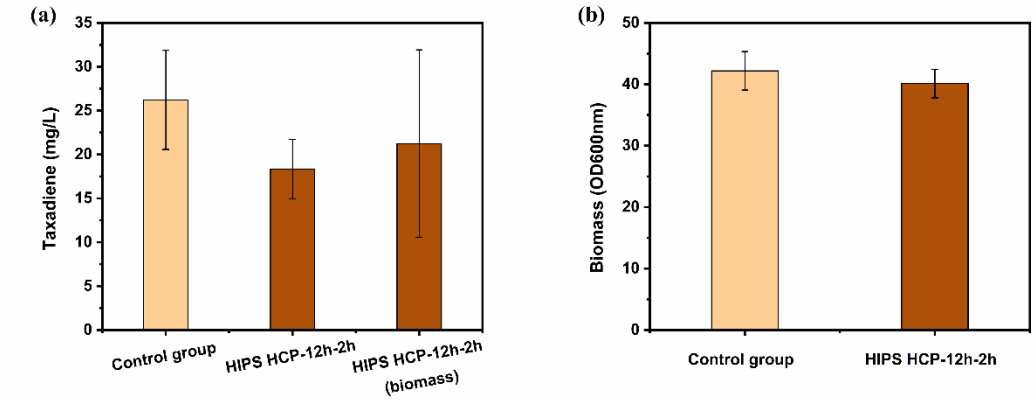


Figure 4-9: The recovery of taxadiene using HIPS-HCP-12h-2h monoliths

## 4.4 Conclusion

In this work, structure-retained porous HIPS HCPs have been successfully synthesised via 3D printing and stepwise hypercrosslinking reactions. By adjusting the reaction durations of two-step hypercrosslinking process, I managed to find a middle state to overcome the trade-off effect between mechanical strength and microporosity. This strategy pointed out a controllable and mass-produced method for processable HCPs, and overcame the shortcomings of limited application of powder HCPs. This method is expected to be potentially compatible for broader applications due to its tunable porosity, surface area and even surface chemical functionalization. Moreover, the shape of porous monoliths can be customised via 3D printing to satisfy different applying requirements and even large-scale production. HIPS HCP-12h-2h monoliths demonstrated a recovery capacity for biomolecules such as taxadiene, which is on par with that of commercial adsorbents like HP-20 resins. This indicated that 3D-printed porous monoliths have great potential for biomolecules adsorption. On top of that, functionalised PS-based filaments are expected to be produced into hypercrosslinked porous monoliths using the same method and further broaden their application in separating specific molecules.

## 4.5 References


[1] Wood, C.D., et al., *Hydrogen storage in microporous hypercrosslinked organic polymer networks.* Chemistry of materials, 2007. **19**(8): p. 2034-2048.

[2] Chakraborty, S., et al., *Hierarchically porous organic polymers: highly enhanced gas uptake and transport through templated synthesis.* Chemical science, 2015. **6**(1): p. 384-389.

[3] Yang, X., et al., *Hypercrosslinked microporous polymers based on carbazole for gas storage and separation.* Rsc Advances, 2014. **4**(105): p. 61051-61055.

[4] Zhang, C., et al., *Triptycene-based hyper-cross-linked polymer sponge for gas storage and water treatment.* Macromolecules, 2015. **48**(23): p. 8509-8514.

[5] Hu, A., et al., *Magnetically hyper-cross-linked polymers with well-developed mesoporous: a broad-spectrum and highly efficient adsorbent for water purification.* Journal of Materials Science, 2019. **54**: p. 2712-2728.

[6] Sheng, Q., W. Tian, and C.D. Wood, *Hyper-cross-linked polymer-decorated surfaces with ultrahigh efficiency for oil/water emulsion separation and recovery.* ACS Applied Materials & Interfaces, 2021. **13**(33): p. 39925-39933.

[7] Huang, J. and S.R. Turner, *Hypercrosslinked polymers: a review.* Polymer Reviews, 2018. **58**(1): p. 1-41.

[8] Tan, L. and B. Tan, *Hypercrosslinked porous polymer materials: design, synthesis, and applications.* Chemical Society Reviews, 2017. **46**(11): p. 3322-3356.

[9] Davankov, V., V. Rogozhin, and M. Tsjurupa, *Macronet polystyrene structures for ionites and method of producing same*. 1973, Google Patents.

[10] Li, B., et al., *A new strategy to microporous polymers: knitting rigid aromatic building blocks by external cross-linker.* Macromolecules, 2011. **44**(8): p. 2410-2414.

[11] Bandyopadhyay, S., et al., *Fabrication of porous organic polymers in the form of powder, soluble in organic solvents and nanoparticles: a unique platform for gas adsorption and efficient chemosensing.* Polymer Chemistry, 2015. **6**(20): p. 3775-3780.

[12] Patra, A. and U. Scherf, *Fluorescent microporous organic polymers: potential testbed for optical applications.* Chemistry–A European Journal, 2012. **18**(33): p. 10074-10080.

[13] Qiao, Z.-A., et al., *Polymeric molecular sieve membranes via in situ cross-linking of non-porous polymer membrane templates.* Nature communications, 2014. **5**(1): p. 1-8.

[14] Liu, A., et al., *Photo-Modulating CO2 Uptake of Hypercross-linked Polymers Upcycled from Polystyrene Waste.* ChemSusChem, 2023: p. e202300019.

[15] Yang, X., et al., *Hierarchical porous polystyrene monoliths from polyHIPE.* Macromolecular rapid communications, 2015. **36**(17): p. 1553-1558.

[16] Su, Y., et al., *Hypercrosslinked Polymer Gels as a Synthetic Hybridization Platform for Designing Versatile Molecular Separators.* Journal of the American Chemical Society, 2022.

[17] Wang, S., et al., *Unprecedented processable hypercrosslinked polymers with controlled knitting.* Macromolecular Rapid Communications, 2022. **43**(2): p. 2100449.

[18] Maya, F. and F. Svec, *A new approach to the preparation of large surface area poly (styrene-co-divinylbenzene) monoliths via knitting of loose chains using external crosslinkers and application of these monolithic columns for separation of small molecules.* Polymer, 2014. **55**(1): p. 340-346.

[19] Lv, Y., et al., *Preparation of porous styrenics-based monolithic layers for thin layer chromatography coupled with matrix-assisted laser-desorption/ionization time-of-flight mass spectrometric detection.* Journal of Chromatography A, 2013. **1316**: p. 154-159.

[20] Liu, H., et al., *Stepwise Crosslinking: A Facile Yet Versatile Conceptual Strategy to Nanomorphology-Persistent Porous Organic Polymers.* Advanced Materials, 2017. **29**(27): p. 1700723.

[21] Lee, J., et al., *3D-printed monolithic porous adsorbents from a solution-processible, hypercrosslinkable, functionalizable polymer.* Chemical Engineering Journal, 2022. **427**: p. 130883.

[22] Sun, Q., et al., *Effect of processing conditions on the bonding quality of FDM polymer filaments.* Rapid prototyping journal, 2008. **14**(2): p. 72-80.

[23] Olmos, D., E. Martín, and J. González-Benito, *New molecular-scale information on polystyrene dynamics in PS and PS–BaTiO 3 composites from FTIR spectroscopy.* Physical Chemistry Chemical Physics, 2014. **16**(44): p. 24339-24349.

[24] Thommes, M., et al., *Physisorption of gases, with special reference to the evaluation of surface area and pore size distribution (IUPAC Technical Report).* Pure and applied chemistry, 2015. **87**(9-10): p. 1051-1069.

[25] Yang, B., et al., *Evaluation of activated carbon synthesized by one-stage and two-stage co-pyrolysis from sludge and coconut shell.* Ecotoxicology and environmental safety, 2019. **170**: p. 722-731.

[26] Wang, T., et al., *Recent research progress in taxol biosynthetic pathway and acylation reactions mediated by Taxus acyltransferases.* Molecules, 2021. **26**(10): p. 2855.

[27] Tong, Y., Y.F. Luo, and W. Gao, *Biosynthesis of paclitaxel using synthetic biology.* Phytochemistry Reviews, 2021: p. 1-15.

[28] Santoyo-Garcia, J.H., et al., *In situ solid-liquid extraction enhances recovery of taxadiene from engineered Saccharomyces cerevisiae cell factories.* Separation and Purification Technology, 2022. **290**: p. 120880.

# Chapter 5 Green HCPs synthesised in DESs

This work is published on Chemsuschem, named as 'Synthesizing Hypercrosslinked Polymers with Deep Eutectic Solvents to Enhance $CO_2/N_2$ Selectivity'. ( https://doi.org/10.1002/cssc.202301602 )

## 5.1 The intention and target of this project

In the last chapter, 3D-printing technology was integrated with 2-step hypercrosslinking reactions to produce porous structure-retained HIPS monoliths. This work proposed a practicable method to make multiple structure-defined porous monoliths for adsorption, contributing to the processability of HCPs effectively. However, one of the drawbacks of this work is the massive consumption of hazardous solvents which may impose a big burden on our living environment if commercial HCPs market expands. Currently, the global market for HCPs is expected to reach $2 billion by 2028 with the emergence of various HCPs reported [1]. This projected growth in HCP demand brings on an unexpected problem – the generation of hazardous solvent waste arising from using halogenated solvents during HCP synthesis.

The main synthesis approach for HCPs is underpinned by Friedel-Crafts alkylation where halogenated solvents such as dichloroethane (DCE), dichloromethane (DCM) and chloroform promote polymer crosslinking. A typical HCP synthesis protocol requires the use of halogenated solvents to initiate and promote the transfer of charged halides from Lewis acid catalysts such as $FeCl_3$, $AlCl_3$, $SnCl_4$ to link up substrates via the formation of methylene bridges using internal electrophiles or external crosslinkers. Depending on the substrate, HCP synthesis can be achieved by: (1) internal and (2) external crosslinking where electrophiles on the monomer and additional reagents are used for forming methylene bridges that link up monomers, respectively and (3) post-crosslinking where polymers are crosslinked *via* internal electrophiles [2].

Since 2007, the European Chemicals Agency has adopted the 'Registration, Evaluation, Authorisation and Restriction of Chemicals' (REACH) regulation to protect human health and the living environment from potential risks of chemicals. DCE, DCM and chloroform are regarded as carcinogenic and are 'substances of very high concern' [3,4]. In line with green chemistry concepts, the use of these solvents in HCP synthesis should be minimised by adopting feasible greener alternatives. Another potential source of environmental pollution arising from HCP synthesis lies in the use of $FeCl_3$, $AlCl_3$ and $SnCl_4$ where these Lewis acid catalysts could enter the water circulation system and be enriched in biosomes. Therefore, this chapter focus on seeking for sustainable solvents to substitute current halogenated solvents used in HCPs synthesis.

Overcoming the use of halogenated solvents and metal halide catalysts can potentially transform HCP synthesis into a sustainable process. For e.g., an approach that improves the sustainability of HCP synthesis is solvent-free mechanochemical synthesis [5]. However, this approach requires specialised equipment. Su and co-workers synthesised a HCP gel via thermal-induced polymerisation of a tetrahedral monomer bearing four maleimide pendant groups without using any catalysts and initiators [6]. This represents a breakthrough from the conventional HCP synthesis protocol. A limitation of this approach is the requirement of specific monomers. A more general strategy for sustainable HCP synthesis is replacing metal halide Lewis acid catalysts with metal-free Brønsted acids [7] where the catalysts can be recycled for subsequent HCP synthesis or replacing the halogenated solvent with sulfolane [8], an organosulfur solvent, commonly used in industrial chemical reactions. Considering safety, health, and environmental risks, sulfolane is less toxic than the frequently utilised DCE, as per guidelines for solvent selection [9]. This approach enhanced the sustainability of HCP synthesis and fine-tuned the pore structure for improved $CO_2$ capture.

As reviewed in the Chapter 2, deep eutectic solvents (DES) are regarded as perspective candidates for replacing hazardous halogenated solvents which are widely

used in chemical synthesis. Wang and co-workers deployed a range of DESs comprising choline chloride (ChCl) and various metal halides to catalyse reactions between aldehydes and electron-rich arenes to yield triarylmethanes and diarylalkanes via Friedel-Crafts alkylation [10]. This is the same chemistry underpinning polymer crosslinking in HCPs synthesis. As far as we know, there has been no reported research on synthesising HCPs in DESs. Inspired by their successful work in the organic small molecules, this project aims at expanding the application of DESs to the polymer chemistry and developing a versatile strategy for producing HCPs materials sustainably.

The DES deployed in HCP syntheses here were $[ChCl][ZnCl_2]_2$ and $[ChCl][FeCl_3]_2$. Although reports have shown that $[ChCl][ZnCl_2]_2$ is toxic for the aquatic environment [11], its toxicity is still 500-fold less than that of dichloroethane [12]. From this point, $[ChCl][ZnCl_2]_2$ can be regarded as a good substitute for dichloroethane (DCE) during organic synthesis. $ZnCl_2$ and $FeCl_3$ were preferred here as these metal halides are highly efficient for catalysing the polymer hypercrosslinking process. The metal halides functioned as both the HBD component of the solvent and as catalysts during Friedel-Crafts alkylation. In this project, the reliability of replacing halogenated solvents with greener DESs will be tested in both internal hypercrosslinking and external hypercrosslinking process. Bifunctional monomers such as α, α'-dichloro-p-xylene (DCX), 4,4′-bis(chloromethyl)-1,1′-biphenyl (BCMBP) were selected for internal hypercrosslinking. External hypercrosslinking, as a process which is friendly to a broad range of monomers, employed benzyl alcohol (BA), 1,3,5-triphenylbenzene (TPB) and triptycene as starting monomers and formaldehyde dimethyl acetal (FDA) as an external crosslinker. It is observed that the use of DES to synthesise HCPs reduced both pore volume and size when compared to HCPs yielded in DCE, as shown in Figure 5-1. However, the narrower pore size distribution was also key to increasing $CO_2/N_2$ selectivity from 14 to 105 at 273 K, demonstrating the advantage of synthesising HCPs in DES. I also exploited the water solubility of the DES components used here, ChCl and metal halides, to facilitate the post-treatment of

obtained HCPs products. Outcomes from this work can potentially open up new polymerisation applications for DESs and transform HCP synthesis into a more benign process.

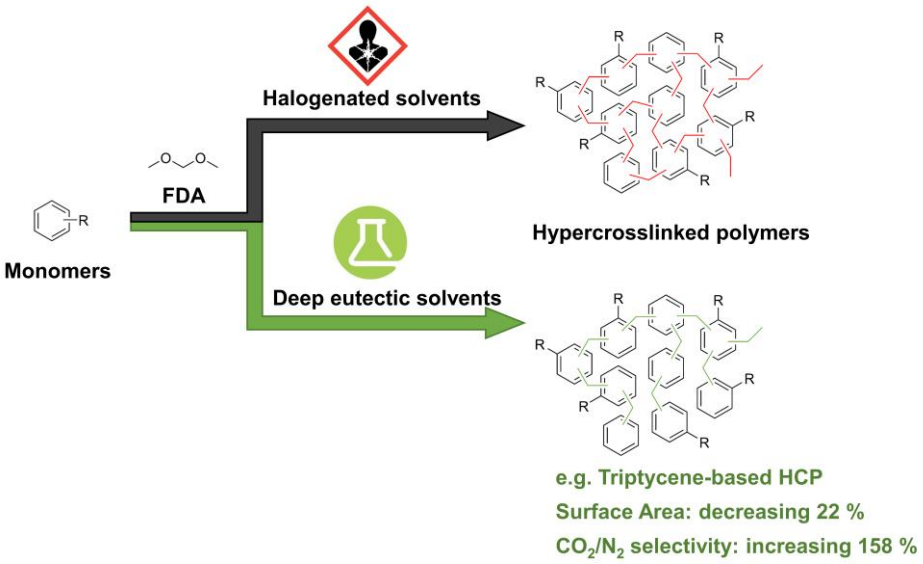


Figure 5-1: Synthetic process of HCPs and comparison between traditional halogenated solvents and sustainable DESs respectively

## 5.2 Results and discussion

### 5.2.1 HCPs synthesis via internal crosslinking with DES

HCP synthesis *via* internal crosslinking is limited to self-polymerising small molecules comprising bis(chloromethyl), bis(bromomethyl) and hydroxy groups [13]. Cooper and co-workers [14] reported that the Bruanuer-Emmett-Teller (BET) surface areas of HCPs derived from DCX and BCMBP in DCE and using $FeCl_3$ i.e., *p*-DCX and *p*-BCMBP reached 1431 and 1874 $m^2 \cdot g^{-1}$, respectively. As such, I chose these monomers to demonstrate the feasibility of HCP synthesis *via* internal crosslinking using $[ChCl][ZnCl_2]_2$ and $[ChCl][FeCl_3]_2$ DES. I synthesised a series of HCPs as a function of DES component molar ratio i.e., HBA: HBD and reaction time (Table 5-1).

Table 5-1: The results of HCPs formed in different DESs via internal hypercrosslinking

| Sample | Monomer | DES/Solvents | Temperature (°C) | Molar ratio | Reaction time | Surface area ($m^2 g^{-1}$) |
|---|---|---|---|---|---|---|
| 1 | DCX | [ChCl] $[ZnCl_2]_2$ | 100 | 1:28 | 24h | 106 |
| 2 | DCX | [ChCl] $[ZnCl_2]_2$ | 100 | 1:28 | 72h | 409 |
| 3 | DCX | [ChCl] $[ZnCl_2]_2$ | 100 | 1:50 | 24h | 477 |
| 4 | DCX | [ChCl] $[ZnCl_2]_2$ | 100 | 1:8 | 24h | 6 |
| 5 | DCX | [ChCl]$[FeCl_3]_2$ | 100 | 1:28 | 24h | 1.6 |
| 6 | DCX | [ChCl]$[FeCl_3]_2$ | 100 | 1:8 | 24h | 2.7 |
| 7 | DCX | [ChCl]$[FeCl_3]_2$ | 100 | 1:8 | 72h | 3.0 |
| 8 | DCX | DCE ($ZnCl_2$) | 100 | 1:3 | 24h | No product |
| 9 | DCX | DCE ($FeCl_3$) | 100 | 1:3 | 24h | 964 |
| 10 | BCMBP | [ChCl] $[ZnCl_2]_2$ | 100 | 1:28 | 24h | 35 |
| 11 | BCMBP | [ChCl] $[ZnCl_2]_2$ | 100 | 1:28 | 72h | 143 |
| 12 | BCMBP | DCE ($ZnCl_2$) | 100 | 1:3 | 24h | 852 |
| 13 | BCMBP | DCE ($FeCl_3$) | 100 | 1:3 | 24h | 1519 |

From these reactions, dark brown particulates that were insoluble in DCE, DCM, and chloroform were obtained. This indicated crosslinked DCX and BCMBP. This was validated with solid-state $^{13}C$ NMR analysis (Figure 5-2a, 5-3a). The $^{13}C$ NMR spectra of *p*-DCX and *p*-BCMBP contained characteristic peaks centered at 128 and 140 ppm, corresponding to non-substituted aromatic carbons and substituted aromatic carbons, respectively. The minor resonance around 50 ppm was correlated to chloromethylene carbons. Compared to the NMR spectrum of unreacted DCX monomers, we observed additional peaks at 36 and 66 ppm in the NMR spectra of *p*-DCX. The peak centered at 36 ppm indicated the presence of methylene bridges that linked up the aromatic rings of the substrates to form polymeric networks, while the peak at 66 ppm correlated to hydroxylmethyl carbons i.e., side products from hydrolysis of chloromethyl groups. Similarly, the peaks for chloromethylene carbons and methylene bridges in the NMR spectra of *p*-BCMBP were located around 45 and 38 ppm. These slight chemical shifts could be caused by the difference in the

proportions of di- and trisubstituted benzyl rings [15]. Compared to the NMR spectrum of *p*-DCX in DCE, the peak at 36 ppm of the same polymers yielded in DES studied here were less intense and broader. This could be attributed to lower crosslinking degree in HCPs synthesised in DESs. The lower crosslinking degree in DESs was further confirmed in the case of *p*-BCMBP as the spectrum of *p*-BCMBP in DCE barely displayed the peak of unreacted chloromethylene groups [16].

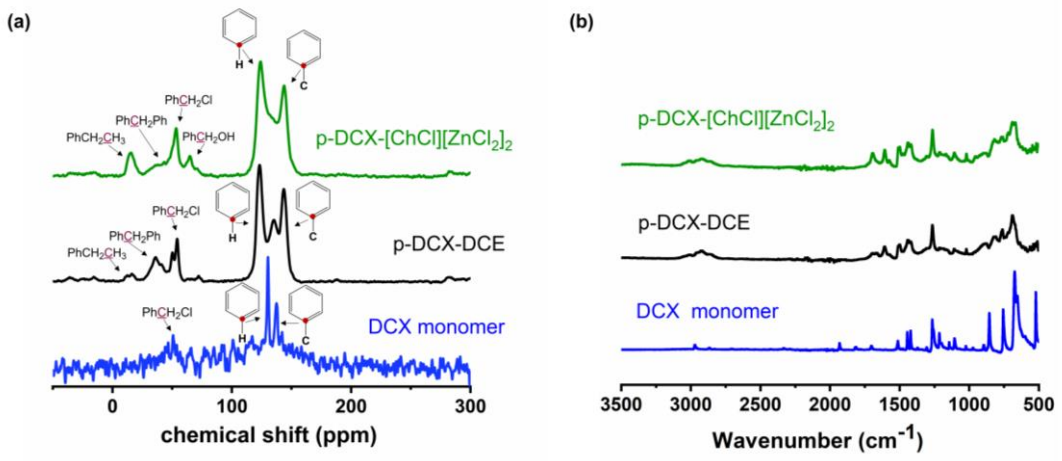


Figure 5-2: (a) NMR, and (b) FTIR spectra of DCX monomer (blue), *p*-DCX in $[ChCl][ZnCl_2]_2$ (green) and DCE (black) for 24h

The FTIR spectra of *p*-DCX and *p*-BCMBP that synthesised in DESs were similar to those produced in DCE (Figure 5-2b, 5-3b), indicating formation of methylene crosslinking bridges. There were several differences between the FTIR spectra of unreacted monomers and their corresponding polymers. New peaks centered at 2925 and 2853 $cm^{-1}$ in the spectra of *p*-DCX and *p*-BCMBP corresponded to stretching vibrations of methylene groups, bands around 1465 $cm^{-1}$ correlated to C-H bending vibrations of methylene groups and peaks at 1600, 1570 and 1500 $cm^{-1}$ were attributed to the stretching of aromatic C=C bonds. Meanwhile, the strong peak centered at 860 $cm^{-1}$ corresponding to the C-H bending vibrations from bis-substituted aromatic rings diminished upon polymerisation. Both NMR and FTIR analyses indicated the formation of multi-substituted aromatic rings linked by methylene bridges.

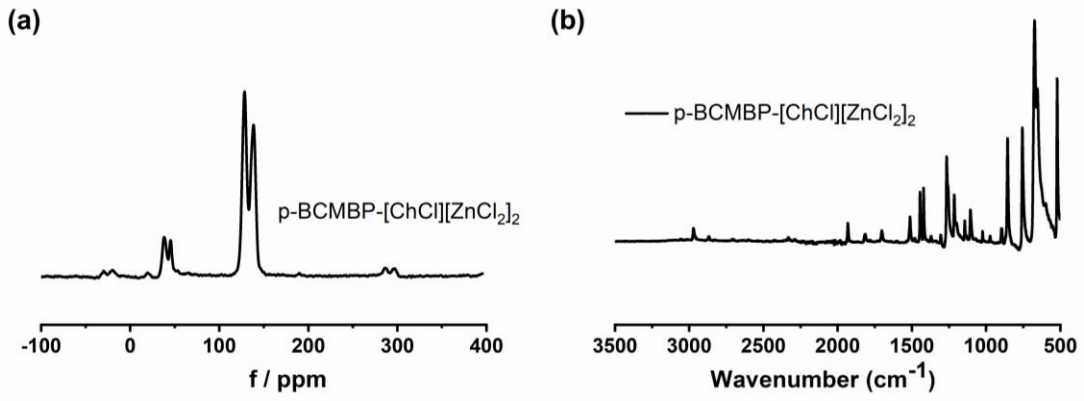


Figure 5-3: (a) $^{13}C$ NMR spectra of *p*-BCMBP synthesised in $[ChCl][ZnCl_2]_2$ for 24h, (b) FTIR spectra of *p*-BCMBP synthesised in $[ChCl][ZnCl_2]_2$ for 24h

I measured the nitrogen adsorption isotherms of *p*-DCX and *p*-BCMBP synthesised *via* internal crosslinking in $[ChCl][ZnCl_2]_2$ and $[ChCl][FeCl_3]_2$ at 77 K (Table 5-1). The BET surface areas of *p*-DCX and *p*-BCMBP synthesised in $[ChCl][FeCl_3]_2$ were negligible. This was despite varying monomer molar percentage, and reaction times, from 6.7 mol.% to 20 mol.%, and 24 h to 72 h, respectively. Meanwhile, the $N_2$ adsorption isotherms of HCPs synthesised in $[ChCl][ZnCl_2]_2$ corresponded to a Type I curve that is associated with microporous materials based on IUPAC classification [17], where we observed a steep rise of $N_2$ uptake at low relative pressure ($P/P_0 < 0.01$, Figure 5-4a), revealing the presence of abundant micropores [18]. We observed that increasing reaction time in $[ChCl][ZnCl_2]_2$, from 24 h to 72 h, enhanced BET surface areas of *p*-DCX by 4-fold, reaching 409 $m^2\ g^{-1}$. This was still 58 % lower than that of *p*-DCX synthesised in DCE catalysed by $FeCl_3$. I also synthesised *p*-DCX in DCE using $ZnCl_2$. However, the obtained solid products were easily dissolved in acetone, indicating that these were most likely to be lightly crosslinked oligomers. This could be ascribed to inferior catalytic effects of $ZnCl_2$ in halogenated solvents [19]. This was confirmed in the case of BCMBP-based HCPs that were synthesised in DCE using $ZnCl_2$ and $FeCl_3$ as catalysts. The BET surface areas of poly-BCMBP synthesised from $ZnCl_2$ and $FeCl_3$ reached 852 and 1519 $m^2\ g^{-1}$, respectively. These results

suggested that DCX is more reactive in $[ChCl][ZnCl_2]_2$ than in DCE when the same metal halide is used.

One reason why $ZnCl_2$-based DES was effective for HCP synthesis was the molar ratio between metal halide catalysts and substrate (3:1 in traditional protocols that use halogenated solvents, and 28:1 in our approach using DES). The molar ratio between metal halide: substrate not only impacted the polymerisation but also HCP BET surface areas. At molar ratio 8:1, there were insufficient metal halides and excessive substrates in the DES, impeding monomer dissolution and subsequent crosslinking reactions. Increasing the metal halide: substrate molar ratio to 50:1, the BET surface area of the resultant *p*-DCX further increased to 477 $m^2$ $g^{-1}$. This meant that more metal halides were available for promoting crosslinking, and this was as effective as prolonging the reaction time. At the same synthetic conditions, the BET surface area of *p*-BCMBP-72h was 66% lower than that of *p*-DCX-72h, reaching only 143 $m^2$ $g^{-1}$. This value was only 17% of that of *p*-BCMBP synthesised in DCE catalysed by $ZnCl_2$. This differed from the trends observed in the work of Cooper and co-workers [14] where the BET surface areas of BCMBP-based networks were 24% higher than DCX-based networks as BCMBP molecules were more likely to construct rigid para geometry between aryl rings that generated more porosity in halogenated solvents. The reactivity of monomers varies in the DCE and DES, which cannot be predicted accurately based on prior knowledge.

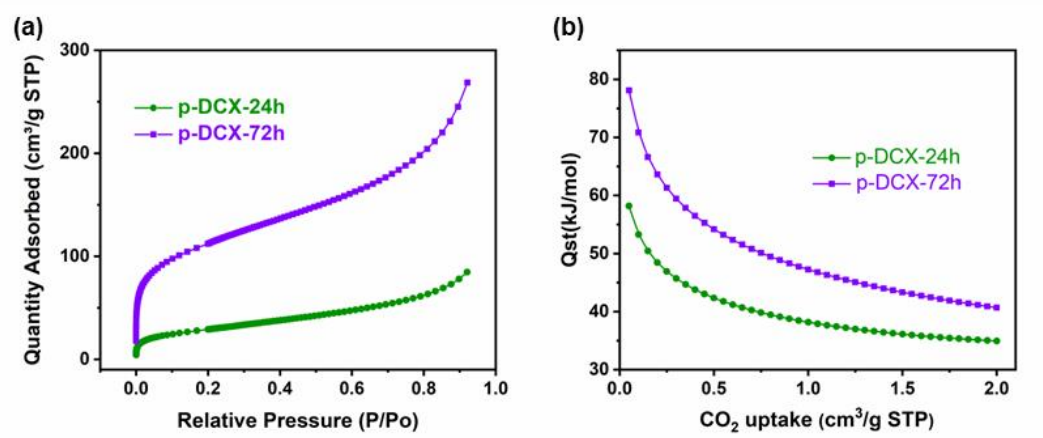


Figure 5-4: (a) $N_2$ isotherms (under 77 K) of *p*-DCX HCPs synthesised in $[ChCl][ZnCl_2]_2$ for 24h and 72h respectively, (b) Isosteric heat of adsorption for $CO_2$ calculation in *p*-DCX HCPs

It was observed that *p*-DCX-72h led to higher $CO_2$ uptakes and $CO_2/N_2$ selectivity when compared to *p*-DCX-24h (Figure 5-5a, b). At 273 K, the $CO_2$ uptake of *p*-DCX-72h reached 28 $cm^3\ g^{-1}$, more than double of that of *p*-DCX-24h. Here we used the ideal adsorption solution theory (IAST) to determine the $CO_2/N_2$ of these HCPs using a gas mixture comprising 15 % $CO_2$ and 85 % $N_2$ (more details of fitting parameters were shown in Table 5-3). At 100 kPa and 273 K, the $CO_2/N_2$ selectivity of *p*-DCX-72h reached 105, more than 7 times that of *p*-DCX-24h and 5.5-fold higher than that of *p*-DCX synthesised in DCE despite the $CO_2$ uptake of the latter *p*-DCX type reached 76 $cm^3\ g^{-1}$ [20]. Interestingly, the $CO_2/N_2$ selectivity of *p*-DCX-72h started to increase after P>20 kPa as the effective kinetic diameter of $CO_2$ (3.3 Å) is smaller than that of $N_2$ molecules (3.8 Å). This is consistent with the previous findings that the adsorbed amounts of binary gas mixture are dominated by the adsorption strength of the individual species under dilute concentrations while the adsorption selectivity shifts toward the smaller molecules at high pressure [21]. The pore size distributions of *p*-DCX synthesised in $[ChCl][ZnCl_2]_2$ showed that the proportion of micropores (between 0 – 2 nm) in HCPs synthesised over 72 hours was significantly higher than those produced over 24 hours (Figure 5-5c). These micropores were mainly centred at 0.67, 0.98, and 1.3 nm. This could be attributed to the significant increase in the reaction time, which enabled the formation of ultra-micropores. Compared with *p*-

DCX synthesised in DCE using traditional method, *p*-DCX-72h synthesised in $[ChCl][ZnCl_2]_2$ demonstrated a higher abundance of micropores. This is evident from the fact that in *p*-DCX-DCE, the first peak emerged at approximately 1.75 nm.

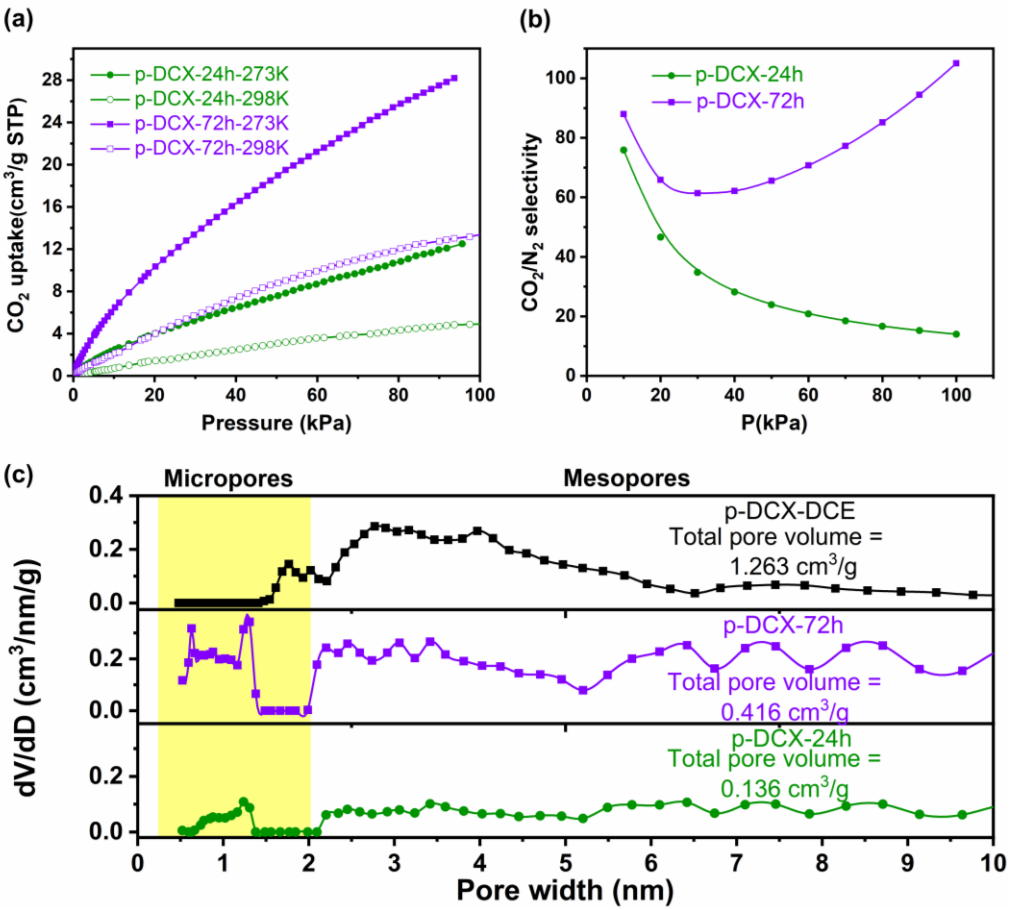


Figure 5-5: (a) $CO_2$ uptake of *p*-DCX-24h and *p*-DCX-72h that synthesised in $[ChCl][ZnCl_2]_2$, the isotherms were obtained under 273 K and 298 K, (b) $CO_2/N_2$ selectivity of *p*-DCX HCPs at 273 K calculated using the IAST theory ($CO_2$: $N_2$ = 15: 85), (c) Comparison of the pore size distributions of *p*-DCX HCPs synthesised in DCE and $[ChCl][ZnCl_2]_2$ for 24h and 72h respectively

Table 5-2 compared the textural properties of HCPs synthesised in DES systems and DCE respectively. In the *p*-DCX-DCE, micropores only accounted for 3.38% while this proportion was improved greatly in *p*-DCX-24h and *p*-DCX-72h, reaching 17.79% and 27.96% respectively. Per the previous study, there is a corresponding increase in the BET surface area with the degree of crosslinking intensifying, primarily ascribed to the formation of pore [22,23]. Despite *p*-DCX HCPs synthesised in DES have inferior surface area, they demonstrated their superiority in the formation of narrower

micropores. I also observed the presence of mesopores and macropores, confirming hierarchical porosity in these materials [24]. The substantial difference in micropore distribution between HCPs synthesised using DCE and DES could come from the different reaction kinetics. In conventional batch synthesis of HCPs with DCE solvents, crosslinking reactions are typically completed within two hours, leading to the fast development of irregular linking bridges between intermolecular polymer chains[25].

Table 5-2: Textural properties (calculated from $N_2$ isotherms at 77K) of six selected HCPs

| Sample | BET SA ($m^2$ $g^{-1}$) | DFT total pore volume ($cm^3$ $g^{-1}$) | DFT micro-pore volume [a] ($cm^3$ $g^{-1}$) | Micro-porosity |
|---|---|---|---|---|
| *p*-DCX-DCE | 964 | 1.263 | 0.0427 | 3.38% |
| *p*-DCX-24h | 106 | 0.136 | 0.0242 | 17.79% |
| *p*-DCX-72h | 409 | 0.416 | 0.1163 | 27.96% |
| *p*-triptycene-DCE | 1502 | 0.936 | 0.4759 | 50.84% |
| *p*-triptycene-24h | 969 | 0.677 | 0.3441 | 50.83% |
| *p*-triptycene-72h | 611 | 0.403 | 0.2387 | 59.23% |

[a] DFT micro-pore volume data was generated from the cumulative pore volume of the pore size up to 2 nm

In the case of DES reacting system, slower reaction rate is favorable for the establishment of micropores. These data provide valuable insights into the intricate process of porosity development within HCPs. They suggest that porosity in HCPs is a sequential process where micropores are developed first and specific experimental conditions affect the creation of these micropores. Generally, the higher BET surface area and narrower pore size distribution of *p*-DCX-72h contribute to its higher $CO_2$ uptakes and superior $CO_2/N_2$ selectivity. The isoteric heat (Qst) of $CO_2$ adsorption in *p*-DCX synthesised in DES here was reduced with an increase in the amount of $CO_2$ adsorbed (Figure 5-4b), suggesting that adsorption sites were heterogenous [26,27]. We also observed a 20 kJ $mol^{-1}$ enhancement in isosteric heat of $CO_2$ adsorption as synthesis time increased from 24 to 72 hours, which was consistent with the

observation of increased porosity. Higher Qst value indicated stronger interaction between $CO_2$ molecules and adsorption sites, benefitting $CO_2/N_2$ adsorption [28,29].

Table 5-3: Fitted Parameters of $CO_2$ and $N_2$ adsorption isotherms using SSLF model under 273 K

| Sample | adsorbate | q | b | n | $R^2$ |
|---|---|---|---|---|---|
| *p*-DCX-24h | $CO_2$ | 71.02477 | 0.00525 | 0.80539 | 0.99916 |
| *p*-DCX-24h | $N_2$ | 68.04976 | 2.2058E-7 | 2.4156 | 0.98620 |
| *p*-DCX-72h | $CO_2$ | 155.8088 | 0.00755 | 0.74375 | 0.99996 |
| *p*-DCX-72h | $N_2$ | 4.04067 | 5.92132E-7 | 3.22163 | 0.99892 |

### 5.2.2 HCPs synthesis via external crosslinking with DES

For external crosslinking in $[ChCl][ZnCl_2]_2$ and $[ChCl][FeCl_3]_2$, we used benzyl alcohol (BA), 1,3,5-triphenylbenzene (TPB) and triptycene as substrates as these monomers yield highly porous HCPs [30] when FDA was deployed as an external crosslinking reagent. The variations of synthesis parameters – reaction duration, molar ratio of substrate: crosslinker: catalyst are listed in Table 5-4. Generally, $[ChCl][FeCl_3]_2$ was a better medium for external crosslinking of monomers, where HCPs could be synthesised at lower temperatures and over shorter durations. Amongst them, triptycene proved to be the most active where surface areas of *p*-triptycene reached 969 $m^2 g^{-1}$, the highest amongst all HCPs studied in this work.

Table 5-4: The results of polymers formed in different DESs via external hypercrosslinking

| Sample | Monomer | Crosslinker | DES/Solvents | Temperature (°C) | Molar ratio | Reaction time | Surface area ($m^2 g^{-1}$) |
|---|---|---|---|---|---|---|---|
| 1 | TPB | FDA | $[ChCl][ZnCl_2]_2$ | 100 | 1:8:8 | 24h | No product |
| 2 | TPB | FDA | $[ChCl][ZnCl_2]_2$ | 150 | 1:8:8 | 24h | No product |
| 3 | TPB | FDA | $[ChCl][ZnCl_2]_2$ | 180 | 1:8:8 | 24h | 44 |
| 4 | TPB | FDA | $[ChCl][FeCl_3]_2$ | 100 | 1:8:8 | 24h | 9 |
| 5 | TPB | FDA | $[ChCl][FeCl_3]_2$ | 150 | 1:8:8 | 24h | 172 |
| 6 | TPB | FDA | $[ChCl][FeCl_3]_2$ | 100 | 1:8:8 | 72h | 4 |
| 7 | TPB | FDA | DCE($FeCl_3$) | 80 | 1:9:9 | 24h | 1418 |
| 8 | Triptycene | FDA | $[ChCl][ZnCl_2]_2$ | 100 | 1:8:8 | 24h | No product |
| 9 | Triptycene | FDA | $[ChCl][ZnCl_2]_2$ | 180 | 1:8:8 | 24h | 426 |
| 10 | Triptycene | FDA | $[ChCl][FeCl_3]_2$ | 100 | 1:8:8 | 6h | 588 |
| 11 | Triptycene | FDA | $[ChCl][FeCl_3]_2$ | 100 | 1:8:8 | 12h | 770 |
| 12 | Triptycene | FDA | $[ChCl][FeCl_3]_2$ | 100 | 1:8:8 | 24h | 969 |
| 13 | Triptycene | FDA | $[ChCl][FeCl_3]_2$ | 100 | 1:8:8 | 72h | 611 |
| 14 | TPB,Triptycene (1:1) | FDA | $[ChCl][FeCl_3]_2$ | 100 | 1:8:8 | 24h | 121 |
| 15 | Triptycene | FDA | DCE($FeCl_3$) | 80 | 1:3:3 | 24h | 1469 |
| 16 | BA | FDA | $[ChCl][ZnCl_2]_2$ | 150 | 1:8:8 | 24h | 245 |
| 17 | BA | FDA | $[ChCl][FeCl_3]_2$ | 150 | 1:8:8 | 24h | 384 |

Solid state $^{13}C$ NMR analyses showed that the chemical structures of *p*-triptycene synthesised in $[ChCl][FeCl_3]_2$ over 24 and 72 hours were similar (Figure 5-6a). We observed two intrinsic peaks corresponding to protonated aromatic carbons (125 ppm) and substituted aromatic carbons (144 ppm) in the NMR spectra of triptycene monomers. In the $^{13}C$ NMR spectrum of *p*-triptycene, I also observed an additional peak centered at 36 ppm that could be attributed to methylene bridge carbons, indicating that crosslinking of triptycene in $[ChCl][FeCl_3]_2$ was feasible. Furthermore, the carbon resonance signals at 49 and 65 ppm were correlated to chloromethyl

carbons and hydromethyl groups, indicating that chloromethylation and hydrolysis side reactions might occur during HCP formation, respectively. I also compared the FTIR spectra of triptycene monomer, *p*-triptycene synthesised in $[ChCl][FeCl_3]_2$ and DCE (Figure 5-6b). The spectra of *p*-triptycene synthesised in $[ChCl][FeCl_3]_2$ and DCE were consistent. The broad peak around 3450 $cm^{-1}$ was attributed to the stretching vibrations of water in the sample. The peak centered at 1460 $cm^{-1}$ could be attributed to C-H bending vibrations of methylene groups, revealing the successful formation of crosslinks comprising methylene bridges.

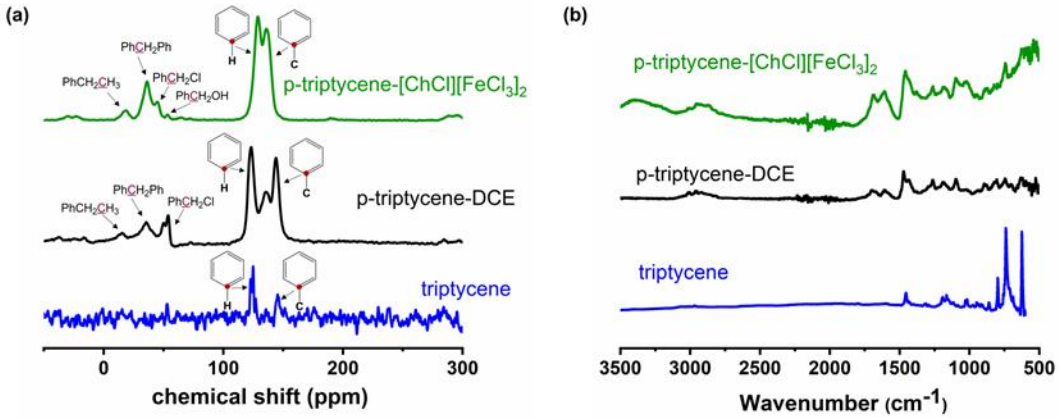


Figure 5-6: (a) NMR, and (b) FTIR spectra of triptycene monomer (blue), *p*-triptycene synthesised in $[ChCl][FeCl_3]_2$ (green) and DCE (black) for 24h

The $N_2$ adsorption isotherms of *p*-triptycene synthesised in $[ChCl][FeCl_3]_2$ (Figure 5-7a) exhibited a rapid rise under low relative pressure, suggesting the presence of significant micropores in these HCPs. The BET surface areas of *p*-triptycene HCPs increased by 65%, from 588 $m^2\ g^{-1}$ to 969 $m^2\ g^{-1}$, as synthesis duration increased from 6 to 24 hours. As reaction time was further increased to 72 hours, the BET surface area was reduced by 37 %, reaching 611 $m^2\ g^{-1}$. This trend reverse can be attributed to the excessively hypercrosslinking in the HCPs, leading to the partial collapse of micro- and mesopores [31,32]. It indicated that triptycene is a more reactive monomer comparing to DCX as it can be fully hypercrosslinked within 72 hours while DCX needs even more time. Apart from this turning point, the trends in BET surface areas and pore size distributions of *p*-triptycene were similar to those of *p*-DCX and *p*-

BCMBP synthesised in [ChCl][$ZnCl_2$]$_2$ via internal crosslinking. This was also why the $CO_2$ uptake of *p*-triptycene-24h reached 64 $cm^3$ $g^{-1}$ at 273 K, the highest amongst all HCPs studied in this work (Figure 5-8a).

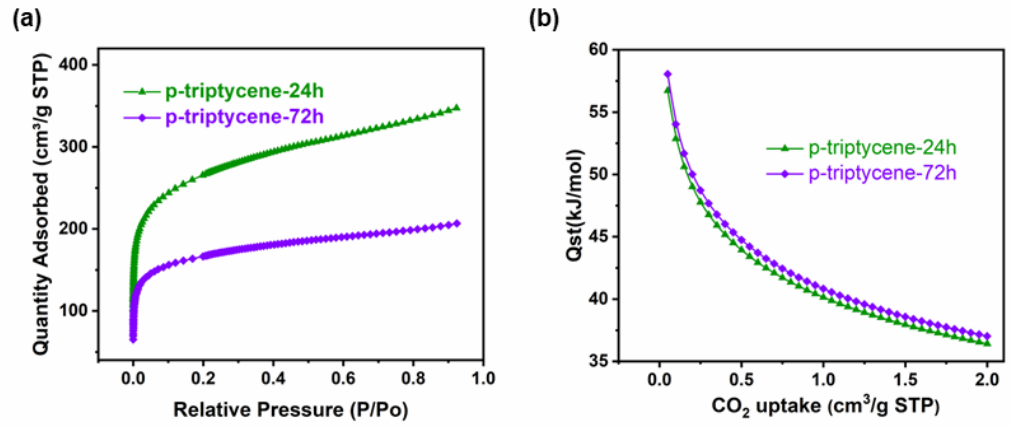


Figure 5-7: (a) $N_2$ isotherms (under 77 K) of *p*-triptycene HCPs synthesised in [ChCl][$FeCl_3$]$_2$ for 24h and 72h respectively, (b) Isosteric heat of adsorption for $CO_2$ calculation in *p*-triptycene

However, the $CO_2/N_2$ selectivity of *p*-triptycene-24h increased with the increasing pressure. This abnormal trend could be attributed to the inaccurate Langmuir equation that failed to fully fitted the whole $N_2$ isotherm (Table 5-5), bringing errors to consequent IAST selectivity calculations [21]. Despite all hypercrosslinked *p*-triptycene have hierarchical porosity, we emphasised on the microporous regime as it is crucial for $CO_2/N_2$ separation. The $CO_2/N_2$ selectivity of *p*-triptycene-24h at 273 K (based on IAST theory and a gas mixture comprising 15% $CO_2$ and 85% $N_2$) was 13% lower than those of *p*-triptycene-72h at 100 kPa (Figure 5-8b). This can be explained by narrower micropore size distribution of *p*-triptycene-72h of which micropores centred at 0.61, 0.85 and 1.85 nm (Figure 5-8c), contributing to its better $CO_2/N_2$ selectivity. Comparatively, the micropores of *p*-triptycene-24h mostly distributed around 0.52, 1.02, 1.23 and 1.98 nm. It meant narrower pores in *p*-triptycene were more likely to be retained when excessive hypercrosslinking took place. As for *p*-triptycene-DCE, it had adequate mesopores centred around 3.8 nm in addition to abundant micropores that centred around 0.53, 1.4 and 1.74 nm. By calculating the micro-porosity of the three *p*-triptycene HCPs, *p*-triptycene-72h exhibited the highest

value up to 59.23% despite its reduced total pore volume. These results reflected findings from an earlier work where it was shown that high BET surface areas do not necessarily correlate to high $CO_2/N_2$ selectivities [33]. Instead, a trade-off effect between $CO_2$ uptake and $CO_2/N_2$ selectivity existed in most porous materials i.e., increased $CO_2$ selectivity is usually accompanied with lower $CO_2$ uptake, consistent with the behavior of *p*-triptycene-72h [34]. The $CO_2/N_2$ selectivities of *p*-triptycene-24h and *p*-triptycene-72h reached 99 and 75, respectively, higher than those produced in halogenated solvents (52) [35]. Overall, the findings of external hypercrosslinking are consistent with the results we summarized from internal hypercrosslinking. It means DES reaction systems excel in yielding narrower pore structures and thus enhancing gas selectivity. Moreover, excessive cross-linking is not inherently undesirable because it can be fine-tuned to create narrower pores as required. The isosteric heat of $CO_2$ adsorption (Qst) of *p*-triptycene-24h and *p*-triptycene-72h (Figure 5-7b) were similar, with Qst of the latter material 2.3% higher, conforming to its better $CO_2/N_2$ selectivity.

Table 5-5: Fitted Parameters of $CO_2$ and $N_2$ adsorption isotherms using SSLF model under 273 K

| Sample | adsorbate | q | b | n | $R^2$ |
|---|---|---|---|---|---|
| *p*-triptycene-24h | $CO_2$ | 160.36514 | 0.01968 | 0.77225 | 0.99992 |
| *p*-triptycene-24h | $N_2$ | 35.71487 | 0.00454 | 0.75876 | 0.99102 |
| *p*-triptycene-72h | $CO_2$ | 128.34969 | 0.02577 | 0.7374 | 0.99986 |
| *p*-triptycene-72h | $N_2$ | 59.15863 | 0.00143 | 0.80432 | 0.97630 |

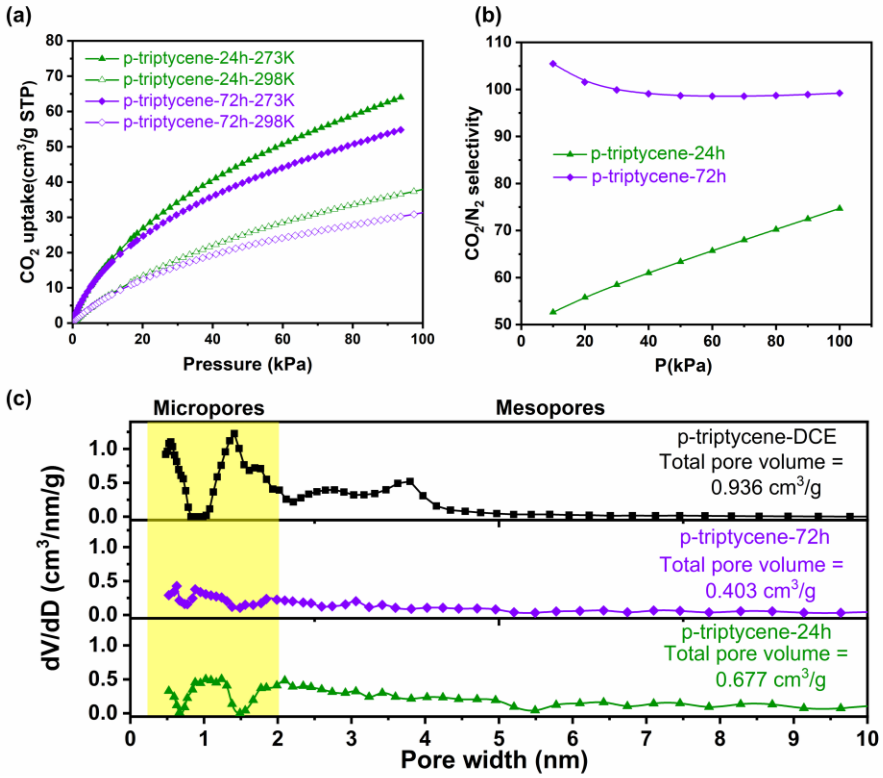


Figure 5-8: (a) $CO_2$ uptake of *p*-triptycene-24h and *p*-triptycene-72h that synthesised in $[ChCl][FeCl_3]_2$, the isotherms were obtained under 273 K and 298 K, (b) $CO_2/N_2$ selectivity of *p*-triptycene HCPs at 273 K calculated using the IAST theory ($CO_2$: $N_2$ = 15: 85), (c) Comparison of the pore size distributions of *p*-triptycene HCPs synthesised in DCE and $[ChCl][FeCl_3]_2$ for 24h and 72h respectively

TPB monomer can also be crosslinked using the same synthetic conditions at 100 °C (Table 5-4) but the BET surface areas of *p*-TPB synthesised in DESs were negligible. This was despite record BET surface areas of *p*-TPB based HCPs synthesised in halogenated solvents (1700 to 2400 $m^2$ $g^{-1}$) [36]. A comparison between the FTIR spectrum of *p*-TPB prepared in $[ChCl][FeCl_3]_2$ with that of TPB monomer (Figure 5-9) showed that these spectra were identical with a few new, but subtle peaks appearing after Friedel-Crafts alkylation. Peaks above 3000 $cm^{-1}$ could be assigned to stretching vibrations of aromatic C-H bonds, while peaks around 1593, 1485 $cm^{-1}$ were correlated to aromatic C=C stretching. Both spectra also contained characteristic adsorption bands at 876, 747 and 683 $cm^{-1}$ that corresponded to C-H bending vibrations, indicating the presence of 1,3,5-trisubstituted benzene rings. Unlike the FTIR spectra of *p*-TPB synthesised in DCE, the absence of a peak at 1465 $cm^{-1}$ that was correlated to C-H bending vibrations of methylene groups indicated minimal

crosslinking of TPB in DESs. When we increased the reaction temperature to 150 °C, we obtained microporous *p*-TPB with BET surface areas reaching 172 $m^2$ $g^{-1}$. This meant that TPB monomer could be crosslinked into HCPs in DESs, but at higher temperatures i.e., TPB was less reactive than triptycene. A possible explanation for this contrasting effect of crosslinking triptycene and TPB in DESs could be due to their chemical structures. Triptycene has a paddle wheel structure while TPB is a planar molecule [35,37].

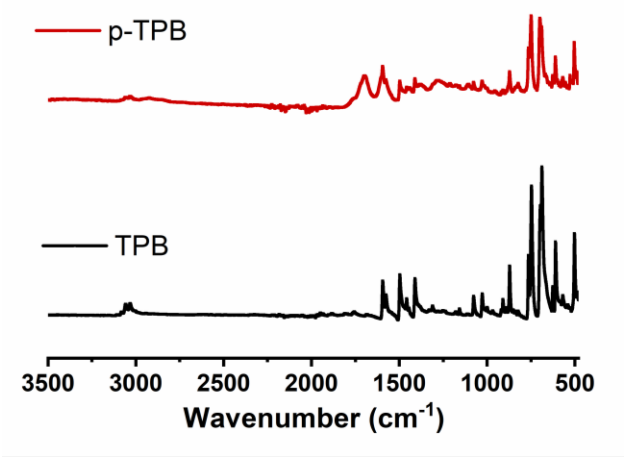


Figure 5-9: FTIR spectra of TPB monomer and *p*-TPB synthesised in $[ChCl][FeCl_3]_2$

To verify this hypothesis, I attempted to synthesise HCPs using equimolar amounts of TPB and triptycene as co-monomers (sample 14 in Table 5-4). By replacing 50 mol.% of triptycene with TPB, the BET surface area of these copolymerised HCPs only reached 121 $m^2$ $g^{-1}$, an 88% reduction when compared to that of *p*-triptycene (969 $m^2$ $g^{-1}$). This suggested that TPB hindered the formation of porous HCPs, and a reactive substrate was required for HCP synthesis in DESs. I also successfully synthesised *p*-BA, but at a higher temperature of 150 °C, in both $[ChCl][ZnCl_2]_2$ and $[ChCl][FeCl_3]_2$ where BET surface areas reached 245 and 384 $m^2$ $g^{-1}$, respectively. These results elucidated that DESs evaluated in this work were applicable for crosslinking different monomers while the specific reaction conditions depended on monomer reactivity. Adjusting reaction temperature and reaction time could be exploited to tailor the (micro)porosity of HCPs.

### 5.2.3 Impacts of textual properties on $CO_2$ uptake and selectivity

HCPs synthesised in DES systems highlighted their supremacy in the formation of narrower micropores, benefitting the adsorption of $CO_2$ molecules. Here, I selected six typical HCPs and compared their performance in $CO_2$ uptake and $CO_2/N_2$ selectivity (Table 5-6). Pore structures of HCPs are closely related to the crosslinking degree, which, in turn determine their adsorption behaviours towards different adsorbates. Basically, the $CO_2$ uptake is directly proportional to the specific surface area. It means high BET surface areas of HCPs ensure their adsorption capacity towards $CO_2$. When the BET surface area is high, HCPs offer a greater number of active sites and, therefore, a more extensive area for $CO_2$ molecules to adhere, resulting in increased adsorption capacity. This is supported from the results that HCPs synthesised in DCE generally have higher specific surface areas and corresponding $CO_2$ uptake.

However, the situation is more complicated when it comes to the $CO_2/N_2$ selectivity of these HCPs. The textual properties such as specific surface area, pore volumes and pore size distribution, influence the ultimate gas selectivity collectively. All of the six HCPs displayed hierarchical pore distributions comprising both micro and mesopores. Notably, *p*-DCX and *p*-triptycene synthesised in DCE own more proportional mesopores, which could be attributed to the fast reaction kinetics undergoing in the halogenated solvent. These mesopores provide extra convenience for $N_2$ molecules to penetrate. At the operating adsorption temperature (273 K), $CO_2$ is recognised to have better accessibility into the narrow micropores because minimum kinetic dimensions of $CO_2$ (0.33 nm) is smaller than that of $N_2$ (0.36 nm) [38]. Therefore, the narrow micropores existing in the *p*-DCX and *p*-triptycene synthesised in DES favor the adsorption of $CO_2$ but limit the adsorption of molecules. This explained why *p*-DCX-DCE and *p*-triptycene-DCE possessed comparatively low $CO_2/N_2$ selectivity despite high BET surface areas. Compared with *p*-DCX-24h and *p*-DCX-72h synthesised in $[ChCl][ZnCl_2]_2$, the latter HCP exhibited both enhanced BET SA and microporosity, consequently resulting in increased selectivity, up to 105. Moving on to the case of

triptycene-based HCPs, the pore size distribution of *p*-triptycene-DCE displayed an obvious peak approximately at 3.8 nm in addition to its 50.8% micropores proportion. This led to its lower $CO_2/N_2$ selectivity (29) as $N_2$ molecules could also diffuse into pores without limitations as well. Conversely, *p*-triptycene-24h-$[ChCl][FeCl_3]_2$ do not possess prominent mesopores, and thus it showed an increment of 158% in $CO_2/N_2$ selectivity while $CO_2$ uptake only dropped by 22%. Excessive crosslinking significantly diminished both BET surface area and pore volume in *p*-triptycene-72h-$[ChCl][FeCl_3]_2$. However, an increasing trend in the $CO_2/N_2$ selectivity was accompanied with a slight increase in microporosity. This was due to the disappearance of partial mesopores resulting from pore collapse during hypercrosslinking. Their pore size distributions above 2 nm were consistent with this explanation. In this work, narrower micropores were confirmed in the HCPs synthesised in the DESs *via* internal and external hypercrosslinking. The relationship between the textural properties of HCPs and $CO_2$ adsorption performance was also revealed. The $CO_2/N_2$ selectivity of HCPs could be improved through adopting new reaction medium such as DESs, adjusting crosslinking degree, etc.

Table 5-6: Comparison of $CO_2$ uptake, $CO_2/N_2$ selectivity at 273 K and textural properties of six HCPs

| Sample | BET SA ($m^2\ g^{-1}$) | $CO_2$ uptake [a] ($cm^3\ g^{-1}$) | $CO_2/N_2$ [b] selectivity | Ref |
|---|---|---|---|---|
| *p*-DCX-DCE | 1063 | 76 | 19 | [20] |
| *p*-DCX-24h-$[ChCl][ZnCl_2]_2$ | 106 | 12 | 14 | This work |
| *p*-DCX-72h-$[ChCl][ZnCl_2]_2$ | 409 | 28 | 105 | This work |
| *p*-triptycene-DCE | 1246 | 78 | 29 | [35] |
| *p*-triptycene-24h-$[ChCl][FeCl_3]_2$ | 969 | 64 | 75 | This work |
| *p*-triptycene-72h-$[ChCl][FeCl_3]_2$ | 611 | 55 | 99 | This work |

[a] $CO_2$ uptake was obtained under 273 K and 1bar. [b] $CO_2/N_2$ selectivity was calculated using the IAST theory ($CO_2$: $N_2$ = 15: 85) at 273 K and 1 bar.

## 5.3 DES suitability for various crosslinking strategies

DES choice was crucial for determining the crosslinking strategy. $[ChCl][ZnCl_2]_2$ was more effective for internal crosslinking but not for external crosslinking, where $[ChCl][FeCl_3]_2$ was a better option. This was intriguing as it is widely accepted that $FeCl_3$ is a Lewis acid that is more effective for catalyzing Friedel-Crafts reactions than $ZnCl_2$ [19]. However, this was not the case in this work, when $FeCl_3$ functioned as both the catalyst and hydrogen bond donor in $[ChCl][FeCl_3]_2$. This could be ascribed to the difference between the Lewis acidity of these catalysts in ionic liquids. Using pyridine and ethanenitrile as infrared probe molecules, Yang and coworkers [39] observed that interactions between the metal halides in ionic liquids and these probe molecules created shifts in IR absorption bands in the 1400 – 1700 $cm^{-1}$ region for pyridine and 2200 – 2400 $cm^{-1}$ region for ethanenitrile where subtle shifts in IR absorption bands were observed. For example, a band at 1450 $cm^{-1}$ corresponded to coordination between pyridine and Lewis acid sites, and shifts in this band increased in the order of $CuCl < FeCl_3 < ZnCl_2 < AlCl_3$. This indicated that the Lewis acidity of $ZnCl_2$ was stronger than $FeCl_3$ in these ionic liquids. This order was also observed with ethanenitrile and in other ionic liquids comprising imidazole cations and chlorometallate anions [40].

Here, I hypothesised that these trends could also be observed with the DESs used in this work. This was validated by using Fourier infrared spectroscopy (FTIR) to investigate the Lewis acidity of $[ChCl][ZnCl_2]_2$ and $[ChCl][FeCl_3]_2$. All samples for FTIR characterisation were prepared by mixing DES and probe liquid (pyridine) in a given molar ratio of 1:1 [41]. The spectra of neat pyridine and mixtures of pyridine and DES are shown in Figure 5-10. The characteristic single peak of pristine pyridine was centered at 1437 $cm^{-1}$. In the presence of $[ChCl][ZnCl_2]_2$, the position of this peak shifted to 1450 $cm^{-1}$ while in the case of $[ChCl][FeCl_3]_2$, there was only a small peak around 1449 $cm^{-1}$. This indicated that the Lewis acidity of $[ChCl][ZnCl_2]_2$ was higher than $[ChCl][FeCl_3]_2$. Considering that this band position shift was minor, all IR

spectra were scanned in triplicates with a resolution of 1 $cm^{-1}$ to ensure reliability. The band near 1540 $cm^{-1}$ corresponded to pyridinium ions coordinated to Brønsted acidic sites and was only observed in the spectrum of $[ChCl][FeCl_3]_2$, indicating that $[ChCl][FeCl_3]_2$ was more likely to behave like a Brønsted acid.

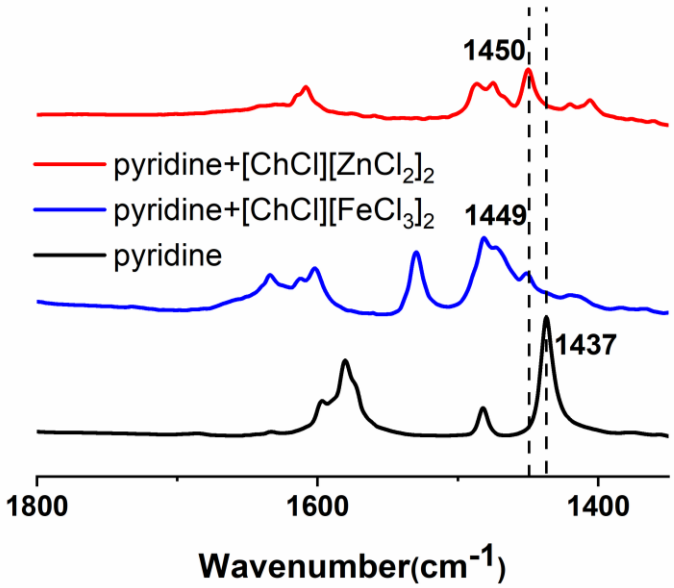


Figure 5-10: FTIR spectra of (a) pyridine (black), (b)pyridine+$[ChCl][ZnCl_2]_2$ (red), (c) pyridine+ $[ChCl][FeCl_3]_2$ (blue) showing a red-shift in peak position associated with pyridine due to different Lewis acidity

To understand how different DES systems facilitate various crosslinking strategies, here we proposed possible routes for internal and external crosslinking. Previous studies [42,43] revealed that $[ZnCl_3]^-$, $[Zn_2Cl_5]^-$ and $[Zn_3Cl_7]^-$ ions were detected in $[ChCl][ZnCl_2]_2$ and $[Zn_2Cl_5]^-$ species accounted for the largest proportion. Here, we took DCX as an example to describe a possible mechanism for internal crosslinking (Figure 5-11a). First, a complex of an aromatic chloromethyl group and a zinc chloride cluster was formed *via* interactions between electropositive zinc atoms and electronegative chlorine atoms. Then the as-formed carbocation continued to be attacked by the benzene ring of another DCX molecule, forming an intermediate of a cyclohexadienyl cation. With the deprotonation of above intermediates and departure of hydrogen chloride side products, the reformation of carbon-carbon double bonds restored aromaticity to the target compound. Interchain methylene linkages were ultimately constructed.

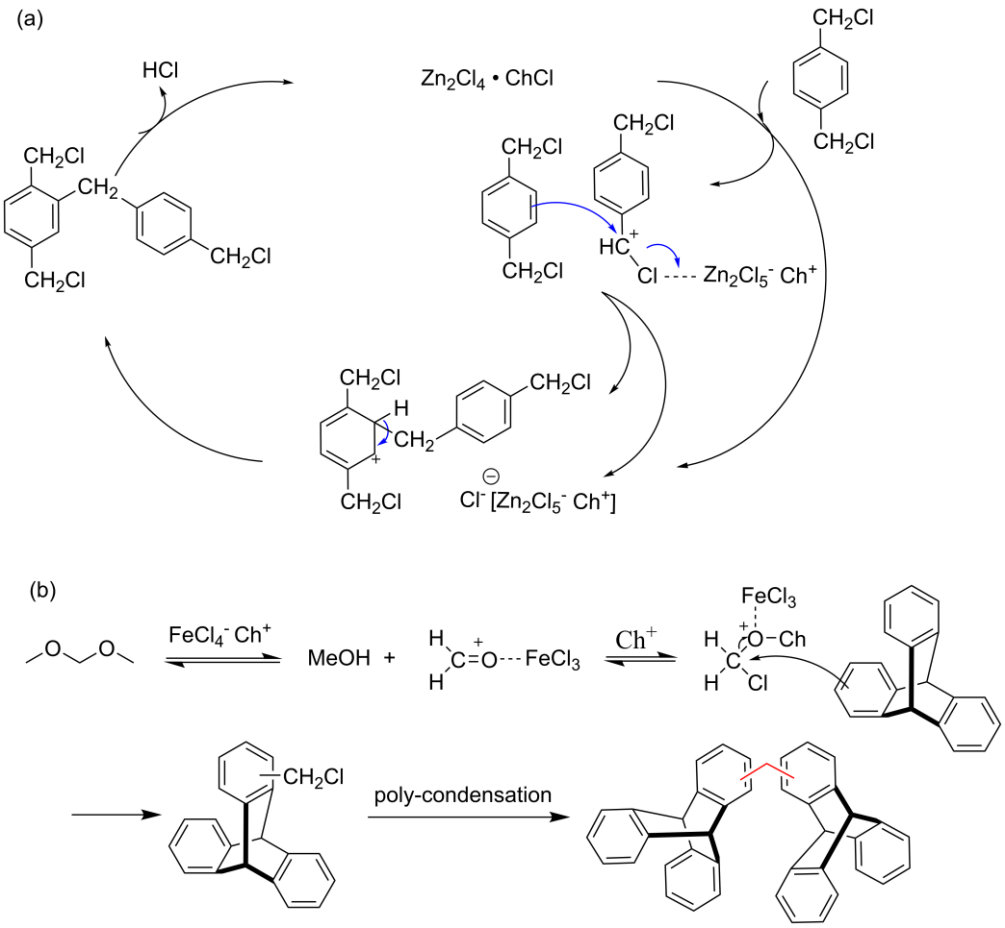


Figure 5-11: Possible mechanism of (a) internal hypercrosslinking reaction catalysed by $[ChCl][ZnCl_2]_2$, (b) external hypercrosslinking reaction catalysed by $[ChCl][FeCl_3]_2$

In the case of $[ChCl][FeCl_3]_2$, only $[FeCl_4]^-$ species and possibly $[Fe_2Cl_7]^-$ clusters were detected. Therefore, here we proposed that the external crosslinking process in $[ChCl][FeCl_3]_2$ was driven by $[FeCl_4]^-$ clusters (Figure 5-11b). In the first step, the Lewis acid catalyst i.e. $[FeCl_4]^-$ formed a complex with formaldehyde which decomposed from FDA and consequently produced electrophile intermediate carbocations. These intermediates were vulnerable to the attack from phenyl rings thus introducing chloromethyl groups. After chloromethylation, they were further converted into methylene bridges and that knitted the aromatic rings into highly-crosslinked polymeric networks. A possible explanation for an inactive $[ChCl][ZnCl_2]_2$ system for external crosslinking could be due to the hygroscopicity of zinc chloride, which might inhibit alkylation [44,45]. Moreover, Cheng et al. showed

that $ZnCl_2$ was a weak catalyst for chloromethylation where only 0.22 number of chloromethyl groups could be grafted on to aromatic substrates [46].

## 5.4 The recycling of DES

The DES systems deployed for HCP synthesis in this work could be recycled, minimizing negative environmental impacts. Choline chloride is widely used as a nutritional additive in animal feeding and classified as non-toxic [47]. Choline chloride is safe enough for direct discharge into the ecological cycle [48]. Therefore, we will not discuss the recycling of choline chloride as it would be first dissolved in water during post-synthesis treatment. Tran and coworkers [49] managed to recover $[ChCl][ZnCl_2]_3$ from Friedel-Crafts acylation reaction with diethyl ether and the recycled $[ChCl][ZnCl_2]_3$ could still be applied in extra four runs. Even though DES can undergo several consequent recycles, we will still need to deal with end-of-life DESs. Therefore, the emphasis of this section is to recover and recycle the halide metal ions.

Solvent extraction is a popular recycling technology for metal ions in DESs. For e.g., Spathariotis and co-workers [50] scaled up the recovery of up to 90% of iron(III), zinc(II) and lead(II) from $ChCl_2$-based DESs using two commercial extractants – trialkylphosphine oxide (Cyanex 923, C923) and Aliquat 336 (A336) using a continuous counter-current circuit and mixer-settlers.

Beside solvent extraction, another strategy is to upcycle ferric ions into high-value catalysts. Karimi and coworkers [51] reported a novel strategy for synthesising amorphous and nanocrystalline hematite ($\alpha$-$Fe_2O_3$) photocatalysts using a mixture of NaOH, water and $[ChCl][FeCl_3]_2$ as the synthesis medium. Adapting this approach, we first added water into the HCP-$[ChCl][FeCl_3]_2$ mixture after the crosslinking reaction. This dissolved choline chloride and ferric chloride whilst the HCPs precipitated from this mixture in the form of insoluble solids and were separated by filtration. Next, I added concentrated sodium hydroxide solution into the aqueous mixture comprising both ChCl and $FeCl_3$ and heated this mixture at 130 ℃, yielding dark iron oxide products. After drying, these iron oxide products were verified to be

magnetic and could be collected easily with magnets, as shown in Figure 5-12b. To figure out the composition of the black product we obtained and the origin of its magnetism, X-ray photoelectron spectroscopy (XPS) was used to differentiate the structures of iron oxides. Fe 2p core-level XPS spectra of α-$Fe_2O_3$ synthesised with Karimi's method and black products collected from spent $[ChCl][FeCl_3]_2$ DES were shown in Figure 5-12a. Both spectra showed two mains of Fe 2p3/2 (around 710.8 eV) and Fe 2p1/2, demonstrating the existence of Fe(III) species. The binding energy of Fe(II) was supposed to be around 708.5 eV, and this peak was invisible in the spectrum of our iron oxides [52]. Therefore, the magnetic black product recycled from used DES is considered to be γ-$Fe_2O_3$. In addition, a characteristic satellite peak around 718.9 eV was observed in the spectrum of α-$Fe_2O_3$, while the satellite peak was much less intensive in the spectrum of γ-$Fe_2O_3$.

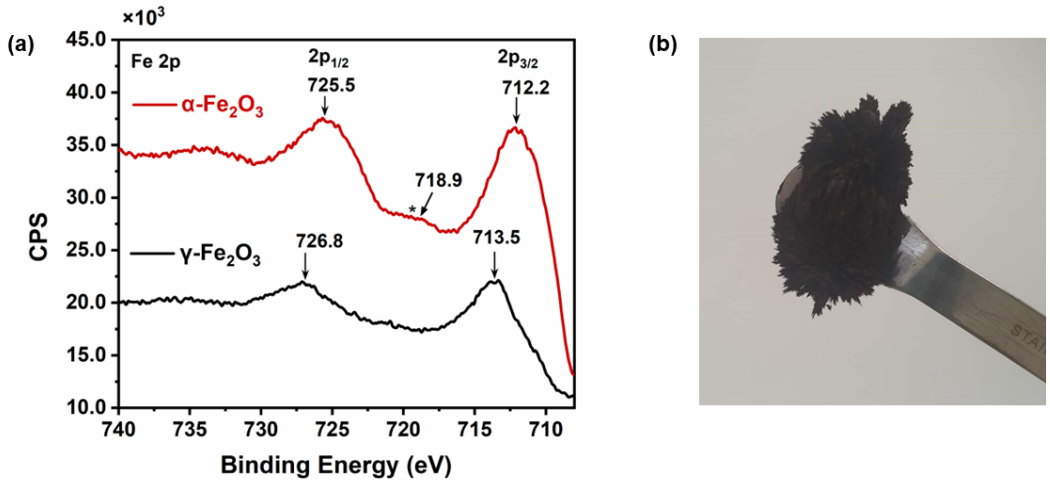


Figure 5-12: (a) Fe 2p core-level XPS spectra of α-$Fe_2O_3$ (red line) and γ- $Fe_2O_3$ (black line), (b) image of the collected magnetic γ- $Fe_2O_3$ particles

By demonstrating the feasibility of transforming metal halides of DESs used in HCP synthesis into magnetic iron oxides, our approach could realise the maximum utilisation of all chemical components, which is highly advocated in green chemistry principles [53]. Instead of disposing chemical waste streams from HCP synthesis, here we showed that the residues or by-products of this process could be repurposed as new feedstock for chemical synthesis.

## 5.5 Conclusion

Two deep eutectic solvents, $[ChCl][ZnCl_2]_2$ and $[ChCl][FeCl_3]_2$, were proven in this work as feasible alternatives for halogenated solvents commonly used in Friedel-Crafts reactions for the synthesis of HCPs. This work successfully expanded the application of DES in polymerisation chemistry and proposed a versatile synthetic strategy for porous HCPs. I demonstrated the feasibility and versatility of this approach using typical monomers that were proven in the past to yield HCPs. I also proposed possible mechanisms for hypercrosslinking process in DESs. $[ChCl][ZnCl_2]_2$ and $[ChCl][FeCl_3]_2$ were suitable for internal and external crosslinking, respectively. Notably, although the specific surface areas of *p*-triptycene HCPs synthesised in DESs were 22 – 52% lower than those produced in halogenated solvents, their $CO_2$ uptake only dropped 18 – 30%. This can be attributed to the narrower pore size distributions of the former materials, benefitting $CO_2/N_2$ separations. This result further proves that micropores boost the $CO_2$ adsorption [54].We believe that the findings from this work would benefit the explorations towards HCPs with ultra-micropores and their applications in gas separation.

## 5.6 References


[1] Chanchaona, N., et al., *Flow synthesis of hypercrosslinked polymers with additional microporosity that enhances CO 2/N 2 separation.* Journal of Materials Chemistry A, 2023. **11**(18): p. 9859-9867.

[2] Liu, H., et al., *Stepwise Crosslinking: A Facile Yet Versatile Conceptual Strategy to Nanomorphology-Persistent Porous Organic Polymers.* Advanced Materials, 2017. **29**(27): p. 1700723.

[3] Byrne, F.P., et al., *Tools and techniques for solvent selection: green solvent selection guides.* Sustainable Chemical Processes, 2016. **4**: p. 1-24.

[4] Gao, F., et al., *Replacement strategies for non-green dipolar aprotic solvents.* Green Chemistry, 2020. **22**(19): p. 6240-6257.

[5] Borrero-López, A.M., A. Celzard, and V. Fierro, *Eco-Friendly Production of Hyper-Cross-Linked Polymers Using Mechanosynthesis and Bioresources: A Critical Review.* ACS Sustainable Chemistry & Engineering, 2022. **10**(49): p. 16090-16112.

[6] Wang, L., Y. Su, and C. Gu, *Solution Processing of Cross-Linked Porous Organic Polymers.* Accounts of Materials Research, 2022. **3**(10): p. 1049-1060.

[7] Prince, L., et al., *Metal-free hyper-cross-linked polymers from benzyl methyl ethers: A route to polymerization catalyst recycling.* Macromolecules, 2021. **54**(19): p. 9217-9222.

[8] Björnerbäck, F. and N. Hedin, *Highly porous hypercrosslinked polymers derived from biobased molecules.* ChemSusChem, 2019. **12**(4): p. 839-847.

[9] Prat, D., J. Hayler, and A. Wells, *A survey of solvent selection guides.* Green Chemistry, 2014. **16**(10): p. 4546-4551.

[10] Wang, A., et al., *Deep eutectic solvent catalyzed Friedel–Crafts alkylation of electron-rich arenes with aldehydes.* RSC Advances, 2015. **5**(73): p. 59022-59026.

[11] Juneidi, I., M. Hayyan, and O. Mohd Ali, *Toxicity profile of choline chloride-based deep eutectic solvents for fungi and Cyprinus carpio fish.* Environmental Science and Pollution Research, 2016. **23**: p. 7648-7659.

[12] Johnson, W.W. and M.T. Finley, *Handbook of acute toxicity of chemicals to fish and aquatic invertebrates: Summaries of toxicity tests conducted at Columbia National Fisheries Research Laboratory, 1965-78*. Vol. 137. 1980: US Department of the Interior, Fish and Wildlife service.

[13] Luo, Y., et al., *Microporous organic polymers synthesized by self-condensation of aromatic hydroxymethyl monomers.* Polymer Chemistry, 2013. **4**(4): p. 1126-1131.

[14] Wood, C.D., et al., *Hydrogen storage in microporous hypercrosslinked organic polymer networks.* Chemistry of materials, 2007. **19**(8): p. 2034-2048.

[15] Law, R.V., et al., *Solid-state 13C MAS NMR studies of hyper-cross-linked polystyrene resins.* Macromolecules, 1996. **29**(19): p. 6284-6293.

[16] Park, H., et al., *A robust ethane-selective hypercrosslinked porous organic adsorbent with high ethane capacity.* Journal of Materials Chemistry A, 2022. **10**(7): p. 3579-3584.

[17] ALOthman, Z.A., *A review: fundamental aspects of silicate mesoporous materials.* Materials, 2012. **5**(12): p. 2874-2902.

[18] Sing, K.S., *Reporting physisorption data for gas/solid systems with special reference to the determination of surface area and porosity (Recommendations 1984).* Pure and applied chemistry, 1985. **57**(4): p. 603-619.

[19] Xu, C., et al., *Enhancement mechanism behind the different adsorptive behaviors of nitro/amine modified hypercrosslinked resins towards phenols.* Journal of the Taiwan Institute of Chemical Engineers, 2019. **102**: p. 340-348.

[20] Sang, Y. and J. Huang, *Benzimidazole-based hyper-cross-linked poly (ionic liquid) s for efficient CO2 capture and conversion.* Chemical Engineering Journal, 2020. **385**: p. 123973.

[21] Akten, E.D., R. Siriwardane, and D.S. Sholl, *Monte Carlo simulation of single-and binary-component adsorption of CO2, N2, and H2 in zeolite Na-4A.* Energy & Fuels, 2003. **17**(4): p. 977-983.

[22] Fu, Z., et al., *Transforming waste expanded polystyrene foam into hyper-crosslinked polymers for carbon dioxide capture and separation.* Chemical Engineering Journal, 2017. **323**: p. 557-564.

[23] Liu, Q.-Q., et al., *A hyper-cross-linked polystyrene with nano-pore structure.* European polymer journal, 2008. **44**(8): p. 2516-2522.

[24] Chen, D., et al., *Tunable porosity of nanoporous organic polymers with hierarchical pores for enhanced CO 2 capture.* Polymer Chemistry, 2016. **7**(20): p. 3416-3422.

[25] Yang, Y., B. Tan, and C.D. Wood, *Solution-processable hypercrosslinked polymers by low cost strategies: a promising platform for gas storage and separation.* Journal of Materials Chemistry A, 2016. **4**(39): p. 15072-15080.

[26] Watabe, T. and K. Yogo, *Isotherms and isosteric heats of adsorption for CO2 in amine-functionalized mesoporous silicas.* Separation and Purification Technology, 2013. **120**: p. 20-23.

[27] Nuhnen, A. and C. Janiak, *A practical guide to calculate the isosteric heat/enthalpy of adsorption via adsorption isotherms in metal–organic frameworks, MOFs.* Dalton Transactions, 2020. **49**(30): p. 10295-10307.

[28] Zhu, B., et al., *Boosting membrane carbon capture via multifaceted polyphenol-mediated soldering.* Nature Communications, 2023. **14**(1): p. 1697.

[29] Zhu, B., et al., *Ultrapermeable Gel Membranes Enabling Superior Carbon Capture.* Angewandte Chemie International Edition, 2023: p. e202315607.

[30] Alahmed, A.H., et al., *Post-synthetic fluorination of Scholl-coupled microporous polymers for increased CO 2 uptake and selectivity.* Journal of materials chemistry A, 2019. **7**(2): p. 549-557.

[31] Dong, X., et al., *Recycling plastic waste for environmental remediation in water purification and CO2 capture.* ACS Applied Polymer Materials, 2020. **2**(7): p. 2586-2593.

[32] Lee, J.S.M., et al., *Hyperporous carbons from hypercrosslinked polymers.* Advanced Materials, 2016. **28**(44): p. 9804-9810.

[33] Dawson, R., et al., *Microporous organic polymers for carbon dioxide capture.* Energy & Environmental Science, 2011. **4**(10): p. 4239-4245.

[34] Zhu, B., et al., *One-step synthesis of structurally stable CO2-philic membranes with ultra-high PEO loading for enhanced carbon capture.* Engineering, 2023. **26**: p. 220-228.

[35] Chen, D., et al., *Hyper-crosslinked aromatic polymers with improved microporosity for enhanced CO 2/N 2 and CO 2/CH 4 selectivity.* New Journal of Chemistry, 2017. **41**(14): p. 6834-6839.

[36] Xia, X., et al., *Hyper-crosslinked polymers with controlled multiscale porosity for effective removal of benzene from cigarette smoke.* e-Polymers, 2022. **22**(1): p. 19-29.

[37] Liu, L., et al., *Helix-sense-selective polymerization of achiral phenylacetylenes and unique properties of the resulting cis-cisoidal polymers.* Polymer Reviews, 2017. **57**(1): p. 89-118.

[38] Rios, R.V., et al., *Kinetic restrictions in the characterization of narrow microporosity in carbon materials.* The Journal of Physical Chemistry C, 2007. **111**(10): p. 3803-3805.

[39] Yang, Y.-l. and Y. Kou, *Determination of the Lewis acidity of ionic liquids by means of an IR spectroscopic probe.* Chemical Communications, 2004(2): p. 226-227.

[40] Acevedo, O., *Determination of local effects for chloroaluminate ionic liquids on Diels–Alder reactions.* Journal of Molecular Graphics and Modelling, 2009. **28**(2): p. 95-101.

[41] Tao, L., et al., *Application of choline chloride· xZnCl2 ionic liquids for preparation of biodiesel.* Chinese Journal of Chemical Engineering, 2010. **18**(2): p. 322-327.

[42] Abbott, A.P., et al., *Ionic liquids based upon metal halide/substituted quaternary ammonium salt mixtures.* Inorganic chemistry, 2004. **43**(11): p. 3447-3452.

[43] Fanglong, Q., et al., *Preparation and thermal property of ionic liquid based on ZnCl2/ChCl.* Int. Proc. Chem., Biol. Environ. Eng., 2015. **90**: p. 70-75.

[44] Fu, Y., et al., *A new chloromethylation method based on polystyrene–divinylbenzene.* Chemical Papers, 2019. **73**(9): p. 2183-2188.

[45] Shevelev, D. and O. Vladenkova, *Effect of catalyst used for chloromethylation of styrene-divinylbenzene copolymer on the service characteristics of the highly basic anion exchanger obtained.* Russian Journal of Applied Chemistry, 2008. **81**(5): p. 896-898.

[46] Cheng, Z., et al., *Modification of poly (ether imide) membranes via surface-initiated atom transfer radical polymerization.* Macromolecules, 2006. **39**(4): p. 1660-1663.

[47] Radošević, K., et al., *Evaluation of toxicity and biodegradability of choline chloride based deep eutectic solvents.* Ecotoxicology and environmental safety, 2015. **112**: p. 46-53.

[48] Additives, E.P.o. and P.o.S.u.i.A. Feed, *Scientific Opinion on safety and efficacy of choline chloride as a feed additive for all animal species.* EFSA Journal, 2011. **9**(9): p. 2353.

[49] Tran, P.H., et al., *An efficient and green method for regio-and chemo-selective Friedel–Crafts acylations using a deep eutectic solvent ([CholineCl][ZnCl 2] 3).* RSC advances, 2016. **6**(43): p. 37031-37038.

[50] Spathariotis, S., et al., *Separation of iron (iii), zinc (ii) and lead (ii) from a choline chloride–ethylene glycol deep eutectic solvent by solvent extraction.* RSC advances, 2020. **10**(55): p. 33161-33170.

[51] Karimi, M., et al., *Amorphous and nanocrystalline hematite photocatalysts synthesized in ferric chloride-choline chloride acting as a green and reactive synthesis medium.* Optik, 2019. **181**: p. 816-822.

[52] Cui, H., Y. Liu, and W. Ren, *Structure switch between α-Fe2O3, γ-Fe2O3 and Fe3O4 during the large scale and low temperature sol–gel synthesis of nearly monodispersed iron oxide nanoparticles.* Advanced Powder Technology, 2013. **24**(1): p. 93-97.

[53] Zimmerman, J.B., et al., *Designing for a green chemistry future.* Science, 2020. **367**(6476): p. 397-400.

[54] Wang, S., et al., *Prediction by convolutional neural networks of CO2/N2 selectivity in porous carbons from N2 adsorption isotherm at 77 K.* Angewandte Chemie International Edition, 2020. **59**(44): p. 19645-19648.

# Chapter 6 Lignin-based HCPs synthesised in DESs

This work is in peer review, named as ‘Narrowing the pore size distribution of bio-renewable sorbents to enhance $CO_2/N_2$ separations’.

## 6.1 The intention and target of this project

In the last chapter, DESs have been proved to be suitable for the synthesis of hypercrosslinked polymers regardless of internal and external hypercrosslinking. Herein, I continued to expand the feasibility of DESs reaction systems to even post-crosslinking. In addition, the selection of starting monomers also turns to biobased materials to gain greener HCPs. Based on the achieved results, DESs exhibited their advantage in producing narrower pores that are expected to promote selective adsorption of $CO_2$.

Anthropogenic $CO_2$ emissions, particularly from fossil fuel combustion, deforestation and industrial development, are a main cause for global warming and climate change [1]. For example, current atmospheric $CO_2$ content has reached 419 parts per million (ppm) – a 49.6% increment when compared to the atmospheric $CO_2$ content in 1750 prior the Industrial Revolution [2-4]. As such, through The Paris Agreement, global governments have set a target to address global warming through a series of measures, including achieving net-zero green gas emissions by 2050 [5]. A key technology for delivering this target is carbon capture and storage.

Carbon capture and storage is a multi-faceted technology, which can be classified into pre-combustion, oxy-fuel combustion, and post-combustion [6]. Keys for these applications are the types of materials employed for carbon capture – solid sorbents [7,8], advanced ionic solvents [9-11] and membranes [12,13]. Of particular interest are solid sorbents due to excellent thermal and chemical stability, reusability and low costs [14]. Solid sorbents with superior $CO_2$ adsorption capacities that are commonplace in industry include zeolites [15] and activated carbons [16]. In recent years, microporous

adsorbents such as metal organic frameworks [17], and hypercrosslinked polymers have exhibited great potential for carbon capture applications. Notably, an advantage of these microporous materials lies in their fine-tuned porosity, which is key for delivering high $CO_2$ adsorption capacity and exceptional selectivity. For example, with open metal sites in hexagonal channels, the MOF-74 type metal organic frameworks exhibit high $CO_2$ adsorption capacity, reaching a value of 1.35 mmol $g^{-1}$ whilst delivering selective adsorption over $N_2$ even in wet conditions [18-20]. Meanwhile, the $CO_2$ adsorption capacity and $CO_2/N_2$ selectivity of nitrogen-rich HCPs reached 1.56 mmol $g^{-1}$ and 52, respectively, at 273 K and 1 bar [21]. The $CO_2$ adsorption capacities of these solid sorbents are similar to that of the most commonly used amine-solvent, monoethanolamine (1.63 mmol $g^{-1}$), but their $CO_2/N_2$ selectivity are lower [22]. This is because amine-based liquid sorbents do not absorb $N_2$. This is also why despite the limitations of liquid-based absorbents for carbon capture, they are still preferred over solid adsorbents.

To improve the $CO_2/N_2$ selectivity of solid sorbents, Jiang's group suggested a design strategy for creating porous carbons with clearly defined micropores (diameter less than 2 nm) and mesopores (3 to 7 nm), while ensuring a well-separated pore size distribution (PSD) [23]. The distinct segregation of micropores and mesopores enhances $CO_2/N_2$ selectivity by favouring $CO_2$ adsorption within the micropores, whilst simultaneously impeding and diminishing $N_2$ adsorption in the mesopores. The benefits of reducing mesopore content and enhancing micropore volume for enhancing $CO_2/N_2$ selectivity by suppressing $N_2$ adsorption were also observed in other physiosorbents such as metal organic frameworks like [24,25] and USTA-16 [26]. Our group recently showed that this strategy is also applicable to HCPs where we used continuous flow reactions to tailor the PSD of HCPs during direct internal crosslinking, external crosslinking, and post-crosslinking. With flow synthesis, we enhanced the micropore volume of HCPs by 570%, from 0.042 $cm^3$ $g^{-1}$ to 0.281 $cm^3$ $g^{-1}$ while reducing mesopore volume by 40% when compared to those obtained in in batch synthesis. This resulted in a 9.5-fold increase in $CO_2/N_2$ selectivity, from 7.5 to

71.5 (based on IAST calculations using a 15:85 $CO_2/N_2$ mixture at 298 K, 1 bar) [27]. Other than tailoring synthesis conditions to optimise the $CO_2/N_2$ selectivity of HCPs, Chapter 5 reported the use of deep eutectic solvents comprising chloline chloride and iron chloride ([ChCl][$FeCl_3$]$_2$) or chloline chloride and zinc chloride ([ChCl][$ZnCl_2$]$_2$) in batch reactions to deliver a similar effect. Likewise in flow synthesis, the use of DESs enhanced micropore volume, but was unable to reduce mesopore content in HCPs. As a result, the $CO_2/N_2$ selectivity of HCPs was only enhanced by 5.5-fold, from 19 to 105.

Another approach to optimise $CO_2/N_2$ selectivity in HCPs is to exploit the $CO_2$ affinity of functional groups such as $NH_2$ [28,29], $SO_3H$ [30,31], and OH [32,33] to 1) enhance $CO_2$ adsorption and 2) occupy free volume within the pores to reduce $N_2$ adsorption. This strategy has been delivered with lignin, an abundant and low-cost biopolymer existing in nature [34]. To date, > 50 million tonnes of lignin by-products are generated by the wood pulping and related industries annually, while only 2% of these lignin-based by-products are utilised [35]. Lignin is mainly converted into carbonaceous adsorbents for metal, organic and gaseous pollutants, or chemically modified for specific applications [36]. Meng and Weber first reported microporous lignin-based HCPs using formaldehyde dimethyl acetal (FDA) as a crosslinker. The Brunauer-Emmett-Teller (BET) surface areas of these lignin-based HCPs were negligible but demonstrated a moderate $CO_2$ uptake of 1.2 mmol $g^{-1}$ and excellent $CO_2/N_2$ selectivity of 150 [37]. The BET surface areas of lignin-based HCPs could be enhanced when biphenyl was added as a co-monomer [38], or when 1,4-dichloroxylene (DCX) and 4,4’-bis(chloromethyl)-1,1′-biphenyl (BCMBP) were used as crosslinkers [39]. Although these modification strategies enhanced total porosity in lignin-based HCPs, the $CO_2/N_2$ selectivity of these materials were expected to reduce due to the small proportion of micropores.

To optimise the $CO_2/N_2$ selectivity of HCPs, here in this work, I combined both strategies of 1) optimising HCP textural properties to minimise $N_2$ adsorption capacity and 2) exploiting the $CO_2$ affinity of oxygenated functional groups to optimise $CO_2$

adsorption capacity by synthesising lignin-based HCPs in DESs like $[ChCl][ZnCl_2]_2$ and $[ChCl][FeCl_3]_2$, as shown in Scheme 6-1. The $CO_2/N_2$ selectivity (obtained from mixed gas adsorption isotherms using a gas mixture comprising 15 vol.% $CO_2$ and 85 vol.% $N_2$ at 298 K) of our lignin-based HCPs reached a value of 835. I also evaluated how the chemical structure of various external crosslinking reagents such as DCX, BCMBP and FDA and different Lewis acid-based DESs, $[ChCl][ZnCl_2]_2$ and $[ChCl][FeCl_3]_2$, tailored the ratio of micropores and mesopores in our HCPs to optimise $CO_2/N_2$ selectivity. Considering the comparatively lower reactivity of lignin due to steric hindrance effect of substituents [38], all crosslinking reactions underwent harsher conditions such as longer durations and elevated temperature [38].

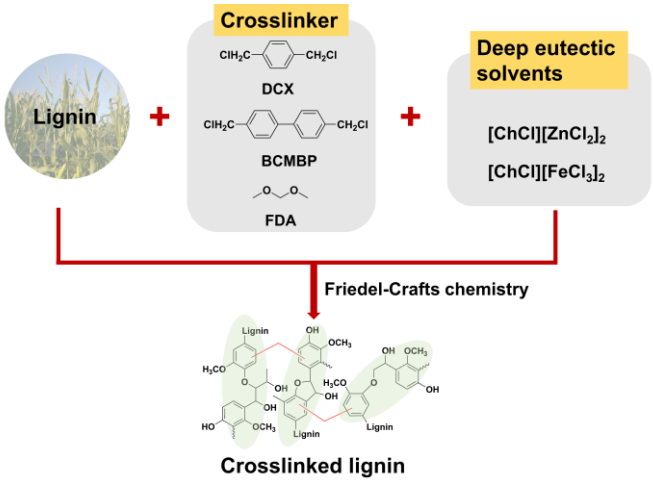


Scheme 6-1: Synthesis of lignin-based hypercrosslinked polymers using different crosslinkers in the deep eutectic solvents such as $[ChCl][ZnCl_2]_2$ and $[ChCl][FeCl_3]_2$

## 6.2 Results and discussion

### 6.2.1 Chemical structures of lignin-based HCPs

Three frequently-used crosslinkers – DCX, BCMBP and FDA were chosen here to crosslink lignin in $[ChCl][ZnCl_2]_2$ and $[ChCl][FeCl_3]_2$ DESscontaining phenolic hydroxyl groups, methoxy groups, carbonyl groups, ether linkages and even carboxylic groups in some cases [40-42]. FTIR spectra in Figure 6-1 showed a broad peak centred around 3440 $cm^{-1}$ that correlated to the aromatic and aliphatic O-H stretching vibrations. Two characteristic peaks centred at 2934 $cm^{-1}$ and 2841 $cm^{-1}$

could also be observed and ascribed to the alkyl C-H stretching vibrations in the methylene (-$CH_2$) and methyl groups (-$CH_3$), respectively [38]. In addition, the peak around 1460 $cm^{-1}$ corresponded to the bending vibration of -$CH_2$ groups, which was a key indicator of the formation of crosslinking bridge [43]. Compared with pristine lignin, the intensity of this peak increased in all lignin-based HCPs especially lignin-FDA-ZnDES and lignin-FDA-FeDES. This was because FDA crosslinker created methylene bridges between neighbouring units while DCX and BCMBP formed methylene benzene linkages. Furthermore, the peak at 1698 $cm^{-1}$ could be attributed to the stretching vibration of conjugated carbonyl groups (C=O) within lignin molecules [38]. I observed that the intensity and position of this peak was enhanced and shifted to 1725 $cm^{-1}$ in all three lignin-based HCPs synthesised in [ChCl][$FeCl_3$]$_2$. This suggested that the amount of carbonyl bonds (C=O), which are electron withdrawing group, increased due to the oxidation of ferric ions [44]. Moreover, the intensities of peaks corresponding to aromatic skeleton vibrations centered at 1606, 1505 and 1426 $cm^{-1}$ increased slightly when DCX and BCMBP served as crosslinkers, implying the successfully incorporation of benzyl-containing linker units [45]. The existence of aryl ether bonds (C-O-C) could be confirmed from the peaks between 1270 and 1120 $cm^{-1}$. These bonds remained in the crosslinked lignin polymers. In addition, the characteristic peak around 828 $cm^{-1}$ could be attributed to the out of plane C-H vibrations on disubstituted benzyl rings [46]. The enhancement of this peak suggested increased crosslinking degree.

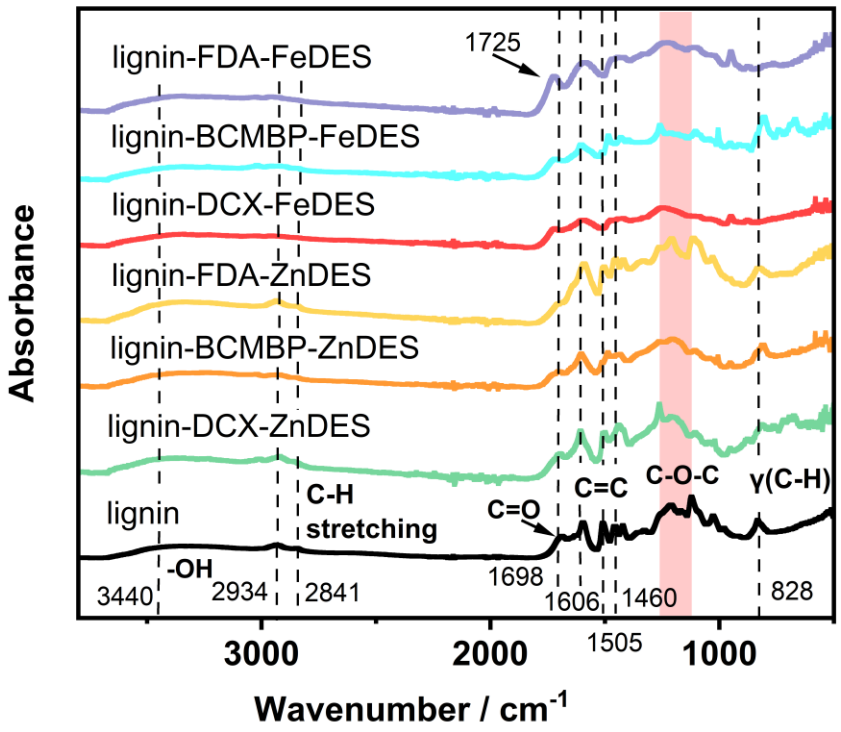


Figure 6-1: FTIR spectra of original lignin and six lignin-based polymers

Solid-state $^{13}C$ nuclear magnetic resonance (NMR) spectroscopy was also used for characterising the chemical structures of lignin and its derived HCPs here (Figure 6-2). Lignin, a highly complex and heterogeneous polymer, does not have a well-defined chemical structure. Depending on the plant resource and extraction methods, the structure of lignin could vary significantly [47]. In the spectrum of original lignin, the carbons of the aromatic rings distributed from 100 – 150 ppm, depending on the chemical environment they were treated in [48]. The peak centred at 56 ppm could be assigned to carbon atoms on methoxy groups ($-OCH_3$) [49]. Compared with the spectrum of pure lignin, I observed the formation of new peaks between 20 – 50 ppm in the spectra of lignin-DCX-ZnDES, lignin-BCMBP-ZnDES, lignin-DCX-FeDES, and lignin-BCMBP-FeDES. These new peaks could be attributed to methylene carbons [39], indicating the formation of crosslinking bridges. In addition, the peak representing methoxy groups almost disappeared in the $^{13}C$ NMR spectra of these four

lignin-based HCPs. This indicated that DCX and BCMBP crosslinking reagents could demethoxylate lignin in the DESs used here. Moreover, the two peaks centred at 128 ppm and 136 ppm could be attributed to phenyl carbons [39]. I also observed that the signals for aromatic carbon atoms located between 100 – 160 ppm were accompanied by overlapping peaks.

The spectra of lignin-FDA-ZnDES and lignin-FDA-FeDES differed from those of HCPs crosslinked with chlorine-containing agents (DCX, BCMBP). When FDA was used as a crosslinker in [ChCl][$ZnCl_2$]$_2$, peaks corresponding to methoxy groups (~ 55 ppm) remained intact, even when the peak indicative of methylene crosslinking bonds (~ 37 ppm) was formed. Meanwhile, from the NMR spectra of lignin-based HCPs that were crosslinked with FDA, it was observed that overlapping of signals for aromatic carbon atoms located between 100 – 160 ppm with other peaks worsened. The two wide peaks centred at 53 ppm and 126 ppm were characteristic of methoxy carbons and aromatic carbons, while the presence of the crosslinking bond could not be confirmed. From solid-state $^{13}C$ NMR results, I deduced that crosslinking and demethoxylation occurred concurrently in both DESs where chlorinated crosslinkers (DCX and BCMBP) were deployed, while FDA-crosslinked lignin was most likely lightly crosslinked as methoxy groups were retained.

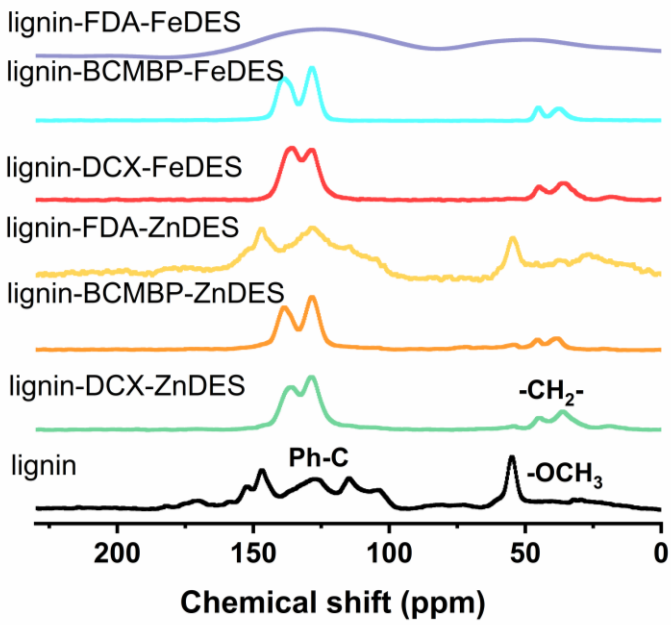


Figure 6-2: $^{13}C$ solid state NMR spectra of original lignin and six lignin-based HCPs synthesised in this work

X-ray photoelectron spectroscopy (XPS) was utilised to evaluate the surface elemental composition of lignin and its six HCP derivatives here in this work (Figure 6-3, Table 6-1). The high level XPS survey spectra of all samples studied here comprised mainly of C 1s (533 eV) and O 1s (285 eV) signals as lignin is mainly composed of carbon and oxygen. The peak area ratio of C 1s to O 1s for pristine lignin studied here was 5.2 (Table 6-1). Compared with pristine lignin, the C 1s/O 1s ratio for lignin-DCX-ZnDES increased by 34.8%, reaching a value of 7.2. This indicated successful crosslinking between the lignin units. However, the C 1s: O 1s ratio of other lignin-based HCPs studied here were lower than that of pristine lignin despite crosslinking. This could be attributed to the hydroxylation and demethoxylation of lignin by crosslinking reagents deployed in the DES-mediated process [50], particularly when FDA was used for crosslinking where the C1s/O1s ratios of lignin-FDA-ZnDES and lignin-FDA-FeDES HCPs were reduced the most. This was because excessive FDA might lead to grafting FDA on the aromatic rings, rather than crosslinking [43]. Consequently, this enhanced O content in these HCPs. Overall, regardless of crosslinker reagent used, the C1s/O1s ratios of HCPs

synthesised in $[ChCl][FeCl_3]_2$ were comparatively lower than those synthesised in $[ChCl][ZnCl_2]_2$. This suggested that $[ChCl][FeCl_3]_2$ was more oxidative than $[ChCl][ZnCl_2]_2$.

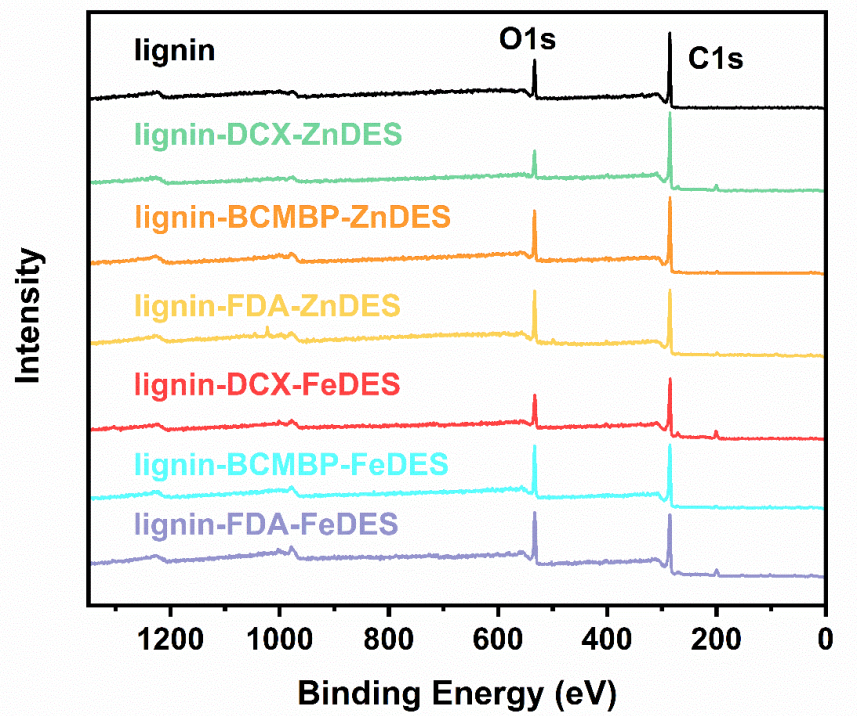


Figure 6-3: XPS survey spectra of pristine lignin and lignin-based HCPs

Table 6-1: The content of carbon and oxygen atoms on the surface of lignin

| Sample | C 1s (%) | O 1s (%) | C 1s/O 1s |
|---|---|---|---|
| lignin | 83.88 | 16.12 | 5.20 |
| lignin-DCX-ZnDES | 87.52 | 12.48 | 7.01 |
| lignin-BCMBP-ZnDES | 81 | 19 | 4.26 |
| lignin-FDA-ZnDES | 77.78 | 22.22 | 3.50 |
| lignin-DCX-FeDES | 81.59 | 18.41 | 4.43 |
| lignin-BCMBP-FeDES | 78.07 | 21.93 | 3.56 |
| lignin-FDA-FeDES | 75.91 | 24.09 | 3.15 |

The XPS C 1s transitions observed for lignin and its derivative HCPs were asymmetric, indicating that they were composed of multiple peaks. Deconvolution of the C 1s spectra was performed using a model comprising four distinct peaks around

284.7 eV (C-C / C=C structure), 285.3 eV (C-O-C / C-OH structure), 286.2 eV (Ph-OH / C=O structure) and 288.5 eV (COO structure (Figure 6-4). The peak area percentages associated with these peaks are shown in Table 6-2. Generally, the peak areas of C1 and C2 decreased while those of C3 and C4 increased after crosslinking in DESs, suggesting the conversion to unsaturated carbon-oxygen bonds. Hence, oxidative reactions were also confirmed in the process apart from crosslinking reactions. In this process, oxidative reactions were prominent than crosslinking. There were more C2 type carbon atoms in lignin-HCPs crosslinked with FDA than those crosslinked by DCX and BCMBP. This was because excess FDA crosslinker could remain in the products and it only formed unilateral substitutions on the lignin units. Regardless of crosslinking agent, C3 type carbons constituted a larger percentage in HCPs synthesised in $[ChCl][ZnCl_2]_2$ while there were more C4 type carbons in lignin-based HCPs synthesised in $[ChCl][FeCl_3]_2$. This meant the formation of ester groups, resulting from esterifications between the hydroxyl phenyl unit and the phenolic hydroxyl groups of lignin, were more likely to occur in $[ChCl][FeCl_3]_2$.

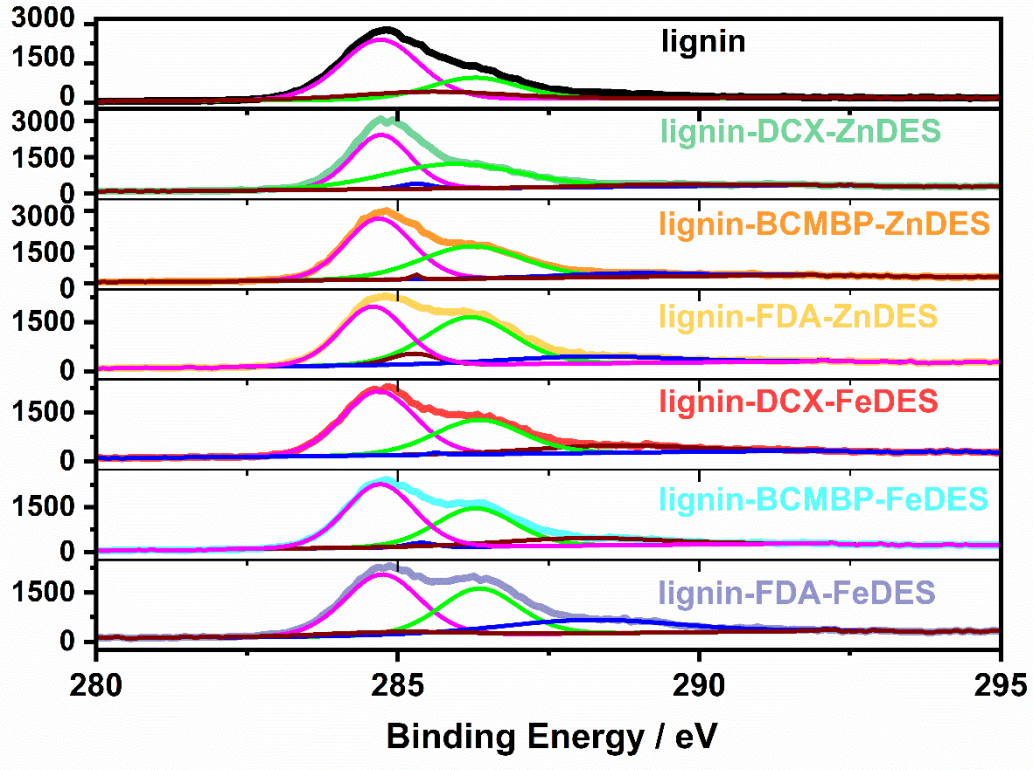


Figure 6-4: C1s spectra of pristine lignin and lignin-based HCPs

Table 6-2: Chemical compositions of carbons in lignin and its six HCP derivatives studied here in this work based on the deconvolution of XPS C 1s spectra

| Sample | C 1s Peak Area (%) | | | |
|---|---|---|---|---|
| | C1 (284.7 ± 0.1 eV) C-C / C=C | C2 (285.3 ± 0.3 eV) C-O-C / C-OH | C3 (286.2 ± 0.3 eV) Ph-OH/C=O | C4 (288.5 ± 0.4 eV) -COO |
| lignin | 56.7 | 13.4 | 22.7 | 7.2 |
| lignin-DCX-ZnDES | 46.4 | 2.2 | 47.9 | 3.5 |
| lignin-BCMBP-ZnDES | 51.5 | 0.5 | 41.8 | 6.2 |
| lignin-FDA-ZnDES | 41.0 | 1.3 | 53.0 | 4.7 |
| lignin-DCX-FeDES | 52.7 | 0.3 | 34.0 | 13.0 |
| lignin-BCMBP-FeDES | 50.0 | 1.4 | 34.9 | 13.7 |
| lignin-FDA-FeDES | 41.2 | 4.7 | 32.6 | 21.5 |

The O 1s spectra (Figure 6-5) could be deconvoluted into two main separate peaks around 531.4 eV (O1) and 533.2 eV (O2). These peaks corresponded to carbonyl groups and hydroxyl or ether groups, respectively (Table 6-3). O2 peak may vary slightly due to the minor difference of the chemical environment of hydroxyl and ether groups, and thus could be denoted as O2a and O2b for better distinction. The XPS O 1s spectrum for pristine lignin could be deconvoluted into two peaks centered at 533 eV and 533.2 eV. This indicated negligible carbonyl groups in pristine lignin. After crosslinking in different DES systems using halogenated crosslinkers (DCX, BCMBP), the O 1s spectra of resultant HCPs exhibited an asymmetric peak with lower binding energy, implicating that a significant increase in C=O content. This could be ascribed to successful esterification or the oxidation of C-O bonds during HCP synthesis. This result also indicated that [ChCl][$FeCl_3$]$_2$ was more conducive for these reactions as more carbonyl groups were detected. The validity of this conclusion was substantiated by the comparison between the deconvoluted O 1s spectra of lignin-BCMBP-ZnDES and lignin-BCMBP-FeDES. Both of these HCPs contained similar amount of carbonyl groups, but the amount of ester groups in lignin-BCMBP-FeDES were more than double of those in lignin-BCMBP-ZnDES. Similar to pristine lignin, there were no detectable carbonyl groups in lignin-FDA-ZnDES while lignin-FDA-

FeDES contained up to 31.2% of carbonyl groups. This further illustrated the stronger oxidative ability of [ChCl][$FeCl_3$]$_2$. The reduction in O2 peak intensity was indicative of the presence of hydroxyl and ether groups as well a reduction in C-C crosslinks. In [ChCl][$FeCl_3$]$_2$, DCX could lead to forming more C=O groups compared with BCMBP under identical experimental conditions. This could be attributed to the smaller molecule size of DCX which improved its mobility and consequently reactivity [51].

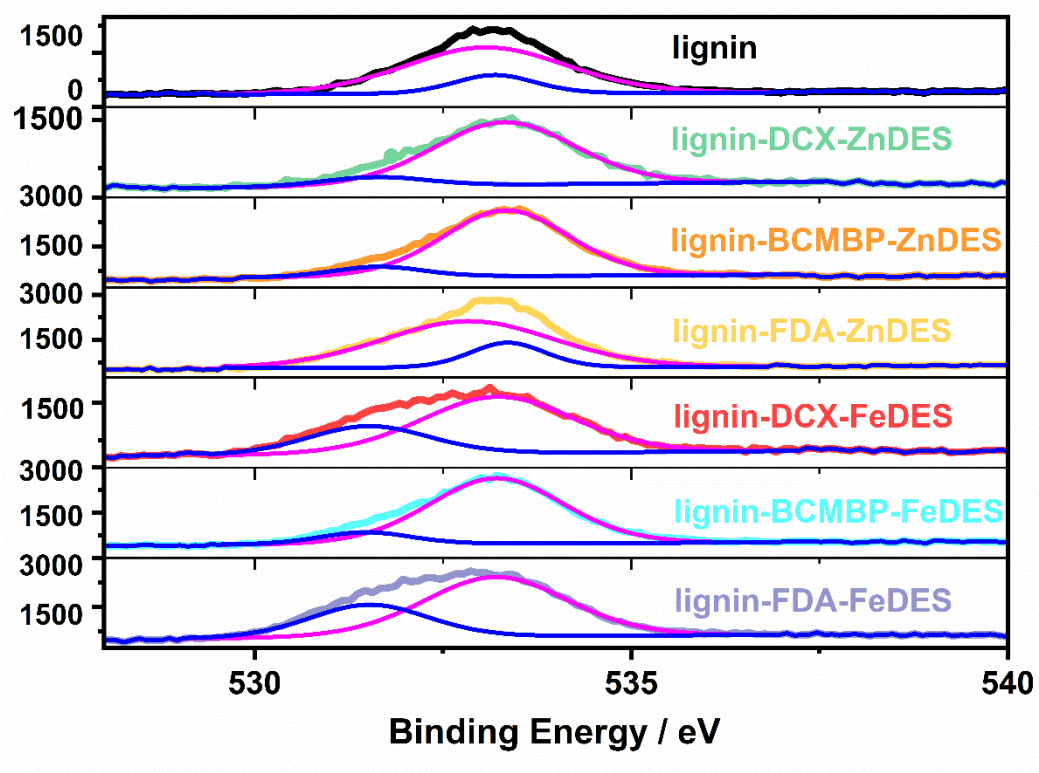


Figure 6-5: O1s spectra of pristine lignin and lignin-based HCPs

Table 6-3: Chemical compositions of oxygens in lignin and its six HCP derivatives studied here in this work based on the deconvolution of XPS O 1s spectra

| Sample | O 1s Peak Area (%) | | |
|---|---|---|---|
| | O1 | O2 | |
| | | O2a | O2b |
| | 531.4 ± 0.2 eV | 533 ± 0.2 eV | 533.2 ± 0.2 eV |
| | C=O | C-OH | C-O-C |
| lignin | - | 86.1 | 13.9 |
| lignin-DCX-ZnDES | 7.95 | 92.1 | |
| lignin-BCMBP-ZnDES | 10.9 | 89.1 | |
| lignin-FDA-ZnDES | - | 79.6 | 20.4 |
| lignin-DCX-FeDES | 25.5 | 74.5 | |
| lignin-BCMBP-FeDES | 10.2 | 89.9 | |
| lignin-FDA-FeDES | 31.2 | 68.8 | |

The morphologies of lignin and its derivative HCPs were characterised with scanning electron microscopy (SEM, Figure 6-6). Pristine lignin appeared an amorphous with aggregated grains of different sizes. The surface of lignin-DCX-ZnDES was rough and porous and consisted of particles with an average diameter of . 4.2 um. This could be ascribed to the enhancement of crosslinking units distributed on the surface. Meanwhile lignin-FDA-ZnDES contained larger size particles with average diameters reaching more than 4 um. Different from particulate lignin-DCX-ZnDES, lignin-BCMBP-ZnDES comprised aggregations of lignin flakes. Lignin-DCX-FeDES and lignin-BCMBP-FeDES also displayed elevated surface roughness and many clusters of particles. The surface morphology of lignin-FDA-FeDES was slightly different as it appeared as a stack of numerous lignin lamellae.

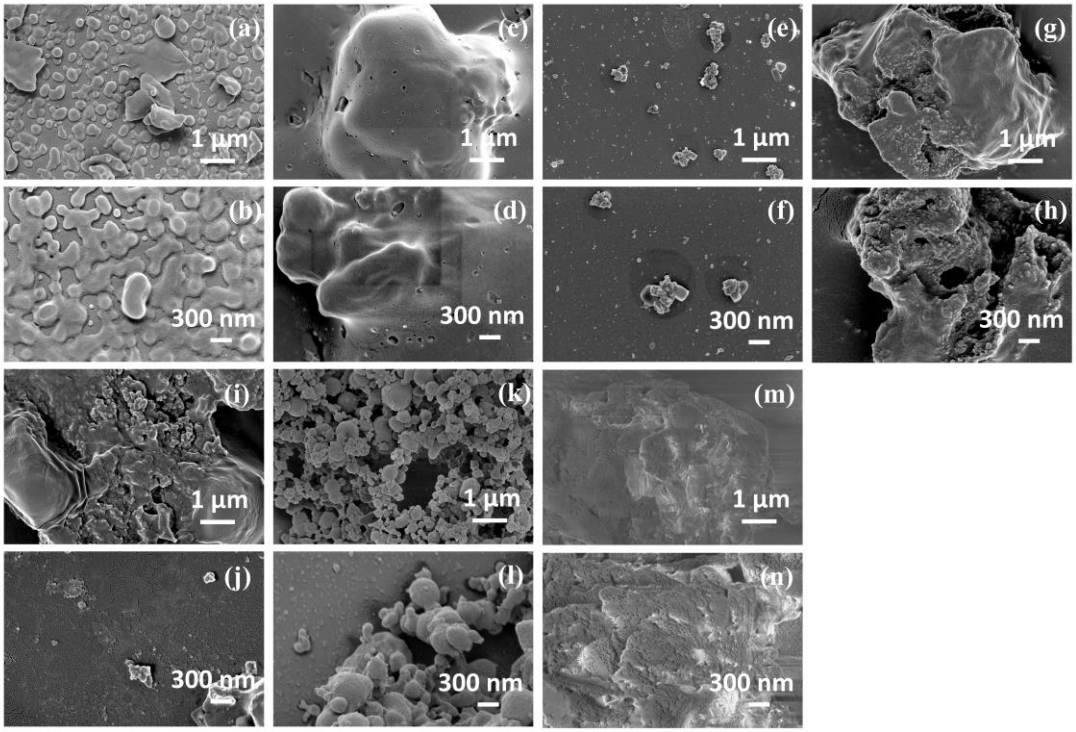


Figure 6-6: SEM images of (a, b) pristine lignin, (c, d) lignin-DCX-ZnDES, (e, f) lignin-BCMBP-ZnDES, (g, h) lignin-FDA-ZnDES, (i, j) lignin-DCX-FeDES, (k, l) lignin-BCMBP-FeDES, (m,n) lignin-FDA-FeDES

### 6.2.2 Textural properties of lignin-based HCPs

The porosities of lignin and our lignin-based HCPs were investigated here by analysing the adsorption and desorption isotherms of $N_2$ at 77 K (Figure 6-7). Pore size distribution (PSD) of all materials studied here was assessed by employing the non-local density functional theory (NLDFT) method on nitrogen adsorption-desorption isotherms (Figure 6-8). Pristine lignin showed negligible $N_2$ uptake. According to IUPAC classification [52], $N_2$ isotherms of pristine lignin were characteristic of Type II, indicating that it was nonporous or macroporous. Together with SEM micrographs (Figure 6-6), it was clear that pristine lignin used in this work was nonporous. As such, the BET surface area of pristine lignin was only 1.2 $m^2\ g^{-1}$. Upon crosslinking, the BET surface areas of all lignin-based HCPs increased.

When dichloroethane (DCE) was used as the solvent [39], the BET surface areas of lignin-DCX-DCE and lignin-BCMBP-DCE (Table 6-4) reached 1118 and 1448 $m^2\ g^{-1}$, respectively, the highest amongst all HCP samples studied here in this work. The $N_2$ isotherms of these lignin-based HCPs synthesised in DCE were characteristic of Type

II materials where micropores are present. However, the BET surface area of lignin-FDA-DCE only reached 1.7 $m^2$ $g^{-1}$ as the $N_2$ uptake of this material was low [52]. In fact, the $N_2$ isotherm of lignin-FDA-DCE was similar to that of pristine lignin. Lignin-based HCPs synthesised in DCE were characteristic of Type II materials and were used as control samples here for elucidating the effects of using DESs for HCP synthesis. The $N_2$ isotherm of lignin-DCX-ZnDES was characteristic of Type I, indicating the existence of micropores. Meanwhile, I observed that the $N_2$ isotherms of lignin-BCMBP-ZnDES and lignin-FDA-ZnDES were similar to Type IV and type H1 hysteresis loop. This suggested mesopores were also present in lignin-BCMBP-ZnDES and lignin-FDA-ZnDES and could cause delayed condensation at the adsorption sites [53].

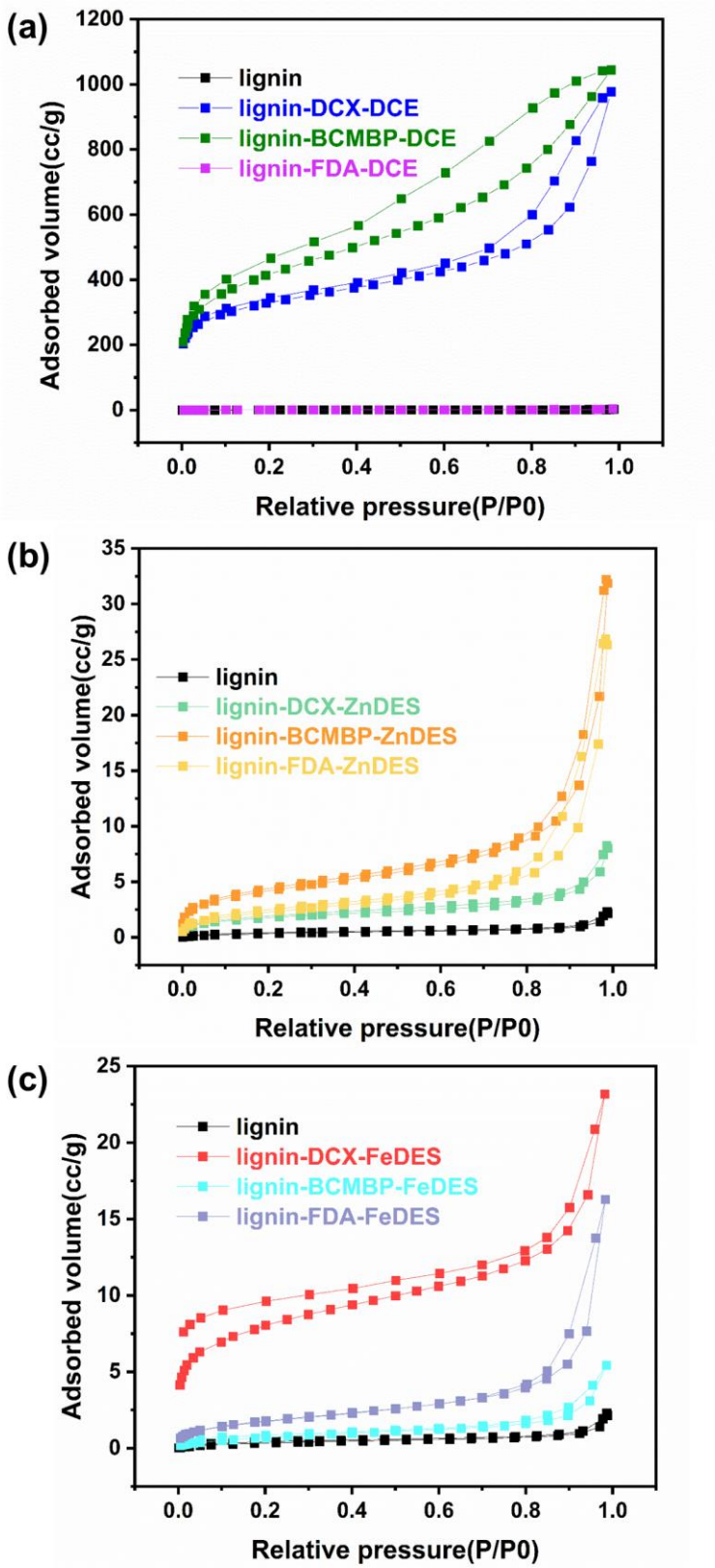


Figure 6-7: $N_2$ isotherms of lignin and lignin-based polymers at 77 K

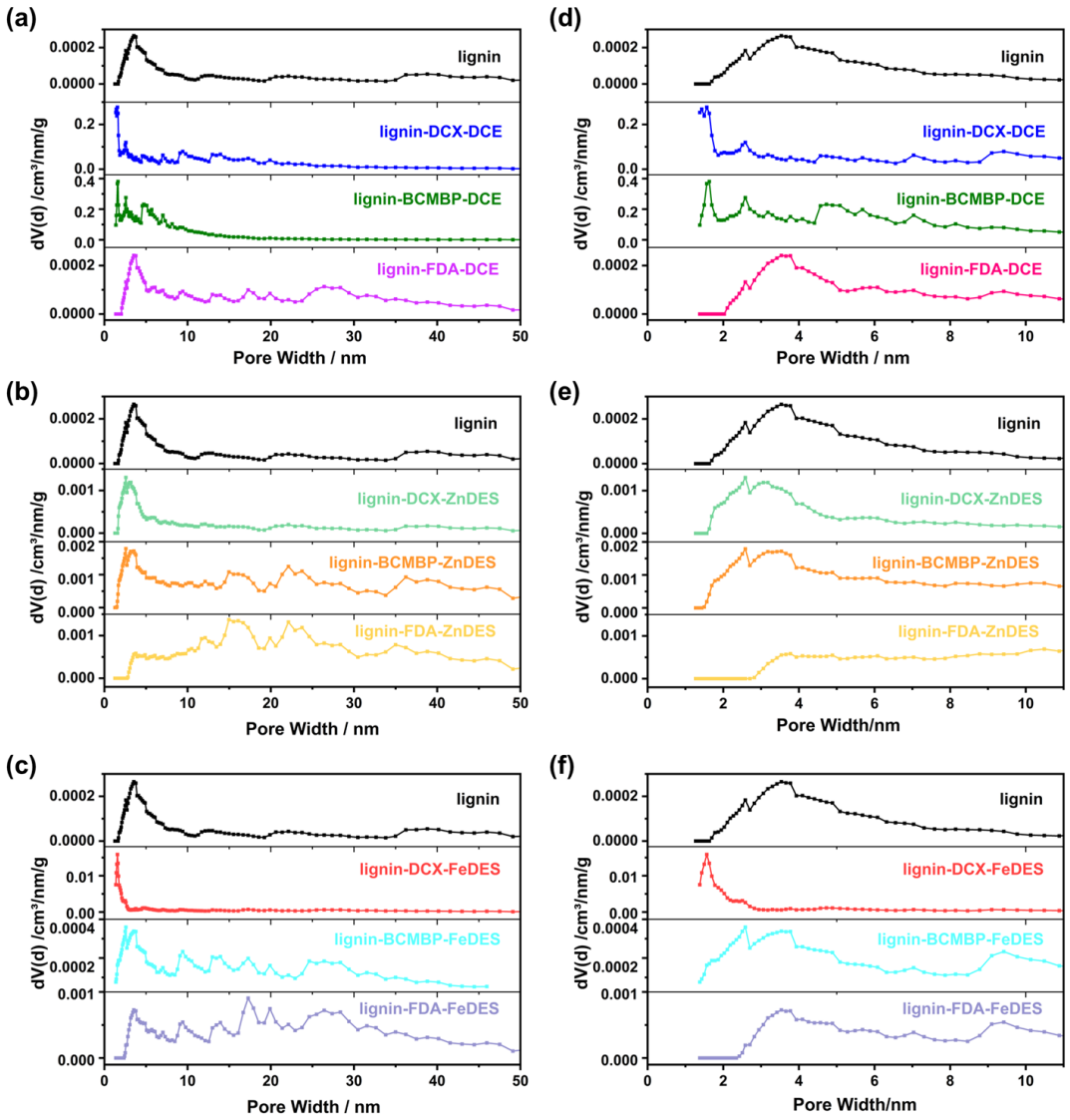


Figure 6-8: (a-c) Pore size distribution (ranging from 0-50 nm) of lignin and lignin-based polymers at 77 K, (d-f) Pore size distribution (ranging from 0-10 nm) of lignin and lignin-based polymers at 77 K

The PSD of these samples also supported these observations. As shown in Figure 6-8, the PSD of lignin-DCX-ZnDES contained pores centred at 2.4 nm while larger mesopores with diameters above 10 nm were present in both lignin-BCMBP-ZnDES and lignin-FDA-ZnDES. These trends were also observed in lignin-based HCPs synthesised observed in [ChCl][$FeCl_3$]$_2$. The BET surface area of lignin-DCX-FeDES reached 27.5 $m^2$ $g^{-1}$, the highest among all lignin-based HCPs synthesised in DESs. Compared to other lignin-based HCPs developed here in this work, the pore size

distribution of lignin-DCX-FeDES was narrower, with a single distinctive peak centred at 1.6 nm. On the contrary, both lignin-BCMBP-FeDES and lignin-FDA-FeDES contained hierarchical pore structures where micropores and mesopores were present.

In summary, I observed that the pore size distributions of lignin-DCX HCPs were quasi-unimodal comprising pores < 5 nm (Figure 6-9), while lignin-BCMBP HCPs comprised a mixture of micropores and mesopores, similar to most other HCPs. Interestingly, lignin-FDA HCPs were mostly mesoporous. The amount of micropores in lignin-DCX-FeDES was the highest amongst all lignin-based HCPs synthesised in DESs. The quasi-unimodal pore size distribution of lignin-DCX-FeDES spanned across a narrow region of 1.5 – 3 nm. Most pores in this material were microporous, with a small portion of mesopores that were less than 3 nm. This was also why the $N_2$ adsorption isotherm of lignin-DCX-FeDES displayed a hysteresis loop that did not close at the lowest relative pressure point. The combination effect of extremely small pores and accessibility issues arising from the pore topology in the lignin-DCX-FeDES should be responsible for it.

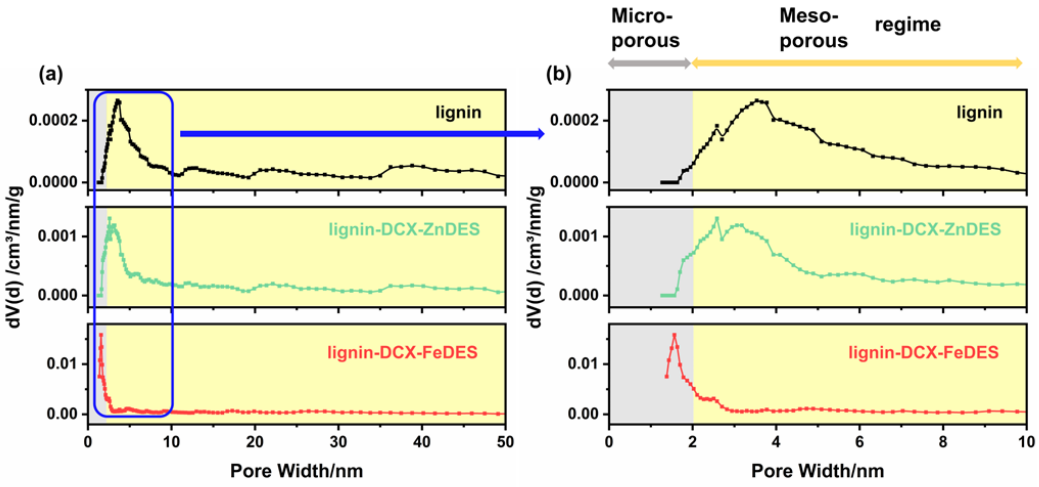


Figure 6-9: Pore size distributions of lignin (black), lignin-DCX-ZnDES (green) and lignin-DCX-FeDES (red) using $N_2$ adsorption isotherms at 77 K. The grey and yellow regions correspond to the dimensions of micropores (< 2nm) and mesopores (2 – 50 nm) as defined by IUPAC classifications.

Using $CO_2$ molecules as the adsorbate at 273 K has been an accepted supplementary method for studying materials with very narrow pores [54,55]. This was due to the smaller effective kinetic diameter of $CO_2$ molecules (3.3 Å) within solid phase when compared to those of $N_2$ molecules (3.8 Å) [56,57]. In addition, the saturation vapour pressure of $CO_2$ at 273 K could reach 3.5 MPa, resulting in easily-achieved moderate-range pressures (0.1 – 100 kPa) for micropore size analysis [52]. Figure 6-10 further confirmed the existence of ultra-narrow micropores in the lignin-DCX-ZnDES and lignin-DCX-FeDES polymers. Both samples showed the new-added micropores around 0.3 nm, compared with pristine lignin. Moreover, most micropores of lignin-DCX-ZnDES distributed between 0.44 nm and 0.69 nm while those of lignin-DCX-FeDES located at 0.46 nm and 0.55 nm, proving that the pore volume of DCX-crosslinked lignin greatly improved.

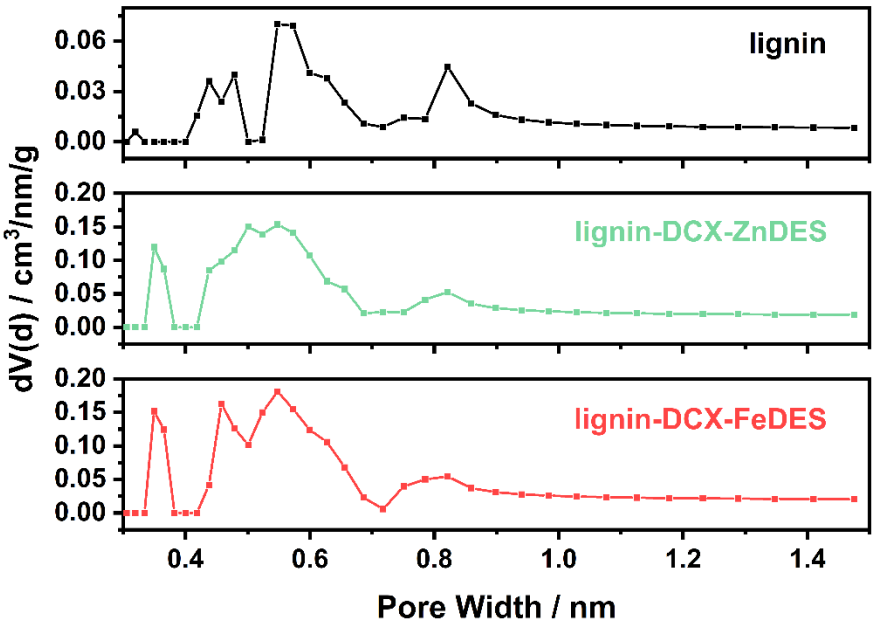


Figure 6-10: Pore size distributions of lignin (black), lignin-DCX-ZnDES (green) and lignin-DCX-FeDES (red) using $CO_2$ adsorption isotherms at 273 K.

Hence, I also used the Grand-Canonical Monte-Carlo (GCMC) method to determine the specific surface areas ($S_{GCMC}$) and pore volumes of samples studied here from

their $CO_2$ adsorption isotherms obtained at 273 K (Table 6-4). Except for lignin-DCX-DCE and lignin-BCMBP-DCE, the $S_{GCMC}$ of other lignin-based HCPs were higher than their $S_{BET}$, validating the presence of ultra-narrow pores which were inaccessible to $N_2$ molecules. Compared to their $S_{BET}$, the $S_{GCMC}$ of lignin-DCX-DCE and lignin-BCMBP-DCE were reduced by more than 50%, indicating a low proportion of ultra-narrow pores. I also observed that the $CO_2$ uptakes of all materials studied here were related to their $S_{GCMC}$ instead of $S_{BET}$. In other words, high $S_{GCMC}$ values usually implied enhanced $CO_2$ uptake. Regardless of calculation method used for determining the textural properties of our HCPs, it was clear that crosslinking of lignin in DESs generated less porous HCPs than those crosslinked in a halogenated solvent like DCE.

Table 6-4: Porosity parameters of lignin-based HCPs

| Sample | $S_{BET}$[a] ($m^2\ g^{-1}$) | $V_{pore}$[a] ($cm^3\ g^{-1}$) | $S_{GCMC}$[b] ($m^2\ g^{-1}$) | $V_{pore}$[b] ($cm^3\ g^{-1}$) | $CO_2$ uptake[c] ($cm^3\ g^{-1}$) |
|---|---|---|---|---|---|
| lignin | 1.2 | 0.003 | 54.9 | 0.02 | 5.2 |
| lignin-DCX-DCE | 1117 | 1.43 | 619 | 0.21 | 62.3 |
| lignin-BCMBP-DCE | 1447 | 1.55 | 618 | 0.24 | 57.7 |
| lignin-FDA-DCE | 1.7 | 0.003 | 235 | 0.07 | 24.2 |
| lignin-DCX-ZnDES | 6.2 | 0.01 | 179 | 0.06 | 15.6 |
| lignin-BCMBP-ZnDES | 14.7 | 0.04 | 149 | 0.05 | 15 |
| lignin-FDA-ZnDES | 8.2 | 0.04 | 119 | 0.04 | 11.8 |
| lignin-DCX-FeDES | 27.5 | 0.03 | 175 | 0.06 | 18.1 |
| lignin-BCMBP-FeDES | 2.7 | 0.006 | 83 | 0.03 | 8.4 |
| lignin-FDA-FeDES | 6.5 | 0.02 | 138 | 0.05 | 13.4 |

[a] Determination of specific surface area and pore volume from nitrogen adsorption isotherms obtained at 77 K. [b] Specific surface area and pore volume determined from carbon dioxide adsorption isotherms obtained at 273 K using GCMC method. [c] $CO_2$ uptake was obtained from the adsorption process at 273 K and 1 bar.

From $CO_2$ adsorption isotherms collected at 273 K (Figure 6-11a), I observed that the amount of $CO_2$ adsorbed in all six lignin-based HCPs increased steadily as the relative pressure increased from 0 to 1. The $CO_2$ uptake of pristine lignin reached 5.2 $cm^3\ g^{-1}$,

the lowest amongst all samples studied here. This could be attributed to the non-porous nature of pristine lignin. Upon crosslinking in DCE, the $CO_2$ uptake of lignin-DCX-DCE and lignin-BCMBP-DCE increased to 62.3 and 57.7 $cm^3\ g^{-1}$, respectively. This was mainly attributed to their outstanding BET surface areas and high pore volume content. Despite a low $S_{BET}$ of 1.7 $m^2\ g^{-1}$, the $CO_2$ uptake of lignin-FDA-DCE reached 24.2 $cm^3\ g^{-1}$. This was due to a pore volume that was 5-fold more than that of pristine lignin. Despite similar $S_{GCMC}$ and pore volumes, the $CO_2$ uptake of lignin-DCX-FeDES (18.1 $cm^3\ g^{-1}$) was 13.1% higher than that of lignin-DCX-ZnDES (15.6 $cm^3\ g^{-1}$). This could be attributed to the difference in pore size uniformity. In lignin-DCX-FeDES, there were 0.001 $cm^3\ g^{-1}$ of 1.6 nm pores while in lignin-DCX-ZnDES the PSD in this region was heterogenous, comprising $1.9\times10^{-4}$ $cm^3\ g^{-1}$ of 1.9 nm and 2.8 nm pores. The higher $CO_2$ uptake in lignin-DCX-FeDES could also be attributed to the presence of significant C=O functional groups where the peak intensity for C=O groups was 3.2-fold higher than that of lignin-DCX-ZnDES (Table 6-2). This highlighted the importance of a combination of narrower PSD and enhanced $CO_2$ affinity that favoured the adsorption of $CO_2$ molecules. As the pore size distributions of other lignin-based HCPs synthesised in DESs were not as uniform and contained a significant portion of mesopores (when compared to micropores), the $CO_2$ uptakes of lignin-BCMBP-ZnDES (15 $cm^3\ g^{-1}$), lignin-FDA-FeDES (13.4 $cm^3\ g^{-1}$), lignin-FDA-ZnDES (11.8 $cm^3\ g^{-1}$) and lignin-BCMBP-FeDES (8.4 $cm^3\ g^{-1}$) were lower.

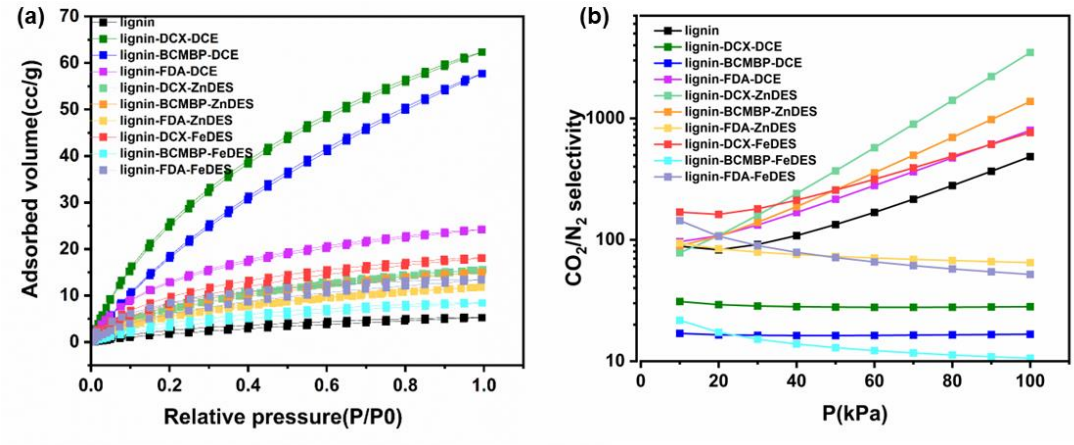


Figure 6-11: (a) $CO_2$ isotherms of lignin and lignin-based polymers at 273 K, (b) $CO_2/N_2$ selectivity of lignin and lignin-based polymers under 298 K (black curve: lignin, olive green curve: lignin-DCX-DCE, blue curve: lignin-BCMBP-DCE, pink curve: lignin-FDA-DCE, pale green curve: lignin-DCX-ZnDES, orange curve: lignin-BCMBP-ZnDES, yellow curve: lignin-FDA-ZnDES, red curve: lignin-DCX-FeDES, sky blue curve: lignin-BCMBP-FeDES, lilac curve: lignin-FDA-FeDES )

Another important evaluation indicator for porous materials is gas selectivity. Here, we used the ideal adsorbed solution theory (IAST) method [58] to determine the $CO_2/N_2$ selectivity of our materials using a simulated binary $CO_2/N_2$ gas mixture ($CO_2$: $N_2$=15:85) and the $CO_2$ and $N_2$ adsorption isotherms at 298 K (Figure 6-11b). This gas mixture was chosen here to simulate post-combustion gas mixtures [59]. Details of the IAST calculations and fitting parameters could be found in Table 6-5. Here it is highlighted that the IAST method is a simulation technique for predicting the gas selectivity from isotherms of pure gas components. While IAST simulation can offer some insight into gas selectivity, it does not entirely mirror the actual scenario. The $S_{BET}$ and $N_2$ uptake at 77 K of lignin, lignin-FDA-DCE and our lignin-based HCPs were quite low, ranging from 1.2 to 27.5 $m^2\ g^{-1}$ and 2.3 to 32.2 $cm^3\ g^{-1}$, respectively. As such, the IAST $CO_2/N_2$ selectivity of lignin-DCX-DCE and lignin-BCMBP-DCE reached 28.1 and 16.7, respectively. This was ascribed to hierarchical pore structures and abundant micropores contributing to competitive sorption between $CO_2$ and $N_2$ molecules [60]. However, the IAST $CO_2/N_2$ selectivity of lignin-FDA-DCE reached a value of 797. This could be explained by a low $S_{BET}$ (< 2 $m^2\ g^{-1}$) that resulted in preferential adsorption of $CO_2$ over $N_2$. The process of $CO_2$ adsorption is a complex

phenomenon that involves both physical and chemical aspects depending on whether chemical bonds form [61]. In the physisorption of $CO_2$, the interactions between $CO_2$ molecules and solid surface are mainly determined by the electric quadrupole moment-electric field gradient interaction. In the binary gas mixtures comprising $N_2$ and $CO_2$, the electric quadrupole moment of $CO_2$ is approximately three times greater than that of $N_2$ [56,62].This significant difference amplifies its interactions with the electrical field gradients present in porous materials, resulting in a stronger bond compared to $N_2$. Therefore, in gas mixtures of $CO_2$ and $N_2$, the affinity of $CO_2$ for surfaces is notably higher, showcasing the selectivity and distinct behaviour of these molecules in adsorption process.

Table 6-5: Fitted Parameters of $CO_2$ and $N_2$ adsorption isotherms using SSLF model under 298 K.

| Sample | adsorbate | q | b | n | $R^2$ |
|---|---|---|---|---|---|
| lignin | $CO_2$ | 11.27502 | 0.004 | 0.94545 | 0.99998 |
| lignin | $N_2$ | 0.14362 | 1.06065E-4 | 1.96132 | 0.99684 |
| lignin-DCX-DCE | $CO_2$ | 146.2844 | 0.00819 | 0.88509 | 0.99997 |
| lignin-DCX-DCE | $N_2$ | 36.36332 | 0.00116 | 0.99729 | 0.99999 |
| lignin-BCMBP-DCE | $CO_2$ | 170.27043 | 0.00303 | 0.92998 | 0.99998 |
| lignin-BCMBP-DCE | $N_2$ | 27.58242 | 0.00118 | 0.98939 | 0.99997 |
| lignin-FDA-DCE | $CO_2$ | 33.53963 | 0.02262 | 0.8014 | 0.99987 |
| lignin-FDA-DCE | $N_2$ | 1.52786 | 0.0026 | 1.34679 | 0.9997 |
| lignin-DCX-ZnDES | $CO_2$ | 38.14456 | 0.00734 | 0.85672 | 0.99991 |
| lignin-DCX-ZnDES | $N_2$ | 0.33948 | 0.00566 | 1.447 | 0.9919 |
| lignin-BCMBP-ZnDES | $CO_2$ | 33.3083 | 0.00811 | 0.83365 | 0.99992 |
| lignin-BCMBP-ZnDES | $N_2$ | 0.53887 | 0.0037 | 1.27682 | 0.99958 |
| lignin-FDA-ZnDES | $CO_2$ | 26.68543 | 0.00855 | 0.82994 | 0.99992 |
| lignin-FDA-ZnDES | $N_2$ | 157.37054 | 1.91556E-5 | 0.97176 | 0.99978 |
| lignin-DCX-FeDES | $CO_2$ | 31.93557 | 0.01479 | 0.80827 | 0.99994 |
| lignin-DCX-FeDES | $N_2$ | 1.13567 | 1.16236E-4 | 1.80577 | 0.99771 |
| lignin-BCMBP-FeDES | $CO_2$ | 21.64021 | 0.00616 | 0.86483 | 0.99992 |
| lignin-BCMBP-FeDES | $N_2$ | 9.36479 | 3.29626E-4 | 1.26807 | 0.99973 |
| lignin-FDA-FeDES | $CO_2$ | 26.18034 | 0.02372 | 0.73459 | 0.99984 |
| lignin-FDA-FeDES | $N_2$ | 435.11472 | 3.92684E-6 | 1.24401 | 0.99974 |

The isosteric heat (Qst) of $CO_2$ adsorption as a function of $CO_2$ uptake was obtained from their $CO_2$ isotherms under 273 K and 298 K using Clausius-Clapeyron equation. As shown in Figure 6-12, the Qst of adsorption at zero coverage (Q→0) of all lignin-based HCPs ranged from 10-43 kJ $mol^{-1}$, indicating physisorption was dominant in the $CO_2$ adsorptions. Previous report proposed that chemisorption for $CO_2$ (60-90 kJ $mol^{-1}$) generally have higher isosteric heat than that of physisorption (25-50 kJ $mol^{-1}$) [63]. The Qst of the three lignin-based HCPs synthesised in $[ChCl][ZnCl_2]_2$ decreased with the adsorbed amount of $CO_2$. This could be attributed to the heterogeneity of the adsorption sites inside the adsorbents [64]. However, the Qst of the three lignin-based HCPs synthesised in $[ChCl][FeCl_3]_2$ started to rise after $CO_2$ loading reached 0.4 mmol, illustrating stronger interactions between the adsorbents and $CO_2$. This abnormal phenomenon could be assigned to the dipolar interaction of $CO_2$-$CO_2$, and interaction between $CO_2$ and more accessed carbonyl sites. The data of isosteric heat provided supportive evidence for the comparatively higher $CO_2$ uptake of lignin-based HCPs synthesised in $[ChCl][FeCl_3]_2$. Additionally, lignin-based HCPs synthesised in $[ChCl][FeCl_3]_2$ had lower Qst (Q→0), which meant it would be easier to regenerate these adsorbents.

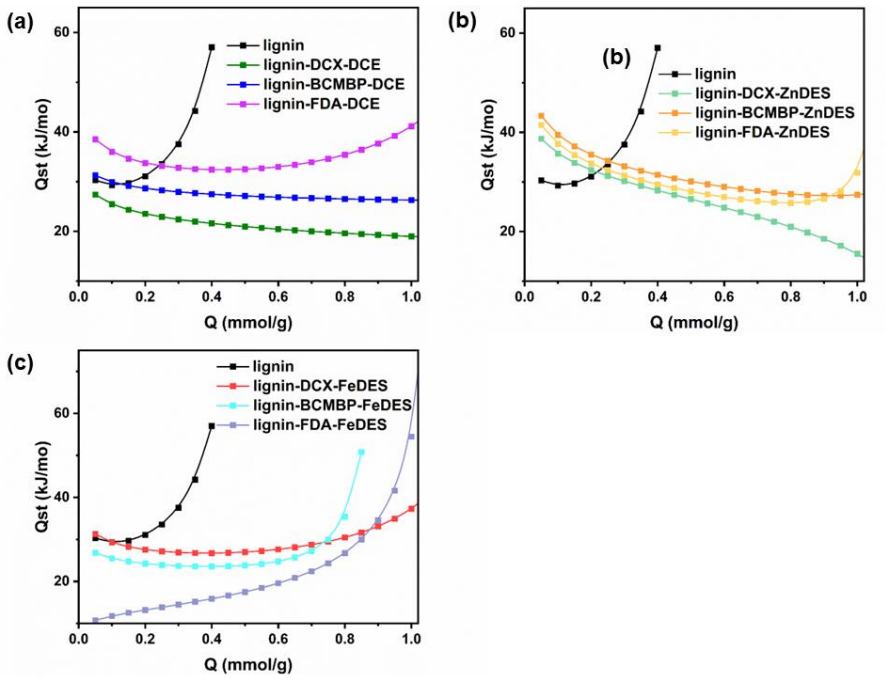


Figure 6-12: Isosteric heat for $CO_2$ adsorption using (a)lignin and lignin-based HCPs synthesised in DCE, (b) lignin and lignin-based HCPs synthesised in $[ChCl][ZnCl_2]_2$, (c) lignin and lignin-based HCPs synthesised in $[ChCl][FeCl_3]_2$

Among the six lignin-based HCPs synthesised in DESs, the IAST $CO_2/N_2$ selectivity of both lignin-DCX-ZnDES and lignin-DCX-FeDES were expected to be significantly high due to their uniform narrow PSDs in the micropore region and lack of mesopores. As expected, the IAST $CO_2/N_2$ selectivity of these materials reached 3484 and 764, respectively. Additionally, the IAST $CO_2/N_2$ selectivity of lignin-BCMBP-ZnDES reached 1378. These three samples, lignin-DCX-ZnDES, ligini-BCMBP-ZnDES and lignin-DCX-FeDES, all displayed a rising trend of $CO_2/N_2$ selectivity with the pressure increasing. These IAST $CO_2/N_2$ selectivity results are competitive even when comparing with previous reported porous adsorbents such as MIP-202 (2129) [65], zeolite 13X (~500), USTA-16 (315) [66], JUK-13-SO3H-SO2 (255) [67] etc. Here it is important to highlight that due to the exothermic nature of adsorption, the amount of $N_2$ adsorbed in these samples at 298 K was lesser than that at 77 K (Figure 6-13a). This was similar to reports elsewhere [56]. As a result, the extremely low $N_2$ uptake at 298 K that were used in our IAST simulations could drastically affect the $CO_2/N_2$ selectivity value. The IAST $CO_2/N_2$ selectivity of lignin-

FDA-ZnDES, lignin-BCMBP-FeDES and lignin-FDA-FeDES were reduced slightly at elevated pressures.

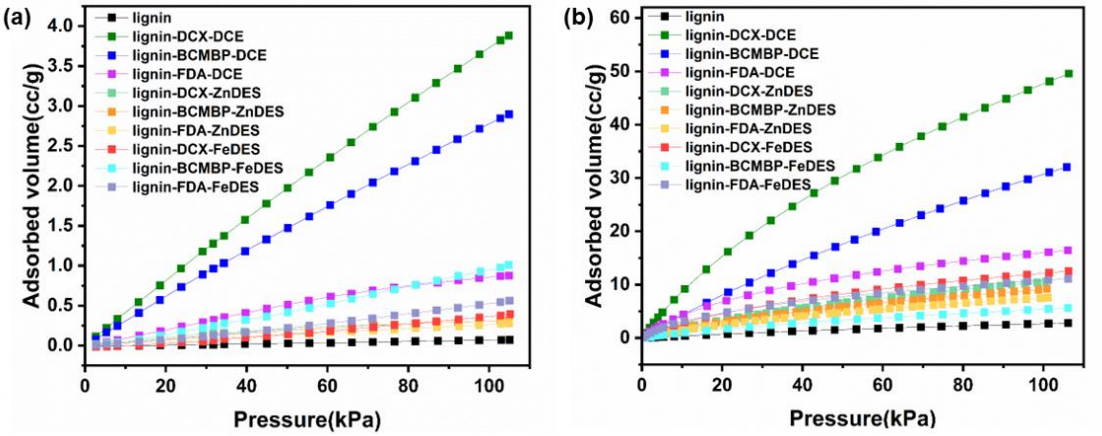


Figure 6-13: (a) $N_2$ isotherms of lignin and all lignin-based HCPs under 298 K, (b) $CO_2$ isotherms of lignin and all lignin-based HCPs under 298 K

### 6.2.3 $CO_2$ capture performance from binary gas mixtures

To validate the IAST $CO_2/N_2$ selectivity of our materials, we evaluated the real $CO_2/N_2$ selectivity of our materials using a binary gas mixture comprising 15 v/v% $CO_2$ and 85 v/v% $N_2$ (Table 6-6) at 1 bar, 298 K. Here, this component ratio was selected to keep consistency with the gas mixture used in the IAST method and also to model real-world post-combustion gas. Each testing duration for adsorption process is 10 minutes. The concentration of $CO_2$ in the out-flue gas can be obtained directly from the detector while the concentration of $N_2$ is indirectly calculated from the difference between total gas amount and $CO_2$ component. This means that the fluctuations in the actual feed gas mixtures may be factored into the nitrogen uptake, resulting in higher $N_2$ uptakes. This can thus explain the abnormal result that lignin sample have higher $N_2$ capacity than other HCPs samples. The mixed gas $CO_2$ uptake of all HCPs studied here were lower than those obtained from pure gases due to the low concentration of $CO_2$ in the mixed gas and their competitive adsorption [68]. Amongst the lignin-based HCPs that were synthesised in DESs, the mixed gas $CO_2$ uptakes of lignin-BCMBP-ZnDES and lignin-FDA-ZnDES were the highest, reaching 7.1 $cm^3\ g^{-1}$ and 6.9 $cm^3\ g^{-1}$, respectively. The mixed gas $CO_2$ uptake of lignin-DCX-

ZnDES only reached 4.4 $cm^3$ $g^{-1}$. This was different from the $CO_2$ uptake of these materials that were obtained with pure $CO_2$ where the $CO_2$ uptake of lignin-DCX-ZnDES was the highest amongst these three materials. The low mixed gas $CO_2$ capacity of lignin-DCX-ZnDES was attributed to a lack of mesopore content in this material. Meanwhile the mixed gas $CO_2$ uptakes of lignin-BCMBP-FeDES, lignin-DCX-FeDES and lignin-FDA-FeDES reached 6.6, 4.5 and 3.9 $cm^3$ $g^{-1}$, respectively. The trends in mixed gas $CO_2$ uptake of lignin-based HCPs synthesised in $[ChCl_2][FeCl_3]_2$ also differed from those obtained using pure $CO_2$ gas where the pure gas $CO_2$ uptake of lignin-DCX-FeDES was the highest amongst all HCPs synthesised here in DESs. These differences could be attributed to the complicated nature of competitive adsorption of gas mixtures on porous materials where this process could be influenced by thermodynamic and kinetic factors [69]. The effects of competitive sorption between $CO_2$ and $N_2$ molecules in binary gases also impacted on mixed gas $N_2$ uptake of HCPs studied in this work (Table 6-6). As expected, all lignin-based HCPs displayed scant $N_2$ uptakes and most samples had lower mixed gas $N_2$ uptake than their pure gas $N_2$ uptake. Such decrease has been previously reported to widely exist in the binary gas system due to the competitive adsorption between $CO_2$ and $N_2$ molecules [70]. Especially, $CO_2$ occupied dominant adsorption sites as it has higher affinity to them, further reducing the $N_2$ uptake. Lignin-DCX-FeDES demonstrated the least $N_2$ uptake (0.03 $cm^3$ $g^{-1}$), explaining its superior $CO_2/N_2$ selectivity in the practical use. Among the lignin-based HCPs synthesised in DESs, their order of the $N_2$ uptake was also different from that concluded from pure gas adsorption isotherms. The capacity order of these six lignin-based HCPs for $N_2$ capture from the gas mixture was lignin-FDA-ZnDES > lignin-BCMBP-FeDES > lignin-DCX-ZnDES > lignin-BCMBP-ZnDES > lignin-FDA-FeDES > lignin-DCX-FeDES. The obvious drop in mixed gas $N_2$ uptake indicated that $CO_2$ had an overwhelming advantage over $N_2$. The mixed gas $CO_2/N_2$ selectivity of pristine lignin and its derivatised HCPs were calculated using $CO_2$ and $N_2$ content in output streams, as shown in Table 6-6. The $CO_2/N_2$ selectivity of pristine lignin was the lowest, reaching a value of 2.6, in

addition to its lowest mixed gas $CO_2$ capacity of 3.4 $cm^3$ $g^{-1}$. Amongst all lignin-based HCPs studied here in this work, the mixed gas $CO_2/N_2$ selectivity of lignin-DCX-FeDES was the highest, reaching 835. This could be attributed to its abundant (10 times more than other HCPs developed here) uniform narrow micropore configuration and lack of mesopores. Comparing the three HCPs synthesised in $[ChCl][FeCl_3]_2$, we observed the trade-off between $CO_2$ uptake and selectivity. The mixed gas $CO_2/N_2$ selectivity order was consistent with that calculated using the IAST method. Meanwhile, for HCPs synthesised in $[ChCl][ZnCl_2]_2$, we observed that the mixed gas $CO_2/N_2$ selectivity of lignin-DCX-ZnDES was mediocre, reaching a value of 9.7, which was 359 times lower than IAST $CO_2/N_2$ selectivity. Despite possessing uniform pores (around 2.4 nm) in lignin-DCX-ZnDES and minimal mesopores (similar to lignin-DCX-FeDES), there were one magnitude less of these micropores. This consequently reduced both mixed gas $CO_2$ and $N_2$ uptakes. These results indicated that the capture of $CO_2$ from mixed gas using porous materials would be significantly impacted by additional components with a high spreading pressure. The disparities between the simulated IAST $CO_2/N_2$ selectivity and experimentally determined mixed gas $CO_2/N_2$ selectivity could be ascribed to weak $N_2$ adsorption of lignin-based HCPs developed in this work, leading to the inaccuracy of IAST simulations. Such discrepancies are not novel, as previous studies have indicated that IAST are less accurate in predicting the surface excess of the component that exhibit weaker adsorption characteristics [70]. This is because IAST simulations rely on the extrapolation of the single-component isotherms. Especially for the $CO_2/N_2$ binary system, this key factor is responsible for the poorer agreement with practical experimental data [71].

Table 6-6: The capacity of lignin-based HCPs synthesised in the DESs for $CO_2$ and $N_2$ in the mixed gas

| Sample | Capacity for $CO_2$ (mg $g^{-1}$) | Capacity for $CO_2$ ($cm^3$ $g^{-1}$) | Capacity for $N_2$ (mg $g^{-1}$) | Capacity for $N_2$ ($cm^3$ $g^{-1}$) | Selectivity |
|---|---|---|---|---|---|
| lignin | 6.67 | 3.7 | 4.86 | 4.2 | 4.9 |
| lignin-DCX-ZnDES | 7.87 | 4.4 | 1.4 | 1.2 | 20.2 |
| lignin-BCMBP-ZnDES | 12.67 | 7.1 | 0.86 | 0.8 | 47.1 |
| lignin-FDA-ZnDES | 12.35 | 6.9 | 2.7 | 2.4 | 16.6 |
| lignin-DCX-FeDES | 8.11 | 4.5 | 0.03 | 0.03 | 835.4 |
| lignin-BCMBP-FeDES | 11.86 | 6.6 | 1.64 | 1.4 | 26.0 |
| lignin-FDA-FeDES | 6.96 | 3.9 | 0.10 | 0.09 | 227 |

I also evaluated the kinetics of $CO_2$ uptake from binary $CO_2$: $N_2$ gas mixtures (Figure 6-14). During $CO_2$ capture using a binary $CO_2$: $N_2$ gas mixture, fast $CO_2$ adsorption took place after a short adaptation period of 30 seconds due to overcoming the starting flow resistance. After 5 minutes, $CO_2$ adsorption in almost all samples gradually reached saturation, entering a plateau phase in which adsorption proceeded slowly (Figure 6-14a).

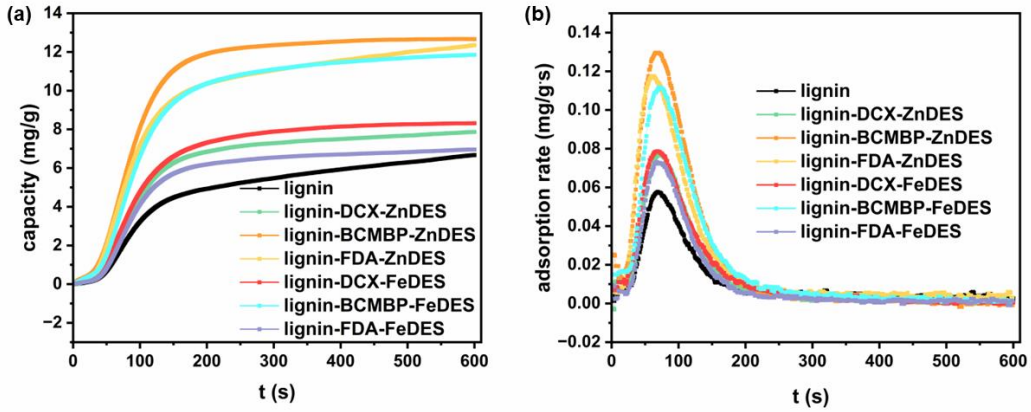


Figure 6-14: (a) $CO_2$ adsorption capacity of lignin and six lignin-based HCPs synthesised in two DESs, (b) $CO_2$ adsorption rate of lignin and six lignin-based HCPs synthesised in two DESs

Here, two models including pseudo-first order and pseudo-second order were deployed to fit the $CO_2$ adsorption behaviours. The fitted parameters and calculated adsorption capacity by both models were shown in Table 6-7. Pseudo-first order model assumes that the process follows first-order kinetics, implying that the rate of the reaction is directly proportional to one parameter. In the $CO_2$ adsorption, it refers to the amount of free adsorption sites. Typically, this model is described as the following equation and used to explain physical adsorption process:

$$q_t = q_e(1 - e^{-k_1 t}) \quad (1)$$

where $q_t$ and $q_e$ refer to the amount of $CO_2$ adsorbed by per gram of adsorbents at any time $t$ and saturated time respectively, $k_1$ represents the rate constant of Pseudo-first order model.

Pseudo-second order model assumes that the reaction follows second-order kinetics, suggesting that the rate of the reaction is directly proportional to the square of specific parameter [72]. The equation of this model is shown below:

$$q_t = \frac{{q_e}^2 k_2 t}{1 + q_e k_2 t} \quad (2)$$

where $k_2$ is the rate constant of Pseudo-second order model. For better accuracy, the fitting parameters of both kinetic models were calculated using non-linear regression with the Origin 2023 software [73].

The validity of both adsorption kinetics models can be evaluated by the coefficient of determination ($R^2$) from non-linear regression and the normalised standard deviation (Δq %) which can be calculated by equation (3) [74]:

$$\Delta q(\%) = 100\sqrt{\frac{\sum\left[\frac{\left(q_{exp} - q_{cal}\right)}{q_{exp}}\right]^2}{n-1}} \quad (3)$$

where $q_{exp}$ and $q_{cal}$ are the amount of $CO_2$ capacity obtained from the real-time experiments and kinetic models respectively, n is the number of data points.

Table 6-7: Parameters of pseudo-first order, pseudo-second order for $CO_2$ adsorption from mixed gas using pristine lignin and its six derivative HCPs. All tests were performed at atmosphere pressure and room temperature

| Sample | Pseudo-first order | | | | | Pseudo-second order | | | |
|---|---|---|---|---|---|---|---|---|---|
| | $q_{e,exp}$ (mg $g^{-1}$) | $q_{e,cal}$ (mg $g^{-1}$) | $k_1$ ($s^{-1}$) | $R^2$ | Error Δq % | $q_{e,cal}$ (mg $g^{-1}$) | $k_2$ ($s^{-1}$) | $R^2$ | Error Δq % |
| lignin | 6.67 | 6.56439 | 0.00644 | 0.95709 | 29.38 | 8.46396 | 0.000723 | 0.947 | 34.40 |
| lignin-DCX-ZnDES | 7.87 | 7.88888 | 0.00856 | 0.9241 | 27.32 | 9.66311 | 0.000946 | 0.877 | 32.03 |
| lignin-BCMBP-ZnDES | 12.67 | 12.93811 | 0.01001 | 0.90646 | 22.28 | 15.36818 | 0.000761 | 0.833 | 26.93 |
| lignin-FDA-ZnDES | 12.35 | 12.15615 | 0.0086 | 0.94884 | 17.85 | 14.82539 | 0.000631 | 0.916 | 21.87 |
| lignin-DCX-FeDES | 8.11 | 8.4909 | 0.00848 | 0.93853 | 23.40 | 10.39928 | 0.000874 | 0.890 | 27.95 |
| lignin-BCMBP-FeDES | 11.86 | 12.03576 | 0.00833 | 0.92939 | 27.59 | 14.81471 | 0.000593 | 0.882 | 32.33 |
| lignin-FDA-FeDES | 6.96 | 7.00814 | 0.00894 | 0.91085 | 32.83 | 8.51875 | 0.00114 | 0.856 | 38.01 |

From Table 6-7, the coefficient of determination ($R^2$) of pseudo-first order model ranged between 0.9 and 0.96 while that of pseudo-second order model is slightly lower (0.83-0.92). Additionally, the normalised standard deviation (Δq) of pseudo-first order model was relatively smaller than that of pseudo-first order model, aligning

with the fitting outcomes. Therefore, pseudo-first order model proved to be more suitable for predicting the $CO_2$ adsorption from mixed gas using lignin-based HCPs. However, we should be aware that such suitability is limited, in other words, a sole kinetic model shows insufficiency in accurately describing the $CO_2$ adsorption process. This indicated the complexity of the whole adsorption process which probably needs piecewise fitting analysis [75,76]. The piecewise fitting results were shown in Figure 6-15, the validity of the pseudo-second order model greatly increased after 150 seconds while the pseudo-first order model behaved better in describing the early stage of the $CO_2$ adsorption process. Similar phenomena were reported by Songolzadeh who modelled the $CO_2/N_2$ adsorption of zeolite 13X [77]. They found that pseudo-first order model suited better at primary seconds (below 100 seconds) while pseudo-second-order model had higher accuracy at average time (between 100 and 1000 seconds), suggesting the mechanism of $CO_2$ adsorption on zeolite 13X is complex. As previously reported, the pseudo-second order model is suitable for characterising adsorption processes associated with chemical adsorption, whereas the pseudo-first order model is observed to effectively describe adsorption processes on physical adsorbents [78,79]. This is because the pseudo-first order model is applicable in the case of low surface coverage, in which the adsorption rate is rapid due to the plenty of active adsorption sites on the surface of solid adsorbents [80]. The rate expression however converted to pseudo-second order after enough adsorbate loadings, suggesting the adsorption mechanism was dominated by chemical adsorption in this stage [81]. The oxygen-containing groups had higher affinity to $CO_2$ gas molecules and thus contributed to the $CO_2$ capacity. Previous research claimed that both the basicity and polarity of the oxygen-containing groups are beneficial for increasing their interactions with $CO_2$ molecules [82]. Notably, basicity is significantly more effective compared to polarity. With regard to above results, it can be concluded that the $CO_2$ adsorption in these lignin-based HCPs is complex. Both physical and chemical adsorption are involved, and they exhibited its dominance at different stages.

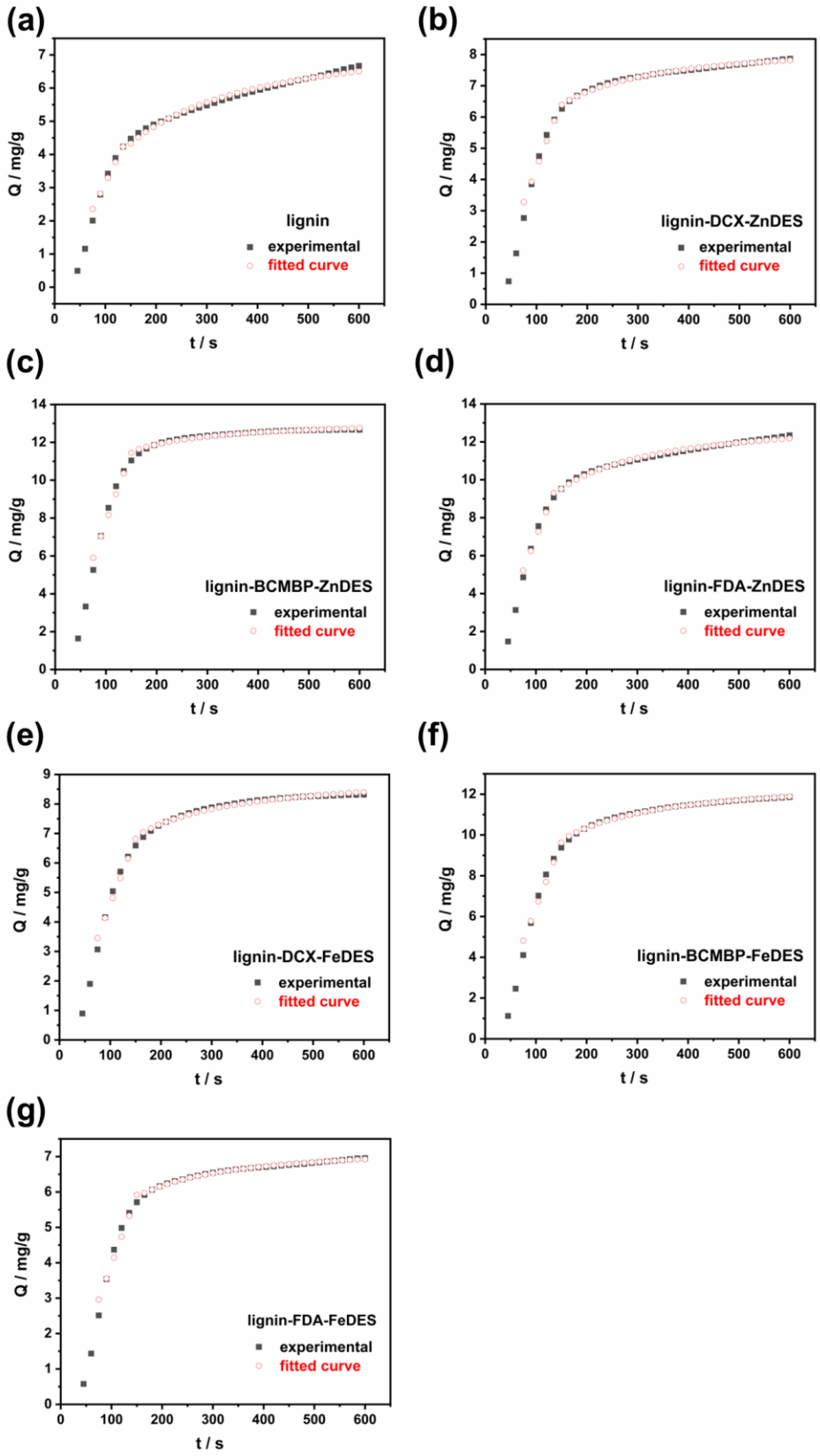


Figure 6-15: Piecewise fitting results of (a) pristine lignin, (b)lignin-DCX-ZnDES, (c) lignin-BCMBP-ZnDES, (d) lignin-FDA-ZnDES, (e) lignin-DCX-FeDES, (f) lignin-BCMBP-FeDES, (g) lignin-FDA-FeDES

### 6.2.4 Recovery of $CO_2$ using pressure swing adsorption (PSA) process

Pressure swing adsorption (PSA) process is widely used for gas separation and purification. Until now, equilibrium-based theories of PSA have been well-established for simulate the adsorption and desorption behaviours in the practical industrial separation [83]. To evaluate the recovery of $CO_2$ using above six lignin-based HCPs, PSA simulation was selected to identify the optimal operating conditions. The modelling and simulation of the PSA process followed a previous report [83]. More details can be found in Supporting Information.

Figure 6-16 showed the recovery of $CO_2$ from gas mixture that consists of 15 v/v % $CO_2$ and 85 v/v% $N_2$ when different desorption pressures ($P_L$) are applied in the purge step. The detailed recovery data were shown in Table 6-8. It is obvious that the recovery of $CO_2$ increases at a lower desorption pressure because larger amount of $CO_2$ is released from the adsorbents [84]. Generally, in five-step PSA cycle, the $CO_2$ recovery ratio of all materials experienced a notable decline, dropping from around 90% at the desorption pressure of 0.01 bar to a recovery rate of around 20% at 0.1 bar. Among the six lignin-based HCPs that synthesised in DESs, lignin-FDA-FeDES had the lowest $CO_2$ recovery, achieving only 83.9%. This can be explained from its $CO_2$ adsorption isotherm which is the closest to irreversible isotherm. Although it has the advantage of capturing $CO_2$ at very low relative pressure range, this proves to be a drawback from in terms of $CO_2$ recovery. It means desorbing $CO_2$ by reducing pressure could be hard. From this respect, lignin-DCX-FeDES came the next with a $CO_2$ recovery of 87.2%, while the remaining four HCPs exhibited slightly higher level around 88% due to their inferior $CO_2$ capture kinetics.

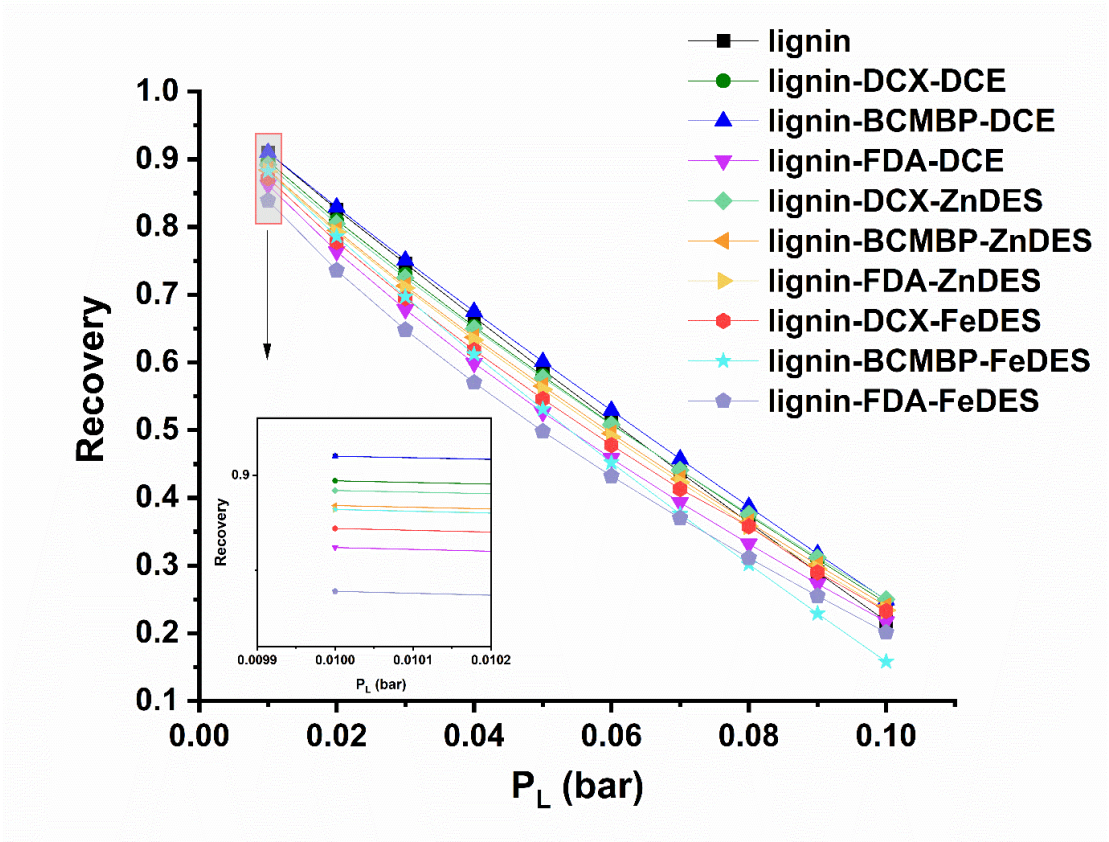


Figure 6-16: The recovery of $CO_2$ of lignin and all lignin-based HCPs from gas mixture that consists of 15 v/v % $CO_2$ and 85 v/v% $N_2$ when different desorption pressures ($P_L$) are applied in the purge step

Table 6-8: The recovery of lignin and all lignin-based HCPs from gas mixture that consists of 15 v/v % $CO_2$ and 85 v/v% $N_2$ when $P_L$=0.01 bar

| Sample | Recovery ($P_L$=0.01 bar) / % |
|---|---|
| lignin | 91 |
| lignin-DCX-DCE | 89.7 |
| lignin-BCMBP-DCE | 91 |
| lignin-FDA-DCE | 86.2 |
| lignin-DCX-ZnDES | 89.2 |
| lignin-BCMBP-ZnDES | 88.4 |
| lignin-FDA-ZnDES | 88.2 |
| lignin-DCX-FeDES | 87.2 |
| lignin-BCMBP-FeDES | 88.2 |
| lignin-FDA-FeDES | 83.9 |

Furthermore, our lignin-based HCPs exhibited comparable $CO_2$ recovery when comparing with several commercial adsorbents such as zeolite 13X [85], PSAO2 HP Molsiv™ [86], zeolite 4A BFK [87] and zeolite 5A BFK [88]. The $CO_2$ recovery of the four commercial adsorbents with the desorption pressure was calculated using the same method and shown in Figure 6-17 and compared with lignin-DCX-FeDES. Similarly, the diminishing trend in $CO_2$ recovery becomes particularly evident as the $P_L$ increases. This can be attributed to a reduced pressure differential between $P_L$ and original feed pressure, leading to a lower driving force for releasing the $CO_2$. Considering lignin-DCX-FeDES demonstrated moderate $CO_2$ uptake and outstanding $CO_2/N_2$ selectivity, it was chosen to compare with several commercial adsorbents. At the desorption pressure of 0.01 bar, the $CO_2$ recovery of above four representative adsorbents ranged from 56.5% to 86.5%. Lignin-DCX-FeDES, with a $CO_2$ recovery of 87.2%, exhibited comparable performance with zeolite 13X, a widely-recognised commercial adsorbent featuring both good $CO_2$ adsorption capacity and selectivity. The findings underlined the competitive nature of lignin-DCX-FeDES in terms of $CO_2$ recovery using pressure swing adsorption method, positioning it favourably among the developed adsorbents in this field.

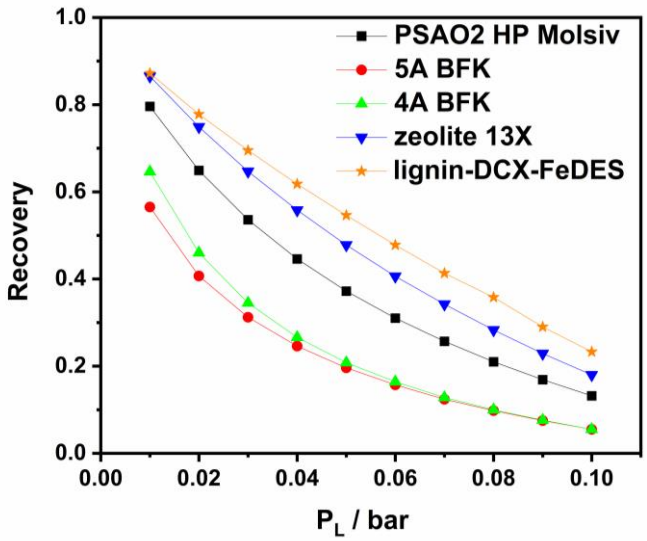


Figure 6-17: The recovery of $CO_2$ of four commercial adsorbents and lignin-DCX-FeDES from gas mixture that consists of 15 v/v % $CO_2$ and 85 v/v% $N_2$ when different desorption pressures ($P_L$) are applied in the purge step

## 6.3 Conclusion

In this work, low-cost lignin was crosslinked in two DESs, $[ChCl][ZnCl_2]_2$ and $[ChCl][FeCl_3]_2$, using different crosslinkers. By varying the DES and the crosslinker, the obtained lignin-based HCPs exhibited different pore size distribution. It was confirmed that hydroxylation and demethoxylation of lignin occurred alongside crosslinking. This created abundant oxygen groups that enhanced interactions with $CO_2$ gas molecules that favoured the $CO_2$ adsorption process. The theoretical $CO_2/N_2$ selectivity of all lignin-based HCPs developed in this work were calculated using the IAST method and a simulated gas mixture comprising 15 v/v % $CO_2$ and 85 v/v% $N_2$. These theoretical $CO_2/N_2$ selectivity values were compared with those obtained experimentally using a fixed bed reactor. Amongst all HCPs developed here, lignin-DCX-FeDES exhibited the highest pure gas $CO_2$ uptake of 18.1 $cm^3\ g^{-1}$ and a mixed gas $CO_2/N_2$ selectivity of 835. This exemplary $CO_2/N_2$ selectivity was due to a uniform and narrow micropore distribution, a lack of mesopores, and abundant oxygen-containing functional groups. I have successfully proved the feasibility of crosslinking macromolecules in DESs to optimise the pore size distribution of resultant HCPs for post-combustion carbon capture applications. Outcomes from this work can potentially deepen the understanding the interplay between $CO_2$ capture and the textural properties of adsorbents. I believe this work will pave the route towards transforming lignin by-products into high-performance adsorbents that can be applied in more separation applications.

## 6.4 References


[1] Vettoretti, G., et al., *Atmospheric CO2 control of spontaneous millennial-scale ice age climate oscillations.* Nature Geoscience, 2022. **15**(4): p. 300-306.

[2] Modak, A. and S. Jana, *Advances in porous adsorbents for CO2 capture and storage.* Carbon Dioxide Chemistry, Capture and Oil Recovery, 2018: p. 165-183.

[3] Pachauri, R.K., et al., *Climate change 2014: synthesis report. Contribution of Working Groups I, II and III to the fifth assessment report of the Intergovernmental Panel on Climate Change*. 2014: Ipcc.

[4] *National Oceanic and Atmospheric Administration & ESRL, Average carbon dioxide ($CO_2$) levels in the atmosphere worldwide from 1959 to 2022 (in parts per million) Statista*. 2023; Available from:

https://www.statista.com/statistics/1091926/atmospheric-concentration-of-co2-historic/

[5] Chao, C., et al., *Post-combustion carbon capture.* Renewable and Sustainable Energy Reviews, 2021. **138**: p. 110490.

[6] Alami, A.H., et al., *Materials and logistics for carbon dioxide capture, storage and utilization.* Science of the Total Environment, 2020. **717**: p. 137221.

[7] Dou, B., et al., *Solid sorbents for in-situ CO2 removal during sorption-enhanced steam reforming process: A review.* Renewable and Sustainable Energy Reviews, 2016. **53**: p. 536-546.

[8] Abd, A.A., et al., *Carbon dioxide removal through physical adsorption using carbonaceous and non-carbonaceous adsorbents: a review.* Journal of Environmental Chemical Engineering, 2020. **8**(5): p. 104142.

[9] Budzianowski, W., *Explorative analysis of advanced solvent processes for energy efficient carbon dioxide capture by gas–liquid absorption.* International Journal of Greenhouse Gas Control, 2016. **49**: p. 108-120.

[10] Theo, W.L., et al., *Review of pre-combustion capture and ionic liquid in carbon capture and storage.* Applied energy, 2016. **183**: p. 1633-1663.

[11] Sarmad, S., J.P. Mikkola, and X. Ji, *Carbon dioxide capture with ionic liquids and deep eutectic solvents: a new generation of sorbents.* ChemSusChem, 2017. **10**(2): p. 324-352.

[12] Sandru, M., et al., *Pilot scale testing of polymeric membranes for CO2 capture from coal fired power plants.* Energy Procedia, 2013. **37**: p. 6473-6480.

[13] Míguez, J.L., et al., *Technology evolution in membrane-based CCS.* Energies, 2018. **11**(11): p. 3153.

[14] Wang, L., et al., *CO2 capture from flue gas in an existing coal-fired power plant by two successive pilot-scale VPSA units.* Industrial & Engineering Chemistry Research, 2013. **52**(23): p. 7947-7955.

[15] Gutierrez-Ortega, A., et al., *A fast methodology to rank adsorbents for CO2 capture with temperature swing adsorption.* Chemical Engineering Journal, 2022. **435**: p. 134703.

[16] Siriwardane, R.V., et al., *Adsorption of CO2 on molecular sieves and activated carbon.* Energy & Fuels, 2001. **15**(2): p. 279-284.

[17] Bae, Y.S. and R.Q. Snurr, *Development and evaluation of porous materials for carbon dioxide separation and capture.* Angewandte Chemie International Edition, 2011. **50**(49): p. 11586-11596.

[18] Chen, C., J. Kim, and W.-S. Ahn, *CO 2 capture by amine-functionalized nanoporous materials: A review.* Korean Journal of Chemical Engineering, 2014. **31**: p. 1919-1934.

[19] Lin, Y., C. Kong, and L. Chen, *Amine-functionalized metal–organic frameworks: structure, synthesis and applications.* RSC advances, 2016. **6**(39): p. 32598-32614.

[20] Choi, S., et al., *Modification of the Mg/DOBDC MOF with amines to enhance CO2 adsorption from ultradilute gases.* The Journal of Physical Chemistry Letters, 2012. **3**(9): p. 1136-1141.

[21] Fayemiwo, K.A., et al., *Nitrogen-rich hyper-crosslinked polymers for low-pressure CO2 capture.* Chemical Engineering Journal, 2018. **334**: p. 2004-2013.

[22] Tan, J., et al., *Mixture absorption system of monoethanolamine− triethylene glycol for CO2 capture.* Industrial & engineering chemistry research, 2011. **50**(7): p. 3966-3976.

[23] Wang, S., et al., *Prediction by convolutional neural networks of CO2/N2 selectivity in porous carbons from N2 adsorption isotherm at 77 K.* Angewandte Chemie International Edition, 2020. **59**(44): p. 19645-19648.

[24] Wang, X., et al., *Reversed CO2/C2H2 separation with ultrahigh carbon dioxide adsorption capacity in Zn-based pillared metal-organic frameworks.* Journal of Solid State Chemistry, 2023. **327**: p. 124280.

[25] Nguyen, T.T., et al., *Separation of CO2 and N2 on a hydrophobic metal organic framework CALF-20.* Chemical Engineering Journal, 2022. **442**: p. 136263.

[26] Gaikwad, S., S.-J. Kim, and S. Han, *Novel metal–organic framework of UTSA-16 (Zn) synthesized by a microwave method: Outstanding performance for CO2 capture with improved stability to acid gases.* Journal of Industrial and Engineering Chemistry, 2020. **87**: p. 250-263.

[27] Chanchaona, N., et al., *Flow synthesis of hypercrosslinked polymers with additional microporosity that enhances CO 2/N 2 separation.* Journal of Materials Chemistry A, 2023. **11**(18): p. 9859-9867.

[28] Didas, S.A., et al., *Role of amine structure on carbon dioxide adsorption from ultradilute gas streams such as ambient air.* ChemSusChem, 2012. **5**(10): p. 2058-2064.

[29] Mason, C.R., et al., *Enhancement of CO2 affinity in a polymer of intrinsic microporosity by amine modification.* Macromolecules, 2014. **47**(3): p. 1021-1029.

[30] Lu, W., et al., *Sulfonate-grafted porous polymer networks for preferential CO2 adsorption at low pressure.* Journal of the American Chemical Society, 2011. **133**(45): p. 18126-18129.

[31] Yang, Y., et al., *Functional microporous polyimides based on sulfonated binaphthalene dianhydride for uptake and separation of carbon dioxide and vapors.* Journal of Materials Chemistry A, 2013. **1**(35): p. 10368-10374.

[32] Di Biase, E. and L. Sarkisov, *Systematic development of predictive molecular models of high surface area activated carbons for adsorption applications.* Carbon, 2013. **64**: p. 262-280.

[33] Liu, Y., Z.U. Wang, and H.C. Zhou, *Recent advances in carbon dioxide capture with metal-organic frameworks.* Greenhouse Gases: Science and Technology, 2012. **2**(4): p. 239-259.

[34] Schutyser, W., et al., *Chemicals from lignin: an interplay of lignocellulose fractionation, depolymerisation, and upgrading.* Chemical society reviews, 2018. **47**(3): p. 852-908.

[35] *Global Lignin Market Report 2023: Industry Developments 2020-2023 and Market Demand Forecasts to 2033*. 2023, Research and Markets.

[36] Supanchaiyamat, N., et al., *Lignin materials for adsorption: Current trend, perspectives and opportunities.* Bioresource Technology, 2019. **272**: p. 570-581.

[37] Meng, Q.B. and J. Weber, *Lignin-based microporous materials as selective adsorbents for carbon dioxide separation.* ChemSusChem, 2014. **7**(12): p. 3312-3318.

[38] Tang, C., et al., *Weaving Hyper-crosslinked Polymer from Alkaline Lignin for Adsorption of Organic Dyes from Wastewater.* ChemistrySelect, 2022. **7**(31): p. e202200638.

[39] Sun, L., et al., *One-pot fabrication of lignin-based aromatic porous polymers for efficient removal of bisphenol AF from water.* International Journal of Biological Macromolecules, 2021. **175**: p. 396-405.

[40] Chung, H. and N.R. Washburn, *Chemistry of lignin-based materials.* Green materials, 2013. **1**(3): p. 137-160.

[41] Mei, Q., et al., *Selective utilization of the methoxy group in lignin to produce acetic acid.* Angewandte Chemie International Edition, 2017. **56**(47): p. 14868-14872.

[42] Kazzaz, A.E., Z.H. Feizi, and P. Fatehi, *Grafting strategies for hydroxy groups of lignin for producing materials.* Green Chemistry, 2019. **21**(21): p. 5714-5752.

[43] Dong, X., et al., *Recycling plastic waste for environmental remediation in water purification and CO2 capture.* ACS Applied Polymer Materials, 2020. **2**(7): p. 2586-2593.

[44] Wheeler, O.H., *Near infrared spectra of organic compounds.* Chemical Reviews, 1959. **59**(4): p. 629-666.

[45] Zhou, L., et al., *Enhanced recovery of acetophenone and 1-phenylethanol from petrochemical effluent by highly porous starch-based hypercrosslinked polymers.* Chemical Engineering Journal, 2021. **418**: p. 129351.

[46] Olmos, D., E. Martín, and J. González-Benito, *New molecular-scale information on polystyrene dynamics in PS and PS–BaTiO 3 composites from FTIR spectroscopy.* Physical Chemistry Chemical Physics, 2014. **16**(44): p. 24339-24349.

[47] Katahira, R., T.J. Elder, and G.T. Beckham, *A brief introduction to lignin structure.* 2018.

[48] Mao, J., et al., *Differences between lignin in unprocessed wood, milled wood, mutant wood, and extracted lignin detected by 13C solid-state NMR.* Journal of agricultural and food chemistry, 2006. **54**(26): p. 9677-9686.

[49] Liu, L.-Y., et al., *Valorization of bark using ethanol–water organosolv treatment: Isolation and characterization of crude lignin.* ACS Sustainable Chemistry & Engineering, 2020. **8**(12): p. 4745-4754.

[50] Hong, S., et al., *Zinc-based deep eutectic solvent-mediated hydroxylation and demethoxylation of lignin for the production of wood adhesive.* RSC advances, 2016. **6**(92): p. 89599-89608.

[51] Martín, C.F., et al., *Hypercrosslinked organic polymer networks as potential adsorbents for pre-combustion CO 2 capture.* Journal of Materials Chemistry, 2011. **21**(14): p. 5475-5483.

[52] Thommes, M., et al., *Physisorption of gases, with special reference to the evaluation of surface area and pore size distribution (IUPAC Technical Report).* Pure and applied chemistry, 2015. **87**(9-10): p. 1051-1069.

[53] Bardestani, R. and S. Kaliaguine, *Steam activation and mild air oxidation of vacuum pyrolysis biochar.* Biomass and Bioenergy, 2018. **108**: p. 101-112.

[54] Rouquerol, J., et al., *Adsorption by powders and porous solids: principles, methodology and applications*. 2013: Academic press.

[55] Thommes, M. and K.A. Cychosz, *Physical adsorption characterization of nanoporous materials: progress and challenges.* Adsorption, 2014. **20**(2-3): p. 233-250.

[56] Hedin, N., et al., *Adsorbents for the post-combustion capture of CO2 using rapid temperature swing or vacuum swing adsorption.* Applied Energy, 2013. **104**: p. 418-433.

[57] Yang, R.T., *Gas separation by adsorption processes*. Vol. 1. 1997: World Scientific.

[58] Fraux, G., et al., *On the use of the IAST method for gas separation studies in porous materials with gate-opening behavior.* Adsorption, 2018. **24**: p. 233-241.

[59] Mason, J.A., et al., *Evaluating metal–organic frameworks for post-combustion carbon dioxide capture via temperature swing adsorption.* Energy & Environmental Science, 2011. **4**(8): p. 3030-3040.

[60] Chen, D., et al., *Hyper-crosslinked aromatic polymers with improved microporosity for enhanced CO 2/N 2 and CO 2/CH 4 selectivity.* New Journal of Chemistry, 2017. **41**(14): p. 6834-6839.

[61] Raganati, F., et al., *Kinetic study and breakthrough analysis of the hybrid physical/chemical CO2 adsorption/desorption behavior of a magnetite-based sorbent.* Chemical Engineering Journal, 2019. **372**: p. 526-535.

[62] Goel, C., et al., *Pure and Binary Gas Adsorption Equilibrium for CO2–N2 on Oxygen Enriched Nanostructured Carbon Adsorbents.* Energy & Fuels, 2017. **31**(12): p. 13991-13998.

[63] Samanta, A., et al., *Post-combustion CO2 capture using solid sorbents: a review.* Industrial & Engineering Chemistry Research, 2012. **51**(4): p. 1438-1463.

[64] Watabe, T. and K. Yogo, *Isotherms and isosteric heats of adsorption for CO2 in amine-functionalized mesoporous silicas.* Separation and Purification Technology, 2013. **120**: p. 20-23.

[65] Lv, D., et al., *Ultrahigh CO2/CH4 and CO2/N2 adsorption selectivities on a cost-effectively L-aspartic acid based metal-organic framework.* Chemical Engineering Journal, 2019. **375**: p. 122074.

[66] Oschatz, M. and M. Antonietti, *A search for selectivity to enable CO 2 capture with porous adsorbents.* Energy & Environmental Science, 2018. **11**(1): p. 57-70.

[67] Szufla, M., et al., *Flattening of a Bent Sulfonated MOF Linker: Impact on Structures, Flexibility, Gas Adsorption, CO2/N2 Selectivity, and Proton Conduction.* Inorganic Chemistry, 2023.

[68] Deng, H., et al., *Adsorption equilibrium for sulfur dioxide, nitric oxide, carbon dioxide, nitrogen on 13X and 5A zeolites.* Chemical Engineering Journal, 2012. **188**: p. 77-85.

[69] Bell, J.G., M.J. Benham, and K.M. Thomas, *Adsorption of carbon dioxide, water vapor, nitrogen, and sulfur dioxide on activated carbon for capture from flue gases: Competitive adsorption and selectivity aspects.* Energy & Fuels, 2021. **35**(9): p. 8102-8116.

[70] Harlick, P. and F. Tezel, *Adsorption of carbon dioxide, methane and nitrogen: pure and binary mixture adsorption for ZSM-5 with SiO2/Al2O3 ratio of 280.* Separation and purification technology, 2003. **33**(2): p. 199-210.

[71] Gharagheizi, F. and D.S. Sholl, *Comprehensive assessment of the accuracy of the ideal adsorbed solution theory for predicting binary adsorption of gas mixtures in porous materials.* Industrial & Engineering Chemistry Research, 2021. **61**(1): p. 727-739.

[72] Rashidi, N.A., S. Yusup, and B.H. Hameed, *Kinetic studies on carbon dioxide capture using lignocellulosic based activated carbon.* Energy, 2013. **61**: p. 440-446.

[73] Kumar, K.V. and S. Sivanesan, *Selection of optimum sorption kinetics: comparison of linear and non-linear method.* Journal of hazardous materials, 2006. **134**(1-3): p. 277-279.

[74] Singh, V.K. and E.A. Kumar, *Measurement of CO2 adsorption kinetics on activated carbons suitable for gas storage systems.* Greenhouse Gases: Science and Technology, 2017. **7**(1): p. 182-201.

[75] Li, Y., et al., *Nitrogen-doped hierarchically constructed interconnected porous carbon nanofibers derived from polyaniline (PANI) for highly selective CO2 capture and effective methanol adsorption.* Journal of Environmental Chemical Engineering, 2022. **10**(6): p. 108847.

[76] Simonin, J.-P., *On the comparison of pseudo-first order and pseudo-second order rate laws in the modeling of adsorption kinetics.* Chemical Engineering Journal, 2016. **300**: p. 254-263.

[77] Songolzadeh, M., M. Soleimani, and M.T. Ravanchi, *Using modified Avrami kinetic and two component isotherm equation for modeling of CO2/N2 adsorption over a 13X zeolite bed.* Journal of Natural Gas Science and Engineering, 2015. **27**: p. 831-841.

[78] Serna-Guerrero, R. and A. Sayari, *Modeling adsorption of CO2 on amine-functionalized mesoporous silica. 2: Kinetics and breakthrough curves.* Chemical Engineering Journal, 2010. **161**(1-2): p. 182-190.

[79] Borah, J.M., J. Sarma, and S. Mahiuddin, *Adsorption comparison at the α-alumina/water interface: 3, 4-Dihydroxybenzoic acid vs. catechol.* Colloids and Surfaces A: Physicochemical and Engineering Aspects, 2011. **387**(1-3): p. 50-56.

[80] Ho, Y. and G. McKay, *The kinetics of sorption of basic dyes from aqueous solution by sphagnum moss peat.* The Canadian journal of chemical engineering, 1998. **76**(4): p. 822-827.

[81] Ho, Y.-S., *Review of second-order models for adsorption systems.* Journal of hazardous materials, 2006. **136**(3): p. 681-689.

[82] Dang, Y., et al., *Molecular simulation of CO2/CH4 adsorption in brown coal: Effect of oxygen-, nitrogen-, and sulfur-containing functional groups.* Applied Surface Science, 2017. **423**: p. 33-42.

[83] Kayser, J.C. and K.S. Knaebel, *Pressure swing adsorption: development of an equilibrium theory for binary gas mixtures with nonlinear isotherms.* Chemical engineering science, 1989. **44**(1): p. 1-8.

[84] Huang, W.-J., C.-Y. Chen, and C.-T. Chou, *Concentration and recovery of SO2 from flue gas by pressure swing adsorption.* Journal of the Chinese Institute of Chemical Engineers, 2006. **37**(2): p. 149-157.

[85] Cavenati, S., C.A. Grande, and A.E. Rodrigues, *Adsorption equilibrium of methane, carbon dioxide, and nitrogen on zeolite 13X at high pressures.* Journal of Chemical & Engineering Data, 2004. **49**(4): p. 1095-1101.

[86] Xiao, P., et al., *Capture of CO 2 from flue gas streams with zeolite 13X by vacuum-pressure swing adsorption.* Adsorption, 2008. **14**: p. 575-582.

[87] Seabra, R., et al., *Adsorption equilibrium and kinetics of carbon dioxide, methane and nitrogen on binderless zeolite 4A adsorbents.* Microporous and Mesoporous Materials, 2019. **277**: p. 105-114.

[88] Mendes, P.A., et al., *Separation of CO2/N2 on binderless 5A zeolite.* Journal of CO2 utilization, 2017. **20**: p. 224-233.

# Chapter 7 Conclusion and Outlook

## 7.1 Conclusion

The development of hypercrosslinked polymers has flourished rapidly since Davankov and Tsyuruna first proposed the synthetic route to produce HCPs following Friedel-Crafts chemistry. Various HCPs have emerged as adsorbents due to their highly-porous structure, tailorable surface end and good stability in harsh environments. Although most researchers still dedicate to developing new advanced HCPs, the challenges of preparing processable and sustainable HCPs desire careful consideration and innovative approaches. These factors are critical for the long-term development and large-scale promotion of HCPs.

This thesis aims at converting the synthesis of HCPs into a controllable, processable and green manner. Here, in this thesis, three main contributions have been achieved:

(1) Porous hypercrosslinked HIPS HCPs monoliths with user-defined shapes were produced via the combination of 3D printing and adjustable 2-step crosslinking strategy. By controlling the crosslinking durations of each step, the final HCPs monoliths successfully maintained the macroscopic structure and mechanical strength simultaneously. This combination protocol is expected to work for all PS-based filaments and the proportion of PS units will highly decide the properties of final HCPs. Notably, in the adsorption of taxadiene, these HIPS HCPs monoliths revealed to stimulate the yield of taxadiene by 51% via *in-situ* adsorption and promote the generation of target products. The capacity of HIPS HCP-12h-2h (SA: 337 $m^2$ $g^{-1}$) for taxadiene reached 20 mg $L^{-1}$, almost comparable to that of the commercial HP-20 resins.

(2) Sustainable deep eutectic solvents that containing metal halides were proved to be suitable for yielding HCPs from different types of starting materials such as dichloro-molecules, aromatic molecules and even bio-derived lignin. DESs can serve as both solvent and catalyst at the same time due to its Lewis acid component. DESs exhibited their superiority in forming narrower micropores than

that in conventional halogenated solvents, contributing to the better $CO_2/N_2$ selectivity. The narrower pore size distributions of HCPs synthesized in DES enhanced $CO_2/N_2$ selectivity at 273 K and 1 atm by 7.5-fold, reaching 105.

(3) The application of DESs has been firstly extended to polymer chemistry based on Fridel-Crafts alkylation. Sustainable lignin-based HCPs have been successfully prepared by varying the crosslinkers in different DESs. Among all samples, lignin-DCX HCPs exhibited quasi-unimodal comprising pores < 5 nm, resulting in a dramatically high $CO_2/N_2$ selectivity up to 835.

(4) The relationship between the textural properties of HCPs and their gas separation performance was deeply studied via IAST calculations. IAST method can be used to simulate $CO_2/N_2$ selectivity from the gas adsorption isotherms of each pure component. The HCPs synthesised in DESs exhibited remarkable affinity to $CO_2$ molecules due to the narrow pore size distribution. Besides that, the $CO_2/N_2$ selectivity obtained from the real binary gas mixtures can also provide strong support to the reliability of IAST method except the case that the $N_2$ net adsorption amount of the material is ultralow. IAST simulations may vary from the realistic situation when the adsorption for the gas component with less-affinity is weak.

## 7.2 Outlook

The fast growth in the advanced HCPs materials has been highly appreciated since Friedel-Crafts reactions were used for crosslinking polymers. However, the development of HCPs slowed down due to several barriers that impede the long-term development. Basically, the fast kinetics of Lewis acid catalysed Friedel-Crafts reactions decide that HCPs have irregular pore structures, which are characteristic of HCPs. While this hierarchical pore structure enhances gas uptake through microporosity, the wide pore size distribution often leads to lower $CO_2/N_2$ selectivity compared to other microporous materials. Additionally, the rigid hypercrosslinked polymer networks typically cause HCPs to exist as powders, hindering the wide

application and promotion of HCPs. Furthermore, the use of halogenated solvents, common in reported literature for Friedel-Crafts reactions, exacerbates reaction uncontrollability and has negative environmental impacts.

To address these mentioned limitations, this thesis proposed to combine 3D printing technology and stepwise crosslinking to obtain specific HCPs monoliths. However, this protocol can only work for polystyrene-based filaments due to the limited choice of commercial filaments on the market. More efforts are required for developing more versatile strategy to produce processable HCPs that can satisfy more application scenario.

When it comes to the sustainability of HCPs production, metal halides containing deep eutectic solvents such as [ChCl][$ZnCl_2$]$_2$ and [ChCl][$FeCl_3$]$_2$ have been demonstrated as feasible alternatives for halogenated solvents. Such DESs outperformed in their benefits of yielding ultranarrow pores, bringing great enhancement in the gas selectivity. However, the precise reaction pathway on the active catalyst sites is yet to be confirmed. Therefore, the full investigation on the reaction mechanism for HCPs in different DESs and even other alternatives is a potential research branch. With the increasing understanding of the roles of DESs in the crosslinking reaction, it will undoubtedly provide guidance for the selection of suitable precursors and the molecular design of advanced HCPs. In addition, the reaction rates of DESs systems are comparatively slower, indicating its potential in the preparing processable HCPs, soluble HCPs and even lamellar HCPs which are attractive to researchers worldwide.

Finally, it is also crucial to consider the economic costs associated with the production of HCPs. While advancements in synthesis methods and the use of alternative solvents aim to address environmental concerns, the economic feasibility of large-scale production remains an important consideration. Developing cost-effective synthetic routes and recycle the reaction components are essential for realizing the full potential of HCPs in various industrial applications.